Universiteit Gent

Faculteit Wetenschappen

Vakgroep Vastestofwetenschappen

Sputter Deposition of MgO Thin Films:

The Effect of Cation Substitution

Thesis submitted to obtain the academic degree of

Doctor in Sciences: Physics

Advisor: Prof. Dr. Diederik Depla

April 2012

Marta Saraiva

DRAFT

Reading Committee:

Prof. Dr. Albano Cavaleiro

Prof. Em. Dr. ir. Roger De Gryse

Prof. Dr. Philippe Smet

Examination Committee:

Prof. Dr. Freddy Callens

Prof. Dr. Albano Cavaleiro

Prof. Dr. Diederik Depla

Prof. Em. Dr. ir. Roger De Gryse

Dr. Stijn Mahieu

Prof. Dr. Philippe Smet

Prof. Dr. Isabel Van Driessche

Prof. Dr. Gustaaf Van Tendeloo

"Eles não sabem, nem sonham,

Que o sonho comanda a vida,

Que sempre que um homem sonha

O mundo pula e avança

Como bola colorida

Entre as mãos de uma criança."

"They do not know, not even dream,

That dream commands life,

That whenever a person dreams,

The world leaps and moves forward

Like a colorful ball

In the hands of a child."

António Gedeão

Motivation....1
References....4
A. Magnetron Sputtering and Film Growth: Background and Concepts....7
1. Magnetron Sputter Deposition of Films....7
1.1. Introduction....7
1.2. Ion-Target Interactions....7
1.2.1. Sputter Yield....9
1.2.2. Energy and Angular Distribution of the Sputtered Particles....11
1.3. Principles of Magnetron Sputtering....12
1.4. Reactive Magnetron Sputtering....15
2. Thin film growth....17
2.1. Introduction....17
2.2. Adsorption....17
2.3. Surface Diffusion....19
2.4. Nucleation and early stages of film growth....21
2.4.1. Deposition Rate and Temperature....23
2.4.2. Film Growth Modes....24
2.4.3. Accounting for Kinetics....26
2.5. From Nucleation to Film Thickening....27
2.5.1. Crystal Growth....27
2.5.2. Grain Growth....28
2.6. Film Thickening....30
2.7. Structure Zone Models....31
2.7.1. Basic Structure Zone Model....31
2.7.2. Influence of Impurities....35
References....38
B. Stoichiometry....41
3. Stoichiometry....41
3.1. Introduction....41
3.1.1. Thin Film Preparation....41
3.1.2. Electron Probe Micro-Analysis....45
3.1.3. Simulation of Metal Transport: SIMTRA....46
3.2. Chemical Composition....46

References....52
C. Crystallographic Properties....53
4. Introduction....53
4.1. X-ray Diffraction....54
4.1.1. Texture Analysis....56
4.1.2. Crystallinity....57
4.1.3. In-situ XRD....58
4.2. Transmission Electron Microscopy....58
4.2.1. Electron Diffraction....59
4.2.2. High Resolution Transmission Electron Microscopy....60
4.2.3. Electron Energy –Loss Spectroscopy....60
4.3. Scanning Electron Microscopy....60
4.4. Molecular Dynamic (MD) Simulations....61
5. Morphology and Angular Scans....64
5.1. Mg-Mg-O Films....64
5.2. Mg-M-O films....65
5.2.1. Mg-M-O Films (with M = Al, Cr, Ti and Zr)....65
5.2.2. The Mg-Y-O System....68
5.2.3. Change in the MgO Lattice Parameter....70
6. From Crystalline to Amorphous....71
6.1. A Simple Geometric Model....74
6.2. Packing Density and Crystalline-to-Amorphous Transition....76
6.2.1. Hard Sphere Model....77
6.2.2. Calculating Packing Density....78
6.2.3. Crystallinity vs. Packing Density....81
6.2.4. Conclusions....83
7. Biaxial Alignment....85
7.1. In-Plane Alignment....86
7.1.1. Mg-Mg-O Films....86
7.1.2. Mg-M-O Films....87
7.1.3. In-Plane Alignment Growth Mechanism....91
7.2. Out-of-Plane Alignment....93
7.3. Effect of M concentration and Atomic Size....94

7.4. Conclusions....98
8. High Temperature Deposition and *Post*-Deposition Heat Treatment....99
8.1. Deposition at High Temperature....99
8.1.1. MgO....99
8.1.2. Mg-Al-O and Mg-Cr-O....100
8.2. *Post*-Deposition Heat Treatments....103
8.2.1. *Ex-Situ* Heat Treatments....103
8.2.2. *In-Situ* Heat Treatment....104
References....108
D. Composition-Structure-Property Relations....111
9. Experimental Techniques....111
9.1. Nanoindentation....111
9.2. VUV-UV-VIS-NIR Spectrophotometry....113
9.3. Impedance Spectroscopy....114
9.4. Contact Angle Measurements....115
9.5. Atomic Force Microscopy....116
10. Functional Properties....118
10.1. Experimental Observations....118
10.2. Influence of Chemical Composition and Crystallinity....121
References....125
Summary....127
Samenvatting....131
Appendices....135
A. Mg-M-O Stoichiometry....135
B. ICDD Data Information....137
C. Publication List....140
Acknowledgments....143

Motivation

The importance of thin films relies on their ability to modify in an easy and, in most cases, cost efficient way the surface properties of bulk materials and thus, their functionality. Furthermore, thin films are commonly synthesized far from equilibrium, which may give rise to metastable configurations with unique attributes. These cannot be achieved in bulk materials synthesized by close-to-equilibrium techniques. Thin films have been deposited already for long time. Their era started with the deposition of elemental films, continuing through binary compounds to complex alloys. To this purpose a vast number of deposition techniques have been used: (i) conduction and diffusion processes, such as the well-known anodization, (ii) chemical processes, among which the chemical vapor deposition, (iii) wet processes (e.g. spin coating), (iv) spraying processes and (iv) physical vapor deposition which encompasses a large number of techniques in the areas of evaporation and sputter deposition. The selection of the deposition process depends on the material to be coated and on the desired film properties. When one deposition process cannot meet all requirements, hybrid processes may be used. Nowadays, the majority of the films are deposited from the vapor phase. The vapor can be provided as a gas precursor (chemical vapor deposition – CVD) or generated from a solid (or liquid) source (physical vapor deposition – PVD). In the latter case (PVD), the vapor is generated either by transferring thermal and/or electrical energy to the solid source (evaporation techniques such as electron beam, thermal and arc evaporation), or by momentum transfer using energetic species (ions, neutral) to a solid surface. This phenomenon is known as sputtering and the solid vapor source is referred to as target.

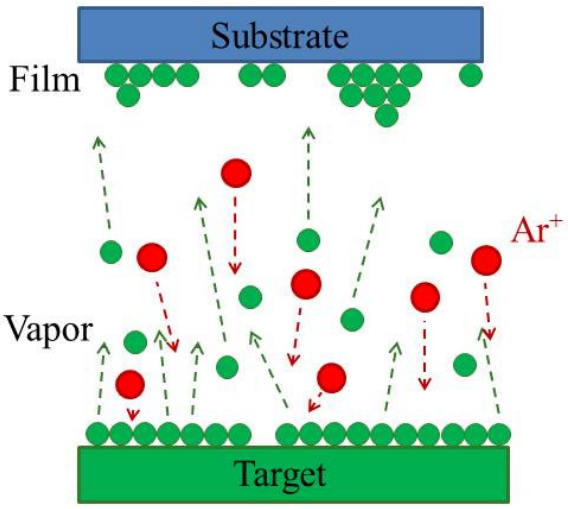

Figure 1: Schematic representation of the sputter deposition process.

In sputter deposition processes (figure 1), ions are commonly employed as energetic species because their energy can be easily controlled by using electric fields. Ions can be provided by an ion source but the most common way is by ionizing inert gas (typically Ar) atoms (i.e. generating a glow discharge/plasma) in an evacuated vessel (referred to as chamber). The

inert gas ionization occurs by applying a potential difference between the target (serving as a cathode) and an anode. Then positively charged Ar ions are accelerated towards the cathode (negatively biased) providing the energy and momentum necessary for sputtering. Magnetic fields can be used along with an electric field to confine the plasma close to the target and improve efficiency of the process. Reactive gases can be added to trigger chemical reactions (primarily on the substrate surface) and thus facilitate synthesis of multicomponent (compound) films. Sputter deposition is a widely used technique, since it combines versatility, control over the composition and microstructure, relatively high deposition rates and conceptual simplicity. Moreover it has the advantage of scalability, to develop deposition processes and films on a laboratory and transfer them to an industrial environment.

As discussed by Willmott *et al.*[1] and Plummer,[2] most of the new technologically interesting materials have a complex chemistry and crystalline structure. An example of the increased complexity is the ternary metal oxides of the group Mg-M-O, where M represents a metal other than Mg. This class of materials has gained considerable research attention the last years and Mg-M-O films find application in catalysis[3,4] and surface protection,[5-8] as well as in high-k dielectrics,[9,10] ionic conductors,[11-14] high T_c superconductors,[15] and thin film batteries.[16-18] Parallel to the increase of complexity of the materials that can be synthesized, research effort has been devoted towards understanding the fundamental atomistic mechanisms that determine growth, structure formation and phase composition in ternary metal oxides. During this course, one of the challenges encountered in the synthesis of multielement oxides was the necessity for precise control of the atomic composition,[1,19] since the latter has dramatic influence on the crystal structure and thus the physical attributes of films thereof. Seeking for strategies that facilitate efficient control over the film composition, researchers have been using one multielement material source when implementing, for example, pulsed laser or magnetron sputter deposition for the growth of multicomponent films.[20-23] In the latter case, it is well known that this approach does not always guarantee compositional control due to the transport of the sputter species through the buffer gas (where the sputtered species may collide and be scattered).[24] Moreover, preferential sputtering by energetic particles during thin film growth - i.e. the fact that different atoms in a compound material may exhibit different sputtering yield – may also contribute to the loss of compositional control. Nonetheless, sputtering from compound targets is commonly used in industrial environments due to its simplicity. On the other hand, for research purposes, a multi-source approach with elemental material sources provides larger flexibility with respect to the control over the composition of the deposited films.[25-27] The present research utilizes this approach to synthesize Mg-M-O films by employing reactive magnetron sputtering (in an Ar-O_2 atmosphere) from a Mg and a M source in a confocal (co-sputtering) arrangement. Along with the better control over the composition, the confocal arrangement generates an off-normal (with respect to the substrate surface) deposition flux. This is known from the literature to have implications for the film microstructure and crystallographic properties, e.g. it leads to deposition of films that exhibit both out-of-plane and in-plane crystallographic alignment (referred to as biaxial alignment.).[28-32] This has implications for the film functionality since, biaxial alignment of films with magnetic[33] and piezoelectric[34] properties has been shown to allow for enhancement

of the performance of the corresponding thin film devices. This feature, i.e. biaxial alignment, is not encountered when the flux of film forming species impinges normally on the substrate.

The overall goal of this research is to contribute towards the understanding of the fundamental growth mechanisms of confocally magnetron sputtered Mg-M-O thin films. The coexistence of two different metals, i.e., Mg and M, with differences in atomic sizes, number of valence electrons and surface mobility is very likely to affect the kinetics and the thermodynamics of film growth and thus, influence the crystallinity and texture of the films. Therefore, the metals (M) Al, Cr, Ti, Y and Zr are chosen to systematically vary the cation valence electron number and the atomic size. The specific objectives are to:

i) Establish the relation between the deposition conditions and the chemical composition in Mg-M-O films with the ultimate goal to control the film stoichiometry.

ii) Investigate the effect of the chemical composition on the currently unexplored structure formation and crystallographic properties of the Mg-M-O films.

iii) Explore the implications of chemistry and microstructure on other functional properties of Mg-M-O films, such as mechanical, electrical, and optical properties, surface topography and energetics.

References

[1] P. R. Willmott, Progress in Surface Science **76** (6-8), 163 (2004).

[2] E. W. Plummer, Ismail, R. Matzdorf, A. V. Melechko, and J. D. Zhang, Progress in Surface Science **67** (1-8), 17 (2001).

[3] J. I. Di Cosimo, V. K. Diez, M. Xu, E. Iglesia, and C. R. Apesteguia, Journal of Catalysis **178** (2), 499 (1998).

[4] S. A. Bocanegra, A. D. Ballarini, O. A. Scelza, and S. R. de Miguel, Materials Chemistry and Physics **111** (2-3), 534 (2008).

[5] G. Bingang, L. Chunliang, S. Zhongxiao, L. Liu, F. Yufeng, X. Xing, and F. Duowang, European Physical Journal-Applied Physics **36** (2), 111 (2006).

[6] N. Yoshida, Y. Takano, M. Yoshinaka, K. Hirota, and O. Yamaguchi, Journal of the American Ceramic Society **81** (8), 2213 (1998).

[7] D. Levchuk, H. Bolt, M. Dobeli, S. Eggenberger, B. Widrig, and J. Ramm, Surface & Coatings Technology **202** (20), 5043 (2008).

[8] J. Ramm, M. Ante, H. Brandle, A. Neels, A. Dommann, and M. Dobeli, Advanced Engineering Materials **9** (7), 604 (2007).

[9] Y. L. Zhao, Z. K. Jiao, and G. H. Gao, Acta Physica Sinica **52** (6), 1500 (2003).

[10] O. Auciello, Journal of Applied Physics **100** (5) (2006).

[11] S. Beg, N. A. S. Al-Areqi, and S. Haneef, Solid State Ionics **179** (39), 2260 (2008).

[12] E. Kendrick, M. S. Islam, and P. R. Slater, Journal of Materials Chemistry **17** (30), 3104 (2007).

[13] P. Laffez, X. Y. Chen, G. Banerjee, T. Pezeril, M. D. Rossell, G. Van Tendeloo, P. Lacorre, J. M. Liu, and Z. G. Liu, Thin Solid Films **500** (1-2), 27 (2006).

[14] Z. Zhuang, X. P. Wang, D. Li, T. Zhang, and Q. F. Fang, Journal of the American Ceramic Society **92** (4), 839 (2009).

[15] H. Hohl, C. Kloc, and E. Bucher, Journal of Solid State Chemistry **125** (2), 216 (1996).

[16] M. S. Tomar and K. A. Kuenhold, Disordered Materials - Current Developments - **223**, 229 (1996).

[17] A. Gies, B. Pecquenard, A. Benayad, H. Martinez, D. Gonbeau, H. Fuess, and A. Levasseur, Thin Solid Films **516** (21), 7271 (2008).

[18] S. W. Jin and H. N. G. Wadley, Journal of Vacuum Science & Technology A **26** (1), 114 (2008).

[19] Z. H. Barber, Journal of Materials Chemistry **16**, 334 (2006).

[20] A. Erlacher, A. Ambrico, G. Perna, L. Schiavulli, T. Ligonzo, H. Jaeger, and B. Ulrich, Applied Surface Science **248** (1-4), 402 (2005).

[21] S. M. Hamidi, M. M. Tehranchi, M. Ghanaatshoar, M. Moradi, and S. M. Mohseni, Journal of Non-Crystalline Solids **354** (47-51), 5178 (2008).

[22] P. R. Willmott and J. R. Huber, Reviews of Modern Physics **72** (1), 315 (2000).

[23] P. Barquinha, A. Pimentel, A. Marques, L. Pereira, R. Martins, and E. Fortunato, Journal of Non-Crystalline Solids **352** (9-20), 1749 (2006).

[24] J. Neidhardt, S. Mraz, J. M. Schneider, E. Strub, W. Bohne, B. Liedke, W. Moller, and C. Mitter, Journal of Applied Physics **104** (6) (2008).

[25] W. D. Sproul, D. J. Christie, and D. C. Carter, Thin Solid Films **491** (1-2), 1 (2005).

[26] W.D. Westwood, *Sputter Deposition*. (AVS Monograph Editor, Ottawa, 2003).

[27] J. Musil and P. Baroch, Ieee Transactions on Plasma Science **33** (2), 338 (2005).

[28] P. Ghekiere, S. Mahieu, G. De Winter, R. De Gryse, and D. Depla, Journal of Crystal Growth **271** (3-4), 462 (2004).

[29] Cho Jung-Min, Lee Kyoung-Ho, Cheon Chae Il, Cho Nam In, and Kim Jeong Seog, Journal of the European Ceramic Society **30** (2) (2010).

[30] K. Kishor Kumar, P. M. Raole, P. A. Rayjada, N. L. Chauhan, and S. Mukherjee, Surface & Coatings Technology **205**, S187 (2011).
[31] S. Mahieu, P. Ghekiere, D. Depla, and R. De Gryse, Thin Solid Films **515** (4), 1229 (2006).
[32] S. Mahieu, G. Buyle, P. Ghekiere, S. Heirwegh, R. De Gryse, and D. Depla, Thin Solid Films **515** (2), 416 (2006).
[33] U. Hannemann, S. Melcher, V. Neu, S. Fahler, B. Holzapfel, and L. Schultz, Ieee Transactions on Magnetics **39** (5), 2726 (2003).
[34] G. L. Messing, S. Trolier-McKinstry, E. M. Sabolsky, C. Duran, S. Kwon, B. Brahmaroutu, P. Park, H. Yilmaz, P. W. Rehrig, K. B. Eitel, E. Suvaci, M. Seabaugh, and K. S. Oh, Critical Reviews in Solid State and Materials Sciences **29** (2), 45 (2004).

A. Magnetron Sputtering and Film Growth: Background and Concepts

1. Magnetron Sputter Deposition of Films

1.1. Introduction

The impingement of an energetic particle (e.g. ion) on a solid material source (target) results in transfer of momentum and energy to the atoms of the target surface. If the energy gained by the surface atoms exceeds their displacement energy, a collision cascade in the bulk of the target may be initiated. This cascade may be terminated at a target surface atom and if the energy gained by the latter exceeds its binding energy with its surface counterparts, and if the atom is moving in the direction which leads it to the target surface, it is ejected.[a] This phenomenon is known as sputtering. The sputter deposition process is widely used nowadays for deposition of thin films and coatings. In sputter deposition an ion gun (ion beam sputtering) or plasma (diode sputtering) can be the sources of energetic particles. In the case of diode sputtering, a cathode (target) is held at a negative potential with respect to the substrate and the chamber walls. In the presence of a gas – normally a rare gas like Ar is used – a glow discharge (plasma) is created and Ar^+ ions are accelerated to the negatively biased cathode.

The current section serves as a brief introduction to the science and technology of sputter deposition. In section 1.2 the interactions between ions and target surface are explained and the basic quantities of the sputtering process – sputter yield, energy and angular distribution of the sputtered species – are derived. Section 1.3 deals with the sputtering technique that is most widely used nowadays for film deposition, i.e. the magnetron sputtering. Finally, section 1.4 presents the principles of reactive sputtering, i.e. sputtering in presence of a reactive gas that it is used for the synthesis of compound (multicomponent) films.

1.2. Ion-Target Interactions

The events occurring upon impingement of an ion (e.g. Ar^+) on the target surface are depicted in figure 1.1. Elastic collisions between the nuclei of the energetic ion and the target atoms, transfer part of the ion's kinetic energy to a single atom target. Depending on the ion energy, there are different possibilities; for low energy a single knock-on event occurs, while higher energy ions undergo multiple collisions before get incorporated in or leave the target. If an Ar^+ ion transfers sufficient energy to a target atom (larger than its displacement energy), the latter is displaced and collides with other target atoms. The series of collision caused by the impact of energetic ions is known as collision cascade. Most of the recoils are scattered forward (deeper into the target), however a fraction of the target atoms are backscattered. When the energy of the surface atom at the end of the cascade is higher than the surface

[a] Apart of atoms, molecules or even larger clusters might be ejected too.

binding energy, atoms, ions (positive and negative), molecules or even clusters are able to leave the target surface.

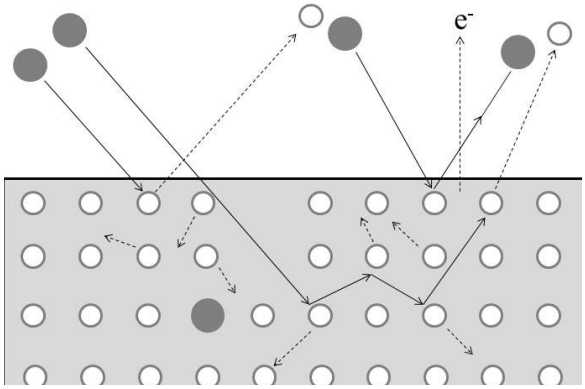

Figure 1.1: Schematic illustration of the ion-target interactions.

In addition, the Ar^+ ions can be trapped (or incorporated) in the target (ion implantation). As the sputtering process proceeds, most of the implanted Ar atoms diffuse from the target[1] and some are re-sputtered. Another alternative is that Ar^+ ions are back-reflected by the target surface. In this case, they are neutralized by an Auger electron and return to the vacuum chamber as neutral atoms. The energy with which the atoms return to the vacuum chamber can be calculated from the binary collision model, which describes the incidence of a moving plasma ion on a stationary target atom. The energy transferred to the backscattered ion E_b with respect to the energy of the incident ion E_i is given by the equation[2]:

$$\frac{E_b}{E_i} = \frac{4m_i m_t}{(m_i + m_t)^2}\left(\cos(\delta_{it})\right)^2, \qquad (1.1)$$

where m_i and m_t denote the masses of the impinging ion and the target atoms respectively, and δ_{it} specifies the travelling direction of the backscattered ion with respect to the initial velocity vector of the incident ion. The maximum of E_b/E_i is obtained for $m_i = m_t$.

Upon impingement, electrons can be ejected from the target to the vapor phase. The number of secondary electrons ejected from the cathode per incident ion is called the ion induced secondary electron emission (ISEE) yield and depends on the target material, energy[b] and type of bombarding particle. The secondary electron emission plays a very important role in the sustaining the glow discharge, since these electrons ionize the Ar atoms in the plasma and, therefore, are responsible for the plasma maintenance. The ionization proceeds through inelastic collisions between electrons and neutral gas atoms[c] that excite core-level or remove valence electrons from the neutrals, causing excitation or ionization, respectively.[3] The excitation of the Ar atoms can also lead to ionization (penning ionization mechanism).[3]

[b] The ISEE depends on the energy for kinetic emission, but not for potential, which is the main mechanism for energies below 1 keV.
[c] This is because of the mass difference between the electrons and the Ar atoms.

1.2.1. Sputter Yield

The sputter yield (Y) is the number of sputtered atoms per bombarding particle and it depends on the bombarding particle's kinetic energy, the surface binding energy of the target, the particle's nature and angle of incidence, target's material, and crystallographic orientation of the target.[4]

Over the years, a vast amount of sputter yield data has been published. Based on analytical models, semi-empirical formulas and computer simulation programs have been developed and published. The analytical formalization developed by Sigmund calculates the yield in a collision cascade by (i) determining the amount of energy deposited by energetic particles near the surface (ions and recoil atoms), (ii) following their collisions while they are converted into a number of low-energy recoil atoms (iii) determining how many of those atoms come to the surface and (iv) selecting the atoms that have sufficient energy to overcome the surface binding energy. A general analytical formula for the sputter yield reads:

$$Y(E) = \Lambda \alpha n_t S_n(E), \tag{1.2}$$

where Λ is a material constant that includes the range of a displaced target atom and the probability of ejection of an atom at the surface, α is a dimensionless correction factor that depends on the mass ratio $\frac{M_2}{M_1}$ in the elastic collision regime where M_1 and M_2 are the atomic masses of the impinging particles (ions) and of the target atoms, respectively, n_t is the atomic density of the target and $S_n(E)$ is the stopping power of the ion. This yield expression applies for low and high energy bombardment particles. For normal incidence of bombarding ions/particles with energies smaller than 1 keV, Equation (1.2) can be simplified to:

$$Y(E) = \left(\frac{3}{4\pi^2}\right)\alpha \frac{\gamma E^{1-2m}}{U_{sb}}, \tag{1.3}$$

in which γ is the energy transfer mass factor, E the energy of the impinging particle, U_{sb} is the surface binding energy of the target material, and the parameter m depends on the energy of the impinging ions and ranges from $m = 1$ at high energies (keV range) down to $m = 0$ at low energies (eV range).

An easier and faster approach to calculate the sputter yield is by using semi-empirical equations such as that developed by Yamamura et al.[5] The other alternative is simulations which describe the trajectory of the incident particles, the evolution of the cascade processes in the target and the ejection mechanism. As an example, binary collision Monte Carlo codes like SRIM,[6] and TRIDYN,[7] are available to simulate the sputter process and through this calculate the sputter yield. As figure 1.2 shows, there is a large scatter in the calculated sputter yields by these different approaches.

In order to surmount this problem of quantification, the sputter yields for the different target materials can be experimentally determined[d]. In a magnetron discharge, the average energy of

[d] Not all the sputter yields were measured by the author.

the ions bombarding the target is defined by the discharge voltage, V_d, and simulations have shown that this average ion energy E_i is approximately 75% of the discharge voltage.[8-10] The number of ions impinging on the target can be retrieved from the discharge current, I_d, and the effective secondary electron emission yield γ_{eff}.[11] Hence, by recording the discharge current during sputtering of a metal target in pure argon at constant discharge voltage, one can calculate the sputter yield at a given ion energy from the weight loss of the target, Δm, using the following equation,

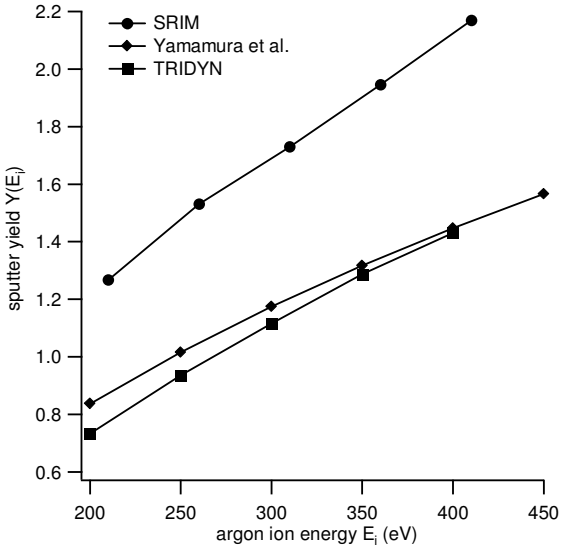

Figure 1.2: The sputter yield of Cu as a function of the argon incident ion energy, calculated with different approaches.

$$Y(E_i) = Y(0.75V_d) = \frac{\Delta m\, N_A}{M \dfrac{I_d}{e(1+\gamma_{\text{eff}})}}, \qquad (1.4)$$

with N_A the Avogadro constant, e the elementary charge and M the molar mass of the metal in amu. For some materials these experimentally determined sputter yields correspond very well to the calculated sputter yields.[8] However, for some other materials, like Mg, strong deviations from the simulations were observed. Probably, these deviations can be attributed to a strong influence of the (sometimes unknown) surface binding energy (due to target roughness and oxidation), and the unknown amount of incorporated Ar atoms in the metal target during sputtering.[12] Moreover, it has been demonstrated that for powder targets, taking into account the re-deposition of particles on the target due to the surface morphology results in a better agreement between experiments and calculations.[13] Figure 1.3 gives an overview of the experimental results obtained in this study, together with a linear fit through the experimental points. This linear dependence of sputter yield can be understood from the Sigmund theory as at these low energies m is approximately 0. Together with the small variation of the ion energy, this explains the linear behavior noticed in the discussed experiments, which is in agreement with results shown in literature.[14,15]

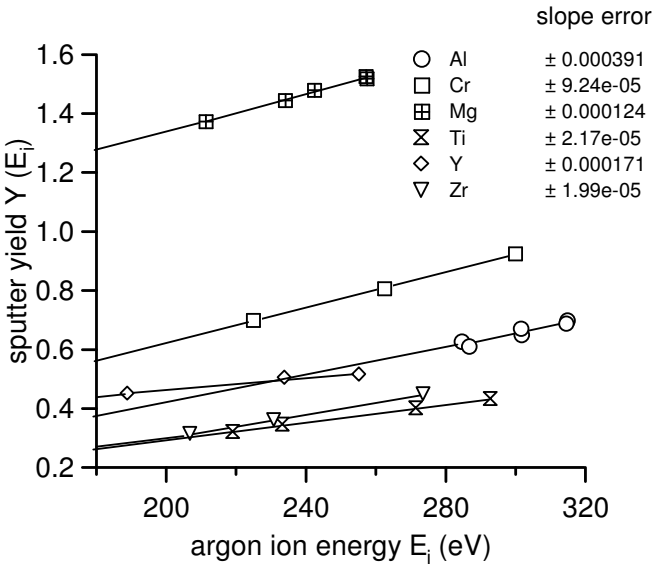

Figure1.3: Experimentally determined sputter yields for different elements. The lines are linear fits to the experimental points. The error on the slope of the linear fit is shown in the table.

1.2.2. Energy and Angular Distribution of the Sputtered Particles

All factors that influence the sputter yield also influence the energy and angular distribution of the sputtered particles. In the collision cascade, the incoming ions dissipate most of their energy to the target and only a small fraction is transferred to the sputtered particles. The following expression of energy distribution, known as the Thompson formula,[16] can be derived for the energy distribution of the sputtered particles:

$$N(E) \approx \frac{E_s}{\left(E_s + U_{sb}\right)^3}, \qquad (1.5)$$

where E_s is the energy of the sputtered particle. In figure 1.4.a) the energy distribution of sputtered Mg in Ar with energy of 400 eV can be seen. The particles are sputtered in a wide range of energies, although most of them in the order of a few eV. The function has its maximum at $U_{sb}/2$. The Thompson formula shows that the most probable energy of the sputtered particle is independent of the ion energy.

The spatial or angular distribution of the sputtered particles is proportional to $\cos^n\theta$, where n depends on the energy of the incident ions and the masses of the ions and target and θ is the emission angle (Figure 1.4.b). The cosine law results from an isotropic angular distribution of recoil velocities. For low incident ion energy, a collision cascade is formed, but is not well developed, which originates a non-isotropic angular distribution of sputtered particles with a under-cosine (n<1) or heart-shaped distribution. For high incident energy, the angular distribution of the ejected particles tends to be over-cosine (n>1).

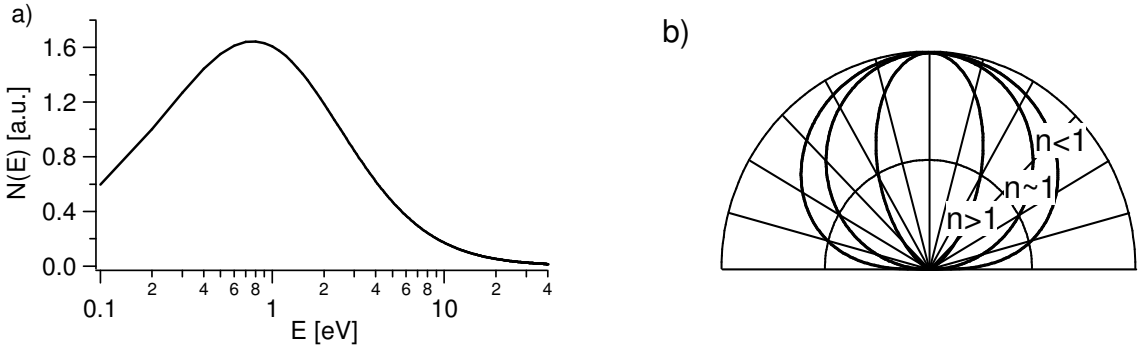

Figure 1.4: a) Energy distribution of Mg sputtered by a Ar^+ bombardment with 400 eV incident energy and U_{sb} = 1.54 eV; b) Spacial distribution of the sputtered particle at normal incidence for different energy bombardment particles.

Yamamura *et al.*[17-19] have shown that the angular distribution for normal incidence can be represented by:

$$Y(E,\theta) \propto \cos\theta(1 + B\cos^2\theta), \qquad (1.6)$$

where B is a fitting parameter. The cosine distribution corresponds to $B = 0$. $B > 0$ and $B < 0$ agree with angular distributions of over-, under-cosine, and heart-shaped types, respectively. The advantage of Equation (1.6) in comparison to $\cos^n\theta$, is that it can describe even the heart-shaped distribution (smaller negative values of B) corresponding to very low incident energy.

The disconnection between the energy and angular distribution as discussed above is an approximation. In reality, the angular distribution is not independent of the energy of the ejected atoms, i.e. the angular and energy distribution of the sputtered particles are not separable.[20,21] In the case of anisotropy, this dependence is more notorious. Stepanova and Dew have shown that the energy distribution produced by sub keV ions are narrower compared to the Thompson distribution[20] and depend dramatically on the ion's angle of incidence and on the direction of emission.[21]

1.3. Principles of Magnetron Sputtering

As stated in the previous section, bombardment of the target by energetic ions is a prerequisite to promote sputtering of the target material. By applying a negative potential to the target and generating a plasma, a continuous bombardment of the target is assured. The plasma is a gas containing positively (ions), an equal number of negatively (electrons) charged particles and a considerably larger number of neutral atoms (in our deposition conditions). The plasma density is defined as the number of electrons (or ions) per volume. The plasma has no net charge as it contains equal number density of positive and negative charges. It can be assumed that those charged particles move in steady-state plasma as free particles. Because electrons have a much lower mass than positive ions and neutrals, they move much faster. If a spherical plasma were created, both types of particles (ions and electrons) would diffuse outwards, but the electrons would diffuse faster because of their velocity. As the electrons move away from the surface of the sphere, the net charge within the sphere becomes slightly positive, exerting an attractive force on the electrons. A steady-state plasma has small electric

fields at the boundary, so that electron and ions can diffuse at the same rate. This difference of potential is in the range of the electron energy (a few eV), and is called plasma potential V_p. If an electrically floating object is placed in the plasma, a space charge layer with negative potential relative to the plasma potential is formed due to the mass difference between the ions and electrons, which results in a much higher electron current than ion current towards the object. Once negatively charged, the object repels the electrons. The potential of the object reaches an equilibrium (floating potential, V_f) when the electron current equals the ion current flux. When a floating or biased object is inserted in the plasma, it disturbs the equipotential plasma, leading to regions of local inhomogeneity, named sheath. Here, the potential drops from plasma potential to floating, grounded or another potential.

If a large negatively charged object is placed in plasma (the cathode case), a wider sheath is created, as can be seen in figure 1.5. The sheath width depends on the potential drop. If the difference between the cathode potential and plasma potential is large enough, some electrons may receive enough energy to ionize neutral gas atoms. When the ionization happens in the sheath (pre-sheath), the ions are accelerated back towards the cathode, and depending on the potential, they may sputter the cathode atoms and promote the emission of secondary electrons. The secondary electrons generated at the cathode are accelerated through the sheath and may gain again sufficient energy to ionize more neutrals.

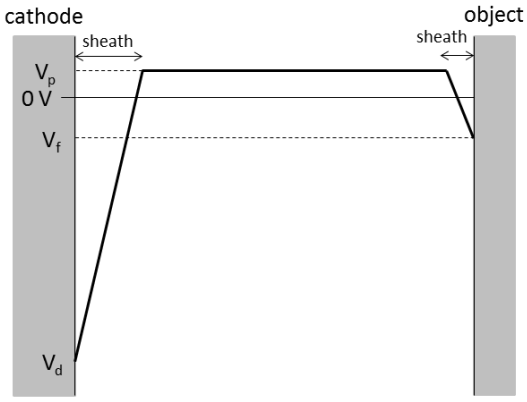

Figure 1.5: Sheath of the distribution of the plasma potential when a negatively biased and a floating object are inserted.

In diode sputtering, the electrons can easily escape from the cathode region. In order to increase the ionization probability by having more energetic electrons and more Ar neutrals to ionize (to maintain the plasma), high working pressures and potentials are needed. This happens at the expense of deposition rate, energy consumption, while very fast generated electrons heat the substrate. In order to increase the ionization by electron trapping, i.e. the same electron is used several times for ionization events, magnets can be placed behind the target. The secondary electrons emitted during the sputter process are trapped by the magnetic field and stay close to the cathode surface, which increases the ionization degree and the bombardment flux in the target. As the ion bombardment increases, the number of emitted secondary electrons also increases. This combined with longer travel distance, as the electrons

follow helical paths around the magnetic field lines (see figure 1.6), induces more ionizations and finally increases the efficiency of the sputtering process. For specific sputtering conditions, the use of magnets allows to obtain the same target erosion rate at lower operating voltage and working pressure. This, in turn, means fewer collisions of the sputtered particles between target and substrate, allowing them to increase the mean free path before reaching the growing film.

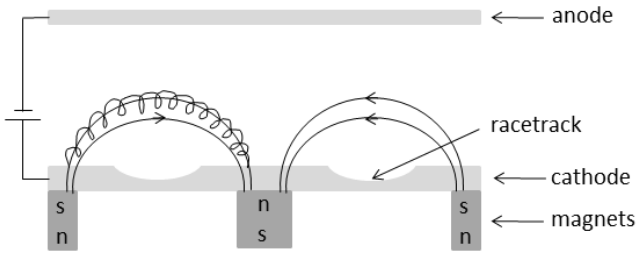

Figure 1.6: Draft of a cross section of a planar balanced circular magnetron: the magnets are placed behind the cathode (target); the magnetic fields provoke the helical paths of the electrons around it, increasing the ionization locally and resulting in the appearance of the racetrack.

In the case of a planar circular magnetron (which is used in the present work), two round magnets are placed behind the target, as can be seen in figure 1.6. The non-uniform ion bombardment across the target surface induces the formation of an erosion profile, known as racetrack. For balanced magnetrons, the magnet strength of both magnets is the same, resulting in strongly confined plasma near the target region. As a consequence, only a few charged particles reach the substrate, which might be useful in the case where low energetic bombardment is mandatory (for example in the case of polymeric substrates), but it is a drawback when energetic ion/electron bombardment in the anode surface is needed (the bombardment with energetic ions or electrons influence the growth of thin films). The bombardment of the substrate with energetic particles can be achieved by unbalancing the magnetic configuration,[22] by using magnets with different strength and/or dimensions. This way, the magnetic field lines are extended to the substrate (figure 1.7), increasing the plasma density near the substrate. Although the presence of magnets increases the efficiency of sputtering, it leads to inefficient target usage where only ~30% of the material is used.

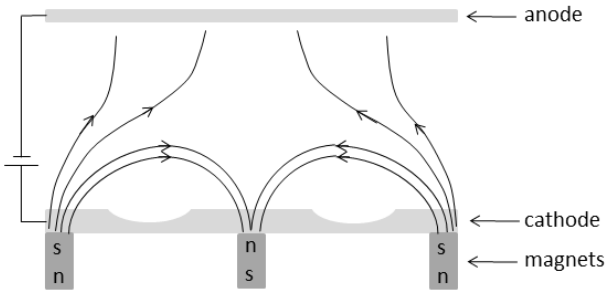

Figure 1.7: Scheme of a planar unbalanced circular magnetron: the unbalanced magnet configuration leads to a higher density plasma near the cathode.

Additionally, an external bias can be applied to the substrate in order to increase the particles' energy towards the substrate. If a negative bias is applied, the ions are attracted to the substrate and the electrons repelled, while a positive bias has the opposite effect.

1.4. Reactive Magnetron Sputtering

One technique to synthesize multicomponent materials in the form of films is magnetron sputtering, employing one or two compound targets. However, co-deposition using one or two metallic sources in an Ar-O_2 (or another reactive gas) ambient is frequently chosen to increase the flexibility with respect to the chemical compositions that can be accessed.[23-25] Sputtering in an Ar-O_2 ambient is known as reactive (magnetron) sputtering, where introducing a reactive gas into the sputter system results in the addition of a chemical interaction to the physical process, and therefore compound thin films can be deposited.

When a reactive gas is added to the sputtering process, it does not only react at the substrate and the chamber walls, but also at the target. At typical working pressures in reactive sputtering ($\leq$ 2 Pa), the reaction between the reactive gas and the sputtered atoms that travel towards the substrate in the gas phase cannot occur, because it is impossible to conserve energy and momentum in a two-body collision. A surface acts as a third body for reaction, and therefore it is needed for the chemical reaction. Once this reaction happens at the target surface, the sputter process is influenced, as sputter yield and ISEE are material dependent.

The presence of the reactive gas affects the entire sputtering process. Although the reactive gas reacts immediately with the metallic particles at the chamber walls, substrate (the gas is gettered by the thin film) and target, the target condition is not significantly affected when the reactive gas flow is relatively low, as the target area is much smaller than the substrate (all surfaces in the vacuum chamber except from the target) and the compound is sputtered away from the target. Thus, when the reactive gas flow is increased, the total pressure does not increase significantly until a critical flow is reached. At the critical flow, the metallic particles cannot consume all the reactive gas and the latter one stays in the gas phase. At this critical flow, an increase in reactive gas flow leads to an increase of the total pressure. Concomitantly, the excess of reactive gas may react with the target. All the ion-target interaction events referred in 1.2.2. for Ar are also valid for O_2 (or another reactive gas). At the target, there is a balance between the sputter process and compound formation. A further increase in the reactive gas flow leads, at a given gas flow, to a linear increase in the total pressure. At the target, the compound formation dominates the sputter process. As a result, the sputter rate decreases because the binding energy of the compounds is much higher than that of pure metals. The decrease in sputter rate leads to the availability of a higher concentration of O_2, which turns out in formation of a larger compound area on the target surface, and this is an avalanche. This process is reversible, meaning that when the flow of the reactive gas is decreased enough, the compound is removed from the target. Because the sputter rate of a compound material is lower than that of the correspondent metallic one, the avalanche happens at lower reactive gas flow. An illustration of the influence of a specific gas (O_2) on the total pressure during the sputtering of a metal (Mg) is shown in figure 1.8.a). This hysteresis behavior is also observed in the discharge voltage (as can be seen in figure 1.8.b)) due to the difference between the secondary electron emission yield of the compound and the

pure metal. A decrease in discharge voltage in an $Ar + O_2$ as compared to the discharge voltage for a pure Ar environment means an increase of the secondary electron emission yield of the compound when related to the pure metal value.[26]

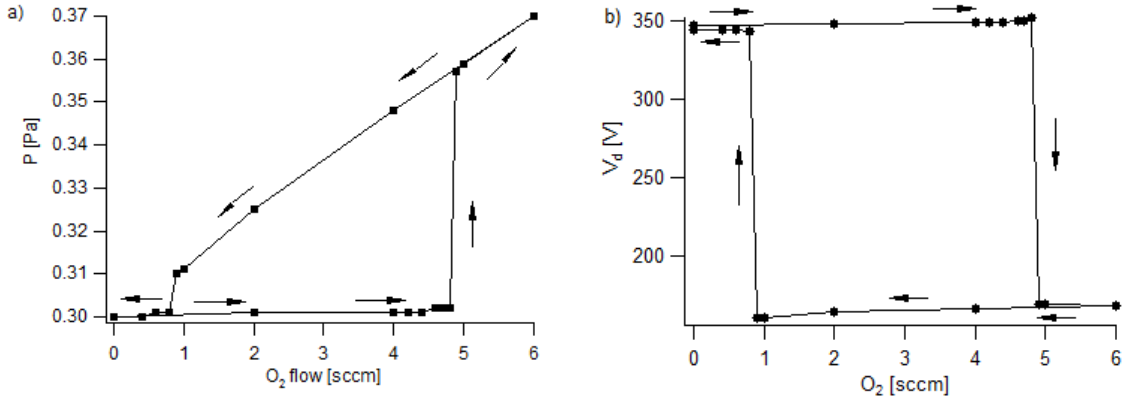

Figure 1.8: Influence of the O_2 flow on the total pressure (a) and on the discharge voltage (b) during the sputtering of a Mg target. The discharge current was kept at 0.65 A.

The formation of a compound layer in the target surface is called poisoning. When the sputter process occurs with the target surface not contaminated (without compound material), it is termed sputtering in metallic mode.

Reactive sputtering is a combination of the physical sputtering process and chemical reactions on the target and/or on the substrate, in a plasma environment, which makes it extremely difficult to develop realistic models for. Because the number of varying parameters is large, some simplifications and assumptions have to be done. Berg et al. were the first ones to model the reactive sputtering of a compound from a metallic target, taking into account the influence of the reactive gas in the target.[27] According to them the reactive gas would chemisorb at the surfaces and would be consumed by the substrate and the walls, the target and pumped out. However, the reactive gas does not only chemisorb at the target surface, as it may also be implanted in the target, due to being accelerated through the cathode sheath. Depla and De Gryse showed that it is needed to account for the ion implantation in the target to explain the discharge voltage behavior.[28] More detailed information about reactive sputtering and models of reactive sputtering can be found in literature.[23,26,28-31]

2. Thin film growth

2.1. Introduction

The formation of a thin film starts when the vapor phase reaches the substrate and can be divided in several stages. Upon their arrival at the substrate, atoms may adsorb or desorb. Moreover, if energetic enough, they may diffuse. The formation of stable nucleus is the next step, followed by its expansion, impingement to other crystals, coalescence, formation of polycrystalline islands and formation of a continuous film.

As the energy of the arriving particles on the substrate is decisive for the nucleation process and surface diffusion, which on their turn are essential to define the growth mechanism of a thin film, it can be concluded that thin film growth is utterly influenced by the deposition conditions.

The current section serves as a brief introduction to the structure evolution of the films. In section 2.2, the arrival of the vapor phase on the surface and the first atoms-substrate interactions are described – the formation of the adatoms. Section 2.3 deals with the mobility of the adatoms species along the surface. In section 2.4 the thermodynamic and kinetic aspects of nucleation are presented. Furthermore, the three growth modes are described. Section 2.5 describes the coalescence, crystal growth and grain growth, while further thickening of the film is discussed in section 2.6. Finally, in section 2.7 the basic structure zone model and a revised model where impurities are taken into account are presented to classify the microstructure of the films.

2.2. Adsorption

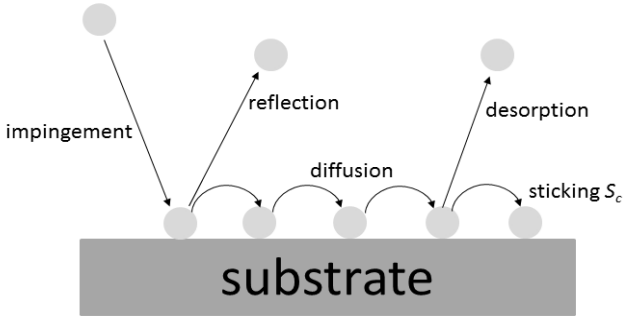

Figure 2.1: Atomistic processes during the initial stage of thin film growth.

When an atom (or molecule) from the gas phase approaches the substrate within a few interatomic distances, it starts to feel an attraction due to the interaction with the substrate surface. The approaching particle is attracted in a potential well by the presence of a surface potential and gets adsorbed on the substrate surface. This adsorption process is called physical adsorption or physisorption. Physisorbed particles are mobile on the surface. If they gain enough energy, they may desorb or increase the interaction with the surface atoms, by means of a chemical bond. The stage where a stronger bond between the particle and the surface atoms exists is termed chemisorption state. These processes are schematically represented in

figure 2.1. When the two adsorption states exist simultaneously, the physisorbed state is called the precursor one.

If the particle that approaches the substrate is bonded to it by Van der Waals forces, it is in physisorbed state. This is valid also for neutral particles, because they behave as oscillating dipoles, creating induced dipoles interaction.[32] Figure 2.2 shows schematically the potential energy curve of a physisorbed particle as a function of its distance to the surface. The particle is attracted into a potential well. When it comes in the proximity of the surface, its potential energy is lowered until it reaches a minimum. If the particle comes even closer to the surface, it is repelled by a sudden increase of the potential energy. The depth of the potential well is the binding energy of a physisorbed particle E_{phys}, which is ~ 0.25 eV.[33]

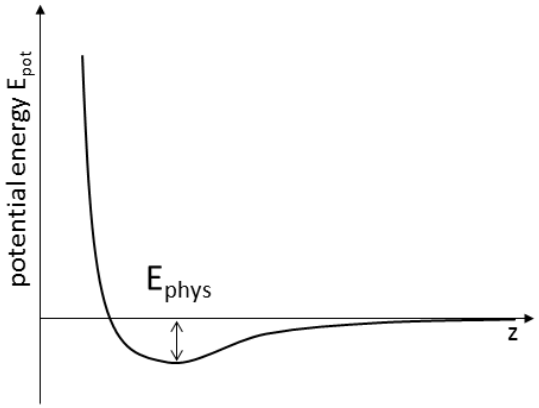

Figure 2.2: The potential energy curve of a physisorbed particle as a function of its distance to the surface.

If new molecular orbitals are created by an electron transfer or by sharing of electrons between the adparticle and the surface atoms, the adparticles are said to be in chemisorbed state.[32] In figure 2.3 the potential energy curve of a chemisorbed particle as a function of its distance to the surface can be seen. Chemisorption state encompasses two situations: the non-dissociative chemisorption, where the incoming particle is adsorbed intact without breaking any intermolecular bonds (see figure 2.3.a)) and the dissociative chemisorption, where the incoming particle dissociates to be able to be chemisorbed (see figure 2.3.b)). In this case, the curves for the physisorbed and chemisorbed situation can intersect one another at energy higher than zero. The chemisorption state is activated by the physisorption, where E_{act} is the activation energy needed to overcome the barrier energy for chemisorption. Because E_{act} is lower than the dissociation energy E_{diss} in the vapor phase, dissociation occurs preferentially on the solid surface. The binding energy of a chemisorbed particle E_{chem} is typically in the order of 1-10 eV.[33]

In spite of the adsorption state of the adparticles, if they obtain enough energy to overcome the desorption barrier, they can desorb from the surface. In the physisorption state, the desorption barrier is equal to the E_{phys} (very low). However, in the chemisorption state, the desorption barrier is equal to $E_{chem} + E_{act}$.

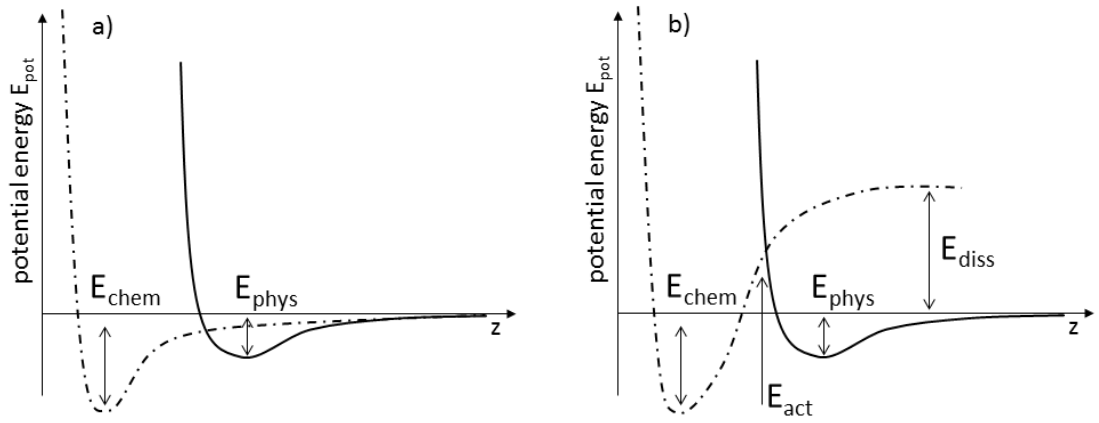

Figure 2.3: The potential energy curve of a chemisorbed particle as a function of its distance to the surface in the case of non-dissociative chemisorption a); and in the case of a dissociative chemisorption of a neutral diatomic molecule on a surface b).

The sticking coefficient S_c describes the probability for an atom to remain adsorbed. Thus, it is the ratio between the particles that do adsorb, or "stick" to a surface to the number of atoms that impinge upon that surface, during the same period of time. S_c varies between 0 and 1, and it is dependent on the particles nature, solid surface nature and deposition conditions, for example. For most metals, for depositions at low temperature, the sticking coefficient is very close to unit.[34] Besides thermal desorption, desorption can also occur due the knock-on event of an energetic arriving particle.

2.3. Surface Diffusion

Once adsorbed on the solid surface, the adparticles (or adatoms) may have enough energy to move across the surface. The adatoms hop from one well to another, and this hopping movement is named surface diffusion. Surface diffusion is one of the key aspects in thin film growth because due to the movement of the adsorbed particles (or atoms), they not only can find each other, as they can find more active sites and epitaxial sites, defining the structure of the thin film. Diffusion can either occur on a flat surface or on step edges. However, the diffusion barriers are higher for step edges than for flat surfaces, due to the higher number of surface bonds. Surface diffusion depends strongly on the chemical state of the surface. Moreover, the existence of impurities causes changes in the diffusion barriers and consequently in the diffusion.

The potential well with depth of E_{phys} or E_{chem}, where the particles are trapped, oscillates with the position x, along the surface. In the case of a perfect surface, this variation is shown in figure 2.4. When a particle seeks to change position in a surface, it does not have to overcome the binding energy (E_{phys} or E_{chem}), but only the variation in potential energy along the surface $E_{D,phys}$ or $E_{D,chem}$.

The surface diffusion can be seen as a two-dimensional random walk (no net motion in any direction) during which an adatom jumps from one potential well of the surface to another. For such a random walk r(t) the mean square displacement raises linearly in time according to[34]

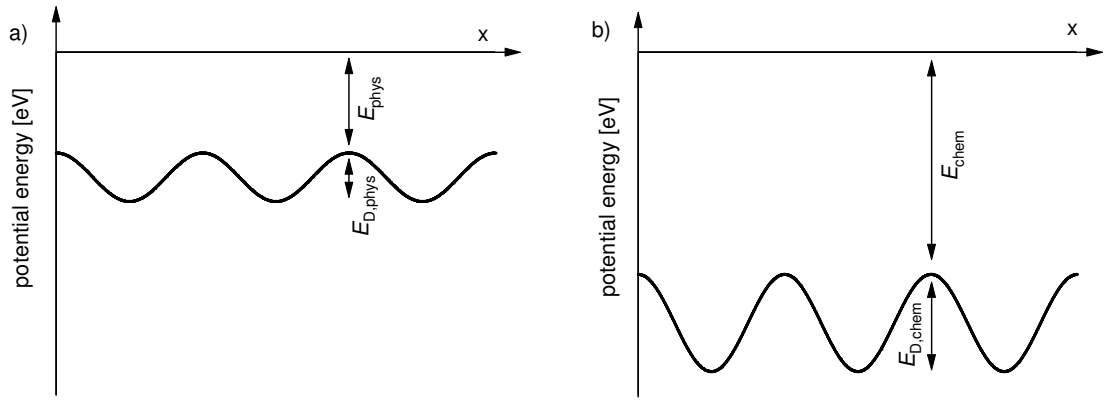

Figure 2.4: Variation of the potential energy along a perfect surface for a) a physisorbed and b) a chemisorbed particle.

$$\left\langle \left(r(t)-r(0)\right)^2 \right\rangle = \nu \ell^2 t = 4Dt\,, \tag{2.1}$$

where ℓ^2 designates the mean square distance covered at a single jump, ν is the jump rate and D denotes the surface diffusion coefficient and it is given as

$$D = \frac{1}{4}\ell^2 \nu\,, \tag{2.2}$$

being the factor ¼ a convention reflecting the two-dimensional nature of surface diffusion.[34]

The transition path between the initial and final positions of the adatom passes over a saddle point, which is separated from the initial position by the energy barrier E_D (see figure 2.4a) and b) for physisorbed and chemisorbed adatoms, respectively). The jump rate is then expected to follow the Arrhenius law for thermally activated processes:

$$\nu = \nu_0 \mathrm{e}^{-E_D/k_B T}\,, \tag{2.3}$$

where ν_0 is the attempt frequency, and k_B represents the Boltzmann's constant. A condition for the applicability of the random walk picture is that jumps are seldom events ($\nu << \nu_0$) in order to guarantee that the adatom spends sufficient time between jumps to reach the equilibrium within a well and lose the memory of where it came from. This implies that, at room temperature, the surface diffusion barrier should be at least 0.1 eV.[34] The adatom diffusion parameters (attempt frequency and energy barriers for diffusion) can be determined either theoretically[35,36] or experimentally.[37-39]

The surface diffusion mechanism described above is valid for diffusion on a terrace. However, when adatoms diffuse on a terrace, they may encounter a lattice step (also termed step-edge). In the specific case that the adatom arrives from the upper terrace, an additional energy barrier termed Ehrlich-Schwoebel (ES) barrier (Figure 2.5), has to be overcome in order for the adatom to descend the step. The ES barrier is larger than that for terrace diffusion due to the temporarily lower number of nearest neighbors that the adatom

encounters. The ES barrier is very important for the subsequent growth, as will be discussed later.

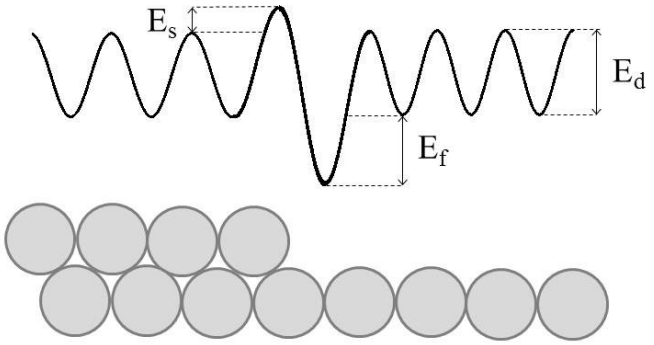

Figure 2.5: Schematic representation of the potential energy barriers for the adatom formation and diffusion course near an island step edge. E_d is the activation barrier for diffusion, E_s the Ehrlich-Schwoebel barrier and E_f the adatom formation energy to the step.

2.4. Nucleation and early stages of film growth

After the accommodation of the atoms from the vapor phase on the solid surface, the adparticles can diffuse across the surface. While diffusing, they may encounter other adatoms. The thin film nucleation starts with the clustering of isolated adatoms on a substrate. Adatoms may form pairs with other adatoms or attach to an already existent cluster.

A simple model for homogeneous nucleation from a supersaturated vapor can be discussed assuming a spherical nucleus with radius r constituted by several atoms.[15] To create a new surface, an energy expenditure of $4\pi r^2\gamma$ is required, where γ represents the surface energy. However, due to the formation of a stable phase, the nucleus gains energy $4/3\pi r^3\Delta G_v$, where ΔG_v denotes the free energy of the nucleus per volume unit. The total free energy is given by

$$\Delta G = 4\pi r^2\gamma + \frac{4}{3}\pi r^3\Delta G_v, \qquad (2.4)$$

and it is depicted in figure 2.6, together with the energy cost (surface energy) and energy gain (volume free energy) to form a nuclei. From the graph one can conclude that the incipient aggregate (nuclei) must reach a critical size r^* before the volume term is able to overcome the surface term in order to form a stable nucleus. Aggregates having a radius smaller than r, with ΔG in the ascending part of the curve spontaneously decompose, while aggregates with a radius bigger than r are stable and incorporate other atoms. The critical nucleus radius r^* at which the ΔG is maximum is found for $d(\Delta G)/dr = 0$, with an equivalent ΔG^* - the free activation barrier for nucleation as follows:

$$r^* = -\frac{2\gamma}{\Delta G_v}, \qquad (2.5)$$

$$\Delta G^* = \frac{16\gamma\pi^3}{3(\Delta G_v)^2}. \qquad (2.6)$$

The factors 2 and $16\pi^3/3$ in Equations (2.5) and (2.6) derive from geometry and the supposition that the nuclei are hemispherical. Important to notice is that $r^* \propto \gamma/\Delta G_v$ and $\Delta G^* \propto \gamma^3/(\Delta G)^2$.

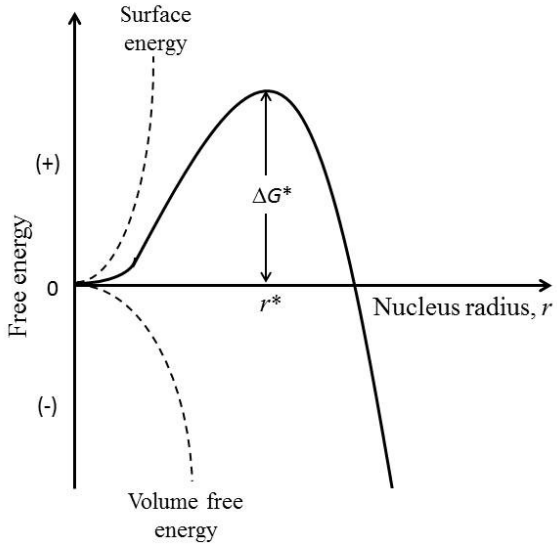

Figure 2.6: Variation of the total free energy of a nucleus, ΔG^*, as a function of its radius, r.

The situation closer to reality is more complex than described above. The heterogeneous 3D nucleation of a condensed film on a substrate can be described using the capillarity theory. The fundamental processes on substrate surface during film growth are represented in figure 2.7. For a relatively low density of stable nuclei the growth occurs mainly through surface diffusion of the adatoms.

Although the adatoms surface diffusion plays an important role in the nucleation process, it is assumed here that there are no constrains regarding the adatoms mobility and therefore, as a first approximation, the process shown in figure 2.7 is treated purely thermodynamically. Assume that a hemispherical 3D cluster (cap) of mean dimension r and contact angle θ forms on a substrate surface as illustrated in figure 2.7. The variation of the total free energy accompanying the formation of a cap is given by,[33]

$$\Delta G = a_3 r^3 \Delta G_v + a_1 r^2 \gamma_{vf} + a_2 r^2 \gamma_{fs} - a_2 r^2 \gamma_{sv}. \qquad (2.7)$$

Similar to the homogeneous nucleation process, the Gibb's free energy change per unit volume due to the gas-solid transformation drives the condensation reaction. The several interfacial energies γ that have to be accounted for are identified by the indices v, f and s which denote the vapor, film and substrate, respectively. A pair of the indices refers to the interface between those two phases. For the spherical cap-shaped nucleus represented in figure 2.7, the curved surface area ($a_1 r^2$), the projected circular area on the substrate ($a_2 r^2$), and the volume involved ($a_3 r^3$), the a_i terms are function of geometry.

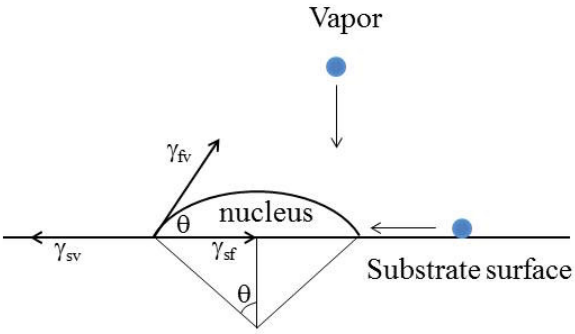

Figure 2.7: Atomistic mechanism during nucleation on a substrate surface during vapor deposition.

The mechanical equilibrium between the horizontal components of the interfacial energies adjacent to the nucleus results in Young's equation,

$$\gamma_{sv} = \gamma_{fs} + \gamma_{vf} \cos\theta\,, \tag{2.8}$$

where θ denotes the wetting angle, as for θ = 0° the films wets the surface, while for θ = 180° the film completely de-wets the surface. Taking into account the Young's equation and the geometric constants, the critical nucleus size r* can be calculated:

$$r^* = \frac{-2(a_1\gamma_{vf} + a_2\gamma_{fs} - a_2\gamma_{sv})}{3a_3\Delta G_v}, \tag{2.9}$$

as well as the corresponding ΔG for $r = r^*$:

$$\Delta G^* = \frac{4\left(a_1\gamma_{vf} + a_2\gamma_{fs} - a_2\gamma_{sv}\right)^3}{27a_3^2\Delta G_v^2}\,. \tag{2.10}$$

Similar to the homogeneous nucleation case, $r^* \propto \gamma/\Delta G_v$ and $\Delta G^* \propto \gamma^3/(\Delta G)^2$. The minimization of the total free energy entails that nuclei with size $r < r^*$ dissociate, while those with $r > r^*$ grow.

2.4.1. Deposition Rate and Temperature

The deposition conditions, such as deposition rate $\dot{R}$ and deposition temperature, are crucial for the nucleation processes. Therefore, knowing their influence on the critical nuclei size r^* and critical free energy ΔG^* is of great importance. The variation of the Gibb's free energy due to the gas-solid transformation ΔG_v can be described as a function of deposition rate and temperature as follows:[33]

$$\Delta G_v = -\frac{k_B T}{\Omega} \ln\left(\frac{\dot{R}}{\dot{R}_e}\right), \tag{2.11}$$

where $\dot{R}_e$ is the equilibrium evaporation rate from the film nucleus at a substrate temperature T, and Ω is the atomic volume. For nucleation to occur, $\Delta G_v < 0$ which requires that $\dot{R} > \dot{R}_e$.

Substituting Equation 2.11 in Equations 2.9 and 2.10, the following relations can be obtained,[33]

$$\left(\frac{\partial r^*}{\partial T}\right)_{\dot{R}} > 0, \tag{2.12}$$

$$\left(\frac{\partial \Delta G^*}{\partial T}\right)_{\dot{R}} > 0, \tag{2.13}$$

$$\left(\frac{\partial r^*}{\partial \dot{R}}\right)_{T} < 0, \tag{2.14}$$

$$\left(\frac{\partial \Delta G^*}{\partial \dot{R}}\right)_{T} < 0. \tag{2.15}$$

The previous inequalities (Equations 2.12 to 2.15) have interesting applications and summarize general trends observed in thin film deposition and growth. An increase in film deposition temperature and a decrease in the deposition rate yields a higher r^* and ΔG^* values. A practical implication is that at high deposition rates and low deposition temperatures the nuclei form at a higher rate suggesting that a continuous film is formed at lower average film thickness. Moreover, associating r* and ΔG* with crystallite sizes in the continuous film, high deposition temperatures and low deposition rates results in the formation of large crystallites or even single crystals.

2.4.2. Film Growth Modes

The growth of two dimensional nuclei is very important for the microstructure of the continuous film. Based on the above presented thermodynamic approach, Young's equation (equation 1.14) provides a way to understand the initial structure evolution based on the nucleation dependence on interfacial free energies. The nucleation process can be divided into three growth modes:[40]

- $a_2\gamma_{sv} < a_2\gamma_{fs} + a_2\gamma_{vf}$: Volmer - Weber growth or island growth;
- $a_2\gamma_{sv} \geq a_2\gamma_{fs} + a_2\gamma_{vf}$: Frank - Van der Merwe growth or layer-by-layer growth;
- $a_2\gamma_{sv} = a_2\gamma_{fs} + a_2\gamma_{vf} + \varepsilon$: Stranski - Krastanov growth or layer-by-layer followed by island growth;

where ε is a parameter which accounts for the strain of the film induced by lattice mismatch. The growth modes are schematically illustrated in figure 2.8.

In the case of island growth, the surface energy of the growing film is higher than the surface energy of the substrate. The energy balance requires minimization of the area covered by the nucleus, which causes the nuclei to grow in form of three dimensional islands (figure 2.8 a)). In this growth type, the contact angle θ varies between 0 and 180°. Typically, the islands aim for a specific shape.

For layer-by-layer growth, the surface energy of the film is smaller than the surface energy of the substrate, implying a minimization of the area covered by the nucleus. This leads the nuclei to try to wet the surface and grow into a smoothly and flat surface. As a consequence, the contact angle θ is 0°.

The layer-by-layer growth may lead, with time, to strained growing layers, if a difference in lattice constant between the substrate and the growing film exists. In this case, the interfacial strain energy γ_{fs} increases upon increasing the number of deposited layers and at a certain layer thickness, the condition to grow layer-by-layer is broken, giving rise to island growth (figure 2.8 c)). According to Wessels,[33,41] the thickness of the film for which the layer-by-layer (epitaxial layer) growth turns into islands growth is given by:

$$h^* = \frac{2\gamma_{fs}}{\left(\varepsilon^2 - \delta^2\right) Y}, \tag{2.16}$$

with ε and Y the strain and elastic modulus of the layer, and δ the lattice mismatch $\delta = \left[a_0(s) - a_0(f)\right] / a_0(f)$, where a_0 is the lattice parameter and f and s refer to the film and substrate, respectively. This relation implies that h^* varies approximately as δ^2.

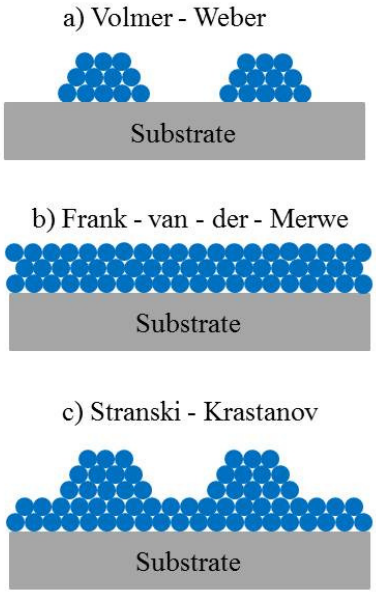

Figure 2.8: Schematic illustration of the three growth modes.

It is worth to mention that the film growth modes presented in the last section are not influenced solely by the surface energy (thermodynamics). The magnitude of the diffusion barriers also plays a role. In deposition conditions far from thermal equilibrium, the growth structure in vapor deposition is determined by the relative height of the step barrier (E_s) and diffusion barrier (E_d). In the case that E_s is comparable to E_d, the adatoms arriving on the step edge do not cross it. They are reflected and diffuse on the terrace until they encounter other adatoms and form a nucleus. The island growth is favored. On the contrary, if E_s is null or much smaller than E_d, the adatoms approaching the step-edge descend and the layer-by-layer

growth is preferred. Furthermore, the deposition rate also influences the growth modes. High deposition rates will favor the island growth as the adatoms do not have time to search for the most energetic favorable site. The presence of impurities also influences the growth – this will be discussed later in this work.

2.4.3. Accounting for Kinetics

Another quantity which is characteristic of the nucleation process is the nucleation rate. The nucleation rate describes how many nuclei of critical size form on a substrate per unit area, and time. In early stages of deposition, when nuclei are spaced apart (small coverage), the rate at which the nuclei grow depends on the rate at which adatoms attach to it. All in all, the nucleation rate $\dot{N}$ is equal to,[33]

$$\dot{N} = 2\pi r^* a_0 \sin\theta \frac{PN_A}{(2\pi MRT)^{1/2}} n_s \exp\left(\frac{E_{ad} - E_d - \Delta G^*}{k_B T}\right), \tag{2.17}$$

with a_0 the lattice parameter, P the vapor pressure, M the mass of impinging atoms, n_s the total density of nucleation sites, T the deposition temperature and E_{ad} the adsorption energy. From equation 2.17 one can see that the nucleation rate is a strong function of the nucleation energetics, which is largely contained within the term ΔG^*. For a given substrate-film combination, the ΔG^* depends on the change of Gibb's free energy ΔG_v and, subsequently, on the supersaturation and deposition temperature. A practical consequence is that a high nucleation rate promotes the formation of fine grains or even amorphous, while a coarse-grained deposits develops at low nucleation rates.[33]

Despite the qualitative utility of the thermodynamic nucleation theory, its quantitative correctness is poor, when film growth far from equilibrium is considered.[33] As an example, the nuclei size are much smaller than the ones predicted by thermodynamics.[15] In a more realistic approach, the role of individual atoms on the nucleation theory should be described. The atomistic nucleation theory comprises this idea.[15,34,40,42] The classical approach to nucleation kinetics balances the areal concentrations n_s of nuclei consisting of s atoms. Considering that the mobility of other species are negligibly small when compared to the adatoms mobility, clusters can only grow by aggregation of single adatoms.[15,34] Defining Γ_s as being the net rate at which s + 1-nuclei form from s-nuclei, for $s \geq 2$,

$$\frac{dn_s}{dt} = \Gamma_{s-1} - \Gamma_s . \tag{2.18}$$

The net formation rates Γ_s can be written as:

$$\Gamma_s = \sigma_s D n_1 n_s - \gamma_{s+1} n_{s+1}, \tag{2.19}$$

where γ_s is the detachment rate of the adatoms from an s-nucleus, D the diffusion coefficient and σ_s the dimensionless capture number, which accounts for the propensity of an s-nuclei to attach to an adatom. The chain (equation 2.18) of aggregation equations is fed by the adatom density n_1,

$$\frac{dn_1}{dt} = \dot{R} - 2\Gamma_1 - \sum_{s\geq 2}\Gamma_s \,. \qquad (2.20)$$

Similar to what was observed in the thermodynamic approach, there is a critical nucleus size distinguishing unstable from stable nuclei. Stable nuclei of size $s \geq i^*+1$ are assumed not to decay, i.e. $\gamma_s = 0$ for $s > i^*$, while nuclei with $s \leq i^*$ are unstable and dissociate. The total density of stable nuclei *N* is defined as,

$$N = \sum_{s=i^*+1}^{\infty} n_s \,. \qquad (2.21)$$

Assuming the restrictions for the nuclei stability in the previous paragraph, the solution of the equations 2.18 - 2.21 delivers the nucleation density *N*. The most important feature of this solution is that,[34]

$$N \sim \left(\frac{\dot{R}}{D}\right)^x , \qquad (2.22)$$

where x is a scaling factor which depends on the nucleus critical size *i**. The equation 2.22 yields to the same qualitative trends as the relations embedded in equations 2.12 – 2.15. However, equation 2.22 comprises information about the kinetics of the nucleation process.

2.5. From Nucleation to Film Thickening

According to the film growth modes presented in section 2.4.2, after nucleation the film thickness increases either by expansion of the islands (Volmer-Weber growth mode) or by addition of layers (Frank- van der Merwe growth mode). In the case of films grown non-epitaxially and far from equilibrium (which is the case of the sputter deposited films in the present work), three dimensional features are observed. The growth of these islands is predominantly kinetically controlled and results in the formation of polycrystalline films.

2.5.1. Crystal Growth

After nucleation, numerous distinct islands are dispersed on the substrate. The individual islands grow by the incorporation of particles. These particles can be incorporated by direct condensation from the vapor phase and/or by capturing mobile adatoms that diffuse along the substrate surface. This process is named crystal growth.[43-45] The main growth stages occurring during crystal growth are schematically depicted in figure 2.9.

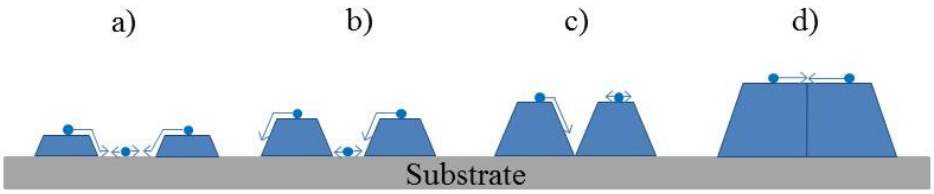

Figure 2.9: Growth stages of polycrystalline films.

When the particles arrive on an already existing nucleus, they may diffuse along the nucleus and ultimately get chemisorbed, or diffuse away from this nucleus to the bare substrate towards their counterparts or other nuclei up to the moment where the particles reach the chemisorbed stage. This phenomenon is represented schematically in figure 2.9 a). Repetition of the phenomenon previously described results in growth and expansion of the individual islands (figure 2.9 b)).

The expansion of the individual islands occurs up to the moment they are wide enough to touch their counterparts. The instance when the islands touch each other is termed impingement (figure 2.9 c)). From this moment on, the substrate surface is completely covered by the film and incoming particles can only condense on already existing islands (hereinafter referred to as grains). Nevertheless, the condensed particles are still mobile, implying that their final location might be in the grain where it first condensed as well as in the groove between grains or even an adjacent grain.

Continuous condensation of particles yields to further growth of the grains and filling up the grooves in between. The different grains are now separated by grain boundaries, which do not imply ceasing of adparticles mobility between grains (figure 2.9 d)).

2.5.2. Grain Growth

The film structure evolution depends on the atoms mobility. If atoms are active, grain restructuration occurs, i.e. the initial structure of the islands is modified. The grain growth can occur either during coalescence or in polycrystalline islands.[43] The three types of islands coalescence are illustrated in figure 2.10.

Prior to impingement of the individual islands, when a difference in size between neighbor islands is observed, the coalescence may happen via two different patterns of grain restructuration:

- **Ostwald ripening:**
  In this grain restructuration mode, the larger islands grow at the expense of the smaller ones. The driving force for this mechanism is the minimization of the surface free energy of the island structure. Consider two spherical islands (for simplicity) of surface tension γ and different radius r_1 and r_2 in close proximity. The free energy of a given island atoms is $4\pi r_i^2\gamma$ (i =1, 2). The island contains a number of atoms n_i given by $4\pi r_i^3/3\Omega$, where Ω is the atomic volume. The free energy per atom μ_i equals the chemical potential (dG/dn_i):[33]

  $$\mu_i = \frac{dG}{dn_i} = \frac{d(4\pi r_i^2\gamma)}{d(4\pi r_i^3/3\Omega)} = \frac{2\Omega\gamma}{r_i}. \qquad (2.23)$$

  Where μ is large, the atomic concentration is large and therefore, there is a tendency to escape to where μ is small. This is the situation outside very small islands. Hence, if $r_1 > r_2 \Rightarrow \mu_2 > \mu_1$, the atoms diffuse along the substrate from island 2 to island 1, leading to the growth of island 1 at the expense of island 2.

- **Cluster migration:**
  Coalescence occurs as a result of collisions between individual islands as they execute random motion along the substrate. The size of the clusters able to migrate is temperature dependent. At low deposition temperatures, dimer and trimer cluster are observed, while at sufficient high temperature, clusters of ~50-100 Å move as individual entities.[33] The motion of the clusters is not restricted to translation, they have been observed to rotate and jump to each other.
  The surface migration of a cap-shaped cluster with a projected radius r occurs with an effective diffusion coefficient $D(r)$, as follows:[33]

$$D(r) = \frac{B(T)}{r^s} \exp\left(-\frac{E_c}{k_B T}\right), \qquad (2.24)$$

  with $B(T)$ being a temperature dependent constant, s is a number between 1 and 3 and E_c is the activation energy for surface diffusion of the cluster. One can clearly see that the motion of the cluster is inversely proportional to its radius.

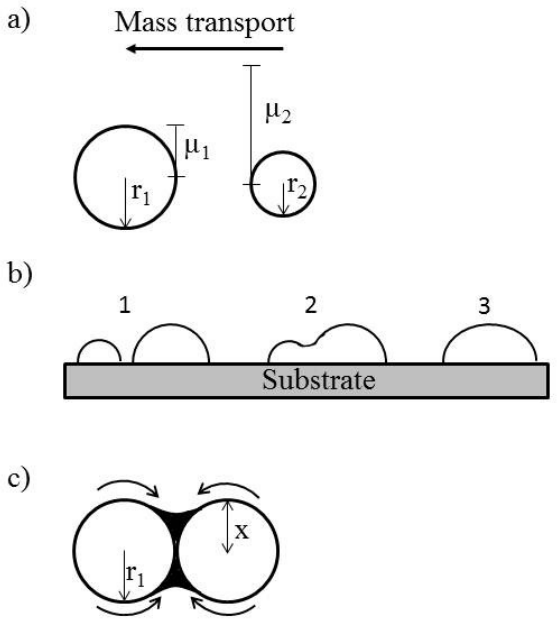

Figure 2.10: Coalescence of islands due to a) Ostwald ripening, b) cluster migration and c) sintering.

These processes, where two differently size islands or grains evolve into a new single crystal, occurs very fast in a liquid like manner. This fast coalescence proceeds at high diffusion rates and temperatures. The new crystal shrinks, creating free space, where nucleation occurs. This nucleation is named secondary nucleation and it keeps on occurring until there is no bare substrate exposed to the vapor phase.

At low temperatures and for high melting point materials, the coalescence is a slow process proceeding through the grain boundaries. In the case that the individual islands have comparable and large sizes, the grain restructuration occurs through **sintering**, which is a slow coalescence process. In this mechanism, the islands establish contact by forming a neck between them. The driving force for the neck growth is the tendency to minimize the total

surface energy (or area) of the system. A concentration gradient between the islands develops, leading to mass transport through the neck. In the case of spherical island of radius *r*, the sintering kinetics is given by:[33]

$$\frac{X^n}{r^m} = A(T)t\,, \qquad (2.25)$$

where *X* denotes the neck radius, *A*(*T*) is a temperature dependent constant that varies with the mass transport, *n* and *m* are constants and *t* is the time. There are several mechanisms for mass transfer in the films, being the two most plausible ones the diffusion either through the bulk or via the surface of the islands. In the case of bulk diffusion, *n* and *m* are 5 and 2, respectively, while for surface diffusion are 7 and 3. It has been shown that surface diffusion dominates sintering.[33] The grain boundaries are formed along the neck and they are able to move (grain boundaries migration). When the mobility is high enough, some atoms are able to detach from the original grain and get incorporated in a neighbor grain. This transition from one grain to another does not include diffusion, just a change in the atoms bonding. If the sintering process is complete, all steps take place and as a result formation of a new single crystalline island is observed. On the contrary, if the sintering process is incomplete and the grain boundaries migration is interrupted, the resulting islands are polycrystalline.

During the first stages of grain growth (coalescence) the small grains grow homogeneously, driven by the tendency to minimize the total grain boundary energy, i.e., reduction of the number of grain boundaries, which results in decrease of the total area of grain boundaries. The grain restructuration driven by the minimization of grain boundaries energy is known as normal growth (or primary growth).[46] However, when polycrystalline islands are formed, the driving force for the grain restructuration is the minimization of the overall energy of the grain, leading to a selective grain growth. This grain restructuration is named abnormal growth (or secondary growth).[46]

2.6. Film Thickening

From the previous section, one can conclude that the final structure and morphology of the film is strongly dependent on the presence (or not) of grain restructuration, which is determined by the mobility of the grain boundaries. In the case that the grain boundaries are immobile, the grain structure resulting from nucleation, growth and impingement is maintained. Therefore, the combination of polycrystalline structure and island growth implies that subsequent thickening of the grains results in the development of a columnar structure. Due to the immobility condition of the grain boundaries, a growth competition between grains and columns can only occur in an evolutionary mode. This evolutionary growth competition is triggered by an anisotropy in growth rate perpendicular to the substrate.[47]

When the presence of grain boundaries does not affect the diffusion of the adparticles, their mobility is enough for them to aim for the kinetically determined growth shape. A direct implication is that the islands and grains are terminated by planes of slowest perpendicular growth rate and therefore, the top of the columns is faceted. Due to the faceted columns, the roughness of the films increases with film thickness.

The existence of mobile grain boundaries allows for grain restructuration and results in the enlargement of some grains at the expense of others. Consequently, the grain structure is not defined by the initial growth stages but it evolves through the film growth process. As a result, a columnar structure where the width of the columns is uniform along the film thickness is formed. Due to the abnormal grain growth, grains with the lowest energy plane parallel to the substrate are preferred yielding to polycrystalline films with a preferential out-of-plane orientation. In ideally conditions, the column tops would be flat and parallel to the substrate. However, in reality, the top columns are smoothly curved.

More details about film thickening and structure evolution dependence on adparticles and grain boundaries mobility are provided in the next section where the structure zone models are presented.

2.7. Structure Zone Models

The fundamental phenomena of structure formation discussed in the previous sections are of crucial importance to understand the structural evolution of polycrystalline films. An opportune way of describing the evolution of polycrystalline films is by means of the so-called structure zone model (SZM), where the microstructure changes are reported as a function of one (or more) process parameters. This approach has been followed by many authors.[43-53] Because the microstructure of the films is strongly influenced by the temperature or surface mobility on the growing surface, the SZMs are often represented as a function of the homologous temperature T, i.e., the ratio between the substrate temperature T_s and the melting temperature of the deposited material T_m. The substrate temperature is normalized with the melting temperature of the material in order to include information about diffusion, as diffusion barriers scales with the binding energy and the melting temperature. However, instead of the classical use of temperature as a variable, one can use the adparticles mobility as it takes into account the energy of the adparticles and the surface diffusion barriers. Petrov *et al.*[45] and Mahieu *et al.*[47] have reviewed the SZM emphasizing the adatoms mobility. Nevertheless, the use of homologous temperature to describe structure evolution is inevitable, as it is difficult to obtain experimental values for the adparticles mobility and surface diffusion barriers for some materials.

Despite the usefulness of those classifications models, one must be aware of their limitations regarding quantities as the transition between regions is very broad.

First a basic SZM for films grown under pure conditions is presented followed by extended SZM where the rule of impurities and energetic bombardment is taken into account. In the subsequent sections, the homologous temperature and the adatom mobility are used concomitantly.

2.7.1. Basic Structure Zone Model

In this section, the most used terminology nowadays, derived from different authors,[50,51] is used. Thus, zone I, T and II are described.

Zone I

The basic feature for the growth in zone I is the limited adatom mobility. The adatom energy is too low to overcome the surface diffusion barriers. Therefore, the adatoms stick at the site of impingement, which is often referred to as hit-and-stick regime.

During nucleation, there is a high island density and most of these islands are amorphous, as the adatoms are not able to diffuse and find energetic favorable sites. The lateral grain size is determined by the nucleation density, and the film evolutions occurs solely by direct capture form the vapor phase. Furthermore, the columns preserve the orientation of the initial nuclei. This structure is predicted by the ballistic deposition model.[54]

The film consists of a columnar structure, separated with voids, mainly caused by statistical roughening and self-shadowing (see figure 2.11).[32] In the case that the material flux does not originate from a single position, but when a spread in the material flux is observed (e.g. sputtering), the self-shadowing effect is more pronounced resulting in more and larger voids between the columns. If deposition onto an inclined substrate occurs, the material flux arrives obliquely at an angle α causing a column tilt towards the incoming material flux by an angle β. The relation between the angle of incidence and the columns tilt is given by the tangent rule: $\tan(\beta) = 1/2 \tan(\alpha)$.[55,56]

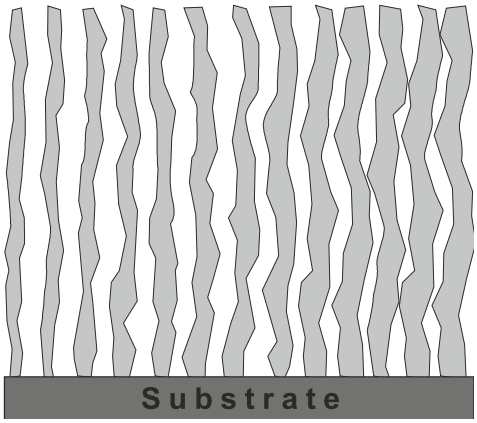

Figure 2.11: Schematic representation of the resulting structure of a film grown under Zone I conditions.

In the absence of surface diffusion, the films do not develop a specific crystallographic orientation. The orientation of the nuclei (amorphous or randomly oriented), defines the orientation of the columns which grow independently of each other. The low temperature deposition on amorphous or polycrystalline substrates yields to nucleation of islands with random orientation,[57] in contrast to epitaxial growth.

It should be noticed that such a zone I structure can evolve at conditions where adatoms diffusion is possible. At very high deposition rate, although the adatoms can overcome the surface diffusion barrier, the adparticles are buried by subsequently deposited adparticles before they can move to a more favorable energetic site.

Depositions carried out under condition yielding to films with microstructure in Zone I, but with continuous bombardment of energetic species, induces the densification of the film structure. The energetic bombardment causes knock-on events,[58] which fill the voids with particles. It must be noticed that no change in crystallographic properties occurs due to the bombardment of the energetic species, as there is only an increase of the kinetic energy delivered to the film. Mahieu *et al.*[47] called Zone Ib to this structure.

Zone T

The film growth in this regime is controlled by the adatom surface diffusion. Increasing the energy of the incoming adatom or increasing its thermal energy, allows adatoms to overcome surface diffusion barriers and diffuse on the surface.

In the beginning of the deposition process, the formed stable nuclei are crystalline with a random orientation distribution. As a result, the growth and coalescence of small islands leads to grain coarsening. Since the mobility is high enough, islands grow according to their kinetically determined crystal habit. The substrate is covered by grains with the same crystal habit, but different crystallographic orientations. The adatoms energy in this regime is not high enough to overcome the activation energy for grain restructuration and therefore the grain boundary is immobile through all the film thickness.

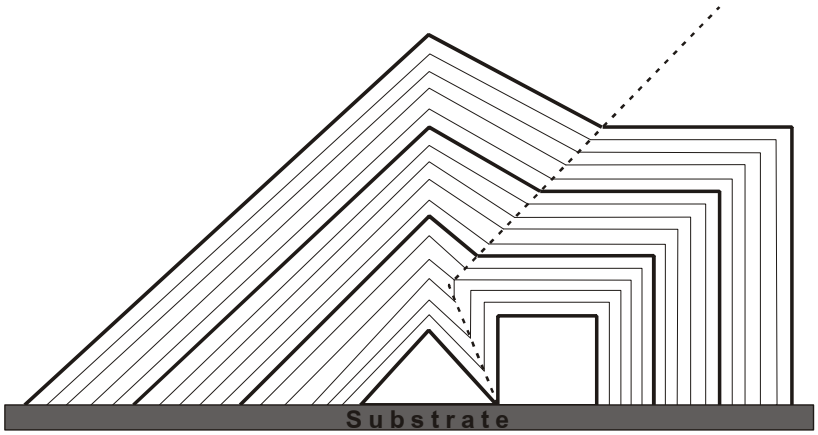

Figure 2.12: Overgrowth mechanism of faceted grains in which the grains with the most tilted facets with respect to the substrate overgrows the others. Figure adapted from Ref. [59].

Although all facets have a similar growth rate, some grains have a high perpendicular growth rate with respect to the substrate. The grains with the most tilted facets with respect to the substrate correspond to the grains with the geometrically fastest growing direction perpendicular to the substrate,[47] as can be seen in figure 2.12.[59] As a result, similar to van der Drift,[60] a mechanism where the grains with the geometrically fastest growing direction perpendicular to the substrate slowly envelope and overgrow the other grains is seen. The anisotropy in perpendicular growth rate is typical for zone T growth.

The adatoms can move from one grain to another which, together with the overgrowth mechanism yields to the development of a preferential out-of-plane orientation with the film thickening. Mahieu et al.[47] have discussed the importance of the adatom mobility being

confined within one grain or not. In the case that the adatom diffusion is restricted to the same grain, faceted grains evolve but there is no development of out-of-plane preferential orientation as the grains grow independent of each other and overgrowth is not possible. In this situation, Mahieu et al.[47] have named this region as Zone Ic.

As it was described in the previous paragraphs, the crystallographic orientation (texture) and the microstructure of the films within Zone T region vary along their thickness. The overgrowth mechanism leads to V-shaped columns with faceted tops. Therefore, the films roughness is also thickness dependent, i.e. an increase of thickness induces an increase in the roughness. A typical zone T structure is schematically illustrated in figure 2.13.

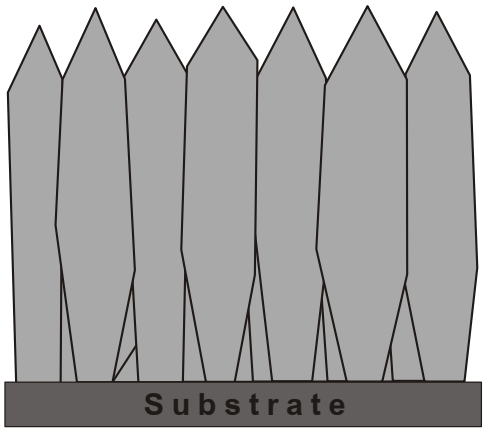

Figure 2.13: Schematic representation of the resulting structure of a film grown under Zone T conditions.

If deposition onto an inclined substrate occurs, the overgrowth mechanism prevails also resulting in the formation of V-shaped columns. However, in contrast to Zone I, the column tilt angle does not follow the tangent rule. On the contrary, the column tilt is less pronounced.

Zone II

In this regime, the temperature is considerably high which causes the adatoms energy to be high and allows grain boundary diffusion.

Similar to the other regimes, the nucleation results in islands with random orientation distribution. Grain boundaries migration occurs not only during the coalescence state but also during the film thickening. The orientation selection during coalescence is more pronounced in comparison to that in zone T, and it is driven by the decrease of the total grain boundary area, as well as the minimization of the interface and surface energy.[57] Due to the tendency to minimize the interface and surface energy, only planes which have a plane with the lowest surface energy parallel to the substrate are stable. The crystallographic orientation perpendicular to the plane with the lowest surface energy parallel to the substrate is the preferential orientation.

In order to reduce the interface and grain boundary energy, the grain boundaries will be straight and perpendicular to the substrate, yielding to broad equiaxed columns for which the

width increases with increasing mobility. Figure 2.14 illustrates the resulting structure of a film grown under Zone II conditions.

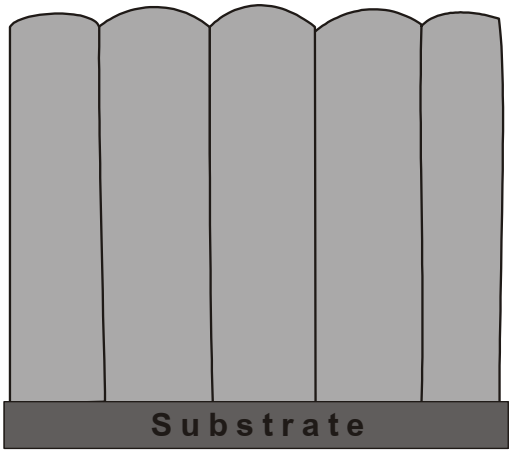

Figure 2.14: Schematic representation of the resulting structure of a film grown under Zone II conditions.

Due to rapid surface diffusion and grain restructuration, shadowing barely influences the growth. Therefore, tilting the substrate with respect to the incoming material flux, does not cause an inclination of the columns.

2.7.2. Influence of Impurities

The presence of impurities during the deposition process is almost inevitable. The origin of impurities is multiple. Impurities in the growing film can originate, for example, from adsorption of residual impurities in the vacuum chamber, bad cleaning of the substrate and contamination of the used gases. Moreover, intended co-deposited additives which content in the film goes beyond the solubility limit is of major importance. Hereinafter, non-intentional impurities and additives are treated as impurities. The impurities affect the atomistic processes during all growth stages and consequently the growth process.

Similar to the pure elemental films, the construction of a SZM for deposited films with impurities requires the determination of the dependence of the fundamental structure forming phenomena on the growth conditions. Barna *et al.*[44,45] have performed this study and published a revised SZM.

Impurities which are dissolved in the crystal lattice have no impact on the morphology or the crystallographic texture as they do not form their own phase. Therefore, these impurities do not induce changes in the SZM. Within the impurities that are not soluble in the crystal lattice, two groups can be distinguished taking into account their influence on the basic phenomena and structure formation. An impurity is called promoter if its presence promotes the diffusion or one of the basic structure forming phenomena. Promoter impurities tend to yield to the development of larger grains. If an impurity forms a two or three dimensional strange phase on the free surface of the film or on the grain boundaries, limiting the surface diffusion, the crystal growth and grain restructuration, it is named inhibitor. Inhibitor impurities often lead

to smaller grains and a strong variation in the structure evolution. Thus, the influence of inhibitors on the SZM is discussed here.

As seen in the basic SZM, the adatoms in Zone I do not have mobility. The impurities are deposited under the same conditions as the main metal. Therefore, the addition of impurities to the system (independently of its concentration) does not influence the microstructure or crystallographic properties of the films. However, the presence of impurities shifts the boundary region between zone I and T to higher energy values, due to the restrain caused in the adatom mobility.

As described in the basic SZM, there is a selective growth in Zone T: the growth occurs according to a specific crystal habit resultant from an isotropy in growth rate of the different crystallographic planes. Due to differences in chemical interaction, the impurities act differently in different crystallographic planes. Consequently, the presence of impurities induces changes on the normal growth rate, as compared to pure conditions, resulting in a different crystal habit and microstructure. At last, a change in preferential orientation can occur. When the impurities concentration is very high, the growth on all facets is blocked and film growth proceeds by repeated nucleation, leading to a nanocrystalline structure.

Zone II is strongly affected by the presence of impurities. As impurities hinder coarsening, the grain restructuration is incomplete. Furthermore, the impurities around the islands sabotage the islands motion as well as the one located at the grain boundaries, which sabotage the grain boundaries movements. The different facets are also affected. A bimodal structure develops at low impurity concentration. The grain restructuration in Zone II is driven by the minimization of the surface and interface energy. In the presence of impurities this process can be affected. In this case, the planes with the lowest surface energy cannot grow and a change in the texture may occur.

A shift on the boundary region between Zone T and Zone II to higher energies is observed. At high impurities concentration, Zone II disappears.

Independently of the impurity concentration on the film, a new Zone is observed. In Zone III globular grains with a random crystallographic orientation along all the film thickness are observed. The size of the grains is inversely proportional to the impurity concentration in the films. These globular grains originate from the impurity layer deposited in the surface of the fastest growing directions, preventing the equiaxed crystals to grow and yielding the growth to proceed by repeated nucleation. An increase in the impurity concentration leads to a decrease of the boundary for Zone III to lower energies and at last extent Zone I is reached.

Figure 2.15 illustrates the revised SZM as proposed by Barna et al.[44,45], including the influence of the impurities in the microstructure.

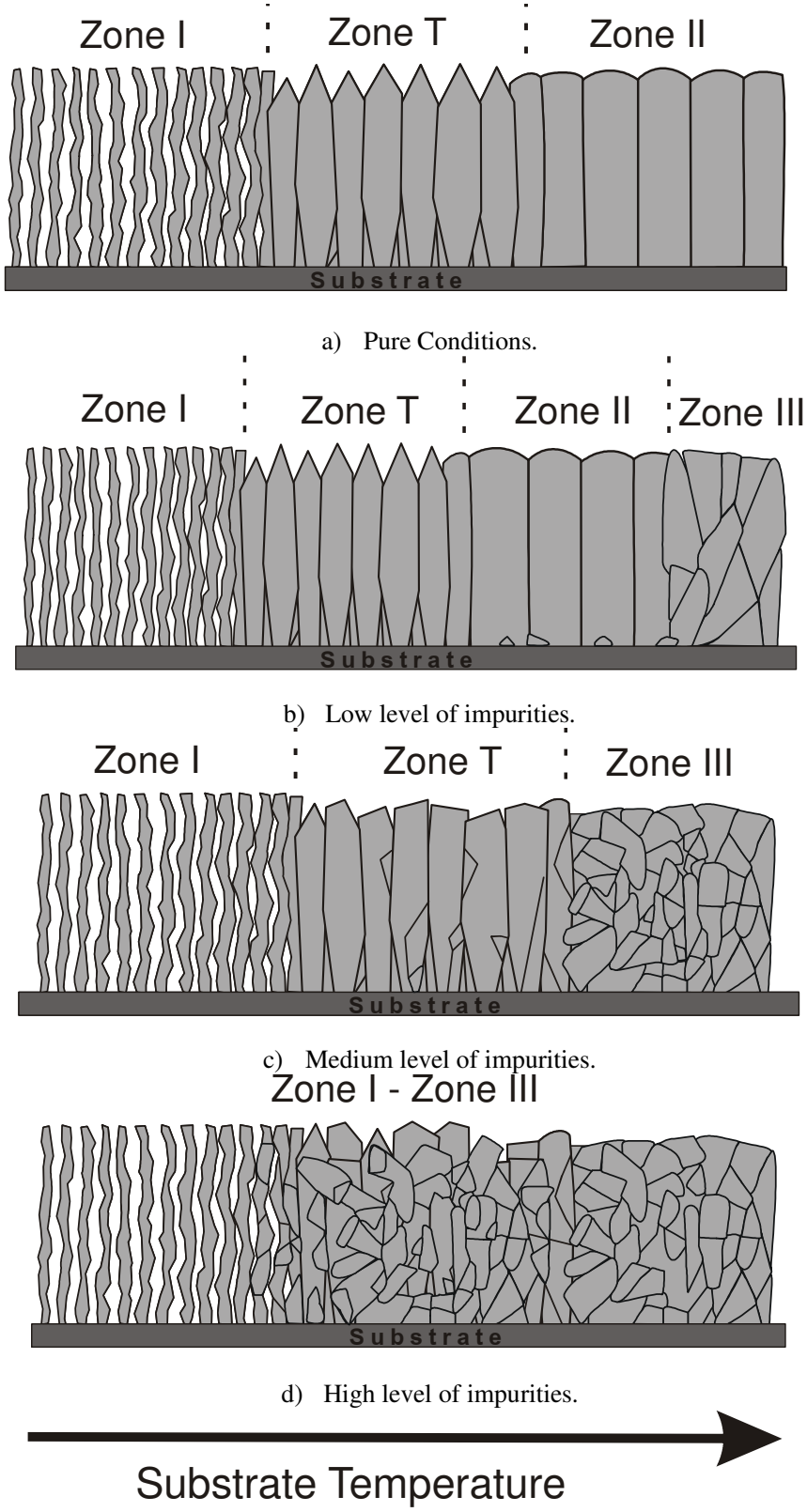

Figure 2.15: Schematic representation of the SZM and the revised SZM as proposed by Barna for different impurity concentrations.[44,45] Figure adapted from Ref. [61].

References

[1] S. Mahieu, W. P. Leroy, D. Depla, S. Schreiber, and W. Moeller, Applied Physics Letters **93** (6), 061501 (2008).

[2] J. E. Mahan and A. Vantomme, Journal of Vacuum Science & Technology a-Vacuum Surfaces and Films **15** (4), 1976 (1997).

[3] R. Behrisch (ed), *Sputtering by Particle Bombardment I*. (Spriger, 1982).

[4] John E. Mahan, *Physical Vapor Deposition of Thin Films*. (John Wiley & Sons, Inc., 2000).

[5] Y. Yamamura and H. Tawara, Atomic Data and Nuclear Data Tables **62** (2), 149 (1996).

[6] in *The Stopping and Range of Ions in Matter 2006,* http://www.srim.org/.

[7] W. Moller and W. Eckstein, Nuclear Instruments & Methods in Physics Research Section B-Beam Interactions with Materials and Atoms **2** (1-3), 814 (1984).

[8] S. Mahieu and D. Depla, Journal of Physics D-Applied Physics **42** (5), 053002 (2009).

[9] D. Czekaj, B. Goranchev, E. K. Hollmann, V. A. Volpyas, and A. G. Zaytsev, Vacuum **42** (1-2), 43 (1991).

[10] M. J. Goeckner, J. A. Goree, and T. E. Sheridan, Ieee Transactions on Plasma Science **19** (2), 301 (1991).

[11] R. A. Baragiola, E. V. Alonso, J. Ferron, and A. Olivaflorio, Surface Science **90** (2), 240 (1979).

[12] S. Mahieu, W. P. Leroy, D. Depla, S. Schreiber, and W. Moller, Applied Physics Letters **93** (6), 061501 (2008).

[13] F. Boydens, W. Leroy, R. Persoons, and D. Depla, Physica Status Solidi A **209** (3), 524 (2012).

[14] Jens Emmerlich, Stanislav Mraz, Rony Snyders, Kaiyun Jiang, and Jochen M. Schneider, Vacuum **82** (8), 867 (2008).

[15] P. M. Martin (Editor), *Handbook of Deposition Technologies for Films and Coatings*. (Elsevier Inc., 2010).

[16] M. W. Thompson, Vacuum **66** (2), 99 (2002).

[17] Y. Yamamura, Radiation Effects and Defects in Solids **55** (1-2), 49 (1981).

[18] Y. Yamamura, T. Takiguchi, and M. Ishida, Radiation Effects and Defects in Solids **118** (3), 237 (1991).

[19] in *Reactive Sputter Deposition*, edited by Depla D. and Mahieu S. (Springer, 2008), Vol. 109.

[20] M. Stepanova and S. K. Dew, Journal of Vacuum Science & Technology a-Vacuum Surfaces and Films **19** (6), 2805 (2001).

[21] M. Stepanova and S. K. Dew, Nuclear Instruments & Methods in Physics Research Section B-Beam Interactions with Materials and Atoms **215** (3-4), 357 (2004).

[22] B. Window and N. Savvides, Journal of Vacuum Science & Technology a-Vacuum Surfaces and Films **4** (2), 196 (1986).

[23] W. D. Sproul, D. J. Christie, and D. C. Carter, Thin Solid Films **491** (1-2), 1 (2005).

[24] W.D. Westwood, *Sputter Deposition*. (AVS Monograph Editor, Ottawa, 2003).

[25] J. Musil and P. Baroch, Ieee Transactions on Plasma Science **33** (2), 338 (2005).

[26] D. Depla, S. Heirwegh, S. Mahieu, J. Haemers, and R. De Gryse, Journal of Applied Physics **101** (1), 013301 (2007).

[27] S. Berg, H. O. Blom, T. Larsson, and C. Nender, Journal of Vacuum Science & Technology a-Vacuum Surfaces and Films **5** (2), 202 (1987).

[28] D. Depla and R. De Gryse, Surface & Coatings Technology **183** (2-3), 184 (2004).

[29] S. Berg and T. Nyberg, Thin Solid Films **476** (2), 215 (2005).

[30] D. Depla and R. De Gryse, Surface & Coatings Technology **183** (2-3), 190 (2004).
[31] D. Depla and R. De Gryse, Surface & Coatings Technology **183** (2-3), 196 (2004).
[32] D.L. Smith, *Thin film deposition, principles and practice*. (McGraw-Hill, 1995).
[33] M. Ohring, *Materials Science of Thin Films, Deposition & Structure*. (Academic Press, 2002).
[34] T. Michely and J. Krug, *Islands, Mounds and Atoms: Patterns and Processes in Crystal Growth Far from Equilibrium*. (Springer, 2003).
[35] C. L. Liu, J. M. Cohen, J. B. Adams, and A. F. Voter, Surface Science **253** (1-3), 334 (1991).
[36] C. Ratsch and J. A. Venables, Journal of Vacuum Science & Technology A **21** (5), S96 (2003).
[37] M. Bott, M. Hohage, M. Morgenstern, T. Michely, and G. Comsa, Physical Review Letters **76** (8), 1304 (1996).
[38] G. L. Kellogg, Surface Science Reports **21** (1-2), 1 (1994).
[39] Y. W. Mo, Physical Review Letters **71** (18), 2923 (1993).
[40] J. A. Venables, G. D. T. Spiller, and M. Hanbucken, Reports on Progress in Physics **47** (4), 399 (1984).
[41] B. W. Wessels, Journal of Vacuum Science & Technology B **15** (4), 1056 (1997).
[42] D. Walton, Journal of Chemical Physics **37** (10), 2182 (1962).
[43] P. B. Barna and M. Adamik, in *Science and Technology of Thin Films*, edited by F.C. Matacotta and G. Ottaviani (World Scientific Publishing Co.Pte.Ltd., Singapore, 1995).
[44] P. B. Barna and M. Adamik, Thin Solid Films **317** (1-2), 27 (1998).
[45] I. Petrov, P. B. Barna, L. Hultman, and J. E. Greene, Journal of Vacuum Science & Technology A **21** (5), S117 (2003).
[46] C. V. Thompson, Annual Review of Materials Science **30**, 159 (2000).
[47] S. Mahieu, PhD Thesis, Ghent University, 2006.
[48] C. R. M. Grovenor, H. T. G. Hentzell, and D. A. Smith, Acta Metallurgica **32** (5), 773 (1984).
[49] R. Messier, A. P. Giri, and R. A. Roy, Journal of Vacuum Science & Technology a-Vacuum Surfaces and Films **2** (2), 500 (1984).
[50] B. A. Movchan and Demchish.Av, Physics of Metals and Metallography-Ussr **28** (4), 83 (1969).
[51] J. A. Thornton, Journal of Vacuum Science & Technology **12** (4), 830 (1975).
[52] J. A. Thornton, Annual Review of Materials Science **7**, 239 (1977).
[53] J. A. Thornton, Journal of Vacuum Science & Technology a-Vacuum Surfaces and Films **4** (6), 3059 (1986).
[54] A. G. Dirks and H. J. Leamy, Thin Solid Films **47** (3), 219 (1977).
[55] L. Abelmann and C. Lodder, Thin Solid Films **305** (1-2), 1 (1997).
[56] Paritosh and D. J. Srolovitz, Journal of Applied Physics **91** (4), 1963 (2002).
[57] C. V. Thompson and R. Carel, Materials Science and Engineering B-Solid State Materials for Advanced Technology **32** (3), 211 (1995).
[58] K. H. Muller, Physical Review B **35** (15), 7906 (1987).
[59] S. Mahieu, P. Ghekiere, D. Depla, and R. De Gryse, Thin Solid Films **515** (4), 1229 (2006).
[60] A. van der Drift, Philips Research Reports **22**, 267 (1967).
[61] P. Ghekiere, PhD Thesis, Ghent Univeristy, 2007.

B. Stoichiometry

3. Stoichiometry

3.1. Introduction

Good control of the stoichiometry combined with the flexibility of the used deposition technique enables to study the influence of the composition on the growth of Mg-M-O thin films, and in this way, this study can be seen as a first step to understand the growth of these ternary metal oxides. Therefore, thin films were deposited by dual reactive magnetron sputtering (section 3.1.1) and their chemical composition was measured with Electron Probe MicroAnalysis (section 3.1.2). Furthermore, the stoichiometry of the thin films was simulated with Monte Carlo (MC) simulations, using SIMTRA code[1](section 3.1.3). Experimental and simulated chemical composition of the Mg-M-O (with M = Al, Cr, Ti, Y, Zr) thin films is presented and compared in section 3.2.

3.1.1. Thin Film Preparation

The Mg-M-O thin films were deposited by dual reactive magnetron sputtering, using a vacuum chamber which setup is shown in figure 3.1. On one home built unbalanced planar circular magnetron a Mg target was clamped. On a second similar magnetron a target of the other element M (= Al, Cr, Ti, Y and Zr) was mounted. All targets were 5 cm in diameter and 3 mm in thickness, with a purity of at least 99.95% (Kurt Lesker). In order to increase the plasma density near the substrate, the outer magnets are stronger than the inner ones with a magnetic field ratio of 1:9. The magnetrons were powered by DC supply units (Hüttinger), designed for magnetron sputtering. Each magnetron source was fixed on a linear shift, allowing in vacuum modification of the target-to-substrate distance. The magnetrons were mounted at 90° with respect to each other, each facing the substrate at 45°.

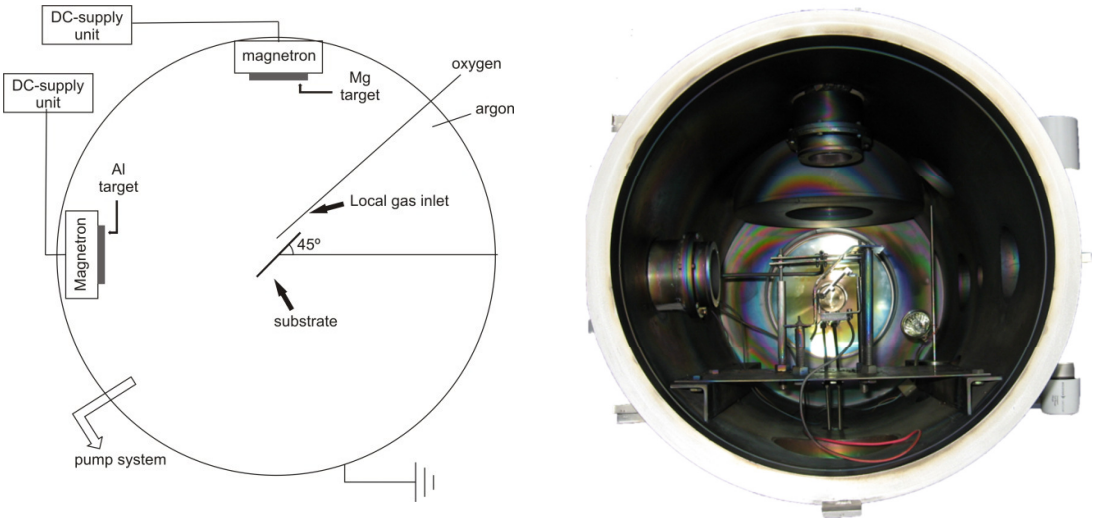

Figure 3.1: Setup and picture of the used deposition system (Panoramix).

The vacuum chamber was pumped down to a base pressure of 10^{-6} mbar as measured by a dual (Pirani + Penning) gauge whereas the pressure during deposition was measured with a capacitance gauge.

The introduction of argon and oxygen into the chamber was controlled by mass flow controllers (MKS). Oxygen was introduced near the substrate (see figure 3.1).

Coatings were deposited on RCA-cleaned silicon substrates with native oxide layer, MgF_2, glass and Si<111> doped with boron (resistivity ~0.001 Ωcm), which were positioned 45º tilted in relation to the cathodes (see figure 3.1) and were fixed on a grounded substrate holder at floating temperature. The choice of the substrate does not influence the microstructure and texture of the Mg-M-O films.

Different series of thin films were deposited. In each series the composition of Mg-M-O was changed from pure MgO to pure M_xO_y. All series of thin films were deposited at a fixed argon pressure (working pressure) of 0.8 Pa. The discharge current for the Mg magnetron $I_{d,Mg}$ was fixed at 0.5 A. For the other magnetron it depended on the material: $I_{d,Cr}$ = 0.5A, $I_{d,Al} = I_{d,Ti}$ = 0.7A, $I_{d,Y} = I_{d,Zr}$ = 0.8 A.

Depending on the used target-to-substrate distances, which were modified in order to achieve the desired stoichiometry, the oxygen flow was high enough to obtain fully oxidized thin films, but low enough to avoid target poisoning. Thus, all depositions were performed in metallic mode.[2] Deposition time was varied to obtain the chosen thicknesses.

Hysteresis

Initially, a global oxygen inlet was used. In order to know the critical oxygen flow for the current setup, and trying to understand the pressure and voltage behavior when oxygen is added to two pure metallic targets, the process characterization (i.e. record process characteristics such as voltage, deposition rate, reactive gas partial pressure) as a function of the reactive gas flow was performed. As an example, figure 3.2 demonstrates the pressure (figure 3.2a/c) and the discharge voltage (figure 3.2b/d) as a function of oxygen flow, for magnesium and aluminum at two different Ar pressures. Plot a) and b) of figure 3.2 are the result of hysteresis measurements performed at 0.3 Pa, while plot c and d) were done at 0.8 Pa.

From observing figure 3.2, one can clearly see that an increase in the Ar pressure leads to a smoother hysteresis for aluminum, increasing the number of stable points where is possible to perform a deposition. On the contrary, in the case of magnesium, the Ar pressure does not affect the hysteresis behavior. Once the two target materials are powered together, the Ar pressure has a strong influence on the hysteresis. At low Ar pressure (0.3 Pa), the two target materials reach the poison mode at the same time, i.e. for the same O_2 partial pressure. For high Ar pressure (0.8 Pa), each material attains poisoning at different O_2 partial pressures.

The chemisorption and ion implantation of the reactive gas on the target are responsible for the target poisoning.[3-5] Increasing the Ar pressure results in a decrease of the O_2 partial pressure and therefore reducing the amount of implanted ions in the target and the

chemisorbed O_2 in the target. As a result, the compound fraction in the target decreases. This way, in the case of aluminum, the hysteresis effect decreases and more workable points are raised. However, for materials with a high reactivity, such as magnesium, the hysteresis behavior is hardly influenced. When the two cathodes are powered together at high Ar pressure (0.8 Pa), as soon as the O_2 partial pressure is enough to fully oxidize the Mg target, this one goes into poison. Though, as the O_2 partial pressure is still not sufficient to fully oxidize the Al target, this one exhibits a poisoning at higher O_2 flow. On the contrary, when the two cathodes are powered together at low Ar pressure (0.3 Pa), the same O_2 flow corresponds to a higher O_2 partial pressure and it is, therefore, enough to fully oxidize the two materials at the same time.

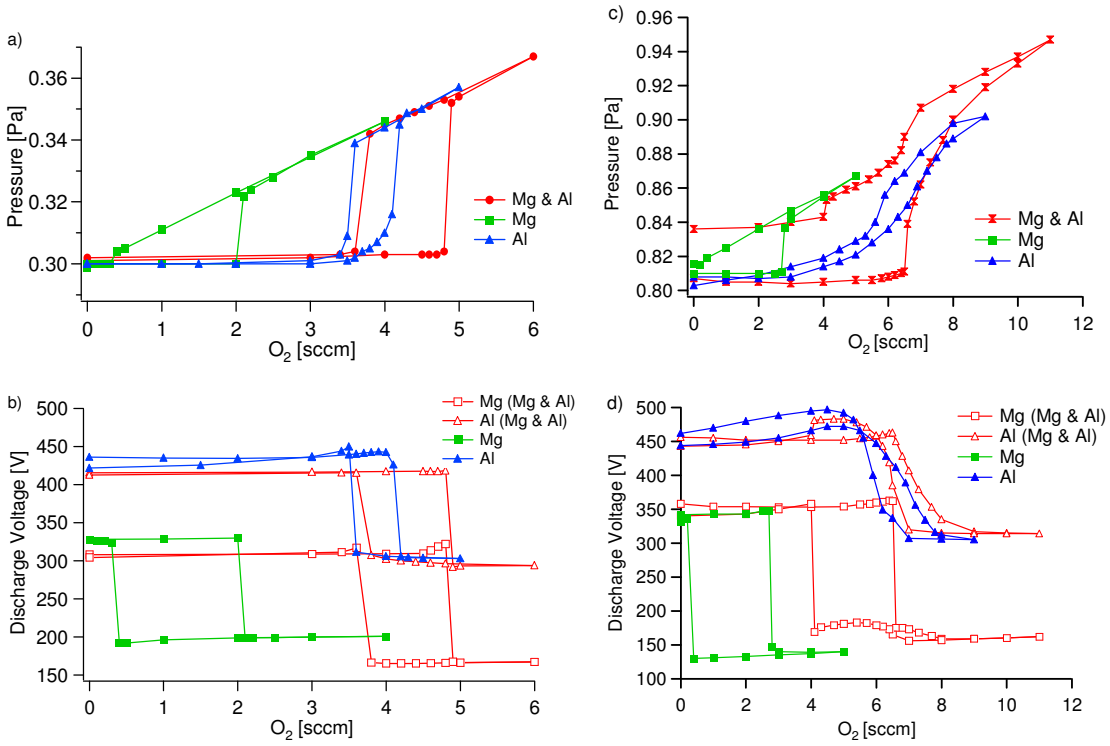

Figure 3.2: Influence of the Ar pressure and O_2 flow on the total pressure (a and c) and on the discharge voltage (b and d) during the sputtering of Mg and Al targets, individually (Mg, Al) and together (Mg & Al). Plot a) and b) were obtained from an Ar pressure of 0.3 Pa with the discharge current of Mg kept at 0.25 A, while the Al one was at 0.7 A. Plot c) and d) were measured with an Ar pressure of 0.8 Pa, Mg discharge current of 0.5 A and Al discharge current of 0.7 A.

The pressure and discharge voltage response to the increase of O_2 flow for magnesium and yttrium is depicted in figure 3.3a and b, respectively. In this case, when the magnesium and yttrium targets are powered together, both targets reach poison mode at the same O_2 flow. Indeed, when compared to aluminum, yttrium is more reactive and therefore the chemisorption has a strong influence.[6]

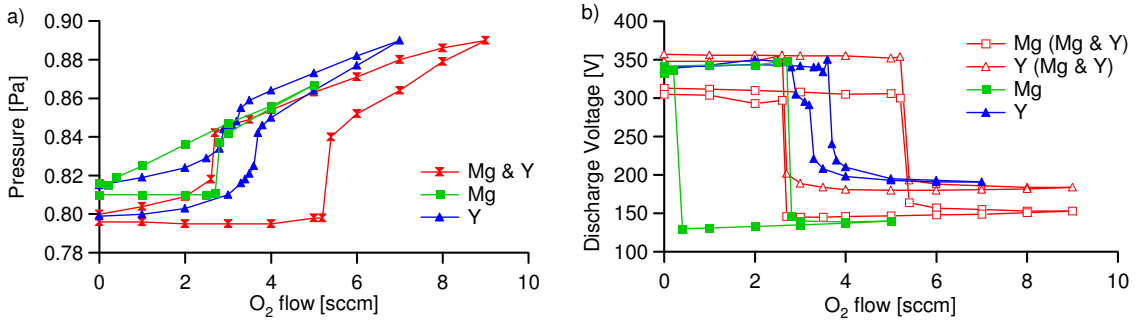

Figure 3.3: Influence of the O_2 flow on the total pressure (a) and on the discharge voltage (b) during the sputtering of Mg and Y targets, individually (Mg, Y) and together (Mg & Y). The discharge current of Mg was kept at 0.5 A, while the Y one was kept at 0.8 A.

Moreover, independently on the Ar pressure, the amount of reactive gas to poison the two targets powered at the same time is not equal to the sum of the targets powered individually. When the reactive gas is added to the vacuum chamber, it will react with all available surfaces (substrate). In the case of co-sputtering (two targets powered together) the available area for the gas to react is not the sum of the substrate available when the targets are powered individually. In co-sputtering deposition, using the present configuration, the deposition profile of each material overlaps one another for a part of the substrate area. Thus, the collecting area when the targets are powered together is less than the sum of the collecting areas when the targets are powered individually. Therefore, one can attempt to explain the deviation between the amount of reactive gas to poison the two targets sputtered simultaneously and the sum of the reactive gas to poison the two targets sputtered individually as being a substrate effect.

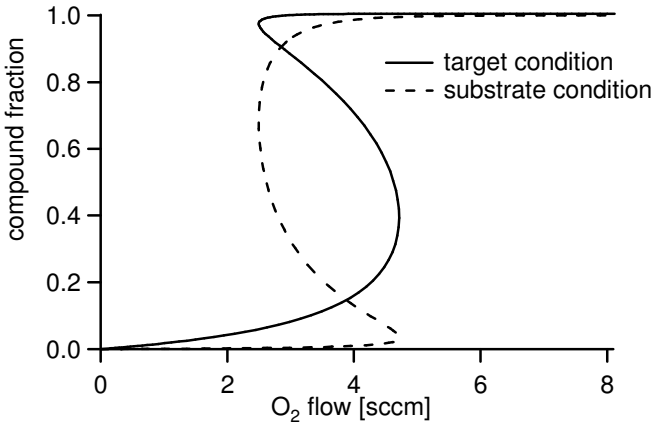

Figure 3.4: Substrate and target compound fraction as a function of the O_2 flow, for Al, $P_{Ar} = 0.8$ Pa, simulation performed using RSD2009.[2]

According to the models of Berg[3] and Depla,[7] a stoichiometric film can only be deposited on the substrate if the reactive gas flow is at least the critical reactive gas flow. The critical flow of the reactive gas is defined as the ratio between the reactive gas flow and the total (sputter and reactive) gas flow needed to induce the abrupt changes noticed during reactive magnetron sputtering. As represented in figure 3.4, at the critical point, the substrate is not fully oxidized.

At the critical point, neither the substrate nor the target is fully oxidized. In order to overcome this problem, a local reactive gas inlet near the substrate is used. This way, a local higher partial pressure of the reactive gas is obtained allowing depositing stoichiometric films on the substrate, without poisoning the target.

The use of a local reactive gas inlet near the substrate does not influence significantly the hysteresis behavior of the targets, neither when powered individually nor together, as is exemplified in figure 3.5.

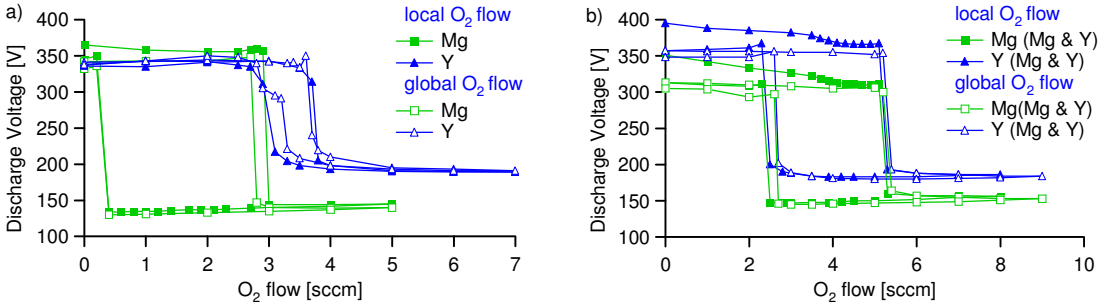

Figure 3.5: Influence of the O_2 flow on the discharge voltage of magnesium and aluminum sputtered individually a) and together b). The discharge current of Mg was kept at 0.5 A, while the Y one was kept at 0.8 A.

3.1.2. Electron Probe Micro-Analysis

Electron probe microanalysis (EPMA) is a non-destructive and analytical method that enables one to determine the chemical composition of solid materials. The sample under investigation is bombarded by an electron beam and x-rays at wavelengths characteristic of the materials present in the sample are emitted. The concentration of each element is determined by comparing the intensity of its characteristic x-ray with the x-ray intensity of a reference sample (measured at the same experimental conditions), which contains the same element at a known concentration.

In this work, the chemical composition was obtained using an EPMA JEOL JXA-8621MX apparatus, with beam current of 30 nA and voltage of 15 keV. This set-up is equipped with detectors for secondary electrons and back-scattered electrons, three wavelength-dispersive detectors with six crystals, two of which specifically for the ultra-light elements (B, C, N, O).

Due to the vacuum chamber configuration and sample position, the chemical composition of the samples is not uniform in all directions. Figure 3.6 depicts the compositional variation in a representative Mg-Al-O sample. The arrows indicate the direction of the Mg and Al flux. As it can be seen the composition varies according to the direction of the metal flux and it is related to the distance of each substrate position to the targets (due to the tilting of the substrate, not all the points of the substrate are equidistant to the two targets). The degree of non-uniformity depends on the target-to-substrate distance and it is more pronounced for shorter target-to-substrate distances.

The non-uniformity in the thin films chemical composition is revised again in section 3.2. The composition values presented in the followings are calculated by averaging the composition

of at least 9 points measured along a virtual line where the composition is uniform. For all the studied systems (with exception of the Mg-Ti-O series, where the standard deviation is ~0.3 at. %.), the standard deviation is ~0.1 at. %.

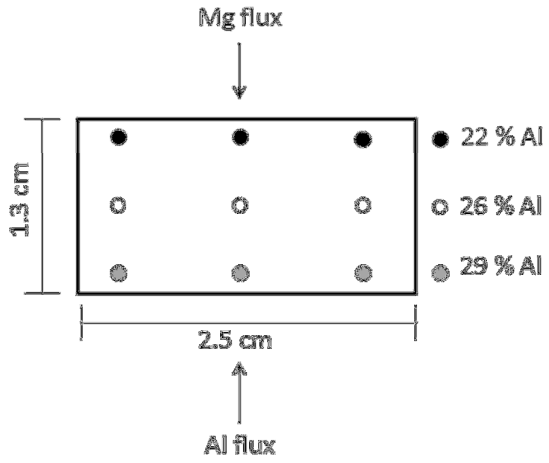

Figure 3.6: Measured Al metal ratio (Al/(Al+Mg) of a thin film produced with Mg target-to-substrate distance of 10.5 cm and Al target-substrate distance of 14.5 cm. The presented Al metal ratio is calculated based on the atomic elemental composition average of 5 measurements.

3.1.3. Simulation of Metal Transport: SIMTRA

The simulations of the different steps involved in the sputtering process are of major importance, not only to reduce the experimental effort but also to gain more insight in some aspects of the process which are experimentally difficult to study.

Knowing the sputter yield, and with the deposition conditions (discharge current, target-substrate distance, total pressure and deposition geometry) as input parameters, SIMTRA enables one to calculate the flux of metallic particles towards the substrate.[1] First, the nascent energy and angular distribution of the sputtered particles leaving a metallic target are simulated with SRIM.[8] Then the transport through an Ar gas is simulated by taking into account the collisions with the background gas. The interaction between the sputtered atoms and the background gas atoms is described by a screened Coulomb interaction potential, with Moliere screening function.[9] The thermal motion of the background gas is also taken into account.[10] Since all depositions were performed in metallic mode, the influence of the small partial pressure of oxygen in the vacuum chamber can be neglected.[11] From the calculated fluxes of the sputtered atoms to the substrate, the film composition or stoichiometry at every position on the substrate can be calculated based on the relative fluxes of the two different metal atoms.

3.2. Chemical Composition

Preliminary depositions were carried out, in order to define the deposition parameters to be used for the growth of the various Mg-M-O films. Table 3.1 lists the chemical composition of Mg-Al-O films grown at fixed target-to-substrate distances (7 cm for Al target and 14.5 cm for Mg target), by varying the Ar pressure and the location of the reactive gas inlet (local and global). The O_2 flow was adjusted to be able to perform the deposition in metallic mode.

O_2 inlet	Ar Pressure [Pa]	Mg % at.	Al % at.	O% at.	Mg% at. theoretic	Al % at. theoretic	O% at. theoretic
Global	0.3	28	65	7	12.8	29.7	57.5
Local	0.3	12	40	48	9.7	32.3	58
Local	0.5	16	31	53	14.6	28.3	57.1

Table 3.1: Chemical composition of the thin films deposited at fixed targets-to-substrate distances and varying the Ar pressure and the type of O_2 inlet. The discharge voltage for Al was 0.7 A, while for Mg was 0.4 A. The theoretic values are calculated maintaining the obtained metal concentrations (Mg+Al), the amount of oxygen needed to fully oxidize them, and performing the normalization.

As predicted by the model of Depla[7] and Berg,[3] it is not possible to deposit a fully oxidized thin film in metallic mode with a global reactive gas inlet. Moreover, the same is the case for a local oxygen inlet and low Ar pressures. Therefore, an Ar pressure of 0.8 Pa was chosen to deposit the Mg-M-O thin films. As described in section 3.1.1 a methodology was developed to facilitate deposition of all Mg-M-O in the same experimental setup. This methodology is based upon simultaneous modification of the discharge current of two magnetron sources, the source-sample distance for each source, and the oxygen flow. As an example, figure 3.7 shows the interplay between target-to-substrate distance, oxygen flow and thin film composition for the Mg-Cr-O series. It is worth noting that the oxygen flow depends strongly on the target-to-substrate distance, or target-oxygen inlet distance. Moreover, as the amount of oxygen introduced in the vacuum chamber is chosen to be just before the critical point for the transition of the process to the compound mode, and the latest depends on the erosion of the targets, this also influences the flux of oxygen used in each deposition. Similar plots to that presented in figure 3.7 for all the other Mg-M-O thin film series and are shown in appendix A. To study the compositional influence on crystallographic and functional properties, series of Mg-M-O films were deposited with increasing concentration of M. Two methods were used to predict the film stoichiometry under different experimental conditions.

At first, a purely experimental method based on some assumptions was used. The composition of the deposited multielement thin film is proportional to the ratio of the material flux from source M to source Mg,

$$\frac{x_M}{x_{Mg}} = \frac{R_M}{R_{Mg}}, \tag{3.1}$$

being x and R the composition and the deposition rate, respectively. In a first assumption, the deposition rate varies inversely as the square of the target-to-substrate distance. Thus, the ratio of the metal concentration can be related with the target-substrate distance as follows:

$$\frac{R_M}{R_{Mg}} = \frac{A \big/ d_M^2}{B \big/ d_{Mg}^2} = C\left(\frac{d_{Mg}}{d_M}\right)^2, \tag{3.2}$$

where *d* denotes the distance. Figure 3.8 shows the Equation (3.2) relation for the various Mg-M-O systems, where the slope of the plots is defined by the constant C in Equation (3.2), and determined by the particle transport. The particle transport, on its turn, depends mainly on the mass and binding energy of the metal.

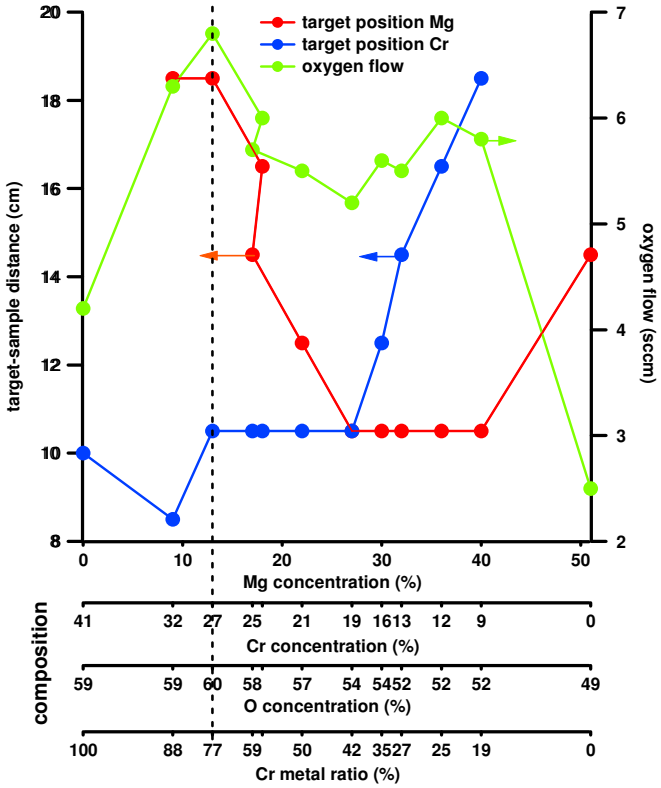

Figure 3.7: Series of Mg-Cr-O thin films. The dotted line is a guideline which relates the sample composition (the 4 horizontal axes which represent respectively the Mg, Cr, O concentration and the Cr metal ratio) to the experimental conditions, i.e. the target-to-substrate distance (left hand axis) and the oxygen flow (right hand axis).

For all different series, which were performed under different conditions in discharge current and target material (with different sputter yield, angular emission profiles and target finishing), this linear relationship holds quite well. Hence, to facilitate the deposition of multielement oxide films, the following procedure can be followed. Two compositions are deposited under a fixed set of experimental conditions, i.e. argon pressure and discharge current. By plotting the ratio of the metal concentrations as a function of the distances ratio (see Equation (3.2)), a calibration line is retrieved (see fitted line in figure 3.8). Based on this calibration line, the relative target-to-substrate distances needed to deposit a given composition are determined. In this way, several compositions can be produced with a minimal number of experiments. The drawback of this method is that first two reference measurements are needed and the method is only applicable to a given system.

Another way to present the chemical composition is the % of M metal ratio, *M/(M+Mg)*. As several metals are mixed with MgO in this work, M metal ratio was the chosen nomenclature, in order to immediately contextualize the reader in a specific Mg-M-O series. This

nomenclature could not be used in the approach presented above due to the fact that the constant parameters (A and B from Equation (3.2)) are not known. In the following the ratio $C_M = \frac{M}{Mg + M}$ is used as a quantity to describe the film composition.

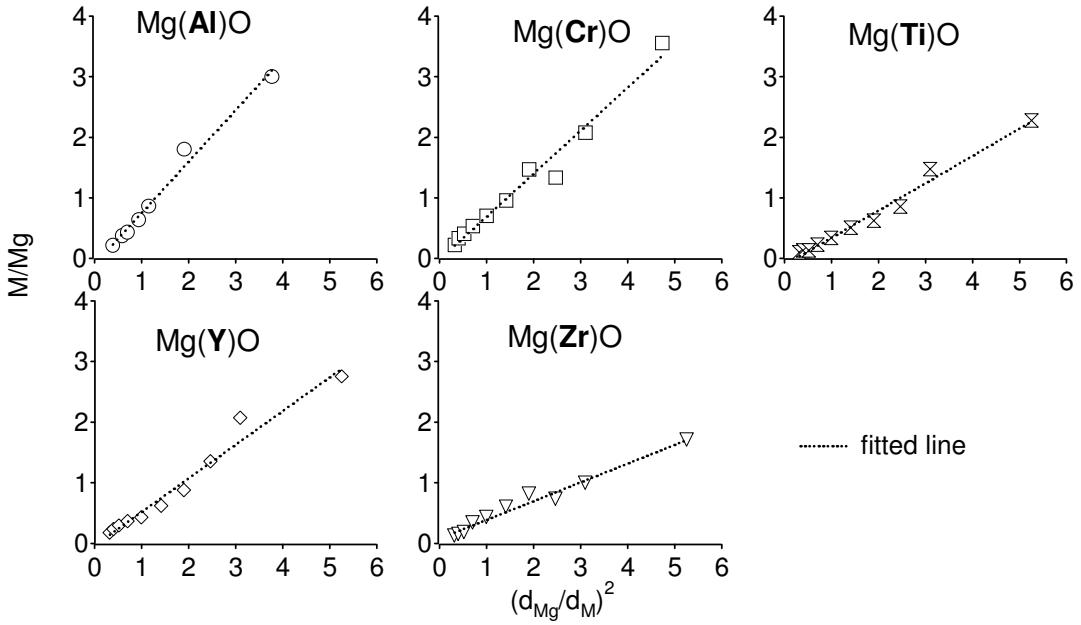

Figure 3.8: Experimental compositions M/Mg for the different studied systems. The horizontal axis refers to the relative deposition rate, taking into account that deposition rate varies inversely as the square of the target-to-substrate distance.

Alternatively to the experimental method, the stoichiometry can be predicted based on the SIMTRA code. As explained before, the thin film composition at every position on the substrate can be calculated based on the relative fluxes of the two different metal atoms. Introducing the configuration details of the vacuum chamber in SIMTRA and the deposition conditions for a certain thin film, the chemical composition of the coating was simulated. The result, presented in its graphical form (one of the SIMTRA output options) is depicted in figure 3.9. The % Al metal ratio in the two magnetrons (Mg and Al) and in the substrate is shown, for a deposition simulation case where the Mg and Al target-substrate distance is 10.5 cm and 14.5 cm, respectively.

The substrate does not have only one color, meaning a non-uniform chemical composition along the substrate surface. Zooming in on the substrate (see figure 3.10), evidences clearly this effect. Nevertheless, the non-uniform chemical composition of the substrate is only pronounced along the direction of the magnetrons, similar to what is experimentally observed and previously reported in this chapter. The graph presented on the right part of figure 3.10 is a quantification of the substrate Al metal ratio along the direction of the magnetrons. Assuming that each point in the substrate has its coordinates (a,b), a certain point in the graphic will be (a_i, $(\sum_{j=1}^{N} b_{i,j})/N$), averaging the obtained chemical composition in the

direction where the composition is uniform. The standard deviation on the averaged values is ~0.8 %.

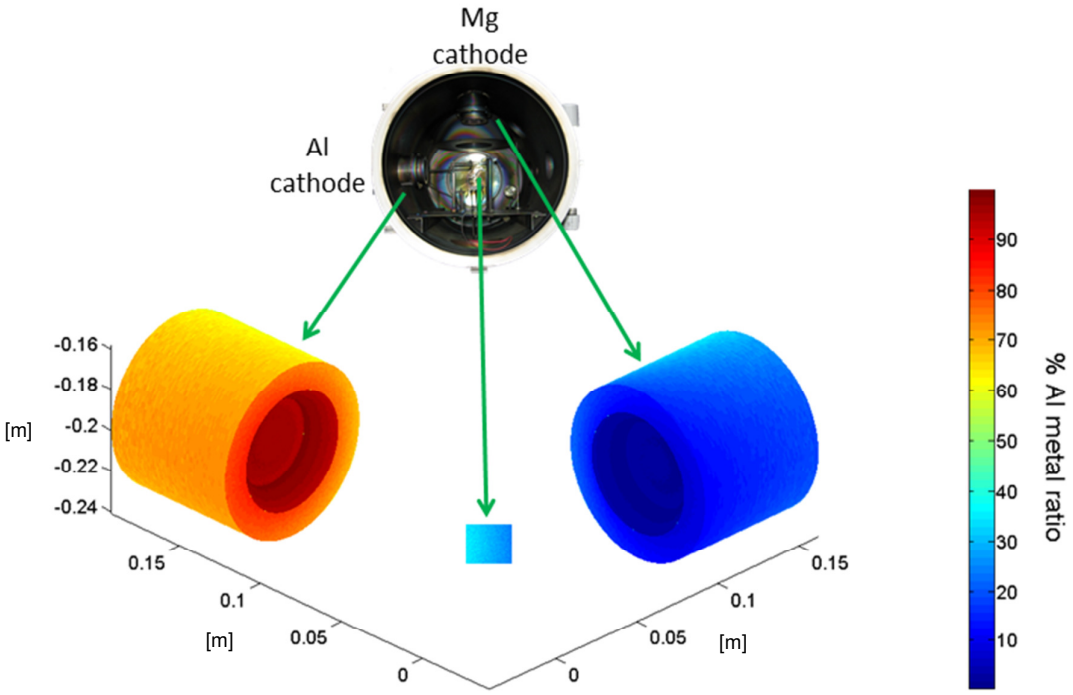

Figure 3.9: C_{Al} as simulated using SIMTRA code in the magnetron surfaces and substrate. The Mg target-to-substrate distance chosen is 10.5 cm, while for Al is 14.5 cm. The substrate dimension is 2 x 2 cm.

For each deposition condition (referring to every deposited thin film), a picture similar to the one depicted in figure 3.9 can be obtained. In order to compare to the experimental results, the chemical composition of all the Mg-M-O thin films was calculated.

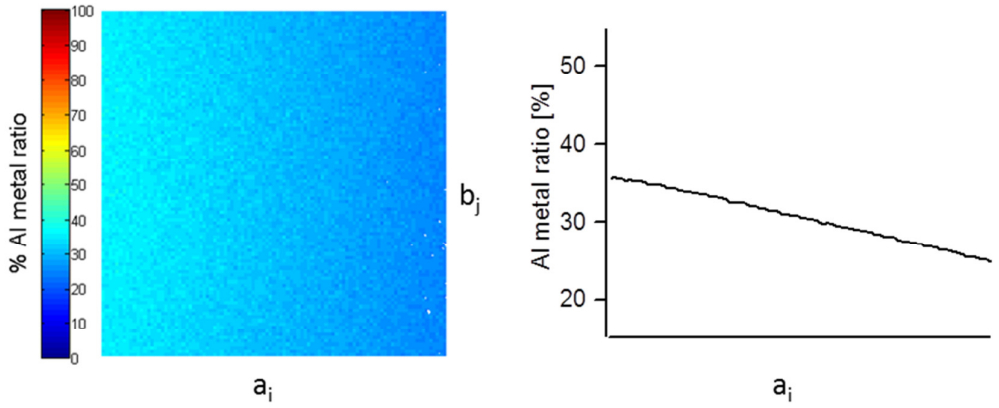

Figure 3.10: Magnification of the substrate presented in figure 3.9. A certain point on the graphic will have coordinates (a_i, $(\sum_{j=1}^{N} b_{i,j})/N$), with a standard deviation of ~0.8 %. The substrate dimension is 2 x 2 cm.

In figure 3.11, the comparison between the composition calculated using the code (horizontal axis), and the composition obtained experimentally (vertical axis) for all systems, is shown to be in good agreement. The small deviations observed are within the error of the experimental composition (error in EPMA measurements) or within the error of the simulated composition (due to an error in the experimental input parameters such as discharge current, sputter yield or statistical error of the simulations). As stated before, the sputtered particles have a certain spatial distribution which can induce some deviation in the simulated results, if the used angular distribution is not the most correct one. This striking agreement between the experimental and simulated composition indicates that SIMTRA, in combination with the correct sputter yields, allows for prediction of the composition of multielemental thin films deposited by dual reactive magnetron sputtering. This method is not limited by changes in the deposition geometry, or the complexity of the deposited material, as these changes can be implemented in the SIMTRA code. Of course, the validity of this approach is limited by the correct values of the angular distribution and sputter yields; in this study the latter ones were obtained experimentally (see section 1.2.1 – sputter yield).

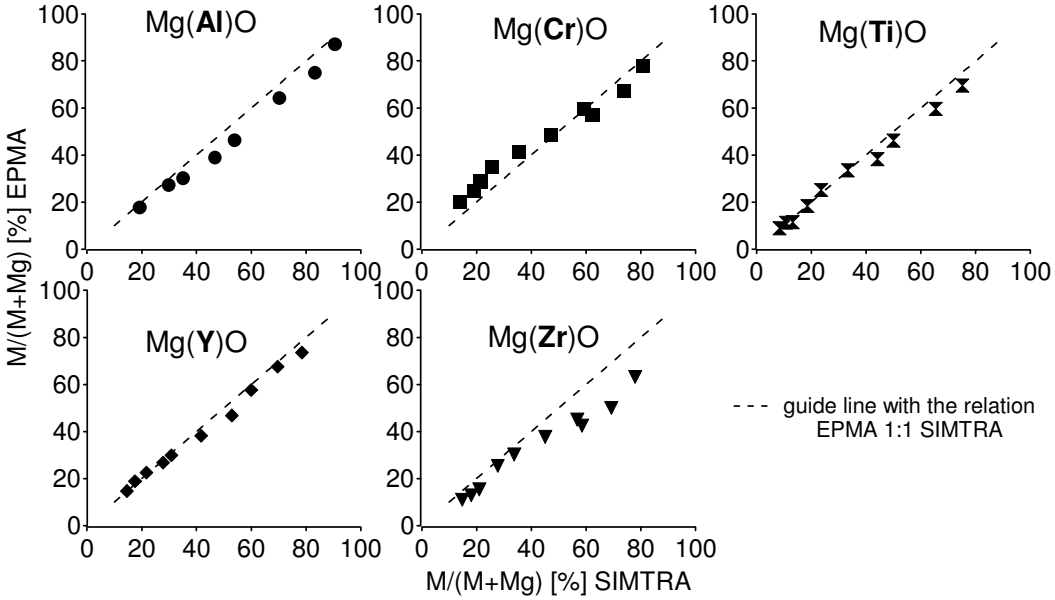

Figure 3.11: Comparison of the experimental (vertical axis) and simulated (horizontal axis) compositions M/(M+Mg) for the different studied systems. The dashed line is a guideline to help the reader to immediately see the deviation between experimental and simulated results.

References

[1] K. Van Aeken, S. Mahieu, and D. Depla, Journal of Physics D-Applied Physics **41** (20), 205307 (2008).

[2] D. Depla, S. Heirwegh, S. Mahieu, and R. De Gryse, Journal of Physics D-Applied Physics **40** (7), 1957 (2007).

[3] S. Berg and T. Nyberg, Thin Solid Films **476** (2), 215 (2005).

[4] D. Depla and R. De Gryse, Surface & Coatings Technology **183** (2-3), 184 (2004).

[5] D. Depla and R. De Gryse, Surface & Coatings Technology **183** (2-3), 190 (2004).

[6] K. Strijckmans, W. P. Leroy, R. De Gryse, and D. Depla, Surface & Coatings Technology ((2012) accepted for publication).

[7] D. Depla and R. De Gryse, Surface & Coatings Technology **183** (2-3), 196 (2004).

[8] in *The Stopping and Range of Ions in Matter 2006,* http://www.srim.org/.

[9] S. Mahieu, K. Van Aeken, and D. Depla, in *Reactive Sputter Deposition*, edited by Depla D. and Mahieu S. (Springer, 2008), pp. 199.

[10] T. Nakano, I. Mori, and S. Baba, Applied Surface Science **114**, 642 (1997).

[11] S. Mahieu, G. Buyle, D. Depla, S. Heirwegh, P. Ghekiere, and R. De Gryse, Nuclear Instruments & Methods in Physics Research Section B-Beam Interactions with Materials and Atoms **243** (2), 313 (2006).

C. Crystallographic Properties

4. Introduction

Film properties and functionality depend crucially on the crystallinity, i.e. on whether a film is crystalline or amorphous. Amorphous films are in general less dense and thus exhibit inferior mechanical strength as compared to their crystalline counterparts.[1] On the other hand, due to the absence of grain boundaries, amorphous films are less prone to diffusion, chemical attack oxidation and corrosion.[2] Furthermore, the lack of long-range order results in isotropic properties, which is frequently not the case for crystalline films. The combination of amorphous and crystalline structure in the same film can also be beneficial. This is the case in the so called nanocomposite films in which control of the relative size and separation of nanosized crystals embedded in an amorphous matrix can result in films with superior mechanical, electrical and tribological performance.[3,4]

Film synthesis at conditions of limited atomic assembly kinetics - realized at relatively low growth temperatures and large arrival rates of the film forming species - leads to amorphous structures in materials with relatively large crystallization energy barriers.[5] Bombardment by energetic species, frequently encountered in plasma-assisted physical vapor deposition techniques (e.g. magnetron sputtering) has also been shown to be crucial for the structure formation.[6,7] Moreover, intentional and non-intentional addition of impurity species which segregate at the grain boundaries may hinder or promote grain growth and thus determine the structure formation.[8,9] Another way to control structure formation is by mixing two materials that exhibit different crystalline structures. In the case of relatively low concentration of the impurity phase in the host lattice, a solid solution may form. However, further increase in the impurity phase content often leads to formation of amorphous structure. Although observed in many systems, the origin of the latter behavior on a fundamental electronic level is still not understood. The presence of atoms with size and valence electron number different than that of the host atom may affect electronic charge distribution and consequently the bond strength and type. These factors are, in turn, known to be crucial for the stability of a certain atomic configuration.

A polycrystalline film consists of many crystallites, called grains, of various size, shape and orientation. Each crystallite is a single crystal with anisotropic properties due to its periodic atomic arrangement in three-dimensional space. In most cases, crystallites have an anisotropic orientation distribution. This anisotropic distribution is referred to as a preferred orientation or a texture. A film having all crystallites fully randomly oriented is said to have no texture. Depending on the degree of the preferred orientation, a film is referred to as having a weak, moderate or strong texture. The texture in thin films can be classified into different types. A first case is simply the absence of any preferential orientation: all grains have a completely random orientation, and this is named random texture (see figure 4.1a)). If all the grains have the alignment of one crystal plane in common, parallel to the substrate, and no additional constrains on the orientation exist, the films is said to have uniaxial alignment (see figure 4.1b)), exhibiting an out-of-plane orientation. This texture is called fiber texture. In the case

that the grains have the alignment of one crystal plane in common, but not parallel to the substrate, an off-normal fiber texture exists and is called axiotaxy. Furthermore, when one crystallographic axis is parallel to the substrate normal and a second crystallographic axis, which is parallel to the substrate is also aligned, there is in-plane and out-of-plane alignment (see figure 4.1c)). A thin film which possesses preferential out-of-plane and in-plane alignment is said to be biaxially aligned. When the orientation of the grains in the film is uniquely defined with respect to the substrate, only one single orientation of the grains occurs. For a substrate which is a single crystal, one used the term epitaxy.

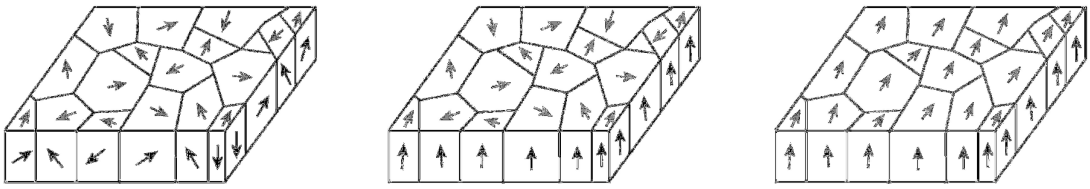

a) Non Aligned b) Uniaxial Alignment c) Biaxial alignment

Figure 4.1: Schematic representation of the alignment in polycrystalline thin films. a) Non aligned; b) Uniaxial alignment and c) Biaxial alignment.

The properties of polycrystalline materials are determined by the combination of the single crystal's properties, the boundary between crystallites and the orientation distribution of the crystallites within the material. Therefore, it is important to understand the crystalline structure and microstructure of the thin films.

In order to evaluate the crystallinity of the thin films, angular scan and pole figure measurements were carried out. In the next sections (4.1 to 4.3) a brief description of the methods is presented, along with the other techniques used to characterize the Mg-M-O films and the Molecular Dynamics (MD) simulations conditions. In chapter 5, general trends observed with Bragg-Brentano XRD configuration are shown and discussed. Further, chapter 6 discusses a model to explain the structure formation of the Mg-M-O films. The texture of the films is shown and atomistic mechanisms that are responsible for the films texture are suggested in section 7. Finally, the influence of temperature (during the growth and after the deposition) in the Mg-M-O films is shown in section 8.

4.1. X-ray Diffraction

X-rays are electromagnetic radiation with a wavelength in the range of 0.01 – 100 Å.[10] The wavelength of typical X-rays used in X-ray diffraction (XRD) is in the vicinity of 1 Å, which is comparable to the range of interatomic spacing in crystals. In this work, Cu Kα X-rays with a wavelength of 1.54 Å are used.

When a monochromatic X-ray beam hits a sample, in addition to absorption and other phenomena, it generates scattered X-rays with the same wavelength as the incident beam. Those scattered X-rays are not evenly distributed in space, but are a function of the electron distribution in the sample. The atomic arrangement in the sample can be ordered like a single crystal or disordered like glass (or liquid). Within the ordered like materials, different atomic arrangements are possible. Therefore, the intensities and spatial distribution of the scattered

X-rays form a specific diffraction pattern that is uniquely determined by the structure of the sample.

Between all the theories and equations that relate the diffraction pattern and the material structure, Bragg's law is a simple way to describe the diffraction of X-rays by a crystal. In figure 4.2, the incident X-rays hit the crystal planes with an incident angle θ and reflection angle θ. The diffraction peak is observed when the Bragg condition is satisfied: $n\lambda = 2d_{hkl}sin\theta$, where λ is the wavelength, d_{hkl} is the distance between each adjacent crystal planes (P_1 and P_2, as an example), θ is the Bragg angle at which is observed a diffraction peak, and n is an integer number, called the order of reflection. In X-ray diffraction using a single wavelength (which is the case) the Bragg equation is typically, from practical point of view, expressed with $n = 1$.

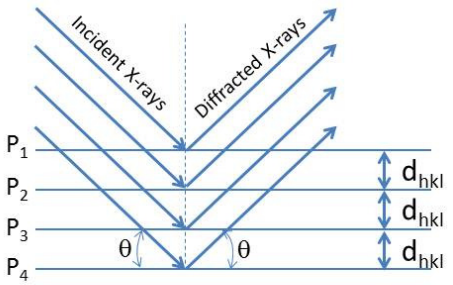

Figure 4.2: The incident and reflected X-rays make an angle of θ, symmetric to the normal of the crystal planes P.

In a typical diffractometer, the angle between the incident X-rays and the substrate plane, and the angle between the substrate and the diffracted X-rays are the same. Therefore, only crystallographic planes parallel to the substrate plane can be detected. Thus, varying the angle θ results in a spectrum containing all the crystallographic planes parallel to the substrate plane, and is commonly named $\theta/2\theta$ spectrum or angular scan. Knowing the angle θ at which the diffraction occurs, the interplanar distance of crystallographic parallel to the substrate can be calculated using Bragg's law. Nevertheless, the intensity of the diffracted peaks (*hkl*) is not only directly related to the number of scatters of planes with a *hkl* planes parallel to the substrate, because the intensity of the peaks is influenced by several other parameters.[10,11] Taking into account some parameters such as the structure factor, absorption factor and temperature factor, the intensity of the diffracted peaks can be related with the number of planes parallel to the substrate plane, by means of the intensity factor I_{hkl}. Those intensity factors are tabulated for a huge amount of powder diffracted material (random distribution) by the International Centre for Diffraction Data (ICDD).

In this work, θ/2θ XRD measurements were performed with a LynxEye Silicon Strip detector mounted into a D8discover apparatus (Bruker axs).

4.1.1. Texture Analysis

When a conventional X-ray diffractometer with a point detector is used for texture measurement, the crystalline orientation distribution in one direction is measured at a time, and full texture information is measured by rotating the sample to all the desired orientations. This is important because realistically, polycrystalline materials usually do not have randomly oriented grains (or crystallites). The deviation of the statistical grain orientation distribution of a polycrystalline material from the ideal powder is measured as a texture or preferred orientation. Texture is a measure of the orientation distribution of all grains in a sample with respect to the sample direction. By using X-ray diffraction to characterize texture, the peak intensity of a particular crystallographic plane at all tilt angles with respect to the sample direction is measured.

Plotting the intensity of a certain (hkl) line with respect to the sample coordinates in a stereographic projection results in a qualitative view of the crystallites' orientation in the sample relative to a sample direction. These stereographic projections are named pole figures and the representation of the thin film texture is normally done by choosing a particular crystallographic plane and presenting its pole figure.

Stated differently, a pole figure is measured at a fixed Bragg diffraction angle (corresponding to a given (hkl) reflection) in order to examine the distribution of that specific orientation. For that, successive ϕ scans are measured for each χ angle; where ϕ and χ denote the azimuthal and polar angle, respectively. The diffraction intensity for each pair of χ and ϕ is proportional to the amount of (hkl) planes in reflecting condition. In short, the pole figures give the probability of finding a given crystallographic orientation as a function of the sample direction.

In case of an amorphous thin film, the measured pole figure does not show any features (see figure 4.3a)), as it lacks of any crystalline arrangement. Pole figures of a polycrystalline material with a random orientation (absence of texture) should be uniform. However, observing figure 4.3b), where the (200) pole figures of MgO powder is presented, one can clearly see that it is not the case. The reason for this discrepancy between theory and the measured pole figures comes from equipment limitations, as the sensitivity of the detector decreases immensely when χ increases. This effect is known as defocusing effect. The existence of an out-of-plane orientation and absence of in-plane alignment gives rise to a ring, indicating the existence of fiber texture. As an example, figure 4.3c) depicts the (200) pole figures of a [111] out-of-plane oriented Mg-Mg-O thin film. When a biaxial aligned thin film is measured, the diffraction ring turns into poles. This way, the (200) pole figures of a biaxial aligned [111] out-of-plane oriented thin film will present three poles, as it is shown in figure 4.3d), while the (111) pole figures of the same sample will evidence only one pole around χ=0° (see figure 4.3e)).

The pole figures measurements were performed using a Sol-X energy dispersive x-ray detector mounted into a D8 discover apparatus (Bruker axs). In these pole figures, χ (the polar angle) and ϕ (the azimuthal angle) were varied from (*i*) 0-80° and (*j*) 0-360°, respectively, in steps of 2°.

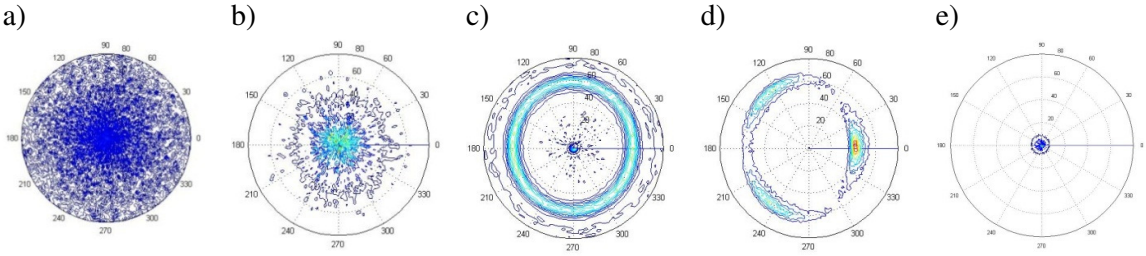

Figure 4.3: (200) Pole figures of a a) amorphous thin film; b) random oriented sample; c) (111) out-of-plane oriented thin film with a random in-plane alignment; d) biaxial aligned thin film with a (111) out-of-plane orientation; e) (111) pole figure of a (111) out-of-plane oriented thin film.

4.1.2. Crystallinity

The MgO structure is similar to the well-known NaCl structure. Another way to present the change in crystallinity observed along the series of thin films is looking to the fraction of crystalline material with a MgO phase. The fraction of crystalline MgO phase in the Mg-M-O thin films was determined based on the (200) pole figures of the different thin films, as follows. The (200) pole figure of MgO powder was measured under the same conditions as the used ones for the thin films. In order to correct the recorded pole figures for the defocusing effect, the average intensity at a given value of the polar coordinate χ_i (χ_i = 0-80°) over the measured azimuthal angle ϕ_j (ϕ_j = 0-360°) was calculated:

$$I_{\chi_i} = \frac{\sum_{j=0}^{360} I_{\phi_{i,j}}}{180}. \tag{4.1}$$

Thereupon, the I_{χ_i} values were normalized according to,

$$I^*_{\chi_i} = \frac{I_{\chi_i}}{\max(I_{\chi_i})}, \tag{4.2}$$

where $\max(I_{\chi_i})$ represents the largest I_{χ_i} value. Afterwards, the initial intensity of each measured I_{χ_i,ϕ_j} point in the pole figures of the MgO powder was divided by the corresponding $I^*_{\chi_i}$ value. The obtained values are the correction factors for defocusing effect, D_{χ_i,ϕ_j}.

To perform the background correction, the (200) pole figures of an amorphous thin film was used. Taking this into account, the crystallinity, *C*, of a certain thin film can be calculated from

$$C = \sum_{\chi=0}^{80} \sum_{\phi=0}^{360} \left(\frac{s_{\chi,\phi}}{D_{\chi,\phi}} - \frac{b_{\chi,\phi}}{D_{\chi,\phi}} \right) \times \sin(\chi), \tag{4.3}$$

being *s* the sample and *b* the background. Moreover, as the thin films do not all have the same thickness, different volumes of material were measured for each sample and therefore the

crystallinity had to be corrected for thickness. Additionally, the X-rays are scattered by the electron cloud of the atom and therefore the scattering amplitude of X-rays increases with the atomic number of the atoms in the sample. The scattering amplitude of X-rays is also dependent on the Bragg angle of scattering. Due to the substitution of Mg by other cations in the sample, the crystallinity of the thin film has also to be corrected for the atomic scattering factor.

The non-dispersive part of the atomic scattering factor for neutral atoms as a function of k ($k = (\sin\theta)/\lambda$) can be calculated by the function:

$$f_{atom}(k) = c + \sum_{i=1}^{4} a_i \exp\left(-b_i k^2\right), \tag{4.4}$$

where a_i, b_i and c (i=1,…,4) are the set of nine coefficients known has the Cromer-Mann coefficients.[12] Equation 4.4 is only valid for $k < 2.0$ Å^{-1}, which is the case. The scattering factor of a determined thin film is determined by the weighted atomic scattering factor (according to its chemical composition).

At last, the relative crystallinity was normalized by using a pure MgO film as reference.

4.1.3. In-situ XRD

In-situ XRD measurements were carried out in order to study the crystallization behavior of the thin films during heat treatment. The used setup was built at Ghent University (Research group COCOON) and consists of a commercially available Bruker D8 diffractometer, a linear 'Vantec' detector and a home-built annealing chamber. The use of the linear Vantec detector in a fixed position allows for the acquisition of an XRD spectrum over a 2θ range of up to 20°.

The samples are heated using a BN-encapsulated graphite heating element produced by Advanced Ceramics. The heating element is covered with a Mo plate which evenly distributes the generated heat. As a result, the heat received by a sample situated on top of this plate is homogeneously spread across the entire sample. The temperature is measured with a Cr/Al thermocouple embedded in the Mo plate. All details of this apparatus can be found in the PhD thesis of Knaepen.[13]

After loading the sample, the system is pumped down to a base pressure of about 4 Pa, in order to ensure a controlled atmosphere during the heat treatment. Successively, the system is purged several times with a purifying gas, He, to remove as much contaminants as possible.

In this work, all the heat treatments were performed in a He atmosphere for a 2θ range between 30 and 50°. The heating ramp was varied and therefore will be mentioned when the results are presented.

4.2. Transmission Electron Microscopy

Transmission electron microscopy (TEM) is a powerful technique due to the large variety of information that it can provide over the wide range of length scales down to the level of atomic dimension. The principle of TEM is schematically shown in figure 4.4. Electrons are

thermionically emitted by a gun and are accelerated to energies of 100 keV or higher. The electron beam is projected to the sample by a condenser lens system, which also controls the illumination of the specimen. During their passage through the sample the electrons experience a variety of scattering processes. The objective lenses focus these electrons on the back focal plane (reciprocal lattice).

To obtain a higher magnification, an intermediate lenses and projector system is used. The intermediate lenses define whether a diffraction pattern or an image is formed. Changing the current in the lenses (and therefore the magnetic field strength) is used to adjust the focal length and decide on the formation of an image or a diffraction pattern. In order to restrain the diffraction pattern to a certain selected area, a diffraction aperture can be used in the plane of the image. The imaging and diffraction mode of TEM are schematically represented in figure 4.4 a) and b), respectively.

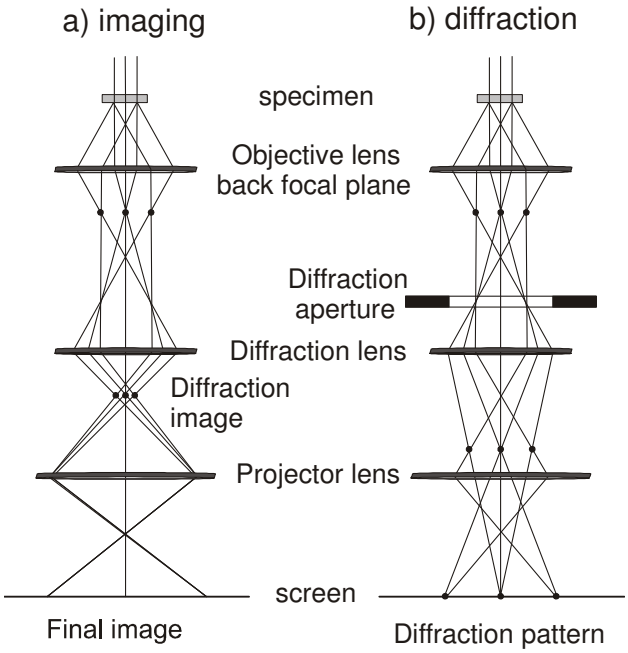

Figure 4.4: Schematic representation of a TEM system in a) imaging and b) diffraction mode.

Images can be formed by several ways. The bright-field image is obtained by blocking all diffracted beams with an aperture and only allowing the primary transmitted one to pass through. When both the transmitted and one diffracted beam are used, then the so-called dark field images are obtained. In the third imaging mode the primary beam is made to recombine with one or more diffracted ones. This technique is employed in high resolution lattice imaging.

4.2.1. Electron Diffraction

Similar to XRD, the diffraction at the planes (electron diffraction, in the TEM case) occurs only if the incident beams are at angles that satisfy Bragg's law of diffraction. The association of a spot or a ring in an Electron Diffraction (ED) pattern to specific diffraction planes is called indexing. The angles and spacing between lattice planes can be determined when the

ED pattern is calibrated based on a known material. Usually, for thin films, the substrate is used for calibration. Structural information can also be obtained from the ED patterns. For polycrystalline thin films with only one [uvw] out-of-plane orientation, the diffraction pattern entails the presence of diffraction rings. In the case of biaxially aligned polycrystalline films, the ED pattern exhibit diffraction spots. If there is a slight variation in the biaxial alignment of the films, the spots become broader. Therefore, the width of the spots is an indication for the alignment degree of the polycrystalline film.

4.2.2. High Resolution Transmission Electron Microscopy

High Resolution (HR) TEM allows to obtain the image of the structure of a sample at an atomic scale. The HRTEM image results from the interference of the direct incident electron beam and the selected diffracted beam.

The exit wave (electron wave at the exit plane of the sample) contains all structural information and has to pass through the lenses of the microscope before being able to be recorded. The Fourier transform allows the transformation of the real (image) space into the reciprocal (diffraction) space, yielding to diffraction patterns from different regions of interest in a HRTEM image, providing structural information from the inter-planar spacing and angles.

4.2.3. Electron Energy –Loss Spectroscopy

Electron energy-loss spectroscopy (EELS) measures the energy loss of electrons during electronic excitations in materials. An EELS spectrum represents the number of scattered electrons (intensity) as a function of their decrease in energy. Therefore, EELS can reveal information about the chemical nature and bonding of the material.

The Energy Filtered (EF) TEM is based on EELS. It is a combination of chemical and spatial information. As a result, an elemental map reveals its distribution from any specific area of the sample.

All the TEM work presented in this thesis was performed by N. Jehanathan.[e] Because TEM results contribute to a better understanding of the thin film growth, when being an asset, they are presented in this thesis.

4.3. Scanning Electron Microscopy

Scanning Electron Microscopy (SEM) is a technique for imaging the surface. In SEM the image is obtained by scanning the surface. A field emission gun generates electrons that are focused and accelerated towards the sample by means of several electromagnetic lenses. Those accelerated electrons carry significant amounts of kinetic energy (in the range of a few keV up to 30 keV), which is dissipated as a variety of electronic excitations as a result of the electron-sample interactions, when the incident electrons are decelerated in the solid sample. These electronic excitations include secondary electrons (that produce SEM images), backscattered electrons (BSE), diffracted backscattered electrons (EBSD, which can be used to determine crystal structures and orientations of minerals), photons (characteristic X-rays

[e] Research group EMAT, University of Antwerp.

that are used for elemental analysis and continuum X-rays), visible light (cathodoluminescence, CL), and heat.

Secondary electrons and backscattered electrons are commonly used for imaging samples: secondary electrons are most valuable for showing morphology and topography on samples and backscattered electrons are most valuable for illustrating contrasts in composition in multiphase samples (i.e. for rapid phase discrimination). The secondary electrons come from outer shell electrons with a low binding energy. If the secondary electrons receive sufficient energy they will escape from the sample surface. The secondary electrons are only emitted from the surface region, as schematically depicted in figure 4.4. The surface topography has a great influence in the contrast obtained in a SEM image. In a horizontal surface, the surface produces less secondary electrons as compared to an inclined surface, due to the smaller interaction volume between the beam and the surface (grey region of figure 4.4).

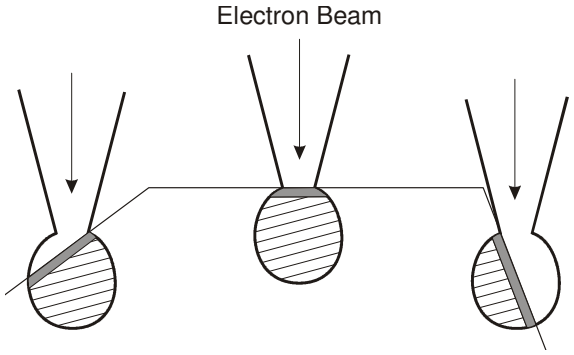

Figure 4.4: Schematic representation of the impact of the incident electrons on the sample. The volume of the interaction region is strongly dependent on the beam intensity and sample nature.

X-ray generation is produced by inelastic collisions of the incident electrons with electrons in discrete orbitals (shells) of atoms in the sample. As the excited electrons return to lower energy states, they yield X-rays that are of a fixed wavelength (which is related to the difference in energy levels of electrons in different shells for a given element). Thus, characteristic X-rays are produced for each element in the sample that is "excited" by the electron beam.

SEM analysis is considered to be "non-destructive"; that is, x-rays generated by electron interactions do not lead to volume loss of the sample, so it is possible to analyze the same sample repeatedly.

In this work, SEM is used not only to study the topography of the films, but also the microstructure evolution (by cleaving the samples and analyzing its cross-section).

4.4. Molecular Dynamic (MD) Simulations

The MD method is a technique for computing the equilibrium and transport properties of a classical many-body system. Giving an initial set of positions and velocities of a system of *N* atoms, Newton's equations of motion are solved for this system.[14] Therefore, the reliability of the MD results is largely determined by the interatomic potential used in the simulation. In the present study, a classical pairwise ionic potential,[15] describes the interactions between atoms:

$$U_{ij} = \frac{q_i q_j}{4\pi\varepsilon_0 r_{ij}} + A\exp\left(-\frac{r_{ij}}{\rho}\right) - \frac{C}{r_{ij}^{\,6}}, \qquad (4.5)$$

where q_i, q_j are the charges of atoms *i* and *j*, r_{ij} is the distance between the atoms, and *A*, ρ and *C* are parameters fitted for each pair of ions. The first term is the Coulomb interaction, the exponential term represents the short range repulsion and the term $(-r_{ij}^{-6})$ accounts for van der Waals attraction. It has been demonstrated that this potential yielded good agreement with experiments for the structure of deposited Mg-Al-O thin films.[16] The same procedure was applied to study also the deposition of Mg-Cr-O and Mg-Y-O thin films. The potential parameters used in the simulations are summarized in table 4.1. For all investigated systems a rigid-ion model has been used, i.e. the ionic polarization is not considered.

i-j	A [eV]	ρ [Å]	C [Å^6 eV]	Ref
Mg^{2+}-O^{2-}	1279.69	0.29969	-	[17]
Al^{3+}-O^{2-}	1374.79	0.3013	-	[17]
Cr^{3+}-O^{2-}	1313.18	0.31650	-	[18]
Y^{3+}-O^{2-}	1766.40	0.33849	19.43	[18]
O^{-2}-O^{2-}	9547.96	0.21916	32.0	[17,18]

Table 4.1: Short-range potential parameters used in the MD simulation.

Mg^{2+}, M^{3+} and O^{2-} ions in different ratios are deposited one by one on an amorphous (Al_2O_3) substrate surface. An amorphous substrate was chosen in order to avoid a possible influence of the crystalline substrate on the structure or orientation of the growing films in the simulations, as it was observed when a MgO (100) substrate was used.[16] Although the experiments were performed at floating temperature, the substrate temperature in the simulation is assumed to be 500 K, to account for the substrate heating during plasma exposure. The simulation pressure is assumed to be zero because of the vacuum slabs added to the substrate, in order to simulate the surface 3D periodic boundary conditions.

The cutoff for short and long range interaction is set to 8 Å. The substrate cell has dimensions (17x17x17) Å^3, otherwise it will be stated. The size of the system was chosen in a way that each dimension would be at least twice the cutoff.

Each ion is placed in the vacuum slab at a random position from 4 to 7 Å above the surface. The velocities of the O^{2-} ions are sampled from a Maxwellian distribution with the most probable energy of 0.025 eV (300 K) and random direction. The velocities of Mg^{2+}, Al^{3+}, Cr^{3+} and Y^{3+} ions have values calculated from a Maxwellian distribution with the most probable energy of 1 eV and the direction at a certain angle to the plane normal to the surface, which corresponds to the position of the two metallic targets in the experiment. The time-step is chosen to be variable and is calculated in the model in the order of 1–2 fs. The deposition of each ion is simulated for 2000 time-steps, i.e. 2–4 ps, at the *NVE* ensemble (i.e. the number of particles *N*, the system volume *V* and the total energy *E* are kept constant) because when an

atom is deposited the system is in the non-equilibrium state. The simulation results show that the high energy of the deposited Mg^{2+}, Al^{3+}, Cr^{3+} and Y^{3+} ions is dissipated in the first 1000 time-steps. In the experiment usually the temperature or both the temperature and the pressure are kept constant. Therefore, after a deposition at the *NVE* ensemble, a relaxation of the system for another 2000 time-steps at the *NVT* ensemble (i.e. the number of particles *N*, the system volume *V* and the temperature *T* are kept constant) is executed before the next deposition takes place.

The films have been grown up to 5-8 nm thickness. This is considerably lower than the experimental film thickness, but necessary to keep the calculation time reasonable. The following *M/(M+Mg)* metal ratios were investigated: 0% (i.e. a pure MgO film), 20, 40, 50, 60, 67 (i.e., the stoichiometry of the spinel structure), 80 and 100 % (i.e. a pure M_2O_3 film).

Usually, a better understanding of the thin film growth can be achieved via simulations. In this work, a classical MD method has been chosen. However, the application of the MD method is limited by the capability to obtain high quality transferable interatomic potentials. Therefore, the experimental results were used to guide the choice of the used potentials. Moreover, it must be pointed out that the deposition rates calculated with MD are several orders of magnitude higher than the obtained experimentally, due to the time-step used in MD, which has to be small enough to resolve the atomic vibrations, i.e. in the order of the femtoseconds.[14] Hence, MD simulation does not consider thermal diffusion (whose constant diffusion is in the order of 10^{-7} to 10^{-12} m^2s^{-1}),[19] which is not a problem because in reactive magnetron sputtering, it can be assumed that the thermal diffusion does not play an important role, when compared to the diffusion promoted by the energetic adatoms arriving onto the substrate.

All the MD simulations presented in this thesis were performed by V. Georgieva.[f] Because MD results contribute to a better understanding of the thin film growth, when being an asset, they are presented in this thesis.

[f] Research group PLASMANT, University of Antwerp.

5. Morphology and Angular Scans

5.1. Mg-Mg-O Films

The reference material for all the studied samples in this work is MgO. There has been an extensive research dedicated to the growth of MgO thin films produced by different techniques.[20-24] Within the research group DRAFT, attention has been directed to MgO thin films grown by DC reactive magnetron sputtering.[25-28]

Among other features that will be discussed further in this thesis (see section 7), Ghekiere has shown that pure MgO thin films grown using a single cathode exhibit a clear zone T structure.[29] The evolution of the out-of-plane alignment can be understood as an overgrowth mechanism of neighboring grains with a different perpendicular growth rate. The difference in crystallographic orientation results as an anisotropy in growth rate. Because all grains grow according to a specific crystal habit, it can be concluded, based purely on geometric consideration, that the grains whereby the facets of the crystal habit have the largest tilt angle, will have the largest perpendicular growth rate and will determine the preferential out-of-plane orientation.[29]

Thus, the crystal habit is decisive for the evolution of the out-of-plane alignment. This crystal habit is built up of facets with the lowest growth rate. If one way or another it could be possible to change the crystal habit, hence change the growth rate of the various crystallographic planes, than it could be possible to tailor the preferential out-of-plane orientation and the topography of the thin films.[29]

During dual magnetron sputtering in the configuration as shown in figure 3.1 (chapter 3), the atoms originating from both magnetrons, arrive on an inclined surface, and diffuse in the opposite direction on the substrate surface. To understand how this affects the out-of-plane orientation of these films, a Mg target was mounted on both magnetrons. With the same power delivered to each magnetron, the target-to-substrate distance of one of the targets was modified. As a result, angular scan from single and dual magnetron sputtering with one and two Mg targets is presented in figure 5.1.

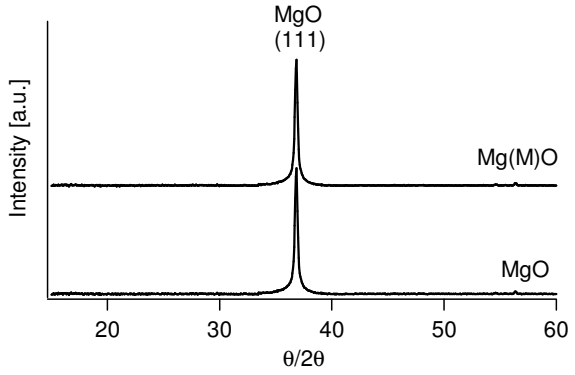

Figure 5.1: Angular XRD of MgO (single cathode) and Mg-Mg-O (dual cathode) thin films with different target-substrate distances. The θ/2θ pattern of the Mg-M-O thin films is not influenced by the target-to-substrate distances.

All deposited MgO thin films resulted in a well defined [111] out-of-plane orientation, independently of the used deposition conditions. As it can be seen in figure 5.1, the degree of out-of-plane alignment is not affected by the use of single or dual cathode. This observation corroborates with the idea that the MgO thin films are grown under zone T conditions, and therefore the mechanism of out-of-plane orientation results from the overgrowth of the fastest growing direction upon all the others, which is not influenced by the direction of the arriving adatoms at the substrate.

5.2. Mg-M-O films

5.2.1. Mg-M-O Films (with M = Al, Cr, Ti and Zr)

When one of the magnesium cathodes is replaced by a different metal M (Al, Cr, Ti or Zr), a series of Mg-M-O thin films with different stoichiometry is produced, by changing the targets-to-substrate distances. Comparing to the pure MgO, some changes are noticed in the Mg-M-O systems as it is observed in the θ/2θ XRD patterns exhibited in figures 5.2 and 5.4-5.7.

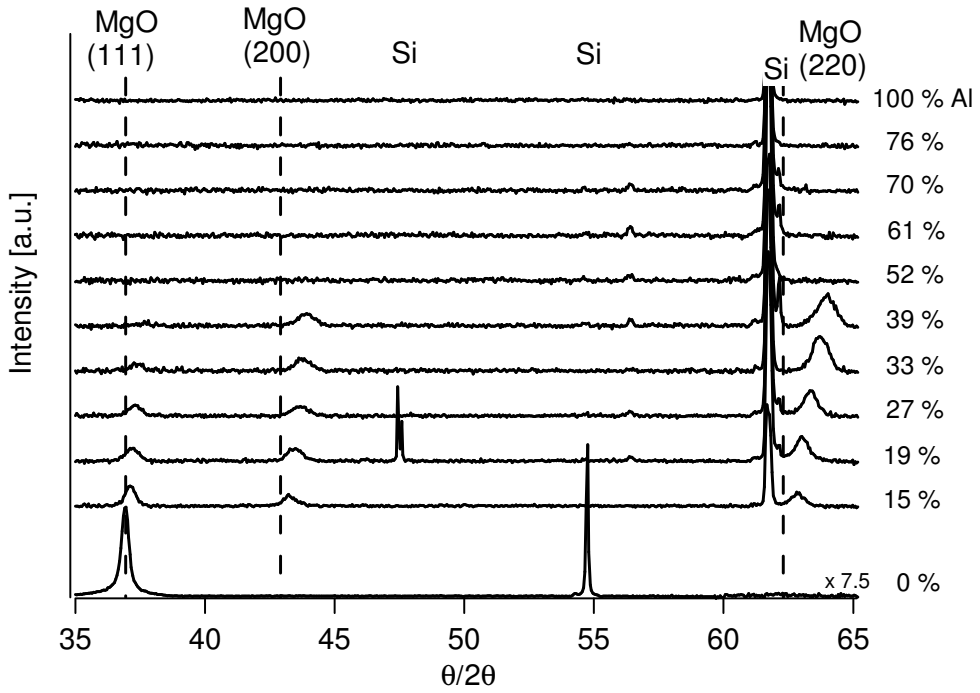

Figure 5.2: θ/2θ patterns of the Mg-Al-O thin film series deposited on Si. A clear transition from (111) out-of-plane orientated thin films (MgO) to amorphous (Al_2O_3) is noticed.

Changing the cathodes distances in the Mg-Mg-O system does not affect the θ/2θ pattern of the resulting thin films, meaning that the crystalline structure of the thin films remains the same. On the contrary, in the Mg-M-O thin films, the crystalline structure of the thin films is affected. By observing the XRD patterns from figures 5.2 and 5.4-5.7, one can clearly see that the preferential orientation is affected (for example, in the Mg-Al-O series, a decrease in the (111) peak intensity is registered and two other peaks, (100) and (220) appear and enlarge (see figure 5.2) with increasing aluminum content).

In figure 5.3 SAED of three Mg-Al-O with different C_{Al} is presented. The TEM study[g] shows the same tendency as the XRD measurements, namely the structure of the Mg-Al-O films varying from crystalline (low C_{Al}) to amorphous (higher C_{Al}). The electron diffraction pattern of the coating with $C_{Al} = 70$ % Al metal ratio confirms the amorphous result revealed by XRD.

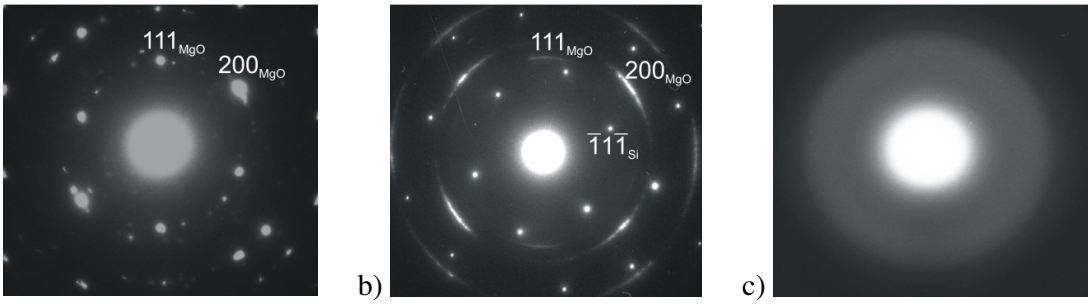

Figure 5.3: Selected area ED pattern of Mg-Al-O samples with a) $C_{Al} = 0\%$, b) $C_{Al} = 27$ and c) $C_{Al} = 70\%$.

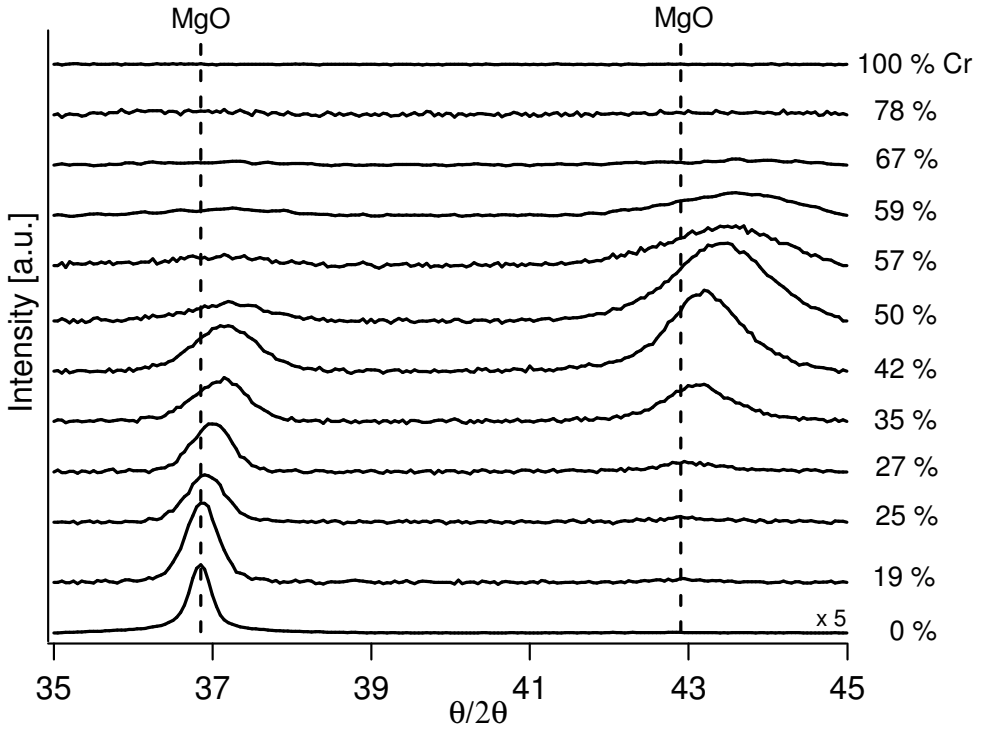

Figure 5.4: θ/2θ patterns of the Mg-Cr-O thin film series deposited on Si. A clear transition from (111) out-of-plane orientated thin films (MgO) to amorphous (Cr_2O_3) is noticed.

Furthermore, when adding another metal to MgO, two important trends are noticed. The first observed trend is a shift of the MgO Bragg peaks compared to the peak positions in the pure MgO θ/2θ patterns. This indicates that the lattice parameter of this phase changes by addition of another metal, M. The second trend is that the crystallinity of the MgO phase decreases by

[g] Work performed by the Research Group EMAT, University of Antwerp

the addition of another metal, which is represented by an intensity decrease of the MgO peaks in the XRD patterns. The decline in crystallinity might be caused by a decrease of the overall adatoms mobility, due to the addition of the second metal. Such an influence of additives (or impurities) has been extensively described by Barna[8] and Ghekiere[25] as well. Furthermore, the influence of aluminum on crystallinity has also been observed for the Ti-Al-N system.[30]

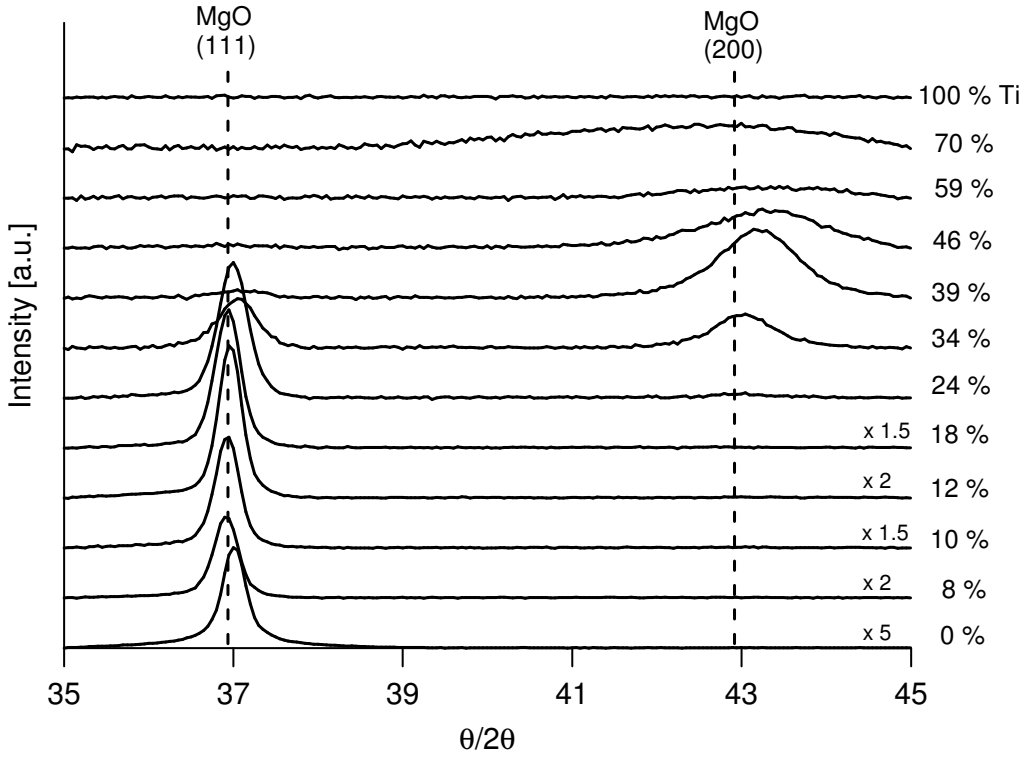

Figure 5.5: θ/2θ patterns of the Mg-Ti-O thin film series deposited on Si. A clear transition from (111) out-of-plane orientated thin films (MgO) to amorphous (TiO_2) is noticed.

At sufficiently high concentration of the other metals, the film becomes x-rays amorphous, except for the Mg-Zr-O (see figure 5.6) series, where the film becomes polycrystalline again at a Zr metal ratio higher than 63%. In the Mg-Y-O series, broad peaks were found for an Y metal ratio higher than 23%, probably due to nanocrystallites (see section 5.2.2 for a detailed description). The crystallinity of the pure metal oxide depends on the material, i.e. an amorphous film was obtained for Al_2O_3, Cr_2O_3, and TiO_2, while a crystalline thin film was deposited for ZrO_2 and Y_2O_3, as reported in literature.[25,31-40]

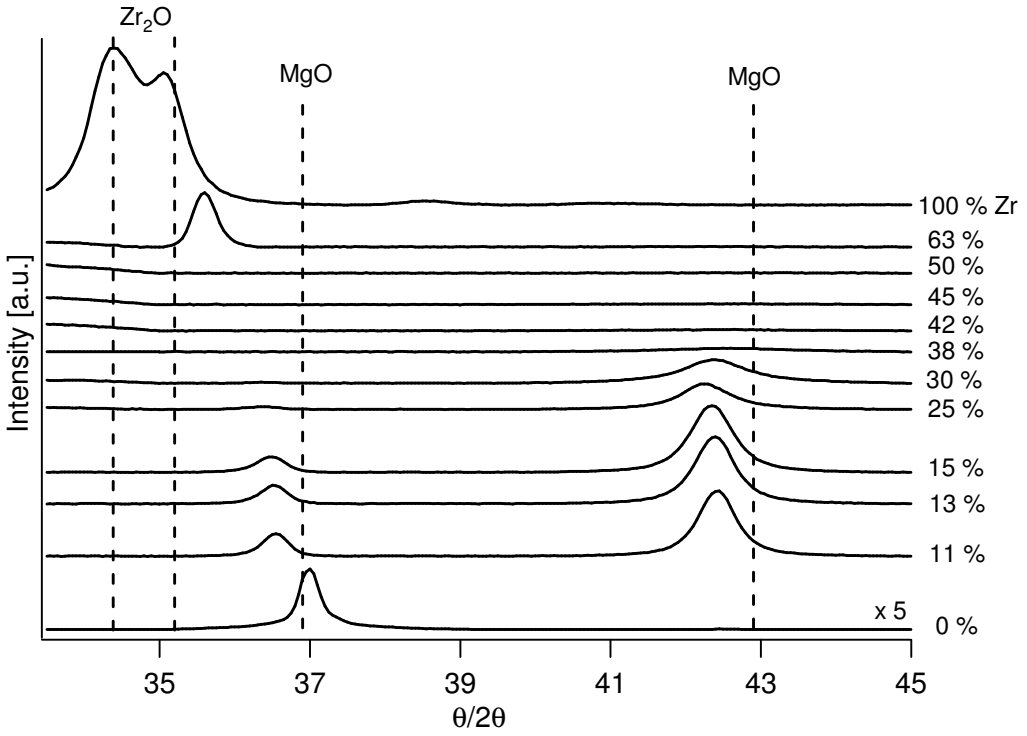

Figure 5.6: θ/2θ XRD patterns of the Mg-Zr-O thin film series deposited on Si.

5.2.2. The Mg-Y-O System

The angular XRD patterns of the Mg-Y-O films are depicted in figure 5.7. The shift of the Bragg peaks when yttrium is added to MgO is higher than the shift observed when other elements or added, due to the fact that the difference in ionic radius between Mg(II) and Y(III) is greater than between Mg(II) and the other metals M.[41,42] Therefore, even when the thin film has only 15 % Y metal ratio, the peak positions are already rather shifted. Because Y_2O_3 has Bragg diffraction for the planes (411) at $2\theta = 35.907°$ and (422) at $2\theta = 41.695°$ (see figure 5.8), there was the doubt about whether the peaks which were assumed to be (111) and (200) MgO, respectively, were correctly identified. After all, the peak positions deviates ~2° from the theoretic value. In order to solve this problem, further angular XRD measurements were performed.

If the second peak would be assigned as belonging to (422) Y_2O_3, another peak would be expected at 2θ ~20.495°, which corresponds to the planes (211). In fact, these peak would be present at a slightly lower 2θ value, due to the distortion provoked by the magnesium, as it happens for the peak at 2θ ~42°. Moreover, a theoretic higher intensity is expected for the (211) than for the (422). However, no peak is observed at low angles. Around 2θ ~90.7°, a reflection due to the (844) planes was also expected, but no intensity was registered for these angles. Therefore, it was concluded that the peak at 2θ ~43° is (200) MgO. Observing carefully figure 5.8, one can see that when the content of yttrium in the thin films increase, the deviation of the peaks to the theoretic Y_2O_3 position increases, which should not be the case, if the peak at 2θ ~35.5° and 43° would be due to the presence of the Y_2O_3 phase.

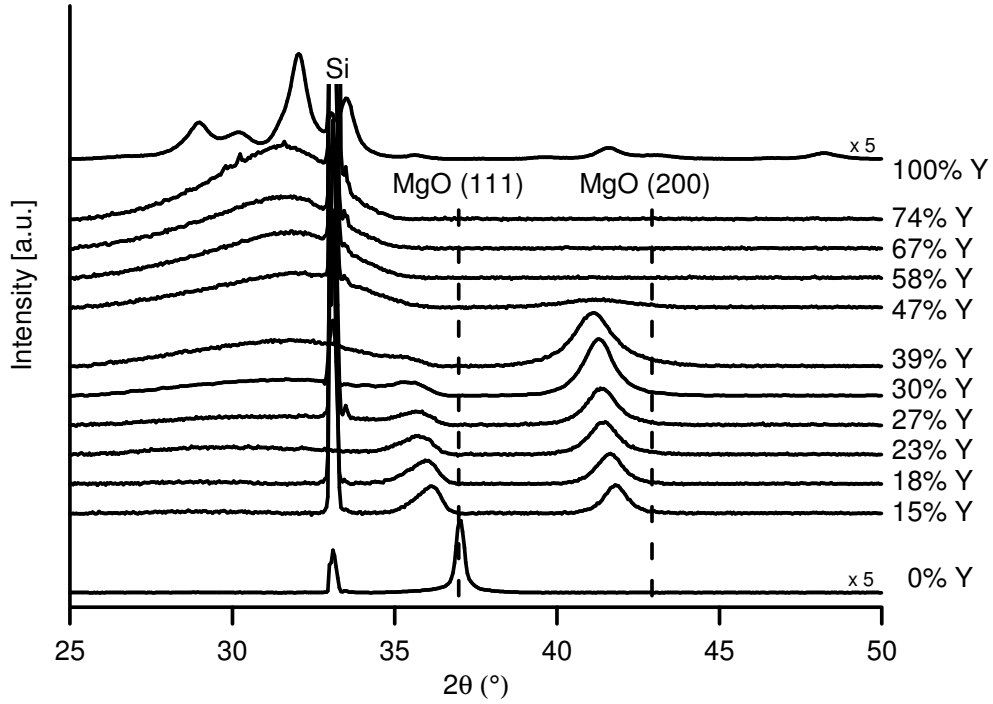

Figure 5.7: θ/2θ XRD patterns of the Mg-Y-O thin film series deposited on Si.

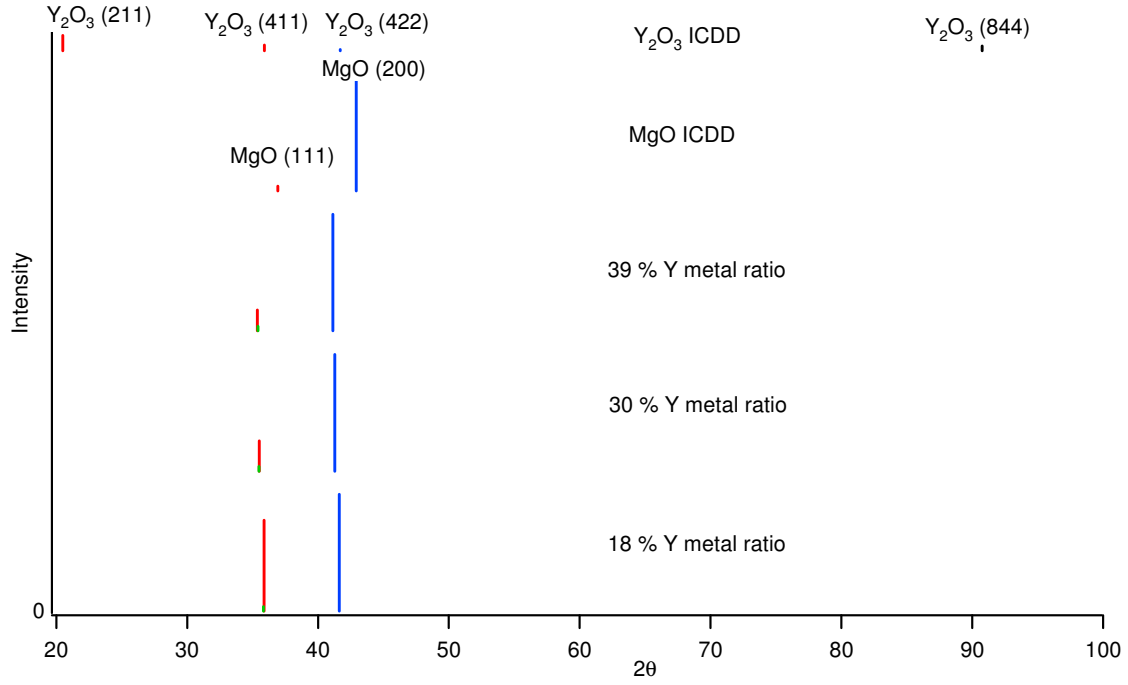

Figure 5.8: Schematic representation of the peak positions obtained in θ/2θ XRD measurement of three samples, with its relative intensities. The theoretic peak positions and intensities for pure Y_2O_3 (body-centered cubic with space group Ia-3 (206)) and MgO are also shown.

Besides the two MgO peaks ((111) and (200)), a very broad peak was found for an yttrium metal ratio higher than ~23 %, probably due to the presence of nanocrystallites. This broad

peak is in a region where Y_2O_3 peaks are expected and its intensity increases as the yttrium content in the thin films increases. An yttrium metal content higher then ~47 % shows no more evidence of the MgO crystalline phase in the thin films.

5.2.3. Change in the MgO Lattice Parameter

The positions of the MgO peaks in the θ/2θ XRD patterns (figures 5.2 and 5.4-5.7) enables one to calculate, using Bragg's law, the lattice parameter. Knowing this lattice parameter, also the shortest distance between two oxygen anions can be calculated based on the rock salt (NaCl) structure of MgO. Figure 5.9a) shows the shortest distance between two oxygen anions as a function of the metal content. Depending on the added metal, the shortest distance between two oxygen anions either decreases (in the case of Al, Cr and Ti) or increases (as in the case of Y and Zr), as the metal content in the thin films increase. For the different studied systems, an almost linear behavior of the lattice parameter as a function of the metal ratio was found. This trend is known as the empirical Vegard's law, which states that the lattice parameter depends on the composition and it is related with the cation radius. Indeed, Mg(II) has a radius of ~0.72 Å, and in a first approximation, replacing Mg by a cation with a smaller radius (such as Al(III), Cr(III), Ti(IV))[41,42] results in a decrease of the lattice parameter, or the O-O distance. The opposite is noticed when a larger cation (such as Y(III) or Zr(IV))[41,42] replaces the Mg cation.

There is a linear relation between the lattice parameter and the composition of the thin films for relatively low M/(Mg+M) ratios. Therefore, at low M/(Mg+M) ratios, a linear function can be fitted to the corresponding experimental data points of each system. The slope of this line should be proportional to the relative change of the cation radius. Figure 5.9b) proves this hypothesis to be right. From this behavior, one can conclude that the Mg-M-O thin films behave as a solid solution, as already discussed by others.[43,44]

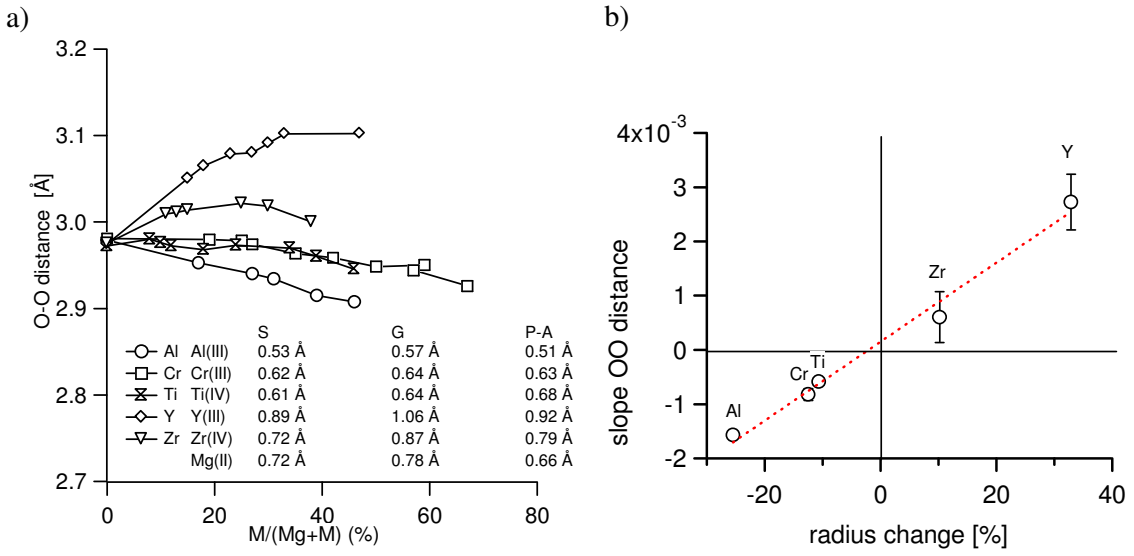

Figure 5.9: a) Oxygen-oxygen distances for the Mg-M-O system calculated from the θ/2θ XRD measurements. The ionic radii were taken from Shannon (S),[42] Goldschmidt (G),[41] and the Pauling radii, which were revised and supplemented by Ahrens (P-A).[41] b) Relation between the lattice parameter of the Mg-M-O thin films and the respective cation radii change.

6. From Crystalline to Amorphous

As seen in the θ-2θ XRD patterns in chapter 5, addition of another metal to MgO leads to a decrease of the MgO crystallinity and eventually to the formation of amorphous films. However, the θ/2θ XRD patterns provide only information about crystallographic planes parallel to the substrate, which may lead to misinterpretations with respect to the effect of the composition on the structure formation of the Mg-M-O films. In order to investigate the crystallographic properties of planes that are not parallel to the substrate, pole figures of the Mg-M-O thin films were performed. Figures 6.1 present the (200) pole figures of the Mg-Al-O thin films deposited at different target-to-substrate distances.

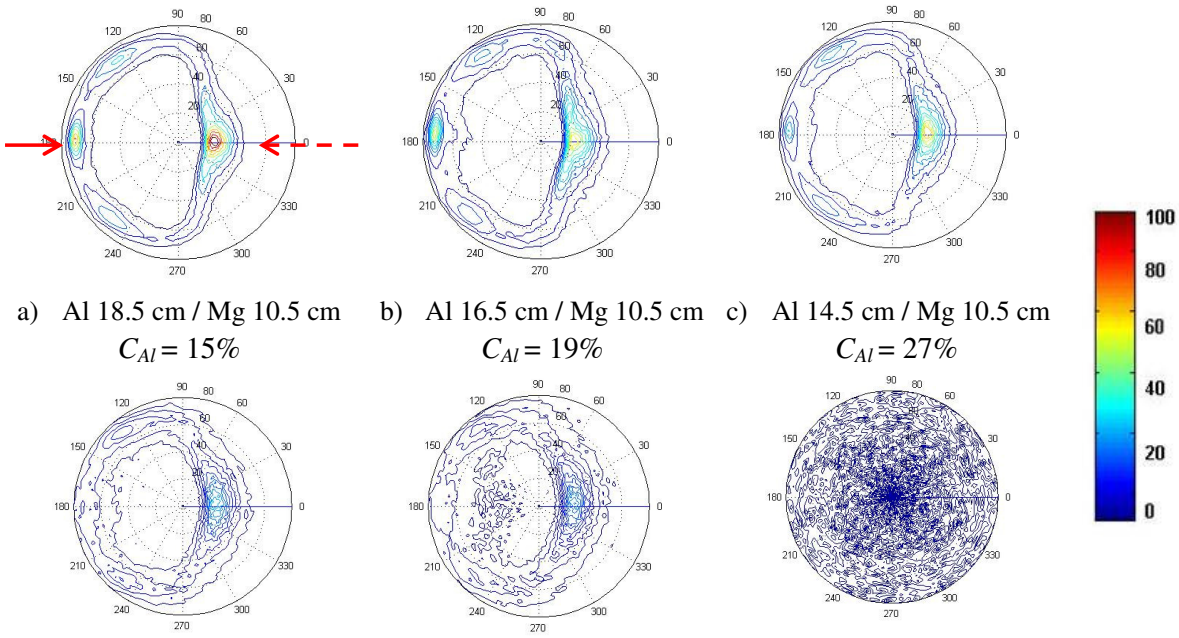

a) Al 18.5 cm / Mg 10.5 cm $C_{Al} = 15\%$ b) Al 16.5 cm / Mg 10.5 cm $C_{Al} = 19\%$ c) Al 14.5 cm / Mg 10.5 cm $C_{Al} = 27\%$

d) Al 12.5 cm / Mg 10.5 cm $C_{Al} = 33\%$ e) Al 10.5 cm / Mg 10.5 cm $C_{Al} = 39\%$ f) Al 10.5 cm / Mg 12.5 cm $C_{Al} = 52\%$

Figure 6.1: (200) pole figures of Mg-Al-O thin films deposited with different target-to-substrate distances. The dashed arrow indicates the direction of the magnesium target, while the full arrow indicates the aluminum one.

A decrease of the fraction of the crystalline (200) MgO phase, followed by full amorphization of the thin films as the content of aluminum in the coating increases, can be observed from the decrease in the total intensity in figure 6.1. The color scale presented here is valid for all groups of pole figures, as within each series of Mg-M-O films the intensity was first corrected for thickness and then normalized. The first pole figure (figure 6.1a)) corresponds to a thin film produced with the magnesium target 10.5 cm apart from the substrate, while the aluminum one stood at 18.5 cm. The next thin films were produced decreasing the aluminum target-to-substrate distance in steps of 2 cm, and keeping the magnesium target-to-substrate distance constant (10.5 cm). The thin film presented in figure 6.1f) was produced using magnesium target-to-substrate distance of 12.5 cm while the aluminum target was 10.5 cm apart from the substrate (corresponding to an amorphous thin film).

Similar measurements were carried out for the other Mg-M-O thin films, the results being comparable. As the crystallinity in all Mg-M-O thin films decreases when the content of M increases, a quantitative way to describe the crystallinity can be an asset. A quantification of the crystallinity of the thin films can be obtained by applying the procedure described in section 4.1.2, where the fraction of MgO phase in the thin film is determined.

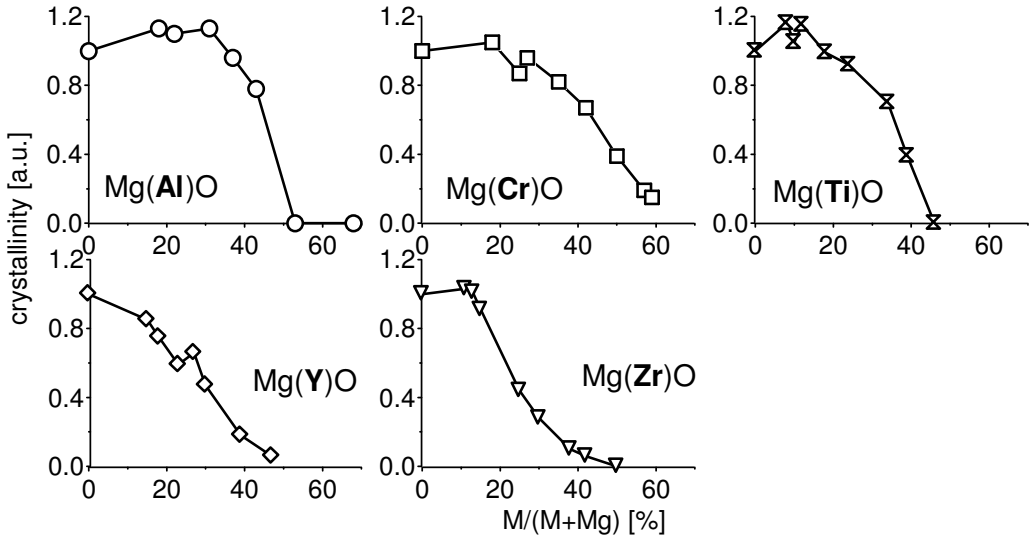

Figure 6.2: Crystalline fraction of MgO phase as a function of the composition for the different Mg-M-O systems.

Figure 6.2 shows the crystalline fraction of MgO phase as a function of the composition for the different Mg-M-O systems. The trend observed in the pole figures is also to be seen, for all the systems, i.e., a decrease in the crystallinity is seen as the content of the other metal (Al, Cr, Ti, Zr, Y) increases. Moreover, the transition region from crystalline-to-amorphous appears to be at similar values for the different studied systems.

In figure 6.3, as an example, TEM[h] cross-sectional images of Mg-Cr-O thin films with different chromium metal content are depicted. It can be seen that there is an increase of the thin film density when the magnetron source is brought closer to the substrate. This finding might explain the existence of a value higher than 1 for the crystallinity of some samples. The thin films density could not be experimentally measured (quantitatively) due to technical problems. X-ray reflectometry (XRR) could not be used because to retrieve the thin film density with this technique, a very thin film (maximum 100-150 nm) has to be used. As the Mg-M-O crystalline thin films have a preferential orientation and the first 200-250 nm are the thickness needed to develop this preferential orientation, a thin film with 150 nm would not be representative of the real thin film.

Another prospect for the increase of crystallinity can be related with the addition of the other metal (impurities). As Barna pointed out in his revised SZM,[8] in the case that impurities segregate as foreign phases at the grain boundaries of crystal surfaces, depending on the

[h] Work performed by EMAT, University of Antwerp.

orientation, they segregate differently and therefore the orientation can be changed. However, in the Mg-M-O thin films studied by HRTEM, the impurities did not segregate to the grain boundaries as they were found to be in solid solution with MgO, confirming the interpretation done with the XRD patterns. In this case, Barna does not acknowledge a change in the growth of the thin film.[8,9] Perhaps adding another metal to MgO, until a certain extent, favors the crystallinity of the (200) phase, or stated differently, hinders the degree of preferential orientation.

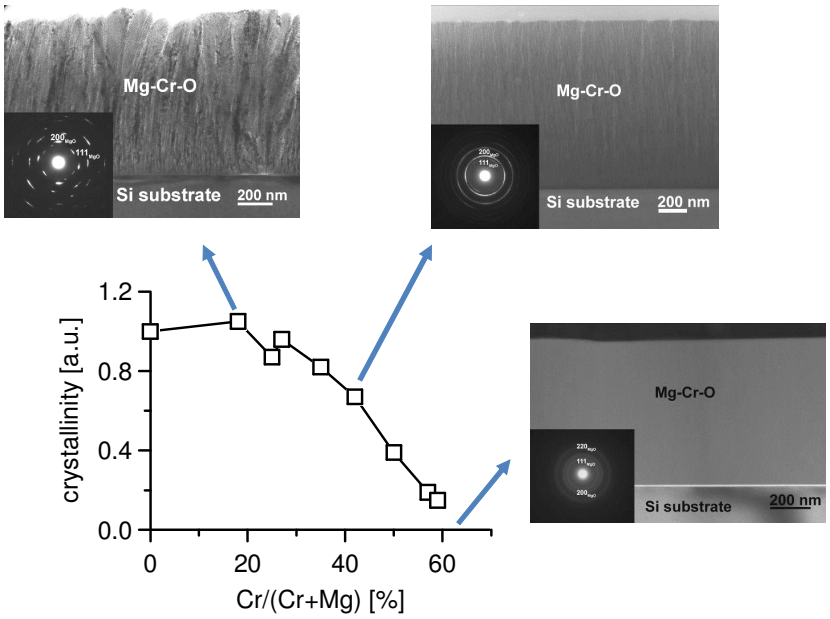

Figure 6.3: Crystalline fraction of MgO as a function of the composition for the Mg-Cr-O thin films. The insets of the figure represent the TEM cross-sectional images of three thin films with different chromium content.

The decrease of the fraction of crystalline material in the thin films, when C_M in the coating increases, is also observed in MD simulations[i]. As an example, figure 6.4 depicts the snapshots for Mg-Al-O thin films with different chemical composition. Hence, for low M concentrations (left side of the figure) the thin film structure is crystalline and resembles the MgO structure, while for high M concentrations (right side of the figure) the structure is amorphous. Mg-Cr-O and Mg-Y-O thin films were also simulated with MD, which results are also in good agreement with the experiments. However, it was not possible to perform the simulation for the Mg-Ti-O and Mg-Zr-O systems, due to the fact that no suitable interatomic potentials were found, i.e. the simulations could not resemble the experimental results. The reason for the absence of a suitable interatomic potential is probably related to the different oxidation states that Ti and Zr can have, which are not comported in one single interatomic potential. More details on the performed MD simulations work linked to this thesis can be found in the literature.[16,45]

[i] Work performed by V.Georgieva, PLASMANT, University of Antwerp

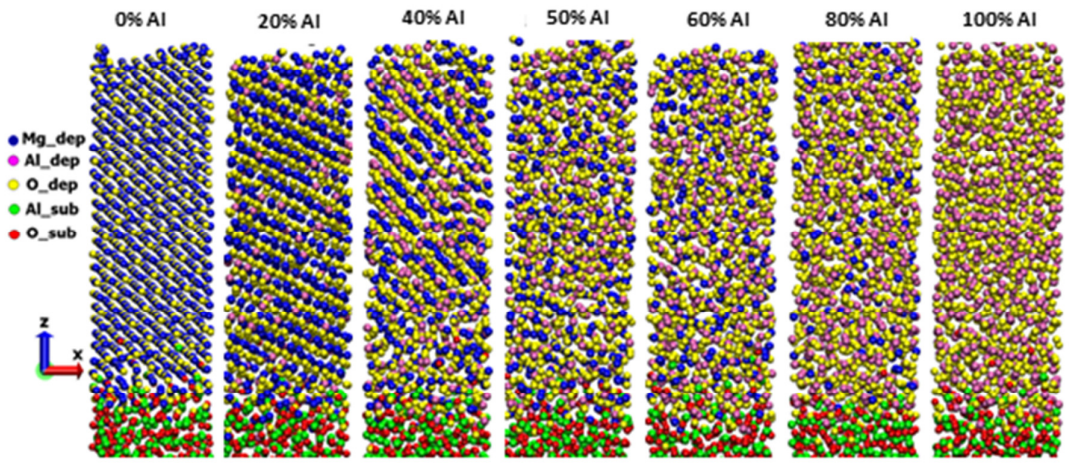

Figure 6.4: Snapshots of Mg-Al-O thin films "deposited" on an amorphous Al_2O_3 substrate at different aluminum metal contents.

Hereupon, a question that can be raised is why does this transition from crystalline-to-amorphous occur in all the systems? Furthermore, why is the transition point at similar values for all studied systems?

6.1. A Simple Geometric Model

The transition from crystalline-to-amorphous phase can be interpreted as follows. In case the thin films had been deposited under thermodynamical conditions, one would have observed a transition from NaCl structure (pure MgO) over spinel ($MgAl_2O_4$) to corundum (Al_2O_3) for the Mg-Al-O series. Similar transitions would have been observed for the other series. Hence, the transition to an amorphous structure with increasing metal ratio indicates that the structure of the thin films is not thermodynamically, but kinetically determined.

A good starting point to understand the C_M where the crystalline MgO phase disappears is a description of the MgO structure. As stated before, the MgO structure is similar to the well-known NaCl structure (see figure 6.5a)). Hence, the O anions are in a cubic closest packing, and the magnesum cations fill all octahedral sites, as schematic depicted in figure 6.5a). Therefore, the coordination number (CN) for magnesium is 6. In a polyhedron representation, the magnesium cations are within an octahedron, and the octahedrons are linked by the edges, i.e. the MgO_6 octahedra share all twelve edges with adjacent octahedra. Summarizing, the MgO structure can be seen as a stable stacking of MgO octahedra. Figure 6.5b) shows a sketch of the MgO structure as a stacking of MgO octahedra.

Addition of another metal M with a higher valence electron number than the Mg^{2+} ion will substitute the Mg^{2+} in the octahedral positions. This substitution at low concentration will be compensated by vacancies on the Mg sublattice,[44,46] as it is schematically represented in figure 6.5c). Based on chemical rules, i.e. the Pauling rules, one could reason as follows. The addition of the metal M will destabilize the MgO structure. First, the third Pauling rule states that the presence of shared edges in a coordinated structure decreases its stability. This effect is especially large for cations with a high valence. Secondly, as indicated by the Vegard's law

behavior, the size of the octahedra is changed, hence decreasing the stability of the octahedral stacking in the MgO structure even more.

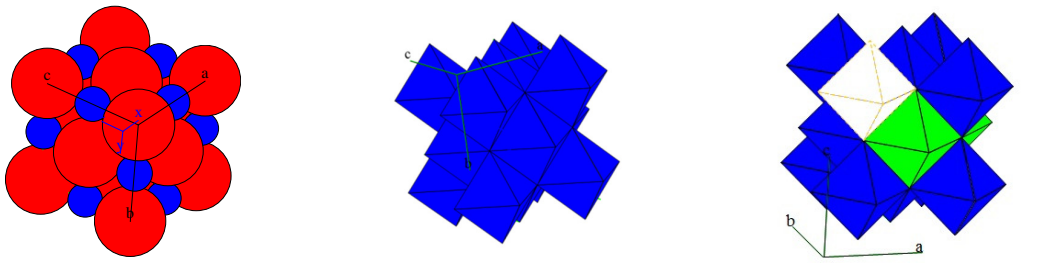

a) NaCl Structure b) MgO Octahedra representation c) Mg-M-O Octahedra representation

Figure 6.5: Schematic representation of a) NaCl structure, b) MgO structure as a packing of octahedra, c) Mg-M-O structure as a packing of octahedra.

The question can now be raised as how many magnesium positions can be removed by introducing magnesium vacancies and substituting the magnesium positions by a different cation. Replacing the magnesium with a cation with the same valence but with a different size can assist in answering this latter question. For the system Mg-Zn-O,[73] and Mg-Al-O,[67] authors report a Vegard's law behavior for the lattice parameter as also noticed for the systems discussed in this work (see figure 6.2). A transition from the MgO structure to ZnO wurzite structure is reported at 50 % *Zn/(Zn+Mg)*.[47,48] Hence, it seems that when half of the octahedral positions are replaced, the MgO structure becomes unstable. Building further on this idea, the number of octahedral positions in the $Mg_xM_{1-x}O_{[2x+z(1-x)]/2}$ with a rock salt structure is equal to the number of available oxygen, i.e. [2x+z(1-x)]/2, with z the charge of the substituting M ion. When (1-x) M atoms are present, z(1-x)/2 Mg must be replaced. When this number equals half of the octahedral positions, the structure becomes unstable, i.e.

$$\frac{z(1-x)}{2} = \frac{2x + z(1-x)}{4}$$
$$\frac{2}{2+z} = 1-x \qquad (6.1)$$

For z = 2 as in Mg-Zn-O this would result in a transition point for M/(Mg+M) at 50% as published by several authors.[73] For z = 3 (Cr, Al and Y) this would set the transition point for a structural change at 2/5 or 40% M/(M+Mg), while for z = 4 (Ti and Zr) the transition should occur at 33% M/(M+Mg). This corresponds more or less with the experimental results (see figure 6.2) but two major remarks must be given. First, it is generally accepted that the Pauling rules can only be used as guidance because it assumes a pure ionic bond between the atoms. Secondly, this simple reasoning does not account for any modification in the coordination of the Mg which could stabilize the structure. Indeed, the MD simulations (see figure 6.6) clearly show that the coordination of the Mg deviates from 6 as in MgO with M-metal addition. Hence, the MD simulation shows that before the transition occurs, the Mg position changes towards a tetrahedral site (CN = 4). This coordination is the same as in the spinel structure, and shows that this transition from an octahedral to a tetrahedral site

stabilizes the structure, and is energetically preferred. In this way, more M can be added to the Mg-M-O structure than predicted by equation (Equation 6.1).

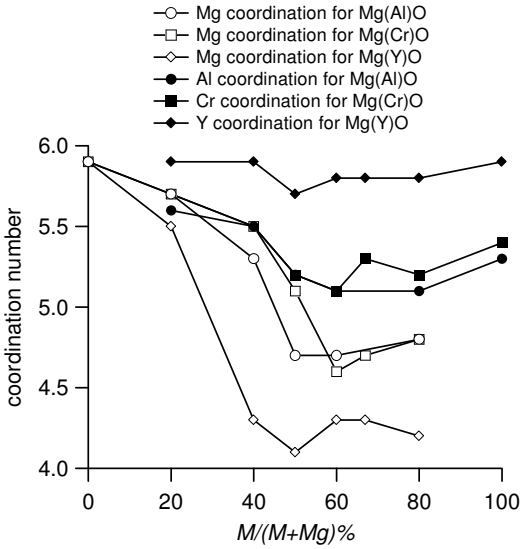

Figure 6.6: Calculated coordination number of magnesium and M (M = Al, Cr, Y) in the different systems studied by the MD simulations.

6.2. Packing Density and Crystalline-to-Amorphous Transition

The origin for the crystalline-to-amorphous transition, when the M content in the thin films increases, cannot be explained from the same kinetic arguments that explain the preferential orientation. This idea is supported by MD simulations, where bulk diffusion is omitted due to its long time scale. In the previous section, a structural basis for the transition was used. When the Mg^{2+} is substituted by a higher valence cation M^{n+}(with n>2), some octahedral positions will be empty, in order to compensate the charge effect. This creates a number of vacancies in the Mg-M-O structure. Furthermore, the new M^{n+} cation has a different radius than Mg^{2+}, which also influences the structure. The combination of the difference in valence electron number and radii leads to the destabilization of the MgO structure.

It is known that the structure formation in thin films is determined by both surface diffusion and structure stability. Studies on Mg-M-O films have shown that all crystalline films exhibit features of zone T microstructure (this will be discussed in chapter 7), i.e. V-shaped columns close to the film-substrate interface and faceted columns close to the film surface. In addition, all crystalline films are biaxial aligned (see complete discussion in chapter 7). These findings indicate that the microstructure and texture of the films is kinetically constrained. Along the same lines, one would expect that the transition from crystalline-to-amorphous would be induced by changing energy barriers due to the substitution of Mg by another cation. Nonetheless, there are a few points which are not consistent with this argument. The crystallite size, calculated for all Mg-M-O systems using the Scherrer's formula,[49] was found to be inversely proportional to C_M, as can be seen figure 6.7. The slope is independent of M (except for Y). It would be surprising if the thin film growth kinetics hardly depends on the nature of the substituting cation, taking into account that several cations were studied.

Furthermore, it is known that the presence of impurities which solubilize in the lattice do not influence the growth mechanism.[8,9] Another argument is that the transition from crystalline-to-amorphous occurs quite abruptly, i.e., the crystallinity drops dramatically within a narrow range of C_M. These facts point to a structural reason for the transition. As in the Mg-M-O films the bond strength of the M-O bonds is, for all metals M, in the same order of magnitude (-530 +/-100kJ/mole), it is not expected that incorporating M in the metal sublattice accounts for the observed transition. On the other hand, the substitution of Mg by M introduces metal vacancies, which introduces disorder, hampering the crystal formation and yielding to amorphous thin films. The correlation between disorder and structural stability has been described by the hard sphere model.

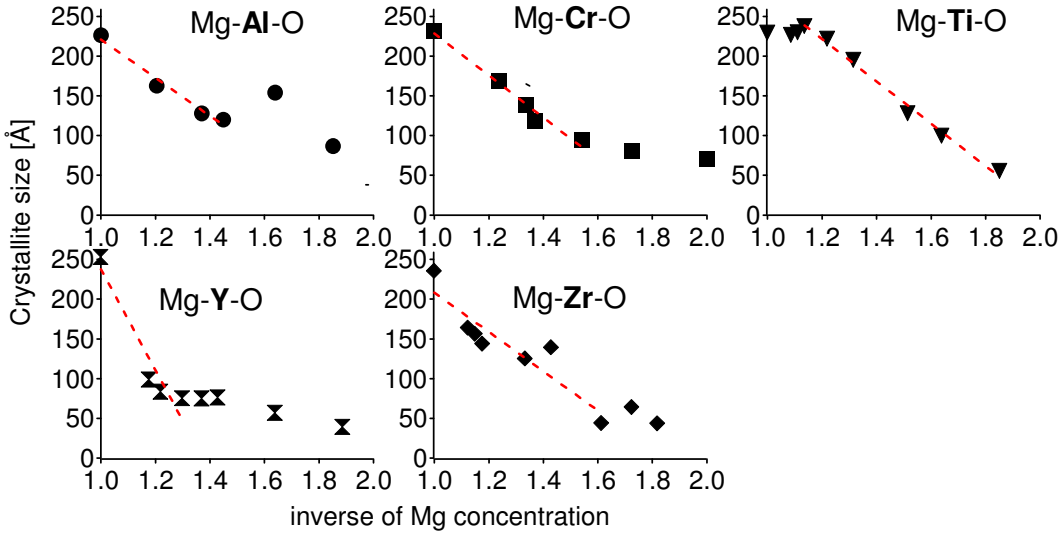

Figure 6.7: Crystallite size of the Mg-M-O films as a function of the inverse of Mg concentration, calculated from the Scherrer's formula. The dashed lines are a fit through the data points.

6.2.1. Hard Sphere Model

The efficient packing of hard particles represents a ubiquitous ordering principle in materials. Irrespective of how atoms or molecules interact with one another, the fact that no two particles can occupy the same volume of space is universal and, when coupled to the condition of maximization of the number of neighbor contacts, this exclusion is sufficient to account for the basic features of the crystal structure.

In 1611, Kepler proposed that close packing (either cubic or hexagonal close packing, both of which have maximum densities of $\pi/\left(3\sqrt{2}\right)\approx 74.048\,\%$) is the densest possible sphere packing, and this assertion is known as the Kepler conjecture. Finding the densest (not necessarily periodic) packing of spheres is known as the Kepler problem.[50] Over the last centuries, several researchers had tried to solve the problem. However, the long quest for a solution of the Kepler conjecture, only ended in 2005 with the paper by Hales [51]. Moreover, not only the packing of hard spheres has drawn the attention, but more recently researchers have investigated the dense packing of other solid shapes: Torquato's group have been

studying ellipsoids,[52] superballs,[53] Platonic and Archimedean solids.[54,55] In the same context several papers discuss the phase diagram of hard spheres.[56,57]

In spite of the simplicity of the hard-sphere model, there is strong numerical evidence for the existence of a first disorder-order phase transition.[58] There are three important branches shown in the phase diagram depicted in figure 6.8, where the pressure is plotted versus the packing density ρ. Starting at $\rho = 0$ is a fluid ramification, that continues up to the freezing point whose packing density $\rho \approx 0.494$. At this point, the phase diagram splits in two parts. One part is a metastable extension of the fluid ramification which follows continuously from the previous branch and is estimated to end at a point known as random close packing, RCP. Extensive numerical work indicates that the packing density of the random close packed state is approximately 0.64.[59] The other ramification that splits off the freezing point represents the thermodynamically stable part of the phase diagram. Along the horizontal portion of this ramification, both fluid and solid can coexist until the melting point is reached, $\rho \approx 0.545$. The slice of the curve that continues above the melting point is referred to as the solid or ordered branch, ending at the closed packed face centered cubic (fcc) or hexagonal closed packed (hcp) crystal at a packing density of 0.74, which is the maximum packing density for a packing of spheres in three dimensions.

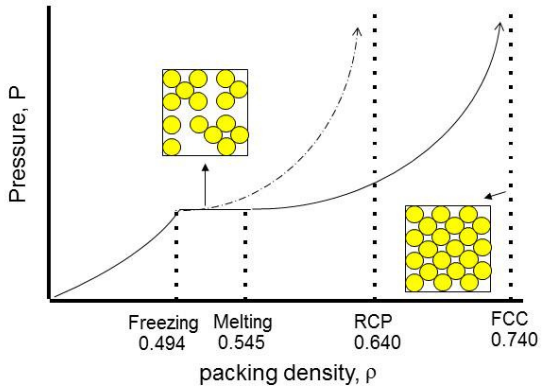

Figure 6.8: Schematic representation of the phase diagram of a system of hard spheres. The boxes represent two specific situations: the densest packing structure (on the right hand side) and the structure in the boundary region (on the left hand side).

Summarizing, when the packing density is slowly decreased from the densest packing as defined by the Kepler conjecture, i.e. $\rho = \pi/\sqrt{18}$, to lower values, a first order transition from a crystalline state to a liquid state is noticed at a packing density of 0.545. In the reverse way, i.e. from low to high packing densities, the transition is noticed at a packing density 0.494, indicating that between 0.494 and 0.545 there is a boundary region where both phases exist simultaneously.

6.2.2. Calculating Packing Density

The MgO structure can be described as a dense packed configuration of O^{2-} anions where the Mg^{+2} cations occupy octahedral positions, see figure 6.9a). If a fictitious sphere with the same radius as O^{2-} is defined around each octahedral position (shown in figure 6.9a)), those spheres

will also form a dense packed configuration. Substitution of Mg by a metal M with a larger valence number leads to the generation of vacant octahedral positions, in order to maintain charge neutrality over the crystal (see figure 6.9b)). When Mg is replaced by a cation M with the same valency but different ionic radius, the radius of the fictitious spheres will also increase, as shown in figure 6.9c). In the current study all the substitutional cations have a different radius and different valence number than Mg, inducing both changes in the radius of the fictitious spheres and creation of vacancies, as illustrated in figure 6.9d).

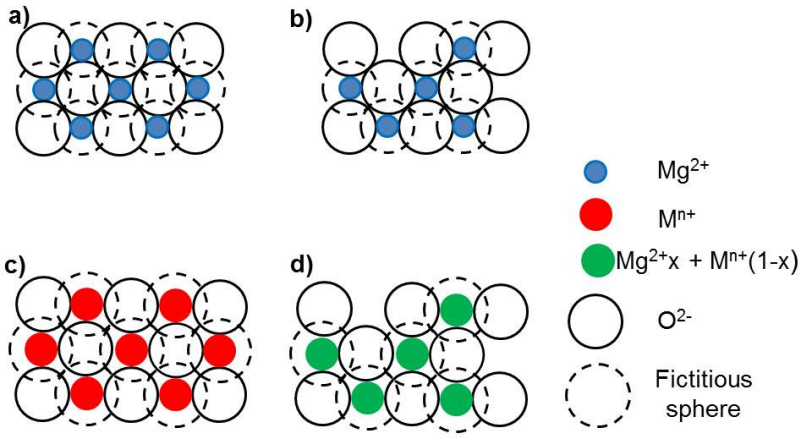

Figure 6.9: a) Schematic representation of the MgO structure ((200) plan) either as a dense packing of oxygen anions, or as a dense packing of fictitious spheres related to the Mg cation, whose radius is the same as the oxygen anion. Schematic representation of the effects that affect the MgO structure: b) This transition represents the creation of a metal vacancy in the MgO structure. c) The hypothetic substitution of all Mg^{2+} by another cation with a larger radius, which results in a larger fictitious sphere than in the first schematic; d) When replacing Mg^{2+} by M^{n+}(combination of b) and c)), the size of the unit cell is affected (because of the replacement of Mg^{2+} with a cation of larger radius) and there is formation of vacancies. The change in the lattice parameter depends on the amount of Mg^{2+} and M^{n+} and on the radius of M^{n+}.

The composition of the metal sublattice in the studied Mg-M-O systems can be described by the form,

$$\left[Mg_x\ M_{1-x}\right]\Phi_{\frac{n-2}{2}(1-x)}\ O_{\frac{2x+n(1-x)}{2}}, \qquad (6.2)$$

where x is the Mg content, n is the valency of M and Φ represents the vacancies in the lattice. As mentioned in the beginning of the current section the grown films are solid solutions of MgO with M replacing the cation, therefore Equation (6.2) can be rewritten as,

$$Mg_{\frac{2x}{2x+n(1-x)}}\ M_{\frac{2(1-x)}{2x+n(1-x)}}\ \Phi_{\frac{(n-2)(1-x)}{2x+n(1-x)}} O_1, \qquad (6.3)$$

which is a straightforward demonstration of the interplay between metal content and vacancies, when the metal composition is changed. As an example when x is 1 (pure MgO) there are no vacancies in the system, while when x is 0 (for a M^{3+}, Al_2O_3) 1/3 of the metal sites is vacant.

To compare the vacancy formation in the Mg-M-O thin films with the hard sphere model, it is needed to calculate the packing density of the fictitious spheres. Therefore, a good description of the Mg-M-O material density is needed.

The material density cannot be retrieved from the thin film density as the latter is not only defined by the intrinsic material density but also by the thin film morphology. Nonetheless, it was not possible to quantify the density of the Mg-M-O thin films. However, the packing density of the fictitious spheres can be retrieved from XRD measurements, as follows.

The Mg-M-O packing density is equal to the volume occupied by the fictitious spheres divided by the cell volume. The volume of the unit cell can be calculated by the lattice parameter as determined by the XRD patterns. The number of atoms within the unit cell can be determined by the chemical composition. This is illustrated by Equation (6.3) which shows that per formula unit the fraction of filled octahedral positions, i.e. the number of fictitious spheres is equal to $2/[2x+n(1-x)]$. Although the substitution of Mg by M induces variations in the packing density of the fictitious spheres due to changes in the cation radii and due to the creation of vacancies, the hard sphere model only takes into account the changes in packing density resulting from vacancy formation. Therefore, the effect of change in radius in the packing density had to be eliminated. In the case that Mg is substituted by an atom different in size than Mg, the radius for the fictitious sphere will change by r_M-r_{Mg}, being r_M and r_{Mg} the radius of the metal M and Mg, respectively, as compared to the radius of the sphere in the MgO crystal. Therefore, the weighted average radius of the fictitious sphere (which is used for the calculation of the occupied volume) for a Mg content x will be given by the expression

$$r_{fs} = \frac{r_O + (r_{Mg}x + r_M(1-x))}{r_O + r_{Mg}} \times r_O , \qquad (6.4)$$

where r_{fs} and r_O are radius of the fictitious sphere and O^{2-} anion, respectively.[41]

To elaborate on the effect of the corrected radius, as calculated in Equation (6.4), one can consider the MgO structure. The O^{2-} anions and Mg^{2+} cations touch one another. By introducing a larger (or smaller) cation (see figure 6.9b), this condition is changed. When $r_M > r_{Mg}$ ($r_M < r_{Mg}$) the fictitious sphere has a radius equal or larger (smaller) than the radius of the oxygen anion depending on the composition. Hence, the size of the fictitious sphere is proportionally increased (decreased), allowing the spheres to touch each other again. In this way, the calculated packing density is not changed by changing the size of the cation, and changes only by the introduction of vacancies, similar to the hard sphere model.

The packing density ρ is given by

$$\rho = \frac{Z \times \frac{4}{3}\pi r_{fs}^3}{a^3}, \qquad (6.4)$$

Where Z and a denote the number of fictitious spheres and lattice parameter, respectively.

In figure 6.10 is presented the packing density of the different Mg-M-O systems as a function of the thin film composition. As expected, it can clearly be seen that the packing density of the thin films decreases with the increase of the M content.

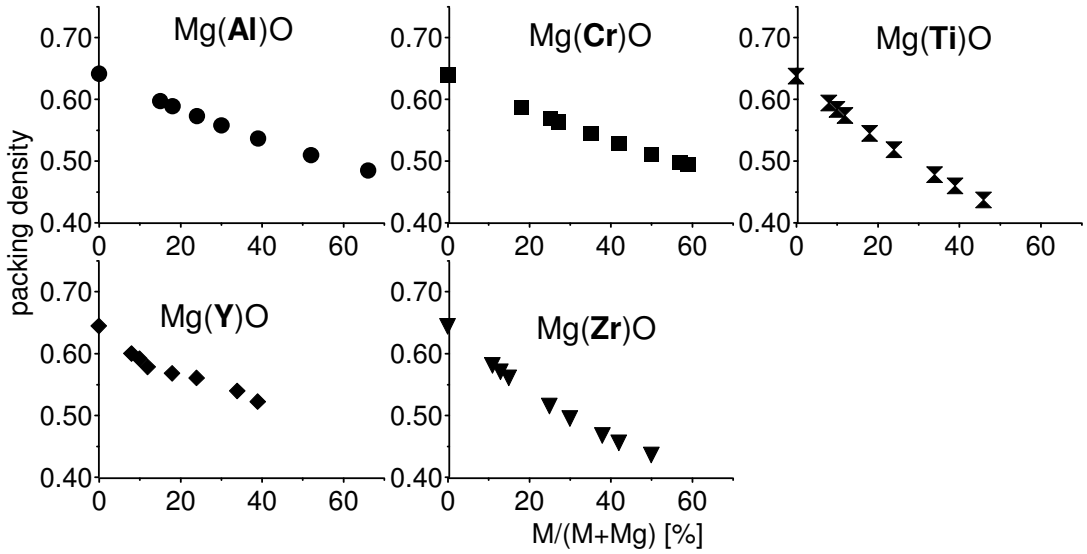

Figure 6.10: Mg-M-O packing density as a function of chemical composition.

6.2.3. Crystallinity vs. Packing Density

To understand the influence of the packing density on the crystalline-to-amorphous transition observed for the Mg-M-O thin films, the crystallinity was plotted as a function of the packing density and is presented in figure 6.11.

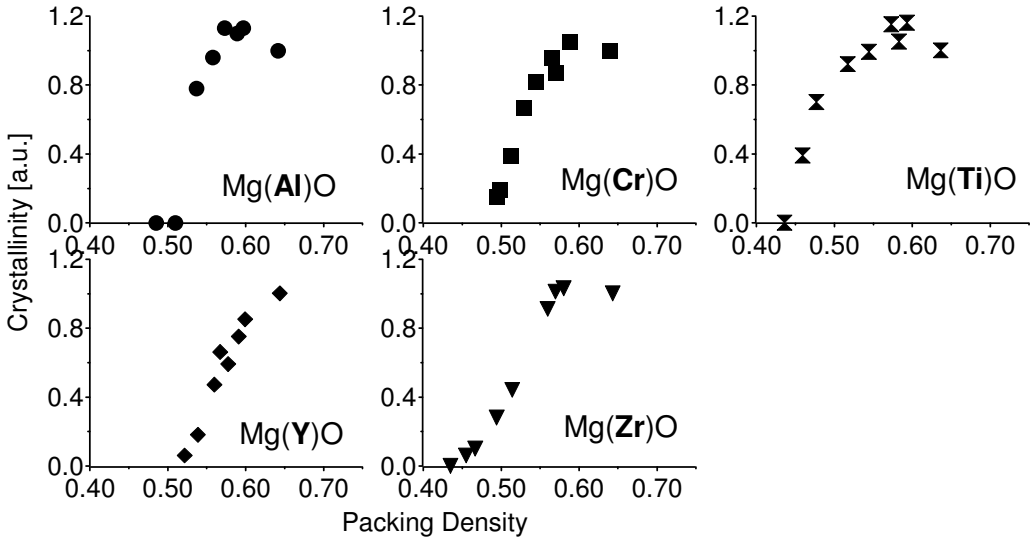

Figure 6.11: Crystallinity of the deposited Mg-M-O thin films as a function of the calculated packing density of the fictitious spheres.

It can be noticed that for all studied systems, the transition from crystalline-to-amorphous occurs approximately in the same region, although there exist a certain deviation between the different systems. The causes for this deviation can be several. First, the model does not account for the bonding details. Hence, as the thin films are highly preferential oriented, a distortion of the octahedra formed by oxygen around each cation can lead to some anisotropy of the lattice changes. As a result, an error in the determination of the unit cell volume can occur. Additionally, as already mentioned previously, the density of the thin films could not be accounted for in the calculation of the crystallinity, although it was proven that increasing the metal content in the thin films leads to an increase of the density, i.e. more crystallites were measured per film volume. Therefore, it is reasonable to have some variance between the different systems.

By using the initial fictitious sphere radius as fitting parameter, all the Mg-M-O systems can be matched on one graph, as exhibited in figure 6.12a). The error on the initial fictitious sphere radius is not larger than 3%. The line in the plot is guide to the eye.

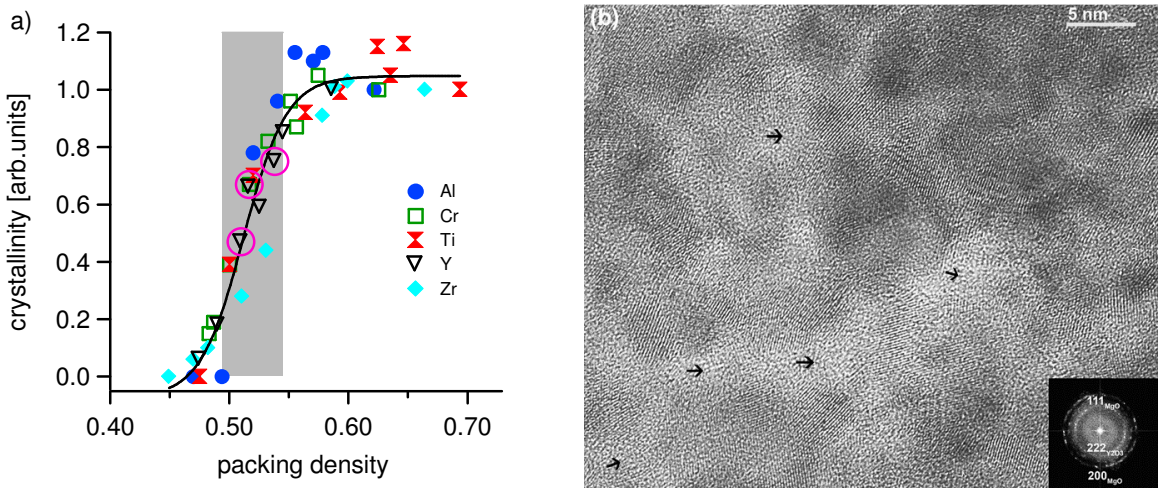

Figure 6.12: a) Crystallinity of the deposited Mg-M-O thin films as a function of the calculated packing density of the fictitious spheres, using the initial fictitious sphere radius as fitting parameter. The grey region corresponds to the phase boundary region between the amorphous and crystalline states, as described by the hard sphere phase diagram. The open circles indicate the samples which were studied with HRTEM. b) HRTEM image of a Mg-Y-O thin film with a composition of 18% metal ratio. The arrows indicate the amorphous regions.

The phase boundary region, predicted by the hard sphere model, is indicated by the grey shadowed area. On the right side of this area, films with a high crystallinity are found. When lowering the packing density and entering the transition region, the crystallinity factor decreases abruptly. Films with a packing density lower than 0.494 have an insignificant crystallinity or are completely amorphous. HRTEM measurements were performed for the films marked with purple circles in figure 6.12a). Figure 6.12b) shows a representative HRTEM image, for the thin film with 18% Y metal ratio, where the presence of nanocrystals within an amorphous matrix can be seen. This finding is consistent with the suggestion of two phases in equilibrium predicted by the hard-sphere model. Based on these facts, one can

conclude that the hard sphere model is valid to explain the crystalline-to-amorphous transition observed in the Mg-M-O films.

The crystalline-to-amorphous transition has been discussed in literature in quite some detail, and it is claimed that this transition is a first order transition.[57] One could argue that this thermodynamic reasoning is not valid under the given conditions of zone T where the sample temperature is low (<150°C). However, the transition is studied as a function of the composition, not temperature. At higher temperature, or at higher energy per particle, the basic condition for this model system, i.e. the presence of a solid solution, is not fulfilled. Here, only the influence of the composition on the transition is investigated, and hence the arguments valid for the hard sphere system can be transferred to this model system.

Of course there exist limitations in this simple model, preventing it from being used for every other system. This reasoning is valid only for dense packed structures and ionic structures. Most likely, if one is willing to apply this model to systems that do not fulfill these requirements, some adjustments have to be done.

6.2.4. Conclusions

In conclusion, the substitutional effect on the crystallographic structure of Mg-M-O thin films deposited by reactive magnetron sputtering is controlled by vacancy formation. The substitution of Mg by M results in an increased disorder, which is mimicked in the presented model by relating a hard sphere to each filled octahedral position in the MgO structure. In this way, it is shown that these systems behave similar as a hard sphere model and a crystalline-to-amorphous transition is induced for the same reasons.

In the next part of this thesis (D.), the packing density will be used to study the influence of the crystallinity in several functional properties of the Mg-M-O films.

Structure Zone Models

The SZM presented in the section 2.7 presupposes that the materials can grow crystalline. The first SZM were developed for pure metals, which are almost always crystalline. Although the revised SZM from Barna accounts for impurities,[8,9] it also implies that the films are crystalline. Mahieu *et al*. also assumes that the films are crystalline.[60] However, not all materials can grow crystalline, even if the adatoms mobility is very high. From section 6 and 7 of this thesis, it was shown that adding a metal M to MgO results in Mg-M-O solid solution (meaning that M cannot be treated as an impurity when it concerns the SZM). Furthermore, the films exhibit features of zone T, meaning that introducing a new metal does not imply that the kinetic constraints change is enough to shift the microstructure of the film to another zone. In the light of these finding, we suggest that the crystallization barriers (which are very small in the case of pure metals) are of major importance when referring to compound materials. The transition from crystalline-to-amorphous of the Mg-M-O films shows that not all materials can grow crystalline. The introduction of vacancies induces amorphization independently on the adatoms mobility, because from the structure stability point of view it is impossible to grow a crystalline material.

Georgieva *et al.*[61] have calculated the energy barriers for surface diffusion in the Mg-Al-O films and have shown that increasing the C_{Al} yields the increasing of those energy barriers. However, taking into account the diffusion lengths of the simulations, we suggest here that the energy barriers for surface diffusion are in fact energy barriers for crystallization (or recrystallization barriers).

7. Biaxial Alignment

Polycrystalline biaxially aligned thin films possess a well-defined preferential out-of-plane and in-plane orientation, i.e., the majority of the film grains exhibit a certain crystallographic plane oriented parallel to the substrate surface (out-of-plane) and the crystal facets are aligned along certain direction perpendicularly to the substrate surface (in-plane). Biaxial aligned thin films are used as buffer layers between non-textured substrates and superconductive thin films to minimize the current losses at the film-substrate interface.[62] Moreover, biaxially alignment of films with magnetic[63] and piezoelectric[64] properties has been shown to allow for enhancement of the performance of the corresponding devices.

Understanding the fundamental mechanisms that determine the out-of-plane and in-plane orientation is very important since it would enable one to synthesize biaxially aligned films in a controlled manner. Out-of-plane grain alignment is determined by thermodynamics and kinetic conditions during film growth.[9] Different crystallographic planes exhibit differences in the energy barriers for surface diffusion. A larger diffusion barrier implies shorter diffusion lengths and, as a consequence, longer residence times of adatoms on a certain crystallographic plane. The latter, under conditions of restricted surface adatom mobility (e.g., during low temperature film deposition), results in a net flux of adatoms from planes characterized by relatively small to planes characterized by relatively large energy barrier for surface diffusion. The latter planes incorporate a large amount of adatoms overgrowing the former ones and giving rise to a preferred out-of-plane-orientation.[8,9]. Characteristic example is magnetron sputtered films with the NaCl crystal structure (TiN[60,65,66] and MgO[25,26,60]) that exhibit [111] out-of-plane texture when grown at room temperature. In magnetron sputtering processes the flux of the film forming species exhibits a symmetric, with respect to the source (target) surface normal, angular distribution. This distribution is a consequence of the limited size of the sputtering target and of the collisions that sputtered species undergo with buffer gas (typically Ar) atoms *en route* to the substrate. In the case that substrate and target normal are not parallel with respect to each other, i.e., when off-normal deposition is performed, the substrate encounters an asymmetric flux of film forming species. Under these conditions the momentum conservation of the impinging species results in anisotropic diffusion of adatoms to the direction of the incident vapor flux.[60] Crystal facets exhibit different adatoms capture lengths depending on their angle with respect to the deposition flux. Thus the growth of grains with the largest capture length is favored giving rise to in-plane alignment, which in combination with a preferred out of plane orientation results in biaxially aligned films.[60]

The extensive work performed on the biaxial alignment of thin films has been so far mainly focused on single metals or binary systems (metal-oxides and metal-nitrides). Adding a third metal to a binary system enables one to modify chemical composition and structure of the material and, thus, synthesize biaxially aligned films with a wider range of properties.[67,68] Ternary metal oxides of the group Mg-M-O, where M represents a metal other than Mg, have gained considerable research attention the last years.

One way to synthesize these films is by employing reactive magnetron sputtering (in an Ar-O_2 atmosphere) from a Mg and a M source in a confocal (co-sputtering) arrangement. This arrangement induces an angle between the substrate and the target normal which is known to

result in biaxially aligned films.[26,60,65,69,70] The co-existence of two different metals, i.e., Mg and M, with different sizes, density of valence electrons and surface mobility is very likely to affect kinetics and thermodynamics of film growth and thus results in substantially different out-of-plane and in-plane alignment behavior as compared to the well studied Mg-O binary system.[25-27] The goal of the current chapter is to contribute towards understanding the atomistic mechanisms that determine out-of-plane and in-plane alignment in ternary Mg-M-O films.

7.1. In-Plane Alignment

7.1.1. Mg-Mg-O Films

During dual magnetron sputtering in the configuration as shown in figure 3.1 (section 3.1.1), the atoms originating from both magnetrons arrive on an inclined surface, and diffuse in the opposite direction on the substrate surface. To understand how this affects the preferential orientation of these films, a Mg target was mounted on both magnetrons. With the same power delivered to each magnetron, the target-to-substrate distance of one of the targets was modified. As a result, pole figures from single and dual magnetron sputtering with one and two Mg targets are presented in figure 7.1.

Figure 7.1a) shows the (200) pole figures of a MgO thin film obtained by single magnetron sputtering. The existence of three poles at χ ~55° and φ ~60, 180 and 300° can be seen. When connecting the poles, a triangle pointing to the left is noticed. The three poles presented in the (200) Mg-O pole figure represent the stereographic projection of the {200} facets. Because the poles are positioned at $\chi = 55°$, and in combination with the corresponding Bragg-Brentano scan presented in figure 5.1 it can be concluded that the film exhibit a [111] out-of-plane orientation, which is the direction for $\chi = 0°$. As suggested by Mahieu[60] and Ghekiere,[29] the degree of in-plane alignment is caused by directional diffusion and therefore expected to be affected by the use of either a single or dual cathode. As such, changing the target-substrate distance can also influence the degree of in-plane alignment.

Figure 7.1 b)-f) present the (200) pole figures of the Mg-Mg-O films deposited at various distances of one magnetron from the substrate, while the other magnetron was at a fixed target-substrate distance of 14.5 cm. Figure 7.1b) corresponds to the (200) pole figure for a Mg-Mg-O thin film deposited by two sources positioned at 18.5 and 14.5 cm. The arrows indicate the position of the sources with respect to the substrate. All other pole figures are oriented in the same way. For the largest distance (figure 7.1b)) three poles can be seen at χ ~55° and φ ~60, 180 and 300°. When connecting the poles, a triangle pointing to the left source is formed. The decrease of the distance of one source from 18.5 to 16.5 cm results in a new set of three poles (along with the original ones) with position χ ~55° and φ ~0, 120 and 240°. By connecting these poles a triangle pointing to the right source is formed. Further decrease of the distance to 12.5 cm leads to a pole figure that consists of three poles, forming a triangle pointing to the right source (figure 7.1e)), i.e., to the opposite direction as compared to that in figure 7.1b). The intensity of these poles increases progressively as the target to substrate distance decreases from 12.5 to 10.5 cm (figure 7.1e) – f)).

When both cathodes are at the same distance (figure 7.1d)), six poles with the same intensity were expected. However, the three pole figures that form the triangle pointing to the right have a higher intensity than the other ones. As the angle between the substrate and both cathodes is the same, the difference in the intensity of the poles can only be explained by a difference in the magnetic field prevenient from the magnetrons. Measuring the magnetic field of both magnetrons after this experiment, revealed that they were slightly different, being the first one (responsible for the triangle pointing to the left) ~150 G stronger than the other one. When the magnetic field is stronger the voltage is lower. At constant current, a lower deposition rate is obtained because the sputter yield decreases with the voltage.

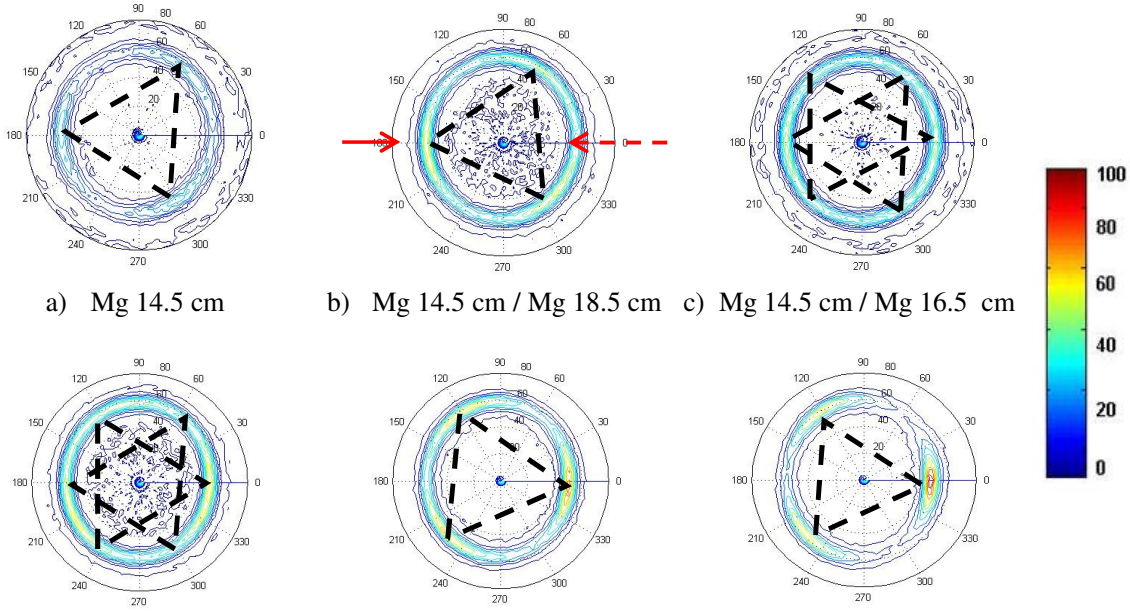

a) Mg 14.5 cm b) Mg 14.5 cm / Mg 18.5 cm c) Mg 14.5 cm / Mg 16.5 cm

d) Mg 14.5 cm / Mg 14.5 cm e) Mg 14.5 cm / Mg 12.5 cm g) Mg 14.5 cm / Mg 10.5 cm

Figure 7.1: 200) pole figures of Mg-Mg-O films deposited at various target-to-substrate distances. The arrows in (b) indicate the position of the two magnetron sources.

Furthermore, in figure 7.1, a weak pole is observed for $\chi = 0°$ in the (200) pole figures. It is suggested that this originates from the first ~150 nm of the film, where the out-of-plane is not developed yet, and a random orientation exists. Intensity is only detected for $\chi = 0$, and not for all χ and φ values as one would expect for a polycrystalline randomly oriented film. This can be attributed to the defocusing effect, i.e., the intensity of the detector decreases drastically upon χ increase.

7.1.2. Mg-M-O Films

Although the pole figures of the Mg-Al-O thin films were already presented in section 5.2, their analysis was only done in terms of crystallinity (crystalline-to-amorphous transition). Therefore, they are brought back to discussion in order to complete the interpretation of the results and figure 7.2 exhibits the pole figures of the Mg-Al-O thin films deposited with different target-to-substrate distances.

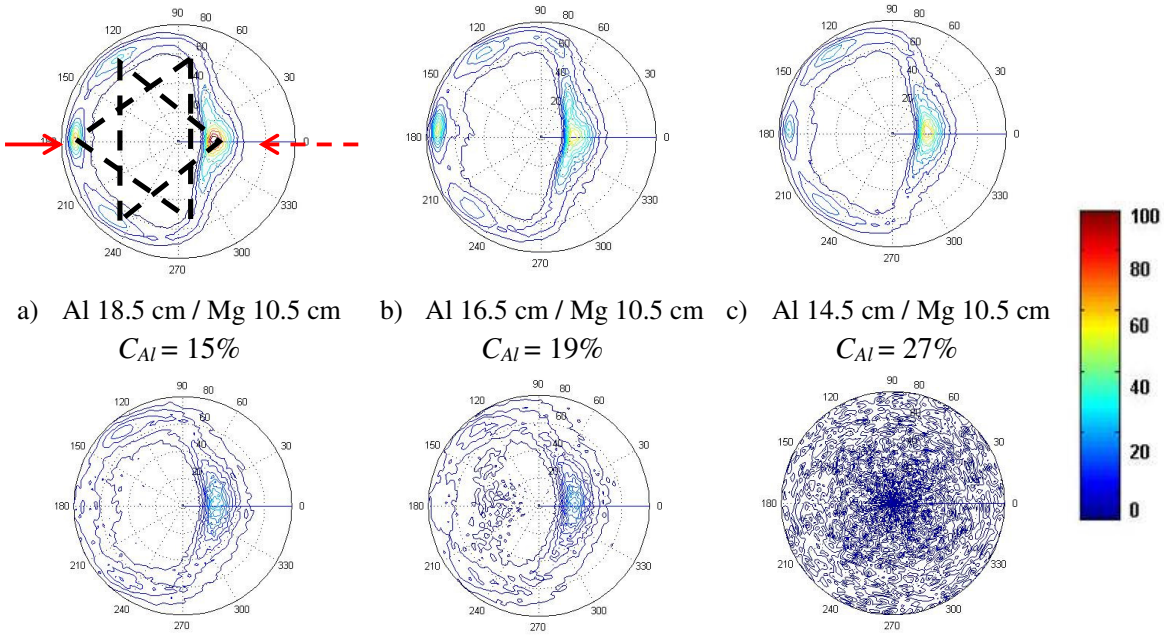

a) Al 18.5 cm / Mg 10.5 cm C_{Al} = 15%

b) Al 16.5 cm / Mg 10.5 cm C_{Al} = 19%

c) Al 14.5 cm / Mg 10.5 cm C_{Al} = 27%

d) Al 12.5 cm / Mg 10.5 cm C_{Al} = 33%

e) Al 10.5 cm / Mg 10.5 cm C_{Al} = 39%

f) Al 10.5 cm / Mg 12.5 cm C_{Al} = 52%

Figure 7.2: (200) pole figures of Mg-Al-O thin films deposited with different target-to-substrate distances. The dashed arrow indicates the direction of the magnesium target, while the full arrow indicates the aluminum one.

Similarly to what has been observed in some cases for the Mg-Mg-O system, the use of two sources results in pole figures that exhibit two sets of three poles forming each set a triangle, pointing to opposite directions. A decrease of the Al source-substrate distance (or an increase in C_{Al}) results in a diminution of the poles intensity.

Comparable to what was observed for the Mg-Mg-O system, the use of two sources resulted in a material with a double biaxial alignment distribution. The presence of biaxial alignment up to the moment that the thin film becomes amorphous, means that all those thin films are grown under zone T conditions.[60] A disparity when compared to the Mg-Mg-O system regards the tilt of the (111) direction towards the aluminum source. This tilt can be evaluated by the fact that the ring center does not coincide with the center of the pole figure.

In figure 7.3 is depicted the pole figures of the Mg-Cr-O films. When compared to the Mg-Al-O system (see figure 7.2), it cannot be stated that the two sets of poles pointing opposite directions exist while the films are crystalline – it is not possible to distinguish 6 poles in the pole figures depicted in figure 7.3d)-f). Nevertheless, the biaxial alignment is still present up to the moment when the thin films become amorphous, meaning that, also all those thin films are grown under zone T conditions, as well.[60] Once again, a tilt of the (111) direction towards the chromium source is observed, though, not so notorious as in the Mg-Al-O system.

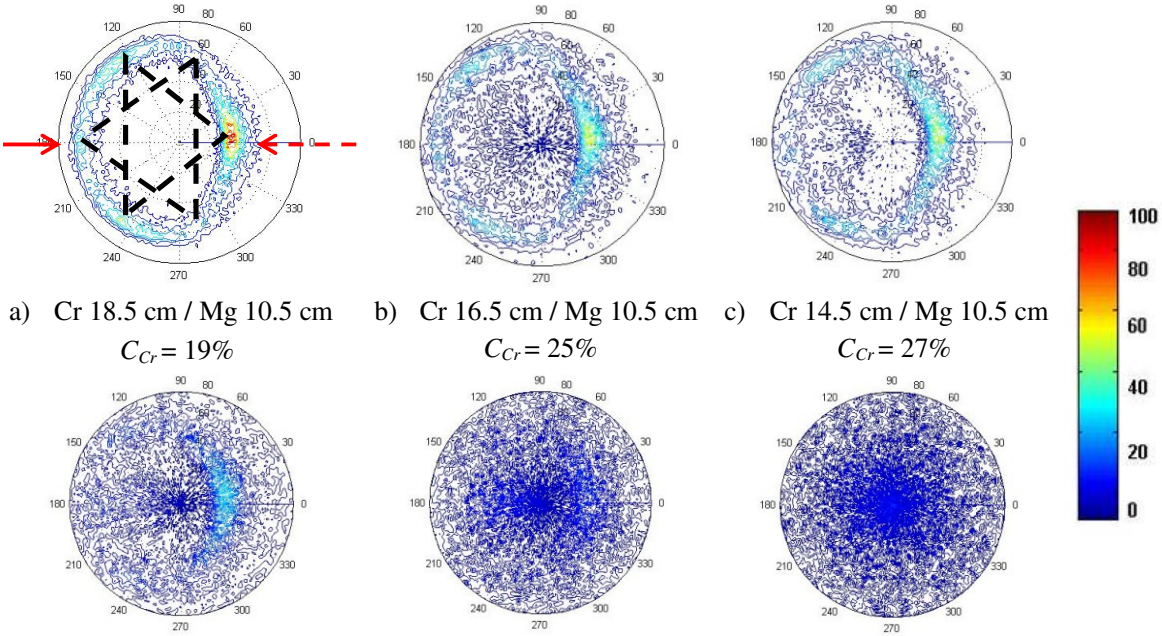

a) Cr 18.5 cm / Mg 10.5 cm $C_{Cr} = 19\%$

b) Cr 16.5 cm / Mg 10.5 cm $C_{Cr} = 25\%$

c) Cr 14.5 cm / Mg 10.5 cm $C_{Cr} = 27\%$

d) Cr 12.5 cm / Mg 10.5 cm $C_{Cr} = 35\%$

e) Cr 10.5 cm / Mg 10.5 cm $C_{Cr} = 42\%$

f) Cr 10.5 cm / Mg 12.5 cm $C_{Cr} = 50\%$

Figure 7.3: (200) pole figures of Mg-Cr-O thin films deposited with different target-to-substrate distances. The dashed arrow indicates the direction of the magnesium target, while the full arrow indicates the chromium one.

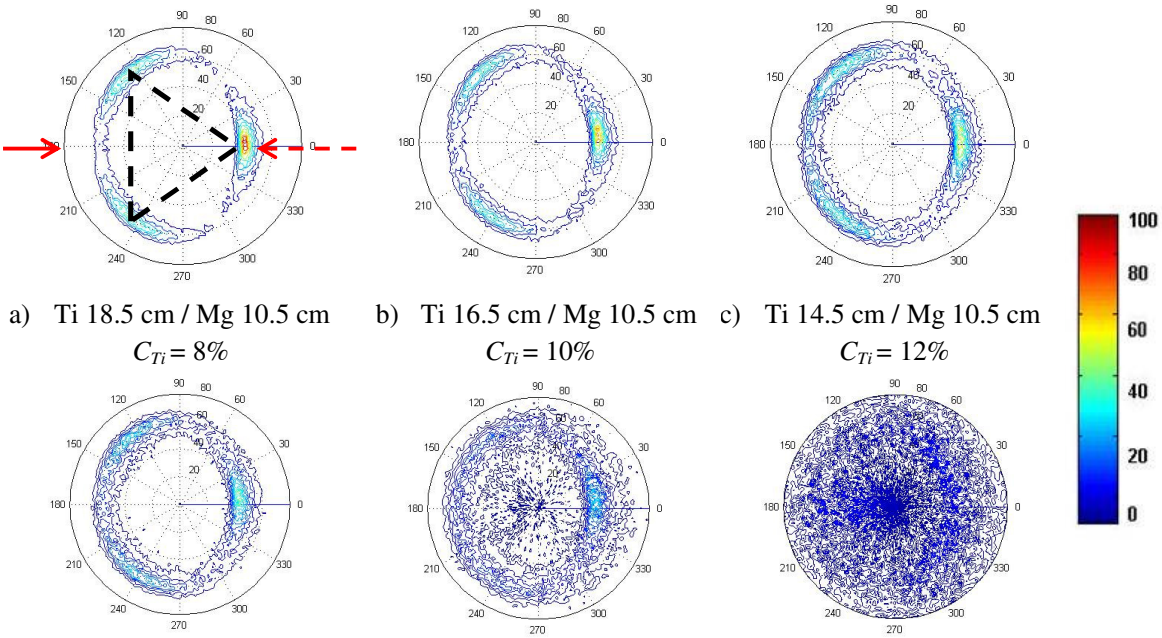

a) Ti 18.5 cm / Mg 10.5 cm $C_{Ti} = 8\%$

b) Ti 16.5 cm / Mg 10.5 cm $C_{Ti} = 10\%$

c) Ti 14.5 cm / Mg 10.5 cm $C_{Ti} = 12\%$

d) Ti 12.5 cm / Mg 10.5 cm $C_{Ti} = 18\%$

e) Ti 10.5 cm / Mg 10.5 cm $C_{Ti} = 24\%$

f) Ti 10.5 cm / Mg 12.5 cm $C_{Ti} = 34\%$

Figure 7.4: (200) pole figures of Mg-Ti-O thin films deposited with different target-to-substrate distances. The dashed arrow indicates the direction of the magnesium target, while the full arrow indicates the titanium one.

Observing figure 7.4, where the pole figures of the Mg-Ti-O films are depicted, it is noticed that while the films are crystalline only three poles at χ ~55° and φ ~0, 120 and 240° are present. These poles form a triangle pointing to the right.

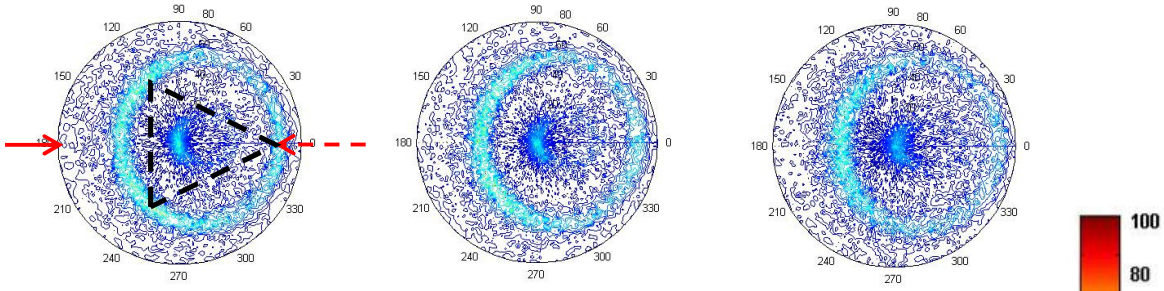

a) Zr 18.5 cm / Mg 10.5 cm C_{Zr} = 11%

b) Zr 16.5 cm / Mg 10.5 cm C_{Zr} = 13%

c) Zr 14.5 cm / Mg 10.5 cm C_{Zr} = 15%

d) Zr 12.5 cm / Mg 10.5 cm C_{Zr} = 25%

e) Zr 10.5 cm / Mg 10.5 cm C_{Zr} = 30%

f) Zr 10.5 cm / Mg 12.5 cm C_{Zr} = 38%

Figure 7.5: (200) pole figures of Mg-Zr-O thin films deposited with different target-to-substrate distances. The dashed arrow indicates the direction of the magnesium target, while the full arrow indicates the zirconium one.

The pole figures of the Mg-Zr-O and Mg-Y-O films are depicted in figures 7.5 and 7.6, respectively. The influence of adding zirconium (or yttrium) to MgO is substantially different than what was observed in the previous systems, where Al, Cr and Ti were added to MgO. The (200) poles are not very well defined, revealing that the texture of the Mg-Zr-O and Mg-Y-O films is not as distinct as in the previous cases. In the case of Mg-Zr-O films, there is a pole close to the center of the pole figures, as can be seen in figures 7.5 a)-c). This pole might be the most intense pole of three poles of the second set of poles (as observed in the Mg-Al-O and Mg-Cr-O systems). The other respective two poles are not present due to their spatial localization (outside measuring area). As the texture of these films is not as well defined as in the previous systems (Mg-Al-O, Mg-Cr-O and Mg-Ti-O), the pole presented in the center of the pole figures can also be the result of the first ~150 nm of the film, where the film is polycrystalline with a random orientation. Similar to the Mg-Ti-O films, the triangle formed by the three poles points to the right.

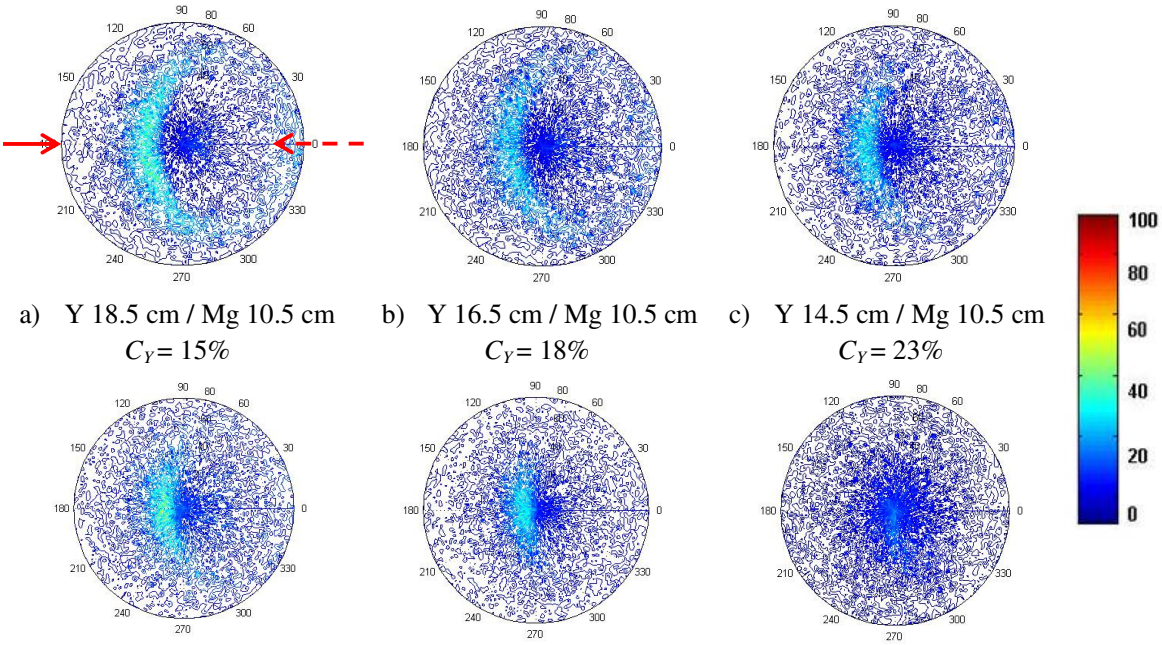

a) Y 18.5 cm / Mg 10.5 cm C_Y = 15%

b) Y 16.5 cm / Mg 10.5 cm C_Y = 18%

c) Y 14.5 cm / Mg 10.5 cm C_Y = 23%

d) Y 12.5 cm / Mg 10.5 cm C_Y = 27%

e) Y 10.5 cm / Mg 10.5 cm C_Y = 30%

f) Y 10.5 cm / Mg 12.5 cm C_Y = 39%

Figure 7.6: (200) pole figures of Mg-Y-O thin films deposited with different target-to-substrate distances. The dashed arrow indicates the direction of the magnesium target, while the full arrow indicates the yttrium one.

7.1.3. In-Plane Alignment Growth Mechanism

The distinct poles indicate the presence of in-plane alignment in the deposited films Mg-Mg-O and Mg-M-O films. This is consistent with previous investigations where Mg-O films deposited from one source forming an angle with the substrate normal also exhibited the presence of in-plane alignment.[25,27,60] This can be understood from a model previously presented by our group.[60] The tilting of the substrate results in a directional flux of the adatoms. Depending on their in-plane orientation the growing crystals have a different adatom capture probability. This probability can be calculated from the so-called capture length which is the projection of the crystallite cross section on a plane perpendicular on the direction of the incoming flux.[60] For the particular case of [111] out-of-plane oriented films, the in-plane alignment is caused by the angular dependence of the adatom capture length of the {100} crystal facets which form a triangle. The angles of largest capture length are 30° and 90° with respect to the flux direction.[60] However, the experimental results reported so far in the literature have shown that in plane alignment occurs only at 90°. The two sets of poles in figure 7.1 b) and c) for the Mg-Mg-O films indicate a double in-plane alignment. In light of that model, we suggest here that the double in-plane alignment is caused by the presence of two material fluxes originating from the two confocally arranged Mg sources each promoting in-plane alignment to one direction, as depicted schematically in figure 7.7. This suggestion is further supported by the fact that the two triangles formed by the distinct poles point towards the direction of the incoming fluxes. Along the same lines, variation of the relative flux of material from each source (by varying the relative target-to-substrate distance) promotes one growth direction at the expense of the other, enabling one to switch between in-plane (one set

of poles) and double in-plane (two sets of poles) and again back to in-plane aligned films (figure 7.1b)-f)). In the case of single in-plane alignment the orientation of the grains coincides with the position of the source placed closest to the substrate, i.e., it is determined by the largest material flux.

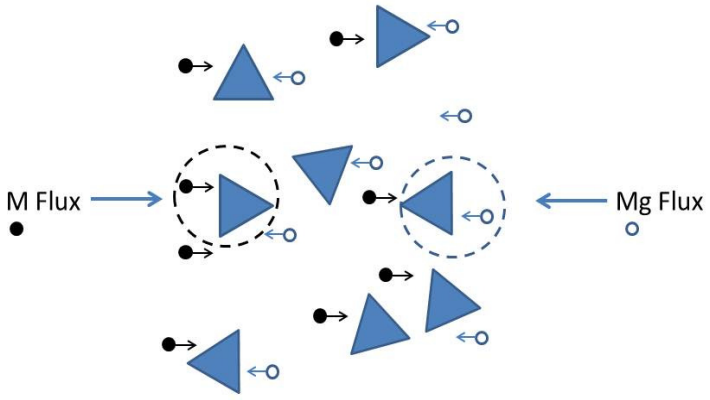

Figure 7.7: Schematic representation of the 2D growth of triangular shaped [111] out-of-plane oriented grains with {100} facets, for deposition using two cathodes, with M = Mg, Al, Cr, Ti, Y and Zr. The dashed lines indicate orientations with the largest capture length.

The plan view SEM image of the Mg-Mg-O and Mg-Al-O films corresponding to the pole figure in figure 7.1b) and figure 7.2a) can be seen in figure 7.8a) and b), respectively. The images reveal a "roof-tile" structure (faceted surface). In the case of the Mg-Mg-O film, the existence of mainly one orientation of the columns facets, although not all perfectly aligned, as is indicated by the solid white lines, is seen. In the Mg-Al-O film the existence of two column directions is indicated by the solid white lines.

a) b)

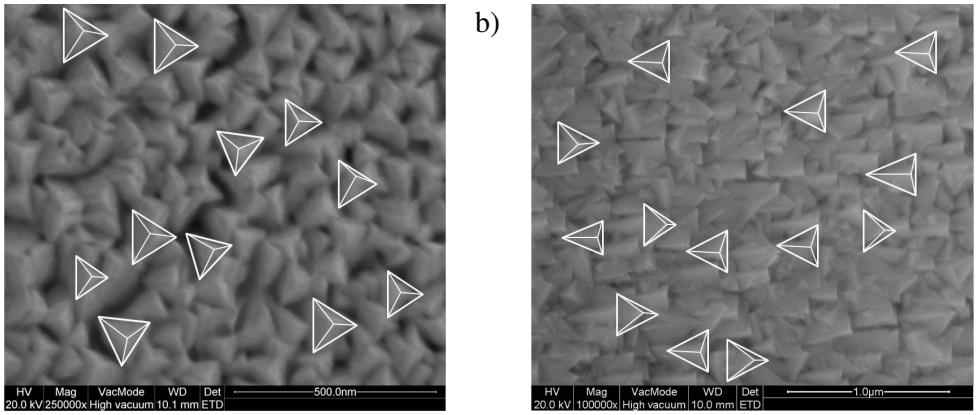

Figure 7.8: Plan view SEM image of the a) Mg-Mg-O thin film produced with different target-to-substrate distances (14.5 cm and 18.5 cm). b) Mg-Al-O thin films deposited with cathode-substrate distance of 10.5 and 18.5 cm for Mg and Al, respectively. The white triangles are guide to indicate the facets direction.

Because in the Mg-M-O case two metal fluxes arrive at the substrate from opposite directions, an influence in the in-plane alignment is observed. In the case of Mg-Al-O and Mg-Cr-O, similar to what was observed for Mg-Mg-O, a double in-plane alignment is noticed. This is

not only clear from the pole figures, showing 6 poles, but also from the SEM top view image showing two sets of triangles pointing in two directions (see figure 7.8b). As stated before, the other three systems, i.e. Mg-Ti-O, Mg-Zr-O and Mg-Y-O thin films are single biaxially aligned. An explanation for the differences in the in-plane alignment in the various Mg-M-O systems is provided in section 7.3.

7.2. Out-of-Plane Alignment

The three poles shown in figure 7.1 represent the stereographic projection of the {200} facets. Because the poles are positioned at $\chi = 55°$ it can be concluded that the films exhibit a [111] out-of-plane orientation perpendicularly to the substrate surface, which is the direction for $\chi = 0°$. For the Mg-Mg-O films, the crystals have the same out-of-plane orientation independently of the target-to-substrate distance of the two sources. This is not the case when the Mg target of one source is replaced by a target of another element. The center of the triangle(s) which connects the three poles does not coincide with the center of the pole figure. This is an indication of a tilt of the [111] out-of-plane orientation. The same conclusion can be drawn from the pole in the (111) pole figure (not shown here) which is also shifted with respect to $\chi = 0°$. For Mg-Al-O, Mg-Cr-O and Mg-Ti-O, the tilt was found to be 22, 16 and 10° towards the Al, Cr and Ti source, respectively. For the Mg-Zr-O and Mg-Y-O thin films, the measured tilt was 12 and 24°, respectively, towards the Mg source. From these findings it is evident that the direction and the magnitude of the grain tilt are material dependent.

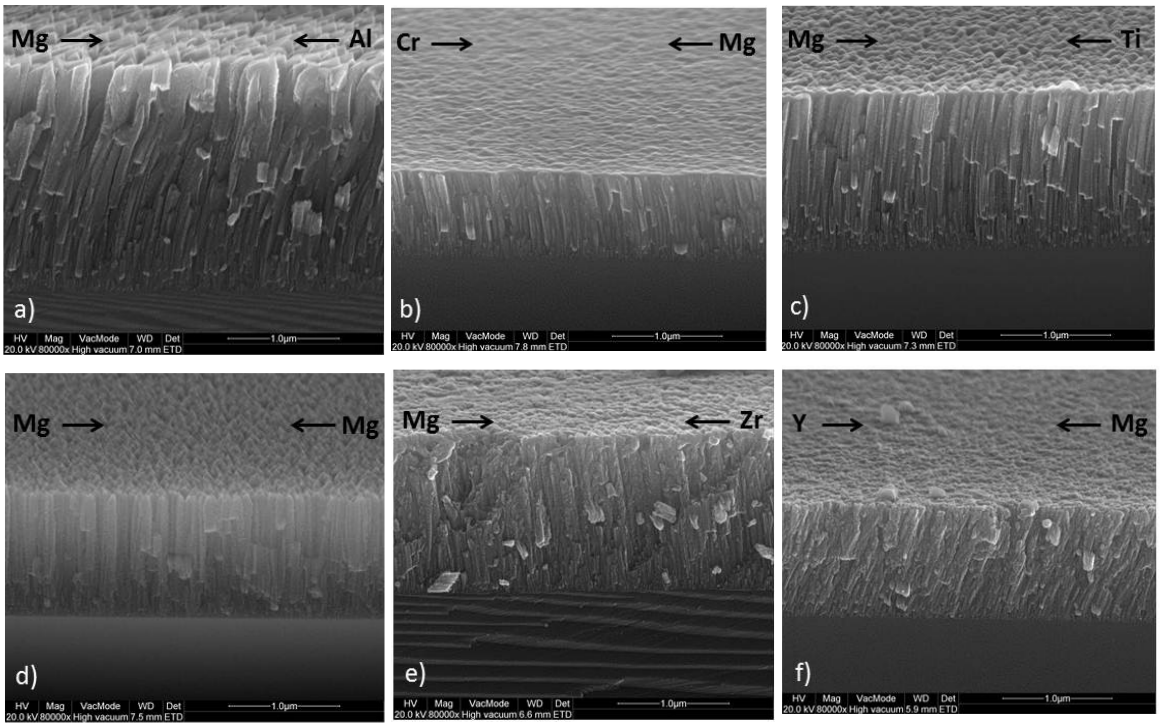

Figure 7.9: Cross-section SEM images of a) Mg-Al-O; b) Mg-Cr-O; c) Mg-Ti-O; d) Mg-Mg-O; e) Mg-Zr-O and Mg-Y-O films. The arrows indicate the material flux direction.

Furthermore, cross-section SEM analysis revealed that all Mg-M-O films exhibit a columnar microstructure. This is shown for the Mg-Mg-O and all the Mg-M-O films in figure 7.9.

There, it is also seen that the columns of the Mg-Mg-O film are parallel to the substrate normal (figure 7.9d)). This is not the case for the Mg-M-O films where the columns are tilted towards one of the sources. In summary, in the case of Mg-Al-O, Mg-Cr-O and Mg-Ti-O the columns tilt towards the Al, Cr and Ti sources, 16, 12 and 6°, respectively while in the Mg-Zr-O and Mg-Y-O systems, the columns tilt towards the Mg cathode 9 and 22°, respectively.

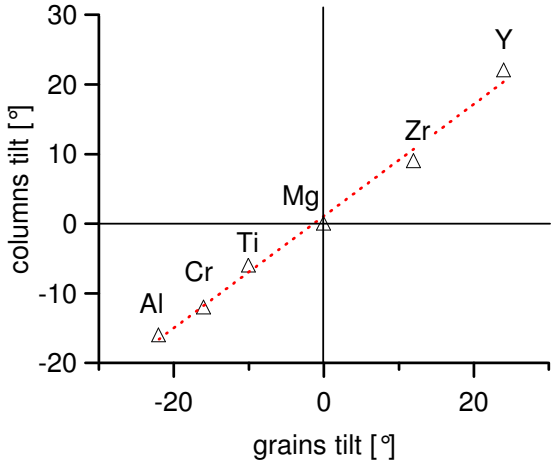

Figure 7.10: Columns tilt of the Mg-M-O thin films as a function of the grains tilt (as measured from the (111) pole figures). The line is a fitting through all the data points.

Similarly to the grain tilt, the direction and angle of column tilt presented in the SEM cross-section images in figure 7.9 is also material dependent. This can be visualized in figure 7.10 where the column tilt is plotted as a function of the grain tilting. It can be seen that the tendency found for column tilting is in optimal concordance with the tendency for grain tilting.

7.3. Effect of M concentration and Atomic Size

The use of two different material sources induces anisotropy in the flux encountered by the substrate during the film growth. The anisotropic deposition flux results in spatial variations in chemical composition along the columns width as observed in the energy filtered TEM (EFTEM) in figure 7.11. The left side of the columns has a higher Cr concentration than the right one. Moreover, figure 7.11 shows also column tilting in agreement with the SEM cross-sectional images as shown in figure 7.9.

Radnóczi *et al.*[71] have demonstrated that a compositional gradient leads to grain tilt in single crystalline $Al_{1-x}In_xN$ whiskers grown epitaxially on ZrN. This was shown to be the consequence of stacking of the crystallographic planes that tilt towards Al due to the existence of a difference in chemical composition along the whisker and the fact that the ionic radius of Al is smaller than the In one. To explore the relevance of this mechanism for our results, the measured tilt on the (111) planes has been plotted in figure 7.12 as a function of the relative change of the cation (M) radii with respect to the Mg radius, using cation radii values from literature.[41] It should be mentioned here that positive and negative values in figure 7.12, correspond to grain tilt towards the Mg and M source, respectively. In agreement with the work of Radnóczi *et al.*[71], the (111) planes tilt towards the source equipped with that target for

which the cation radius is the smallest. The magnitude of tilt is proportional to the cation size difference between host (Mg) and the substituting element (M). When both are the same, i.e., Mg-Mg-O, no tilt is observed.

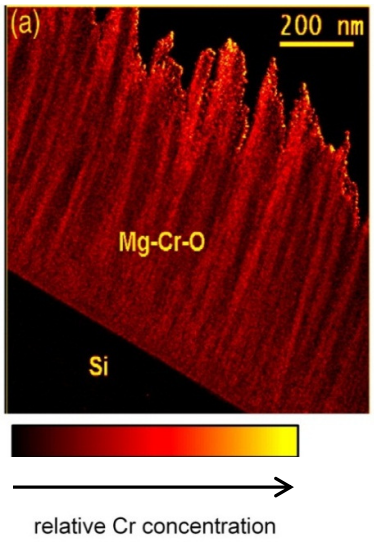

Figure 7.11: High magnification EFTEM color map of the cross-sectional Mg-Cr-O with 19% Cr metal ratio.[j]

In the case of [111] out-of plane oriented grains, the densest packed planes of the oxygen anions are parallel to the substrate with metal atoms positioned between the oxygen planes. In the presence of a composition gradient, the average size of the metal cation will change from one side to the other side of the growing grain, as shown schematically in figure 7.13.

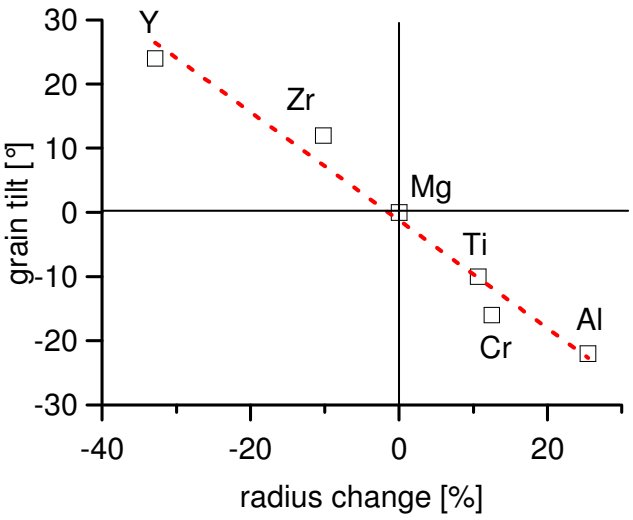

Figure 7.12: Tilt angle of the Mg-M-O thin films (as measured from the (111) pole figures) as a function of the respective change in cation radii. The red line is a fitting through all the data points.

[j] EFTEM work was performed by N. Jehanathan at EMAT, Antwerp.

Consequently the next plane of oxygen anions will be tilted by an angle α defined by the composition gradient $\frac{\partial C_M}{\partial x}$ and the difference in the cation radius $\left(r_{Mg} - r_M\right)$, i.e.,

$$\alpha = arctg\left(\frac{\partial C_M}{\partial x}\left(r_{Mg} - r_M\right)\right). \tag{7.1}$$

As this angle is small, the following simplification is allowed

$$\alpha = \frac{\partial C_M}{\partial x}\left(r_{Mg} - r_M\right). \tag{7.2}$$

As the crystal grows by alternating metal and oxygen layers, the tilt will increase with crystal size. The latter can be expressed by

$$\beta = \frac{k\alpha}{\mathrm{a}/\sqrt{3}}, \tag{7.3}$$

with k the crystal size, and $\mathrm{a}/\sqrt{3}$ accounting for the d-spacing in the (111) orientation.

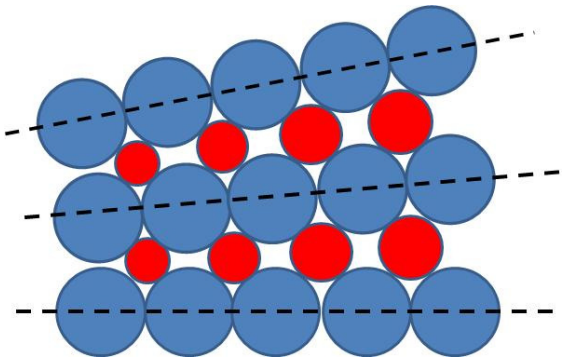

Figure 7.13: Schematic representation of alternating layers of the (111) densest packed planes of oxygen anions (light grey) and metal cations (dark grey).

Combining Equations (7.2) and (7.3) the following formula for the tilt is obtained:

$$\beta = \frac{\sqrt{3}k}{\mathrm{a}}\frac{\partial C_M}{\partial x}\left(r_{Mg} - r_M\right), \tag{7.4}$$

Equation (7.4) predicts that the tilt increases with the composition gradient. The latter, in turn, can be expected to be proportional to C_M. However, the experimental results (see figures 7.2 to 7.6) do not show any correlation between C_M and grain tilt. At the same time, the crystallite size, k, calculated for all Mg-M-O systems using the Scherrer's formula[49] was found to be inversely proportional to C_{Mg} (figure 7.14). This, according to Equation (7.4) counteracts the effect of an increased $\frac{\partial C_M}{\partial x}$ and may explain the constant values of grain tilt

at different chemical compositions. Moreover, the competing effect between composition gradient and crystallite size can explain the linear dependence of the grain tilt on the cation radius change (figure 1.12).

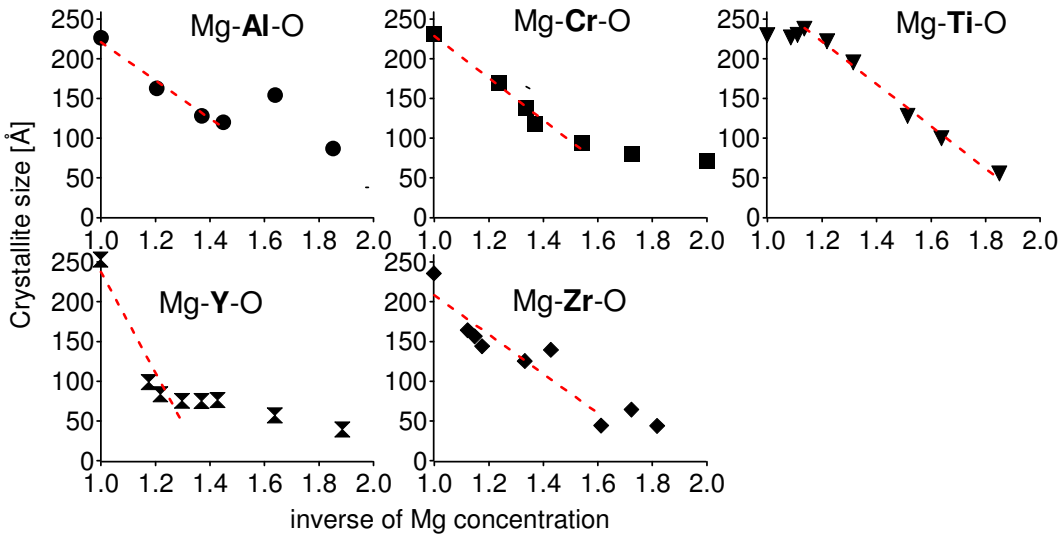

Figure 7.14: Crystallite size of the Mg-M-O films as a function of the inverse of Mg concentration, calculated from the Scherrer's formula. The dashed lines are a fit through the data points.

As stated before, it can be expected that the magnitude of the composition gradient depends on C_M. For a given C_M value, a maximum composition gradient can be estimated assuming that all M atoms reside at one side of the growing crystal. In that case, the gradient is given by twice the average composition divided by the smallest distance between two metal atoms in the MgO lattice, i.e., the distance between two oxygen anions ($d_{O\text{-}O}$);

$$\left(\frac{\partial C_M}{\partial x}\right)_{\max} = \frac{2C_M}{d_{O-O}}. \qquad (7.5)$$

At the same time, since the crystallite size can be determined independently (see figure 7.14), it is possible to calculate the composition gradient $\frac{\partial C_M}{\partial x}$ by combining Equations (7.3) and (7.4) for known values of tilt and atomic radii. Subsequently, the ratio of the calculated $\frac{\partial C_M}{\partial x}$ to the maximum composition gradient $\left(\frac{\partial C_M}{\partial x}\right)_{\max}$ can be used to calculate the relative gradient according to the expression:

$$\left(\frac{\partial C_M}{\partial x}\right)_{relative} = \frac{\mathrm{a}\beta d_{O-O}}{k 2C_M \sqrt{3}\left(r_{Mg} - r_M\right)}. \qquad (7.6)$$

The relative concentration gradient for the various Mg-M-O systems is plotted in figure 7.15. The metals can be classified into two groups, i.e., Al and Cr with a relatively small and Ti, Zr, and Y with a relatively large $\left(\frac{\partial C_M}{\partial x}\right)_{relative}$ values. We suggest here that the small relative gradient for Al and Cr indicates longer – as compared to the other metals –diffusion lengths that can even out compositional variations formed upon deposition. Moreover, enhancement of adatom surface diffusion is known to promote in-plane alignment.[60] Therefore, we argue that the larger diffusivity of Al and Cr leads to double in-plane preferential orientation in the Mg-Cr-O and Mg-Al-O systems, as opposed to the single in-plane orientation observed for Mg-Ti-O, Mg-Zr-O and Mg-Y-O.

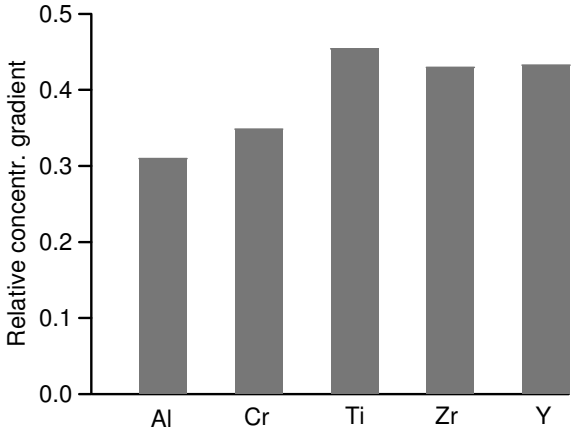

Figure 7.15: Relative concentration gradient in the Mg-M-O films calculated from the experimental column tilting.

7.4. Conclusions

It was found that when the two sputtering cathodes were equipped with the same target material (Mg), the in-plane alignment is defined by the source closest to the substrate, i.e., by the largest material flux. Thus, films exhibiting either single or double in-plane alignment could be deposited. Double in-plane alignment was also observed for the Mg-Al-O and Mg-Cr-O films, while Mg-Ti-O, Mg-Zr-O and Mg-Y-O exhibit single in-plane alignment. It is argued that the double in-plane alignment in the case of Mg-Al-O and Mg-Cr-O films is promoted by the larger diffusivity of Al and Cr compared to Ti, Zr, and Y. The grains and the columns of the Mg-Al-O, Mg-Cr-O and Mg-Ti-O films were found to be tilted towards the Al, Cr and Ti flux, respectively, while for the Mg-Zr-O and Mg-Y-O the tilt occurs towards the Mg material flux. The tilt of the grains can be understood from the difference of the two cation radius in the Mg-M-O cell, which triggers a distortion in the lattice. The stacking of the distorted cells in the grain results in a tilt of the columns. Both, grains and columns, tilt towards the direction of the material flux with the smallest cation radius.

8. High Temperature Deposition and *Post*-Deposition Heat Treatment

The addition of several M to the MgO films yields, according to the phase diagram, to some interesting complex structures such as spinels and perovskites. Nonetheless, as the growth of the Mg-M-O is kinetically constrained, such structures were not achieved at the expense of the formation of Mg-M-O solid solutions. Depositions at high temperature and post-deposition heat treatment increase the importance of thermodynamics in the growth and structure formation of the thin films. Therefore, in section 8.1 is discussed the effect of depositing MgO, Mg-Al-O and Mg-Cr-O at high temperature, while in section 8.2 the heat treatments performed in Mg-Al-O and Mg-Cr-O films are presented.

8.1. Deposition at High Temperature

A high temperature resistive substrate heater from MAK designed to handle temperatures up to 950° C was used to perform depositions at high temperature. Inside the heater there is a resistive coil embedded in a super alloy block. When current is applied, the block is heated up. A sheathed type K thermocouple and a Eurotherm 7100 L temperature control were used. Nevertheless, at 850° C the deposition process was not stable anymore and therefore those thin films are not included in this manuscript. A heating ramp of 20° C/min was used for all depositions performed at high temperature and the deposition was only started after a stable temperature was reached. The same ramp was used to cool down the heater, while an oxygen flow of 8 sccm was kept constant till 200° C, at which temperature the vacuum chamber was vented.

The study was performed for the Mg-Al-O system at 300, 500 and 700° C. In the case of Mg-Cr-O, only deposition performed at 700° C were carried out. For each set of temperature-material, four thin films with different M metal content were performed, being that the targets-to-substrate distance used in each set of samples was the same. As MgO thin films are the starting material of this research, the initial task was to study the influence of substrate temperature on the structure of MgO thin films.

8.1.1. MgO

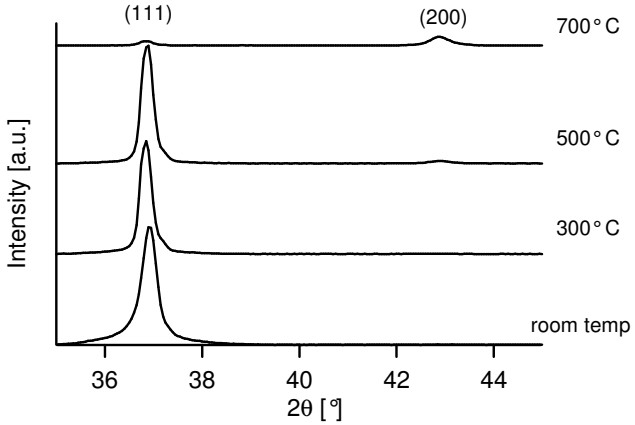

Figure 8.1: Angular XRD of MgO thin films deposited at different substrate temperatures.

As previously reported, MgO films deposited at room temperature (not intentionally heated substrate) are grown under zone T conditions and exhibit a [111] preferential out-of-plane orientation (see figure 8.1). Increasing the substrate temperature does not lead to any change in the preferential out-of-plane orientation, up to 700 °C, where the fraction of out-of-plane is drastically decreased. Nevertheless, a polycrystalline structure is not achieved (in a powder diffraction the (200) planes have a relative intensity of 100 while the (111) planes have relative intensity 4). Therefore, it can be concluded that the MgO thin films deposited at high temperature are still grown under zone T conditions, being the sample deposited at 700 °C very close to the transition from zone T to zone II.

The pole figure measurements (results are plotted in figure 8.2) confirmed the idea that the MgO thin films still grow with some degree of preferential out-of plane alignment. However, at 700 °C the thin film exhibits a fiber texture structure (absence of in-plane alignment).

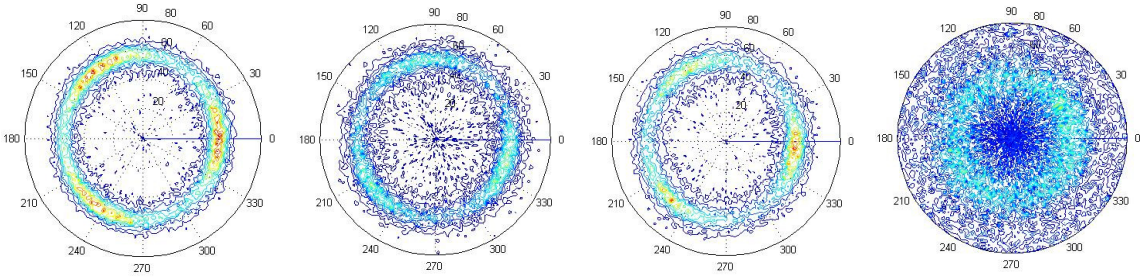

a) Room Temp b) 300° C c) 500° C d) 700° C

Figure 8.2: (200) pole figures of MgO thin films deposited at a) room temperature, b) 300° C, c) 500° C and d) 700° C.

8.1.2. Mg-Al-O and Mg-Cr-O

Mg-Al-O

Depositing Mg-Al-O thin films at 300 and 500 °C (see figure 8.3) did not lead to substantial changes in the XRD patterns as compared with the depositions performed at room temperature. Nevertheless, a broad weak peak (~44°) starts to appear at 500 °C for the thin film with $C_{Al} = 66\ \%$ (the film with the same chemical composition deposited at room temperature was XRD amorphous).

When the thin films were deposited at 700 °C, it was noticed that the amount of Al that can be incorporated into the MgO structure which does not result in an amorphous thin film, is larger (up to $C_{Al} = 65\ \%$). Thus, all the peaks present in the patterns in figure 8.4a) were indexed as belonging to MgO and fit with the understanding of the mixed oxides, i.e., the presence of a solid solution and the transition from crystalline-to-amorphous when C_M increases, as discussed in chapters 5 and 6. The incorporation of Al results in a decrease of the lattice parameter, and as a consequence, a shift of the Bragg reflections towards higher 2θ values is observed. The XRD pattern of the sample with $C_{Al} = 65\ \%$ deviates from this behavior. The lattice parameter of the thin films deposited at room temperature and at 700 °C as a function of its chemical composition is depicted in figure 8.4b. From this figure, one can conclude that

although it is possible to add more Al to the thin film and keep a crystalline structure, it does not mean that more Al can be introduced in the MgO lattice. On the contrary, the amount of Al incorporated in the MgO lattice for the sample with $C_{Al} = 65\ \%$ is lower than in the one with $C_{Al} = 58\ \%$, as can be concluded from the return of the Bragg peak position towards lower values (in other words, the increase of the *d*-spacing).

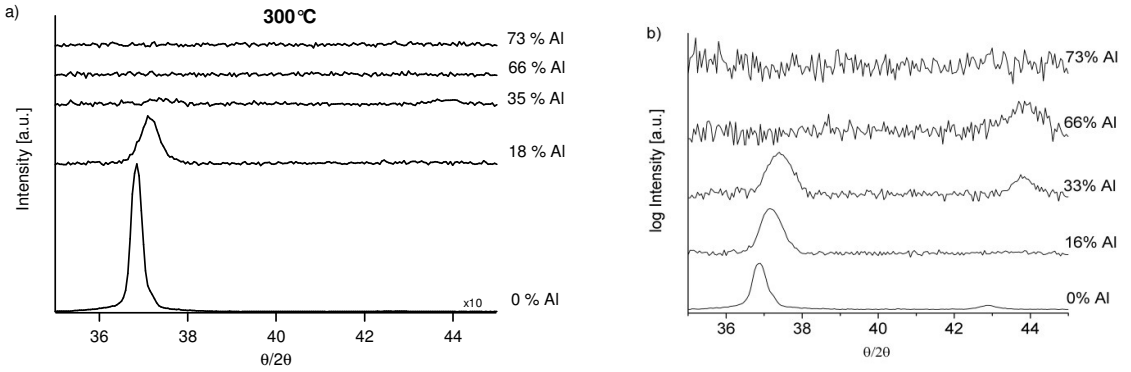

Figure 8.3: Angular XRD patterns of Mg-Al-O thin films deposited at a) 300° C and b) 500 °C.

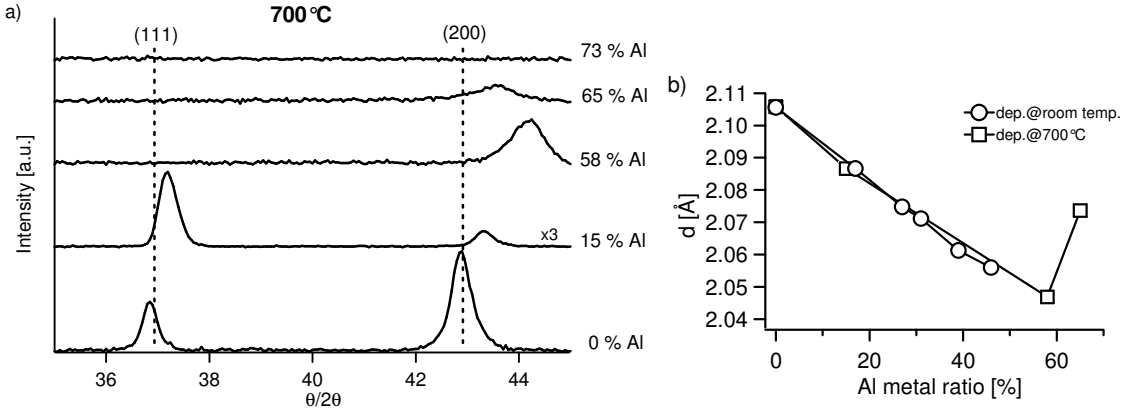

Figure 8.4: a) Angular XRD patterns of Mg(Al)O thin films deposited at 700° C. The dashed lines indicate the (111) and (200) peak positions from the MgO ICDD pattern. b) *d*-spacing of the Mg-Al-O thin films deposited at room temperature and at 700 °C as a function of the Al metal content.

The thin film with $C_{Al} = 65\ \%$ does not exhibit the spinel structure ($MgAl_2O_4$), as it was confirmed by the pole figures. If the present peak at $2\theta \approx 43.6°$ would be from the (400) reflection of $MgAl_2O_4$ (space group Fd-3m),[k] one should be able to see the (311) poles at $2\theta \approx 36.5°$ (four poles or a ring, in case of no in-plane alignment), which is not the case. Measuring at the position of the (200) MgO planes, a typical pole figure of a polycrystalline thin film is obtained. Further TEM work confirmed the XRD results, identifying the crystalline phase as MgO (not shown here). Low magnification TEM images of the Mg-Al-O film with $C_{Al} = 65\%$ (not shown here) show the existence of round shaped columns. Therefore, one can conclude that when the film is grown at 700 °C, the resulting microstructure of the film is in zone II.[8,9,60]

[k] Correspondent ICDD available in Appendix B.

At the temperature of 700° C, the adatoms mobility is higher than at room temperature, allowing them to search for more favorable sites (lowest possible energy). Furthermore, it is possible that at this temperature, recrystallization is already active and grain boundaries are mobile. MD simulations of Mg-Al-O thin films were performed at high temperature (not shown here) and it was observed that two separate phases are formed: MgO with some Al in solid solution and amorphous Al_2O_3. As being trapped in the MgO lattice, replacing Mg cations, is not the most favorable thermodynamic situation for the Al cations, they will try to move out, if they have sufficient energy. Unfortunately, due to the fact that the Mg-Al-O thin films are not stable under the TEM beam (the beam energy promotes crystallization), it was not possible to perform HRTEM to testify the phase separation in the films.

Mg-Cr-O

As depositing Mg-Al-O thin films at 300 °C and 500 °C did not result in significant changes of the crystalline structure, the Mg-Cr-O thin films depositions at high temperature were only performed at 700 °C. In figure 8.5 the θ/2θ XRD patterns of the deposited thin films is displayed. For all the deposited thin films with some Cr content, it was noticed a small peak indexed as being the (116) planes from Cr_2O_3 (Rhombohedral, space group R-3c (167)), for $2\theta \approx 54.8°$. Analogous to the case of Mg-Al-O, the amount of M content that can be introduced in the thin film while keeping the crystalline structure increases, as compared to the depositions performed at room temperature. The film with $C_{Cr} = 67$ % still evidence MgO peaks, while at room temperature the thin films becomes XRD amorphous around 60% Cr metal content. Moreover, pure Cr_2O_3 was found to be crystalline with some degree of (006) preferential out-of-plane orientation.

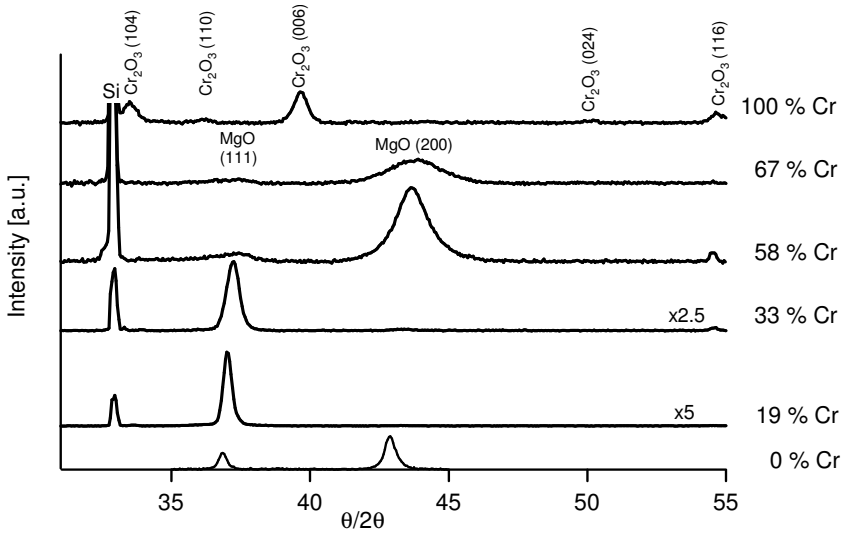

Figure 8.5: Angular XRD patterns of Mg-Cr-O thin films deposited at 700° C. The relevant peak positions from the ICDD pattern for MgO and Cr_2O_3 (Rhombohedral, space group R-3c (167)) are indicated.

8.2. *Post*-Deposition Heat Treatments

When thermodynamic constrains the thin film structure formation, the combination of some of the different studied oxides form, according to phase diagrams, interesting and complex structures, such as spinel's structures. Taking into account that depositions neither at room temperature nor at high temperature provided the required energy to the adatoms species to form such type of structures, a last attempt to achieve those interesting structures was made by post-deposition heat treatments.

Two types of heat treatment were performed. A first set of heat treatments were performed in O_2 atmosphere, with a heating ramp of 1° C/min, dwell time 3h (at 600, 700 and 900° C) and cooling ramp of 2° C/min. The second set of heat-treatments was performed in *in-situ* XRD, in a He atmosphere, varying the heating ramp.

8.2.1. *Ex-Situ* Heat Treatments

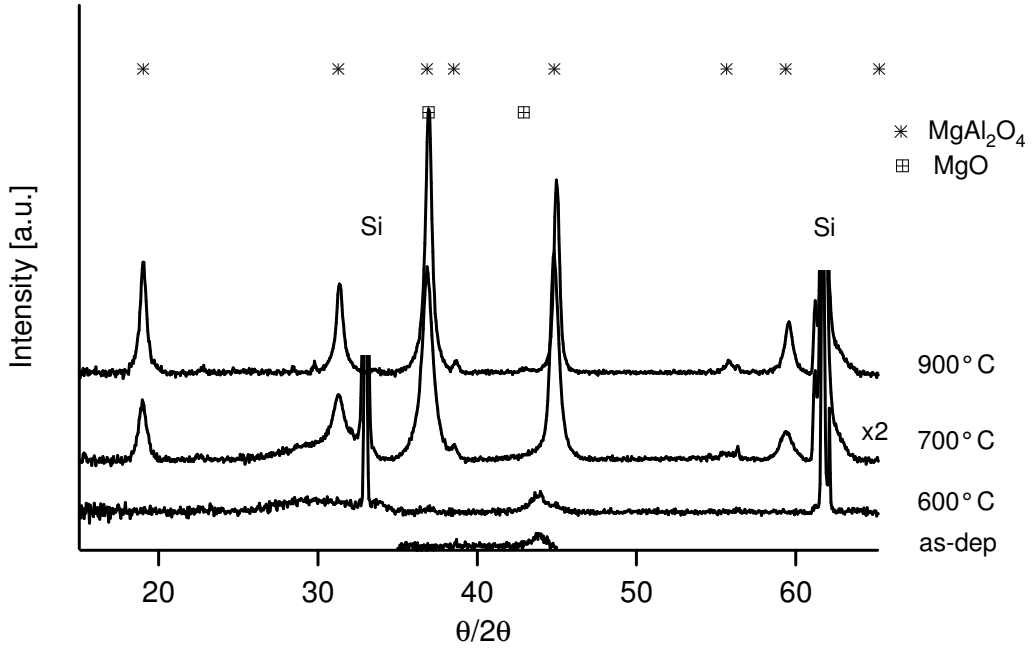

Figure 8.6: Angular XRD patterns of Mg-Al-O thin films with $C_{Al} = 66\ \%$ deposited at 700° C and further annealed in O_2 for 3h, at different temperatures.

The XRD patterns of the Mg-Al-O and Mg-Cr-O thin films deposited at 700 °C and further annealed at several temperatures is shown in figures 8.6 and 8.7, respectively. For the Mg-Al-O films, it was needed to anneal the film at 700°C to obtain the spinel structure. Further increase of the annealing temperature yields an increase of the peaks intensity which indicates an improvement of the crystalline phase of the film. In the case of the Mg-Cr-O films, the spinel structure is formed earlier, at 600 °C. Increasing the temperature to 700 °C improves the crystalline phase of the film. The XRD pattern of the Mg-Cr-O film annealed at 900 °C exhibits less intense peaks that the films annealed at lower temperatures. The reason for this decrease of peaks intensity is not related to the crystallinity of the film, but with the amount of measured film, as the film annealed at 900 °C was partially delaminated.

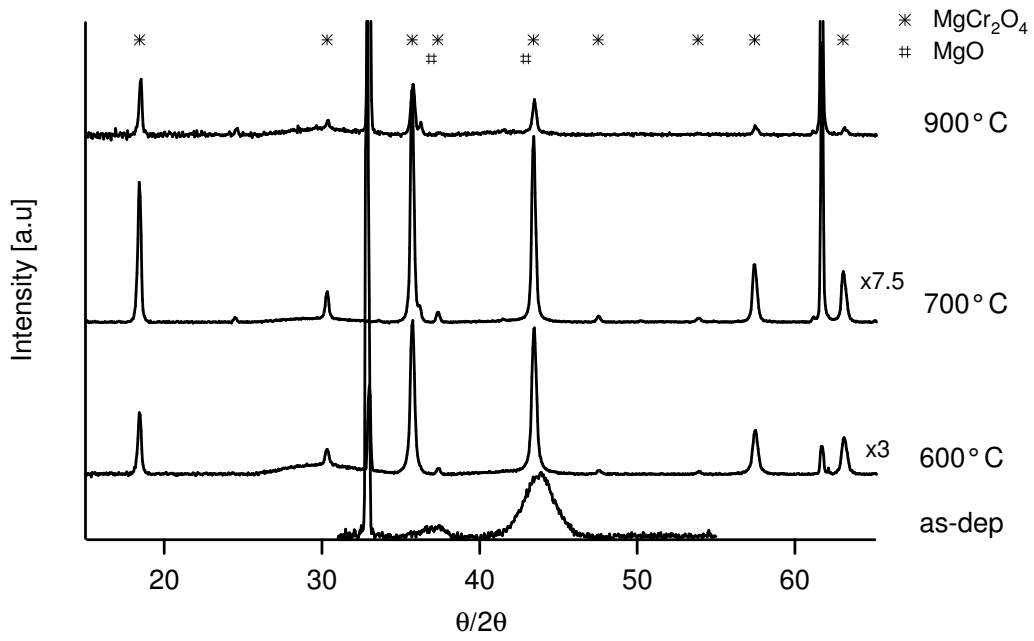

Figure 8.7: Angular XRD patterns of Mg-Cr-O thin films with $C_{Cr} = 67\ \%$ deposited at 700° C and further annealed in O_2 for 3h, at different te mperatures.

The drawback of the *ex-situ* heat treatments is the incapability of following the processes occurring during the heat treatment, as the XRD measurements are performed after the cooling down of the samples. Therefore, *in-situ* heat treatments of the Mg-Al-O films were carried on.

8.2.2. *In-Situ* Heat Treatment

The Mg-Al-O films deposited without intentional substrate heating and at 700 °C, with the chemical composition close to the spinel ($MgAl_2O_4$), were submitted to *in-situ* heat treatments. In figure 8.8 is presented the XRD of the films annealed using an heating ramp of 5 °C/min. The film deposited without intentional substrate heating (figure 8.8a)) crystallizes in two steps, as can be seen more clearly in the summed intensity (upper graph of figure 8.8a)). A first step occurs at ~550 °C and a second step between 750 °C and 800 °C. The obtained crystalline structure is the spinel. In figure 8.8b), can be seen that the (200) MgO phase present in the film deposited at 700°C disappears upon appearance of the spinel phase, indicating that the formation of the spinel structure occurs at the expense of the MgO. Opposite to what was observed for the films deposited at room temperature, the spinel formation happens in only one step at ~750 °C. Furthermore, annealing the film deposited at high temperatures yields to the formation of one more phase of the spinel structure (220) as compared to the film deposited at room temperature.

The fact that the film deposited at room temperature starts to form the spinel structure at temperatures lower than the film deposited at high temperature is related to the crystallization barriers. As discussed previously, the films deposited without intentional substrate heating result in a solid solution where M occupies the octahedral positions along with Mg. In the case of the film deposited at 700 °C, when the content of M is too high to be incorporated in

the film, the mobility is high enough to allow phase separation to occur. This way, the atomic arrangement of the films deposited at low temperature is closer to the spinel configuration, than the atomic arrangement of the films deposited at high temperatures. Consequently, the crystallization barrier for the film deposited at low temperature is lower and therefore it forms the spinel structure at lower temperatures.

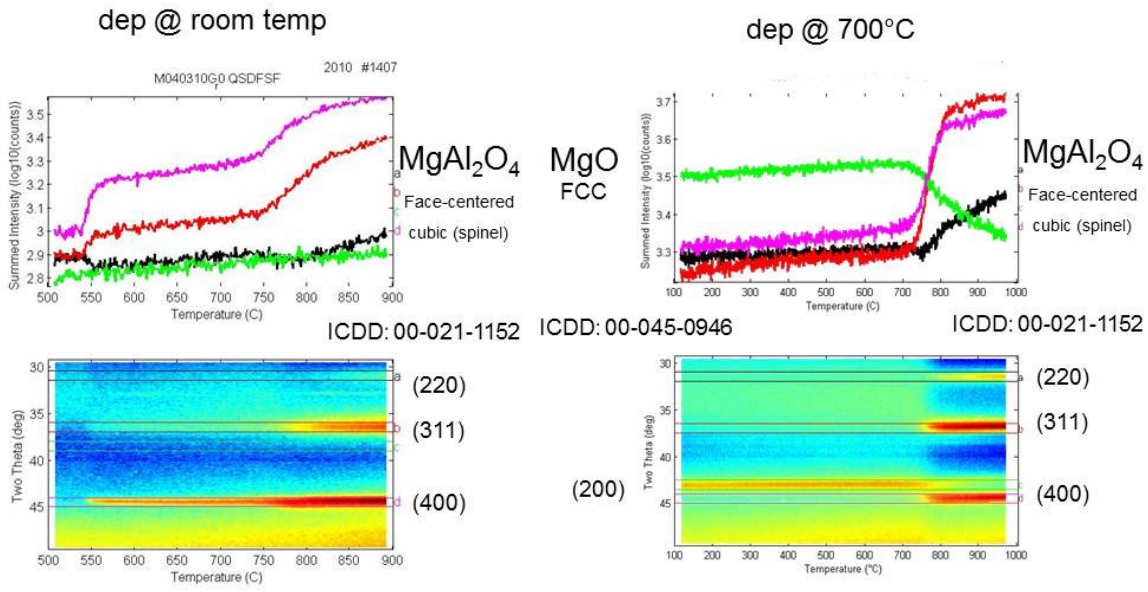

a) 5° C/min b) 5° C:min

Figure 8.8: In-situ XRD of Mg-Al-O films with C_{Al} = 66 % deposited at a) room temperature and b) 700° C and further annealed in He up to 900° C.

The reason behind the two step formation of the spinel structure in the films deposited at room temperature can be interpreted as follows. Giving energy to a system influences its crystallizations in two ways: it gives energy to the atoms which endows them mobility and therefore allowing their diffusion; and provides energy to the system to form a solid state reaction. These two events occur simultaneously. Consequently, when the films are subjected to heat treatment, there is a competition between the de-alloying and solid state reaction between the two phases. The de-alloying or decomposition of the solid solution results from the mobility of the atoms that search for a thermodynamic more favorable site, and brings the reaction partners farther from each other. Thus, although the material starts to react at low temperature, the reaction is hindered by the decomposition of the solid solution. For that reason, the temperature needs to be raised high enough to promote the solid state reaction between the two phases. When the deposition is performed at low temperature, a solid solution is formed and this effect can clearly be seen. On the other hand, if the deposition was performed at high temperature, there was phase separation and the reaction partners are far from each other, which results in only one crystallization step.

Interesting in this context is to notice that the starting point of the first peak depends much stronger on the heating ramp (see lines in figure 8.9) as compared to the second peak. These results show that by changing the heating rate the solid state reaction cannot be strongly influenced, but the diffusion of the species can.

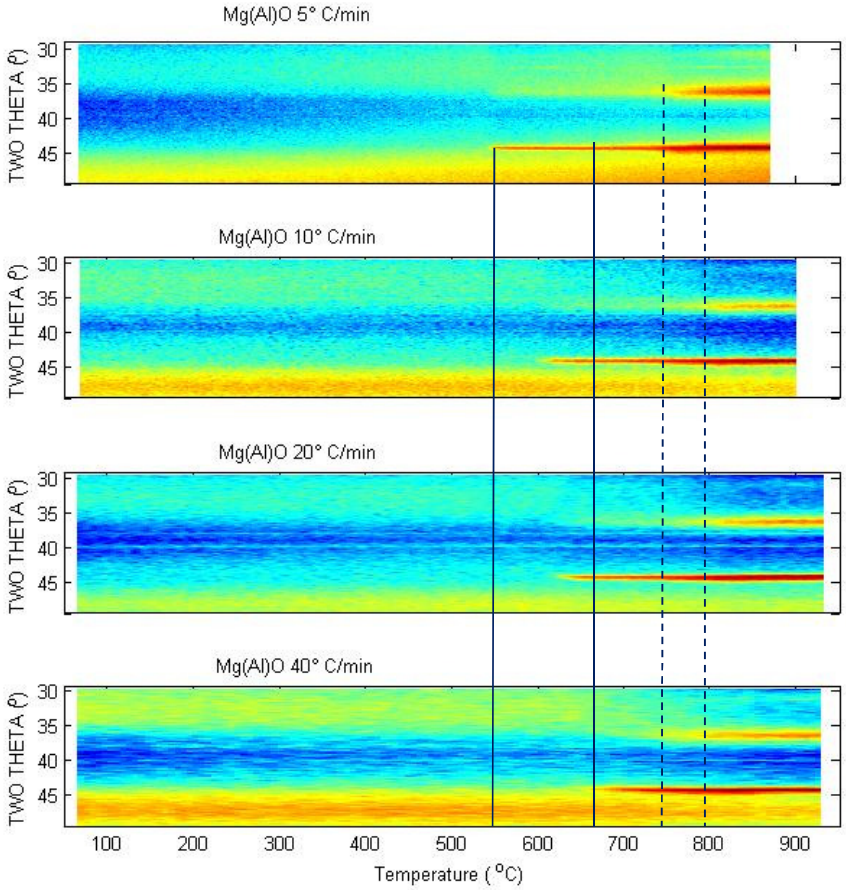

Figure 8.9: In-situ XRD of Mg-Al-O films with $C_{Al} = 66\ \%$ deposited at room temperature further annealed in He up to 950° C with different heating ramps.

It is known that if the structure formation is thermodynamically constrained, it results from the interplay between time and temperature. Hence, in-situ XRD heat treatments at different heating ramps were performed for films deposited at room temperature and at 700°C and are shown in figure 8.9 and 8.10, respectively. Increasing the heating speed of the heat treatments induces a delay in the first step of spinel formation in the film (see figure 8.9). The effect of using different heating ramps is independent on the growth conditions of the film, as the films deposited at high temperatures also see the formation of the spinel phase at the expense of the MgO phase happening at higher temperatures.

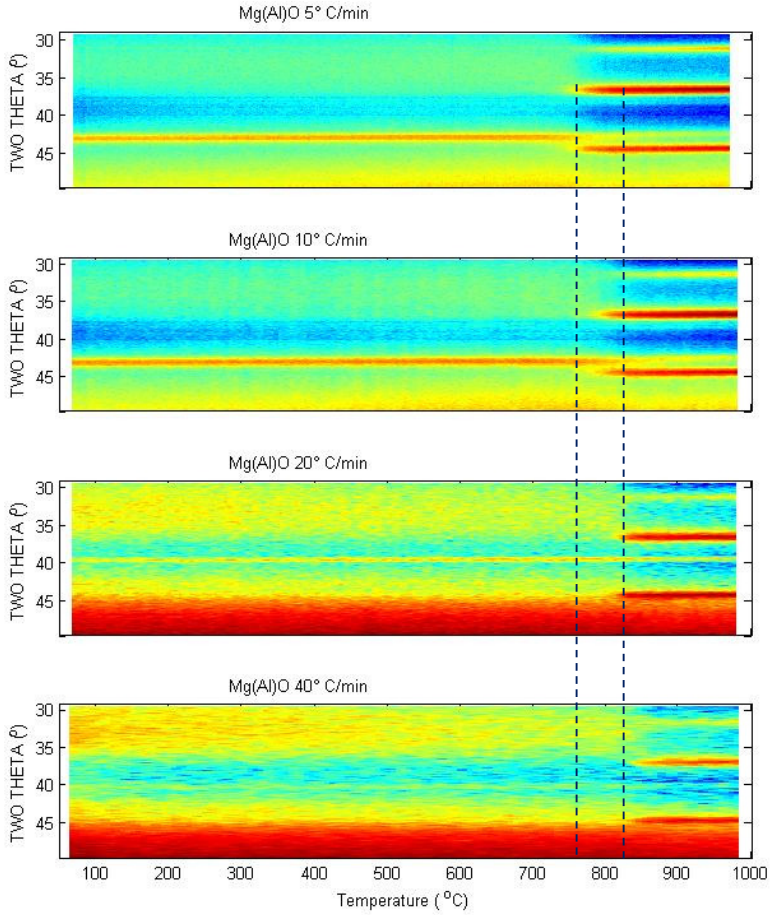

Figure 8.10: In-situ XRD of Mg-Al-O films with $C_{Al} \approx 66$ % deposited at 700 °C further annealed in He up to 950° C with different heating ramps.

References

[1] J. Aarik, A. Kasikov, M. Kirm, S. Lange, T. Uustare, and H. Mandar, in *Optical Materials and Applications*, edited by A. Rosental (2005), Vol. 5946, pp. 94601.

[2] D.L. Smith, *Thin film deposition, principles and practice*. (McGraw-Hill, 1995).

[3] J. Patscheider, N. Hellgren, R. T. Haasch, I. Petrov, and J. E. Greene, Physical Review B **83** (12), 125124 (2011).

[4] G. Gassner, J. Patscheider, P. H. Mayrhofer, S. Sturm, C. Scheu, and C. Mitterer, Tribology Letters **27** (1), 97 (2007).

[5] M. Ohring, *Materials Science of Thin Films, Deposition & Structure*. (Academic Press, 2002).

[6] S. Mraz and J. M. Schneider, Journal of Applied Physics **109** (2), 023512 (2011).

[7] S. Mraz and J. M. Schneider, Journal of Applied Physics **100** (2), 023503 (2006).

[8] P. B. Barna and M. Adamik, Thin Solid Films **317** (1-2), 27 (1998).

[9] I. Petrov, P. B. Barna, L. Hultman, and J. E. Greene, Journal of Vacuum Science & Technology A **21** (5), S117 (2003).

[10] Bob B. He, *Two-Dimensional X-ray Diffraction*, 2009 ed. (John Wiley & Sons, Inc., New Jersey, 1954).

[11] R. Jenkins and R.L. Snyder, *Introduction to X-Ray Powder Dffractometry*, 1996 ed. (John Wiley & Sons, Inc., 1932).

[12] International Tables, Vol. C, pp. 500.

[13] W. Knaepen, PhD thesis, Ghent University, 2010.

[14] D. Frenkel and B. Smith, *Understanding Molecular Simulation*. (Academic Press, 2002).

[15] C. R. A. Catlow, C. M. Freeman, and R. L. Royle, Physica B & C **131** (1-3), 1 (1985).

[16] V. Georgieva, M. Saraiva, N. Jehanathan, O. I. Lebelev, D. Depla, and A. Bogaerts, Journal of Physics D-Applied Physics **42** (6) (2009).

[17] D. Bacorisen, R. Smith, J. A. Ball, R. W. Grimes, B. P. Uberuaga, K. E. Sickafus, and W. T. Rankin, Nuclear Instruments & Methods in Physics Research Section B-Beam Interactions with Materials and Atoms **250**, 36 (2006).

[18] K. J. W. Atkinson, R. W. Grimes, M. R. Levy, Z. L. Coull, and T. English, Journal of the European Ceramic Society **23** (16), 3059 (2003).

[19] P. R. Willmott, Progress in Surface Science **76** (6-8), 163 (2004).

[20] J. R. Groves, P. N. Arendt, S. R. Foltyn, R. F. DePaula, C. P. Wang, and R. H. Hammond, Ieee Transactions on Applied Superconductivity **9** (2), 1964 (1999).

[21] R. Huhne, C. Beyer, B. Holzapfel, C. G. Oertel, L. Schultz, and W. Skrotzki, Crystal Research and Technology **35** (4), 419 (2000).

[22] R. T. Brewer, J. W. Hartman, J. R. Groves, P. N. Arendt, P. C. Yashar, and H. A. Atwater, Applied Surface Science **175**, 691 (2001).

[23] M. P. Chudzik, R. E. Koritala, Z. P. Luo, D. J. Miller, U. Balachandran, and C. R. Kannewurf, Ieee Transactions on Applied Superconductivity **11** (1), 3469 (2001).

[24] R. E. Koritala, M. P. Chudzik, Z. P. Luo, D. J. Miller, C. R. Kannewurf, and U. Balachandran, Ieee Transactions on Applied Superconductivity **11** (1), 3473 (2001).

[25] P. Ghekiere, S. Mahieu, R. De Gryse, and D. Depla, Thin Solid Films **515** (2), 485 (2006).

[26] P. Ghekiere, S. Mahieu, G. De Winter, R. De Gryse, and D. Depla, Journal of Crystal Growth **271** (3-4), 462 (2004).

[27] P. Ghekiere, S. Mahieu, G. De Winter, R. De Gryse, and D. Depla, Thin Solid Films **493** (1-2), 129 (2005).

[28] P. Ghekiere, S. Mahieu, G. De Winter, R. De Gryse, D. Depla, and O. I. Lebedev, Texture and Anisotropy of Polycrystals Ii **105**, 433 (2005).

[29] P. Ghekiere, PhD, Ghent University, 2007.
[30] M. Beckers, N. Schell, R. M. S. Martins, A. Mucklich, and W. Moller, Journal of Vacuum Science & Technology A **23** (5), 1384 (2005).
[31] K. Koski, J. Holsa, and P. Juliet, Thin Solid Films **339** (1-2), 240 (1999).
[32] M. Sridharan, M. Sillassen, J. Bottiger, J. Chevallier, and H. Birkedal, Surface & Coatings Technology **202** (4-7), 920 (2007).
[33] P. Hones, M. Diserens, and F. Levy, Surface & Coatings Technology **120**, 277 (1999).
[34] S. Hong, E. Kim, D. W. Kim, T. H. Sung, and K. No, Journal of Non-Crystalline Solids **221** (2-3), 245 (1997).
[35] E. Aubry, P. Miska, J. Gigleux, A. Mezin, V. Demange, and A. Billard, Surface & Coatings Technology **202** (20), 4980 (2008).
[36] F. M. Meng and Z. Q. Sun, Applied Surface Science **255** (13-14), 6715 (2009).
[37] R. J. Gaboriaud, F. Pailloux, P. Guerin, and F. Paumier, Thin Solid Films **400** (1-2), 106 (2001).
[38] D. Pamu, K. Sudheendran, M. G. Krishna, and K. C. J. Raju, Journal of Vacuum Science & Technology A **26** (2), 185 (2008).
[39] K. Prabakar, A. Park, N. Cho, W. I. Lee, C. K. Hwangbo, J. G. Lee, and C. Lee, Vacuum **82** (12), 1367 (2008).
[40] S. Venkataraj, O. Kappertz, C. Liesch, R. Detemple, R. Jayavel, and M. Wuttig, Vacuum **75** (1), 7 (2004).
[41] Bloss F. Donald, *Crystallography and crystal chemistry : an introduction*. (New York (N.Y.) : Holt, Rinehart and Winston, 1971).
[42] R. D. Shannon, Acta Crystallographica Section A **32** (SEP1), 751 (1976).
[43] C. L. Rohrer and G. S. Rohrer, Chemistry of Materials **6** (4), 501 (1994).
[44] S. Vyas, R. W. Grimes, D. J. Binks, and F. Rey, Journal of Physics and Chemistry of Solids **58** (10), 1619 (1997).
[45] M. Saraiva, V. Georgieva, S. Mahieu, K. Van Aeken, A. Bogaerts, and D. Depla, Journal of Applied Physics **107** (3), 034902 (2010).
[46] R. Kim, Y. Kim, Y. U. Lee, H. J. Kim, and J. W. Park, Surface & Coatings Technology **161** (1), 52 (2002).
[47] D. Fritsch, H. Schmidt, and M. Grundmann, Applied Physics Letters **88** (13) (2006).
[48] S. Choopun, R. D. Vispute, W. Yang, R. P. Sharma, T. Venkatesan, and H. Shen, Applied Physics Letters **80** (9), 1529 (2002).
[49] P. Scherrer, Nachr. Ges. Wiss. Göttingen **26**, 98 (1918).
[50] in *http://mathworld.wolfram.com/KeplerConjecture.html*.
[51] T. C. Hales, Annals of Mathematics **162** (3), 1065 (2005).
[52] W. N. Man, A. Donev, F. H. Stillinger, M. T. Sullivan, W. B. Russel, D. Heeger, S. Inati, S. Torquato, and P. M. Chaikin, Physical Review Letters **94** (19) (2005).
[53] Y. Jiao, F. H. Stillinger, and S. Torquato, Physical Review E **79** (4) (2009).
[54] S. Torquato and Y. Jiao, Nature **460** (7257), 876 (2009).
[55] S. Torquato and Y. Jiao, Physical Review E **80** (4) (2009).
[56] Z. Nussinov, Physics **1**, 40 (2008).
[57] H. Reiss and A. D. Hammerich, Journal of Physical Chemistry **90** (23), 6252 (1986).
[58] W. G. Hoover and F. H. Ree, Journal of Chemical Physics **49** (8), 3609 (1968).
[59] J. G. Berryman, Physical Review A **27** (2), 1053 (1983).
[60] S. Mahieu, P. Ghekiere, D. Depla, and R. De Gryse, Thin Solid Films **515** (4), 1229 (2006).
[61] V. Georgieva, A. F. Voter, and A. Bogaerts, Cryst. Growth Des. **11** (6), 2553 (2011).

[62] D. Dimos, P. Chaudhari, J. Mannhart, and F. K. Legoues, Physical Review Letters **61** (2), 219 (1988).
[63] U. Hannemann, S. Melcher, V. Neu, S. Fahler, B. Holzapfel, and L. Schultz, Ieee Transactions on Magnetics **39** (5), 2726 (2003).
[64] G. L. Messing, S. Trolier-McKinstry, E. M. Sabolsky, C. Duran, S. Kwon, B. Brahmaroutu, P. Park, H. Yilmaz, P. W. Rehrig, K. B. Eitel, E. Suvaci, M. Seabaugh, and K. S. Oh, Critical Reviews in Solid State and Materials Sciences **29** (2), 45 (2004).
[65] S. Mahieu, G. Buyle, P. Ghekiere, S. Heirwegh, R. De Gryse, and D. Depla, Thin Solid Films **515** (2), 416 (2006).
[66] S. Mahieu, P. Ghekiere, G. De Winter, S. Heirwegh, D. Depla, R. De Gryse, O. I. Lebedev, and G. Van Tendeloo, Journal of Crystal Growth **279** (1-2), 100 (2005).
[67] H. Hidalgo, E. Reguzina, E. Millon, A. L. Thomann, J. Mathias, C. Boulmer-Leborgne, T. Sauvage, and P. Brault, Surface & Coatings Technology **205** (19), 4495 (2011).
[68] Tao Bowan, Zhang Ning, Zhang Fei, Xia Yudong, Feng Xiao, Xue Yan, Zhao Xiaohui, Xiong Jie, and Li Yanrong, Ieee Transactions on Applied Superconductivity **21** (3) (2011).
[69] Cho Jung-Min, Lee Kyoung-Ho, Cheon Chae Il, Cho Nam In, and Kim Jeong Seog, Journal of the European Ceramic Society **30** (2) (2010).
[70] K. Kishor Kumar, P. M. Raole, P. A. Rayjada, N. L. Chauhan, and S. Mukherjee, Surface & Coatings Technology **205**, S187 (2011).
[71] G. Z. Radnoczi, T. Seppanen, B. Pecz, L. Hultman, and J. Birch, Physica Status Solidi a-Applications and Materials Science **202** (7), R76 (2005).

D. Composition-Structure-Property Relations

Film properties and functionality depend crucially on the film chemical composition and on crystallinity, i.e. on whether a film is crystalline or amorphous. The nature of each element (i.e. size and electronic configuration) determines the type and strength of the bonds that it forms with its neighboring atoms influencing, for instance, the mechanical strength of the film. At the same time, amorphous films are in general less dense and thus exhibit inferior mechanical strength as compared to their crystalline counterparts. On the other hand, due to the absence of grain boundaries, amorphous films are less prone to diffusion, chemical attack oxidation and corrosion.[1] Furthermore, the lack of long-range order results in isotropic properties, which is frequently not the case for crystalline films. The combination of amorphous and crystalline structure in the same film can also be beneficial. This is the case in the so called nanocomposite films in which control of the relative size and separation of nanosized crystals embedded in an amorphous matrix can result in films with superior mechanical, electrical and tribological performance.[2,3]

In the previous section the effect of deposition conditions on the chemical composition, crystallinity and microstructure of Mg-M-O films was investigated. Building upon this knowledge, in the present section the composition-structure-property relations are elucidated. Investigations are focused on the mechanical, optical, and electrical properties, as well as on surface topography and energetics. It has to be pointed out once again here that the main goal of this thesis is to understand the largely unknown atomistic mechanisms that determine the growth and microstructure of Mg-M-O films. The other functional properties are merely considered in order to highlight how composition and crystallinity can affect these properties. An exhaustive and detailed study of these properties and the performance of the thin films lie well beyond the scope of this thesis.

In section 9 the experimental techniques used to characterize the films are described. The measured properties and their dependence on composition and crystallinity are presented in section 10 and the effect of stoichiometry is decoupled from the influence of crystallinity.

9. Experimental Techniques

9.1. Nanoindentation

One of the most common ways to determine mechanical properties of films is by using nanoindentation. The nanoindenter is a high-resolution nanomechanical test instrument capable of performing both indentation and scratch test. In indentation mode, the instrument is a load-controlled displacement-sensitive device. An indenter tip - for the present thesis a Berkovich indenter (triangle pyramid) was used - is driven into and subsequently withdrawn from the sample under investigation by increasing the applied force. The applied load (P) and the penetration depth (h) into the sample are continuously monitored. The hardness (H) is then

given by $H = P^{\max}/A$, where P^{max} denotes the maximum load and A the projected indentation area, which is calculated based on h and the shape of the indenter. The other property routinely determined by nanoidentation is the elastic modulus (or Young's modulus). In order to determine hardness and elastic properties of a material using load and depth sensing techniques, several methods have been developed. The contact area and the mechanical properties are determined from the data of one complete cycle of loading and unloading. As an example, figure 9.1 depicts a complete cycle. The unloading data is treated assuming that the displacement recovered is largely elastic. Then, the hardness and Young's modulus can be determined by solving the elastic contact problem.[4] In this work, the hardness and Young's modulus were calculated using the formalism developed by Oliver and Pharr.[5] The slope of the curve *dh/dP* upon unloading is indicative of the stiffness (*S*) of the contact (see red line in figure 9.1). The reduced Young modulus ε_r can be calculated,

$$\varepsilon_r = \frac{\sqrt{\pi}}{2}\frac{S}{\sqrt{A}}, \tag{9.1}$$

From ε_r, the young Modulus of the film can be determined,

$$\frac{1}{\varepsilon_r} = \frac{1-\upsilon^2}{E} + \frac{1-\upsilon_i^2}{E_i}, \tag{9.2}$$

where υ_i and E_i denote the Poisson's ration and Young's modulus of the indenter, respectively, and υ the Poisson's ratio of the film.

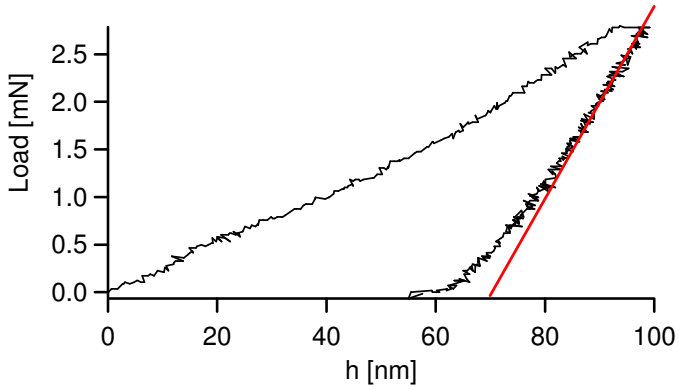

Figure 9.1: Obtained curve from a nanoindentation test. The line represents the characteristic line for the initial unload, which represents the stiffness of the contact.

The nanoindentation measurements were carried out at Vlaamse Instelling voor Technologisch Onderzoek (VITO)[1] in the frame of the SBO project 60030, and not by the author. Films with thicknesses of ~1 µm were indented at a depth of 100 nm in order to eliminate any influence of the substrate on the mechanical properties.

[1] Contact person: Dr. R. Persoons.

9.2. VUV-UV-VIS-NIR Spectrophotometry

A spectrophotometer is a device that measures intensity of a light source as a function of the wavelength. The interaction of the electromagnetic radiation (light) with the sample under investigation causes changes in the light intensity which depends on the optical properties of the sample. Measurements can be carried either in reflection or in transmission mode. In the latter case, a light beam is directed to the sample surface at normal incidence conditions and the intensity of the beam transmitted through the sample is measured. Typically double beam spectrophotometers are used, in which a beam splitter separates the light into two beams; one serves as a reference beam, while the other one is transmitted through the sample. The transmitted beam is then guided to the monochromator which separates light into its constituent wavelengths the intensity of which is measured by a photodetector (silicon photodiodes).

A typical feature of the transmittance spectrum is the existence of interference fringes. The refractive index and the extinction coefficient of the sample, as well as the sample thickness can be extracted from the transmission measurements by the amplitude and the relative position of the fringes. Different methods to calculate the refractive index based on the interference fringes have been suggested in the literature.[6] In this work, the envelop method (also known as Swanepoel method[7]) has been used by means of the Essential Macleod software.

Another quantity that can be determined from the spectrophotometry measurements is the absorption coefficient α. The spectral dependence of α can be used to calculated the magnitude of the fundamental band gap. The relation between the absorption coefficient and the incident photon energy ($h\nu$) can be written as

$$(\alpha h\nu)^{1/n} = A(h\nu - E_g), \tag{9.3}$$

where A is a constant, E_g denotes the band gap of the material and the exponent n depends on the type of transition. For a direct allowed transition, n is equal to 1/2. In figure 9.2 is presented the $(\alpha h\nu)^2$ vs. $h\nu$ for the pure MgO film. Extrapolating the linear part of the graphic to the $h\nu$ axis, the direct band gap is obtained from the interception on the $h\nu$ axis, resulting in a band gap of approximately 6.7 eV for the MgO film.

The optical transmission measurements of the Mg-M-O films deposited in MgF_2 were performed with a double beam – double monochromator UV-VIS-NIR spectrophotometer (Varian Cary 500). VUV transmission measurements were performed at the RD&M research group at TU Delft (The Netherlands). The experimental setup consists of an ARC type DS-775 deuterium discharge lamp, a monochromator (ARC, model VM502 with 1200 grooves/mm blazed at 250 nm with Al/MgF_2 coating for high reflectivity in the VUV region) and an EMI 9426 photomultiplier tube with MgF_2 window. The VUV measurements were performed by Prof. Dr. P. Smet.

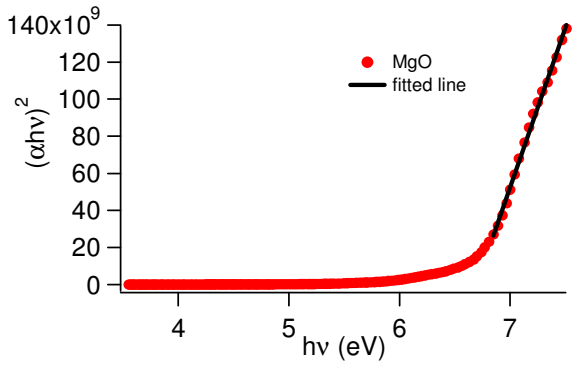

Figure 9.2: Plot to calculate the direct allowed transition for MgO thin film.

9.3. Impedance Spectroscopy

The interaction of electromagnetic wave with matter in the frequency range between 10^{-6} and 10^{12} Hz is the domain of broadband dielectric spectroscopy (BDS). In this extended range, molecular and collective dipolar fluctuations, charge transport and polarization effects at inner and outer boundaries take place and determine the dielectric properties of the material. Therefore, BDS can give information about the dynamics of bound (dipoles) and mobile charge carriers.[8]

At frequencies (ω) below 10^8 Hz, a dielectric sample is view as a complex electrical impedance ($Z^*(\omega)$), expressed in terms of the Resistance ($R(\omega)$) and Capacitance ($C(\omega)$), which are frequency dependent properties. These measurements are typically performed using impedance/admittance analysers or automatic bridges. The complex dielectric permittivity is defined as,[9]

$$\varepsilon^*(\omega) = \varepsilon'(\omega) - i\varepsilon''(\omega) = \frac{C^*(\omega)}{C_0}, \tag{9.4}$$

where $C^*(\omega)$ is the complex capacitance and C_0 is the vacuum capacitance respectively. Applying a sinusoidal electric voltage $V^*(\omega) = V_0 e^{i\omega t}$ to the sample, the dielectric permittivity ($\varepsilon^* = \varepsilon' + j\varepsilon''$) can be derived by measuring the complex impedance $Z^*(\omega)$ of the sample as follows:

$$\varepsilon^*(\omega) = \frac{1}{i\omega\varepsilon_0 Z^*(\omega) C_0}, \tag{9.5}$$

where $Z^*(\omega) = V^*(\omega)/I^*(\omega)$, and $I^*(\omega)$ denotes the complex current through the capacitor (sample).

In this work, the dielectric permittivity was measured using the model capacitance (C_p) and resistance (R_p) in parallel, allowing the calculation of the real (ε') and imaginary (ε'') part of the complex permittivity by the following equations:

$$\varepsilon'(\omega) = C_p(\omega)\frac{d}{A\varepsilon_0}, \tag{9.6}$$

$$\varepsilon''(\omega) = \frac{d}{\varpi R_p(\omega) A\varepsilon_0}, \tag{9.7}$$

where d denotes the sample thickness, A the electrode area and ε_0 the vacuum permittivity (8.854×10^{-12} Fm).

From Maxwell´s equations the complex conductivity is defined as

$$\sigma^*(\omega) = \sigma'(\omega) + i\sigma''(\omega) = i\omega\varepsilon_0\varepsilon(\omega)^*, \tag{9.8}$$

Where the real part ($\sigma'(\omega) = \omega\varepsilon_0\varepsilon''(\omega)$) is commonly named ac conductivity (σ_{AC}). If the sample in study presents high dc conductivity, the dielectric spectroscopy study becomes more complicated because of the need to take into account the effect of this contribution. The dc conductivity σ_0 contributes, in the frequency domain, to the imaginary part of the complex dielectric permittivity as $\sigma_0/(\varepsilon_0\omega)$.

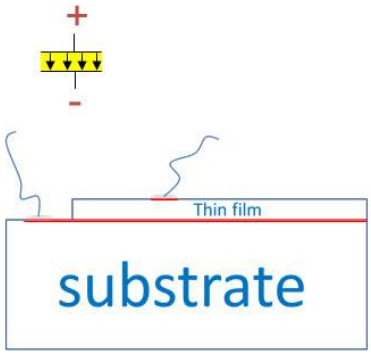

Figure 9.3: Schematic representation of the sample preparation for the dielectric tests.

The impedance spectroscopy measurements were performed for the Mg-M-O films deposited on (111) Si doped with B after cleaning the substrate with HF. The measurements were performed in the frequency range of 40 to 110 MHz, measuring in the C_p-R_p configuration at temperatures between 100 and 400 K. Electrical contacts to perform the electrical measurements were made using silver paint. A contact was made on the film, and a second contact on a non-coated part of the substrate, as illustrated in figure 9.3. During the electrical measurements, the samples were maintained in a helium atmosphere in order to improve the heat transfer and eliminate moisture. These measurements were performed at Grupo de Sólidos Não Cristalinos e Sistemas Desordenados, Aveiro University (Portugal).

9.4. Contact Angle Measurements

The interactions occurring at the interface between two phases are results of various intermolecular forces. It is commonly accepted to differentiate between dispersive (non-polar) and polar forces. This approach results in the separation of the surface energy into a

dispersive and a polar component. A widely used technique to calculate the surface energy is based on measuring the contact angle of a liquid drop on the solid surface. The interaction between the drop and the solid surface is described by Young's equation. The Young's equation describes the balance of the forces at three-phase boundary in equilibrium conditions on an ideal, flat and homogeneous solid surface (see Equation 2.7). In order to be able to determine the surface energy of the solid through a contact angle measurement, the interfacial energy is estimated in terms of the liquid surface energy and the surface energy of the solid. The polar and dispersive components of the surface energy was calculated by the Owens-Wendt method (or extended Fowkes),[10] by means of known values for the dispersive and polar surface energy of the three used liquids.[11] From the measured contact angle (θ) of the liquid on the surface and the known surface energy properties of the liquid (the polar γ_l^p and the dispersive γ_l^d components) the surface energy properties of the substrate can be calculated. By plotting $\gamma_l(1+\cos\theta)/(2\gamma_l^d)^{1/2}$ as a function of $(\gamma_l^p/\gamma_l^d)^{1/2}$ for the different measured liquids, and fitting a line through the points, the polar γ_s^p and the dispersive γ_s^d component of the film surface energy can be calculated as follows,

$$m = \sqrt{\gamma_s^p}\ , \tag{9.9}$$

$$b = \sqrt{\gamma_s^d}\ , \tag{9.10}$$

with m and b the constants from the linear fitted equation : y = mx + b.

Contact angle measurements were performed using OCA 15^+ equipment from Dataphysics equipped with a CCD camera, applying the sessile drop method with three liquids: diiodomethane, ethylene glycol and mercury. These liquids were chosen in order to cover a wide range in polar/dispersive ratio, in order to improve the accuracy of the method.

The contact angle tests were carried out at VITO[m] in the frame of the SBO project 60030, and not by the author.

9.5. Atomic Force Microscopy

The atomic force microscopy (AFM) is a high resolution type of scanning probe microscopy. The AFM consists of a cantilever with a sharp tip (probe) at the end of the cantilever. The tip is used to scan the sample surface. When the tip is brought close to the sample surface, forces between the tip and the sample surface lead to deflection of the cantilever according to the Hooke's law. The magnitude of the deflection depends on the type of forces between the sample surface atoms and the tip, e.g. van der Waals, electrostatic forces and magnetic forces.

The measurement of the cantilever deflection is done by a laser light from a solid state diode, which is reflected off the back of the cantilever and collected by a position sensitive detector. The detector consists of two closely spaced photodiodes whose output signal is collected by a differential amplifier. Angular displacement of the cantilever results in one photodiode

[m] Contact person: Dr. R. Persoons.

collecting more light than the other photodiode, producing an output signal (the difference between the photodiode signals normalized by their sum) which is proportional to the deflection of the cantilever.

The AFM was used to investigate the surface roughness of the Mg-Al-O films. Similar to the nanoindentation and contact angle tests, AFM measurements were performed at VITO[n] in the frame of the SBO project 60030, and not by the author.

[n] Contact person: Dr. R. Persoons.

10. Functional Properties

10.1. Experimental Observations

The hardness of the Mg-*M*-O films as a function of *M* metal ratio is shown in figure 10.1a). The pure MgO film has a hardness of ~4 GPa, which is lower than the values reported in literature.[12] For all Mg-*M*-O systems, the hardness of the films increases upon incorporation of M, up to a M metal content of ~30%. For *M* content higher than ~30%, an increase of the M content either does not influence significantly the hardness of the films (Mg-Al-O and Mg-Cr-O) or leads to a decrease of the films hardness (Mg-Ti-O, Mg-Zr-O and Mg-Y-O). In the case of the Al_2O_3 and Y_2O_3, the hardness of the studied films is similar to the values reported in literature,[13,14] while for the other M oxides the values encountered in this work are lower than the reported ones.[12,15-17]

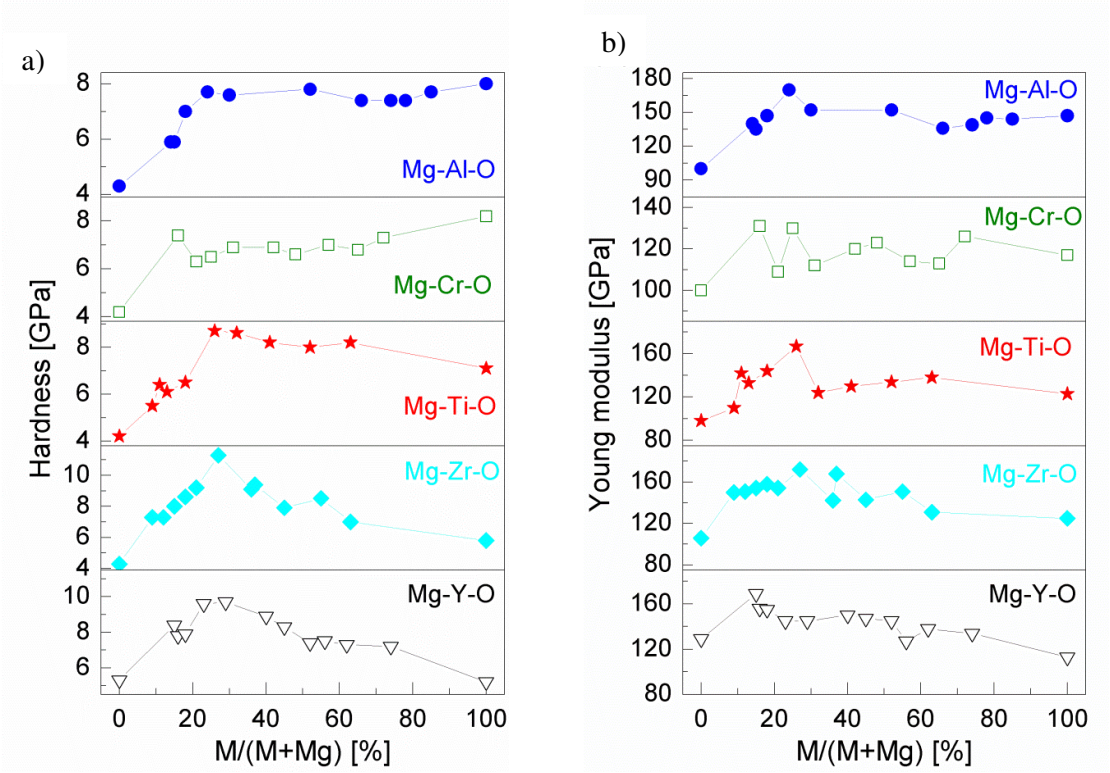

Figure 10.1: a) Hardness and b) Young Modulus of the deposited Mg-*M*-O films as a function of the C_M.

The Young modulus of the Mg-*M*-O films as a function of C_M is illustrated in figure 10.1b). Although the Young modulus is an intrinsic property of the material, the similarity of behavior between the hardness and Young modulus in the Mg-*M*-O films is evident.

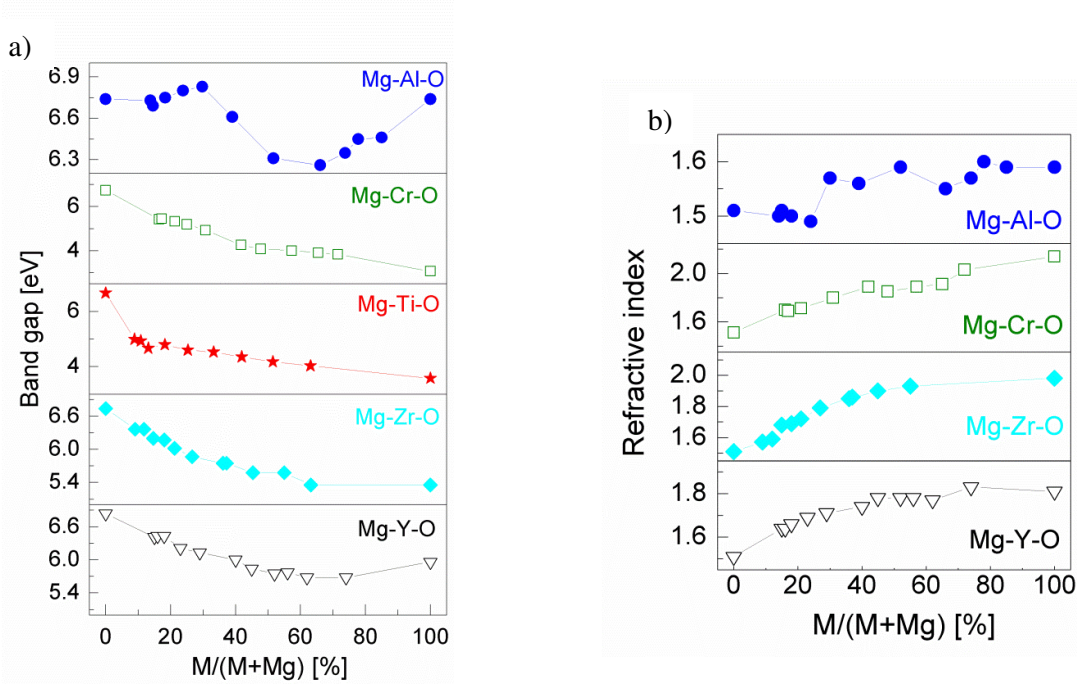

Figure 10.2: a) Band gap and b) refractive index at λ = 550 nm of the deposited Mg-*M*-O films as a function of the C_M.

In figure 10.2a) the band gap as a function of the *M* metal ratio for the Mg-*M*-O films can be seen. The band gap of the pure MgO is 6.74 eV, being considerably lower when compared with reported values from other authors (7.8 eV).[18] Adding a M metal to MgO influences differently the band gap depending on the M element. The band gap of the Mg-Al-O films can be divided in three regions. Starting from pure MgO and up to a C_{Al} ~30%, the band gap of the films is approximately the same as the pure MgO. Increasing the C_{Al} in the films up to 60% leads to a decrease of the band gap (to 6.2 eV). Further increase of the Al induces a progressively increase of the band gap, reaching for the Al_2O_3 film the same value as the pure MgO. The band gap of the Mg-Cr-O films decreases upon increase of the Cr metal content. In the Mg-Cr-O series, two regions with different behaviors can be observed separated at C_{Cr} ~30%. On the contrary to all the other systems, adding a small amount of Ti (C_{Ti} ~9%) to MgO yields a significant decrease in the band gap (from 6.74 to 5 eV), while further increase of the Ti content induces a decrease of the band gap up to the pure TiO_2 film (3.57 eV) at a slower rate. The band gap behavior of the Mg-Zr-O films up to a C_{Zr} of 60% is inversely proportional to the increase of the Zr content, while higher content of Zr results in a film with the same band gap as the pure ZrO_2 (5.36 eV). The Mg-Y-O films have a similar behavior as the Mg-Zr-O films, being the band gap of the Y_2O_3 slightly higher (5.96 eV). The obtained values for the pure oxides are in good agreement with the literature.[18-22]

The refractive index (for λ = 550 nm) of the Mg-M-O films as a function of the composition is plotted in figure 10.2b). The refractive index of the pure MgO is 1.51, which is in good agreement with values reported by other authors.[23] The addition of Al to MgO up to C_{Al} ~30% does not influence the refractive index of the film. For this specific Al concentration, an

increase in the refractive index is observed. Further increase of the Al content in the film (from C_{Al} ~30% on) does not influence significantly the refractive index, being the value approximately the same as for Al_2O_3 (n=1.6). The refractive index of the Al_2O_3 is in good agreement with other values reported in the literature.[24] Adding Cr to the MgO results in a gradually increase of *n*, proportional to the increase of C_{Cr} in the films. The *n* of Cr_2O_3 (2.14) is in good agreement with the values reported in literature.[25] In the case that Zr or Y is added to MgO, an increase of C_M also yields an increase in n. However, the behavior of n as a function of composition changes for C_M ~ 40%. The values reported in the literature for pure ZrO_2 and Y_2O_3 are comparable with the obtained ones (1.81 and 1.98, respectively).[26,27]

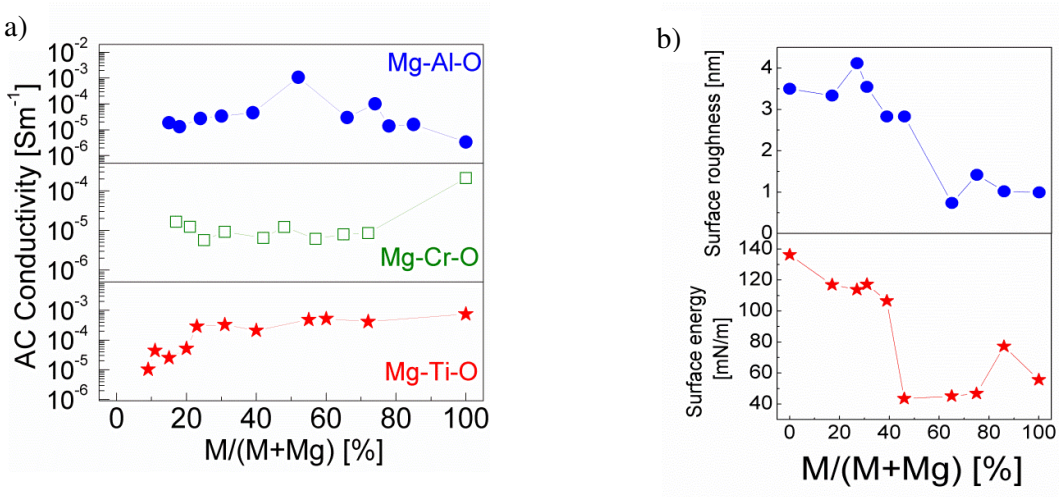

Figure 10.3: a) AC conductivity at 1 MHz and 300 K of the deposited Mg-*M*-O films as a function of C_M. b) Surface roughness and energy of the Mg-Al-O films as a function of C_{Al}.

Figure 10.3a) shows the AC conductivity (σ_{AC}) as a function of C_M for the Mg-Al-O, Mg-Cr-O and Mg-Ti-O films, at 300 K and at a fixed frequency of 1 MHz. The conductivity of the pure MgO film is not shown. Probably due to its high resistivity and chemical sensibility, the results obtained are not reliable. Increasing the concentration of Al in the films results in an increase of the σ_{AC} up to C_{Al} = 50% (~10^{-3}), while further increase of C_{Al} yields a decrease of the σ_{AC} (up to ~10^{-6}). The σ_{AC} of the Mg-Cr-O films is hardly influenced (~10^{-5}), having the pure Cr_2O_3 a higher conductivity (~10^{-4}) than the mixed oxides. Adding Ti to the MgO films, up to C_{Ti} = 25% results in an increase of the σ_{AC}, from ~10^{-5} up to ~10^{-3}. Further increase of Ti content in the films does not influence significantly the σ_{AC}.

The surface energy and roughness of the Mg-Al-O films as a function of the C_{Al} is depicted in figure 10.3b). Both properties exhibit two distinct regions. Beginning in pure MgO up to C_{Al} = 40%, the surface energy has a high value without significant deviation. Afterwards, a significant drop takes place from C_{Al} = 40 to 45%. A second region, with low values of surface energy, goes from C_{Al} = 55% up to pure Al_2O_3. The surface roughness of the Mg-Al-O films follows the same trend as the surface energy, with the difference that the jump from high surface roughness values to low happens between C_{Al} = 45 and 60%.

10.2. Influence of Chemical Composition and Crystallinity

From the results presented in section 10.1 is evident that the films properties do not exhibit a linear behavior as a function of the film composition. At the same time, it is known that besides the composition, the crystallinity also influences the film properties. Therefore, the properties were plotted as a function of the films crystallinity, as presented in figure 10.4. As the Mg-M-O films undergo a transition from crystalline-to-amorphous, several of the films have the same value of crystallinity (zero), which turns difficult to observe the properties behavior, when the films are amorphous.

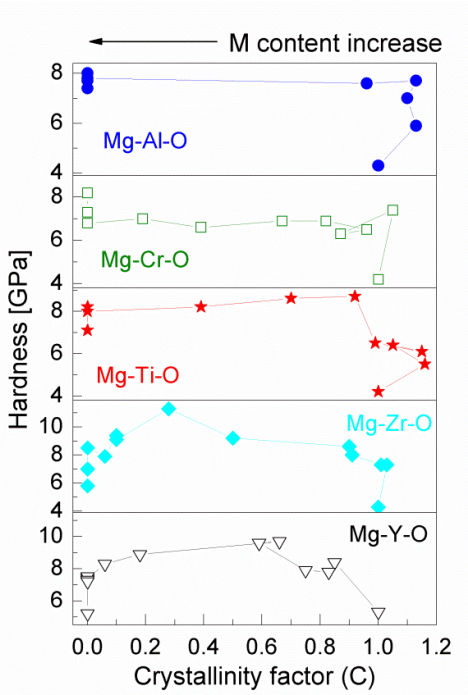

Figure10.4: Hardness of the Mg-M-O films as a function of its crystallinity.

In a previous section (6.2.3), a correlation between the crystallinity and the composition was presented, which enables us to plot the properties of the Mg-M-O films as a function of the packing density (figures 10.5 to 10.7). By using the packing density it is possible to decouple the influence of the crystallinity from the influence of the composition, distinguishing the regions and materials where the composition (crystallinity) has a dominant influence in the properties of the films.

Within the crystalline and transition region (for packing density higher than 0.495), an increase of the hardness with the decrease of the packing density is observed (see figure 10.5 a)). We have shown that the crystallite size of the Mg-M-O films decreases with the increase of the M metal content (see chapter 7). Furthermore, it was previously demonstrated (chapter 6) that within the packing density range of 0.495 to 0.7 the films are crystalline or nanocrystalline. Therefore, an increase of the hardness with the decrease of the crystallite size is demonstrated in agreement to the Hall-Petch relation. For films with packing density lower than 0.495 (i.e. within the amorphous region), the hardness behavior follows the rule of

mixtures, meaning that there is a linear relation between the hardness values and the chemical composition of the films.

In figure 10.5b) the Young modulus of the films as a function of the packing density is presented. With the exception of the Mg-Cr-O system, in all other Mg-M-O systems behavior of the Young modulus resembles that of the hardness. In the case of the Mg-Cr-O, there is no evident distinction in two regimes as a function of the packing density, meaning that the crystallinity does not influence significantly its Young modulus.

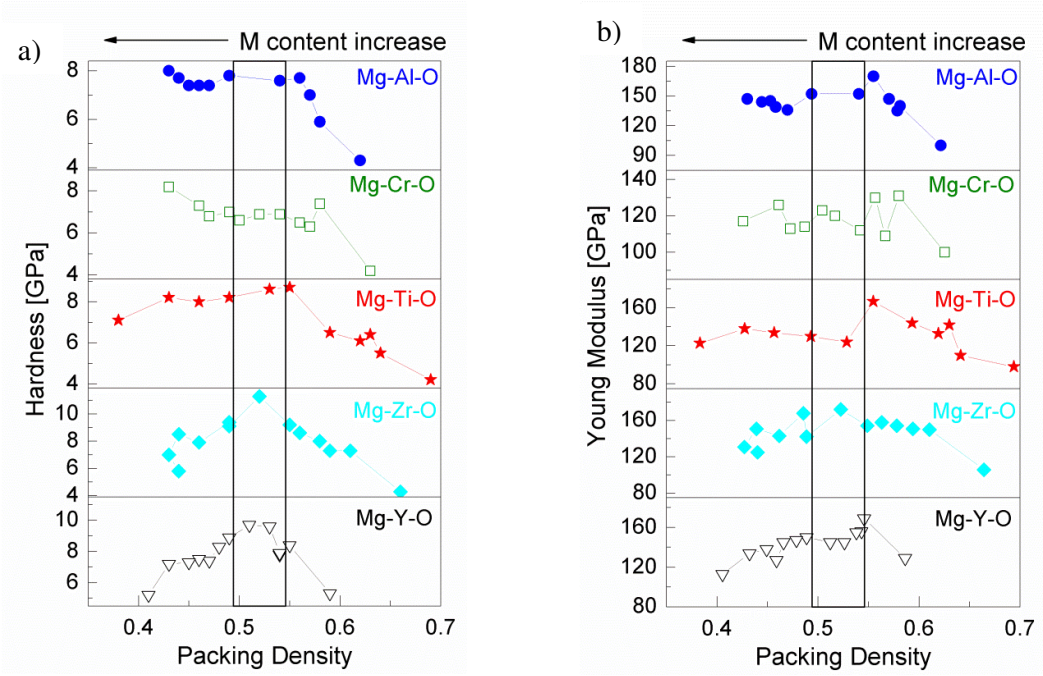

Figure 10.5: a) Hardness and b) Young modulus of the deposited Mg-*M*-O films as a function of the packing density.

The change of band gap in the Mg-Al-O and Mg-Cr-O films as a function of the packing density resembles the behavior of the hardness (figure 10.6a)). Two regions can be identified when studying the change of the band gap as a function of the calculated packing density. A clear change of the slope is noticed when changing from the crystalline (or nanocrystalline) region (high packing density) to amorphous region (low packing density). For the other systems, Mg-Ti-O, Mg-Zr-O and Mg-Y-O, there is no variation in the slope of the band gap change as a function of packing density, implying that crystallinity has a lower influence on this property which is rather determined by changes of the composition.

In figure 10.6b) the refractive index as a function of the packing density for the different Mg-M-O films is shown. In the case of the Mg-Al-O films, the system can be divided in two groups: for high values of packing density (packing density > 0.545) and lower values of packing density. For the Mg-Cr-O and Mg-Zr-O, there is a linear relation between the refractive index and the packing density, implying that the crystallinity does not affect the

referred property. The refractive index of the Mg-Y-O films can also be divided in two regions, with the transition point between the regions at packing density of 0.495.

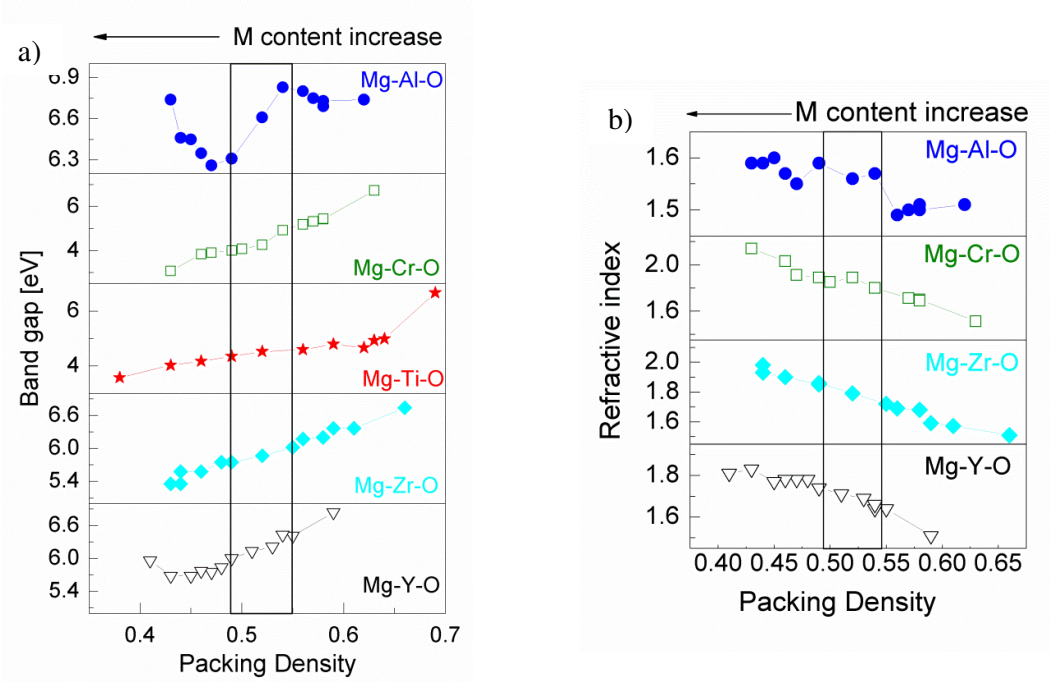

Figure 10.6: a) Band gap and b) refractive index at $\lambda = 550$ nm of the deposited Mg-*M*-O films as a function of the packing density.

The σ_{AC} as a function of packing density for the Mg-Al-O, Mg-Cr-O and Mg-Ti-O is plotted in figure 10.7a). Similar to what was observed for the refractive index, the Mg-Cr-O is not affected by the crystallinity. On the contrary, Mg-Al-O and Mg-Ti-O are influenced by the crystallinity and therefore, the graphs can be divided in two regions, being the transition between region at a packing density of 0.495 and 0.545 for Mg-Al-O and Mg-Ti-O, respectively.

Figure 10.7b) presents the surface roughness and energy as a function of packing density for the Mg-Al-O films. While the surface roughness of the films can be divided into three regions, the surface energy is divided in two regions. For the surface roughness the three regions coincide with crystallinity regimes determined by the packing density, while for the surface energy, the transition from one region to another happens inside the boundary region (packing density between 0.495 and 0.545). The surface roughness and energy can be related to the films surface morphology.

From figures 10.1 to 10.3 a non-monotonous behavior in the properties as a function of the composition can be seen which means that their change does not obey a simple rule of mixtures. The properties are affected by the chemical composition of the film and by its structure. Considering figures 10.5 to 10.7 one can conclude that the influence of the composition compared to the influence of the crystallinity in the properties is material and property dependent.

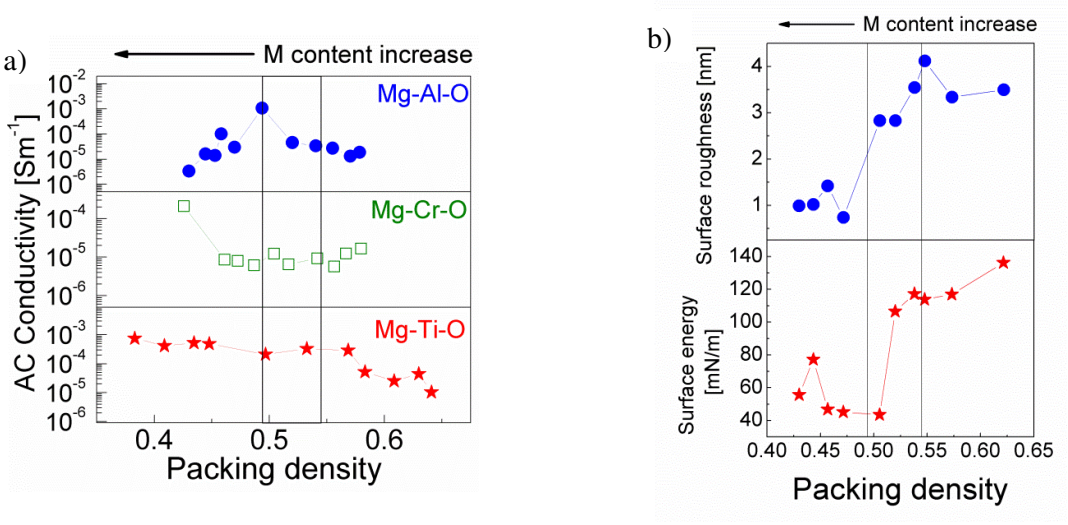

Figure 10.7: a) AC conductivity at 1 MHz and 300 K of the deposited Mg-*M*-O films as a function of C_M. b) Surface roughness and energy of the Mg-Al-O films as a function of C_{Al}.

References

1 D.L. Smith, *Thin film deposition, principles and practice*. (McGraw-Hill, 1995).

2 J. Patscheider, N. Hellgren, R. T. Haasch, I. Petrov, and J. E. Greene, Physical Review B **83** (12), 125124 (2011).

3 G. Gassner, J. Patscheider, P. H. Mayrhofer, S. Sturm, C. Scheu, and C. Mitterer, Tribology Letters **27** (1), 97 (2007).

4 G. M. Pharr, W. C. Oliver, and F. R. Brotzen, Journal of Materials Research **7** (3), 613 (1992).

5 W. C. Oliver and G. M. Pharr, Journal of Materials Research **7** (6), 1564 (1992).

6 D. Poelman and P. F. Smet, Journal of Physics D-Applied Physics **36** (15), 1850 (2003).

7 R. Swanepoel, Journal of Physics E-Scientific Instruments **16** (12), 1214 (1983).

8 F. Kremer and A. Schönhals (editors), *Broadband dielectric spectroscopy*. (Springer-Verlag, Berlin, 2003).

9 A. K. Jonscher, *Dielectric relaxation in solids*. (Chelsea Dielectrics Press, London, 1983).

10 D. K. Owens and R. C. Wendt, Journal of Applied Polymer Science **13** (8), 1741 (1969).

11 R. N. Shimizu and N. R. Demarquette, Journal of Applied Polymer Science **76** (12), 1831 (2000).

12 D. Caceres, I. Vergara, and R. Gonzalez, Journal of Applied Physics **93** (7), 4300 (2003).

13 G. Alcala, P. Skeldon, G. E. Thompson, A. B. Mann, H. Habazaki, and K. Shimizu, Nanotechnology **13** (4), 451 (2002).

14 P. Yashar, J. Rechner, M. S. Wong, W. D. Sproul, and S. A. Barnett, Surface & Coatings Technology **94-5** (1-3), 333 (1997).

15 Harish C. Barshilia and K. S. Rajam, Applied Surface Science **255** (5), 2925 (2008).

16 K. Goedicke, J. S. Liebig, O. Zywitzki, and H. Sahm, Thin Solid Films **377**, 37 (2000).

17 P. J. Kelly, C. F. Beevers, P. S. Henderson, R. D. Arnell, J. W. Bradley, and H. Backer, Surface & Coatings Technology **174**, 795 (2003).

18 S. Ullah, A. H. Dogar, N. Mehmood, S. Hussain, and A. Qayyum, Vacuum, 509 (2009).

19 P. Hones, M. Diserens, and F. Levy, Surface & Coatings Technology **120**, 277 (1999).

20 W. T. Tang, Z. F. Ying, Z. G. Hu, W. W. Li, J. Sun, N. Xu, and J. D. Wu, Thin Solid Films **518** (19), 5442.

21 S. B. Amor, L. Guedri, G. Baud, M. Jacquet, and M. Ghedira, Materials Chemistry and Physics **77** (3), 903 (2003).

22 L. Lou, W. Zhang, A. Brioude, C. Le Luyer, and J. Mugnier, Optical Materials **18** (3), 331 (2001).

23 C. Ye, S. S. Pan, X. M. Teng, and G. H. Li, Journal of Applied Physics **102** (1) (2007).

24 D. H. Kuo and K. H. Tzeng, Thin Solid Films **460** (1-2), 327 (2004).

25 M. F. Al-Kuhaili and S. M. A. Durrani, Optical Materials **29** (6), 709 (2007).

26 D. Pamu, K. Sudheendran, M. Ghanashyam Krishna, K. C. James Raju, and Anil K. Bhatnagar, Thin Solid Films **517** (5), 1587 (2009).

27 X. J. Wang, L. D. Zhang, J. P. Zhang, G. He, M. Liu, and L. Q. Zhu, Materials Letters **62** (26), 4235 (2008).

Summary

The goal of the present thesis is to contribute towards understanding the fundamental growth mechanisms of sputter deposited ternary oxide films with the general formula Mg-M-O (where M is a metal different than Mg). The key objectives of the study are:

(i) To establish the relation between the deposition conditions and the chemical composition in the Mg-M-O films and through this, achieve an efficient and accurate control over the film stoichiometry.

(ii) To understand the effect of the deposition conditions and the chemical composition on the structure formation and crystallographic properties of Mg-M-O films.

(ii) To elucidate the effect of chemistry and microstructure on a number of functional properties of the Mg-M-O films.

Films are deposited employing reactive magnetron sputtering (in an Ar-O_2 atmosphere) from two (Mg and M) confocally arranged magnetron sources. This multisource approach facilitates a large flexibility with respect to the chemical compositions that can be accessed. In addition, the confocal arrangement of the sources leads to an off-normal deposition flux providing a tool to control and tune the crystallographic properties of the films. The metals (M) Al, Cr, Ti, Y and Zr are chosen to systematically vary key physical parameters of the substituting element in the metal sublattice of the Mg-M-O films, i.e. the valence electron number and the atomic size, and to study their largely unexplored effect on the film microstructure and crystallographic properties.

The goal and the objectives of this work can only be achieved with a good knowledge on the fundamentals of the sputter deposition process and the thin film growth. Therefore, in part A of the thesis the magnetron sputter deposition process is discussed. An overview of the ion-target interactions, the factors that influence the sputter yield, the energy and angular distribution of the sputtered particles is presented. The principles of magnetron sputtering and the effect of adding a reactive gas to the process are also discussed. This is followed by the fundamentals of the thin film growth. The formation of a thin film starts when the vapor phase reaches the substrate (adsorption). Once adsorbed on the solid surface, the adsorbed atoms (adatoms) may have enough energy to move across the surface (surface diffusion). While diffusing, they may encounter other adatoms and form stable islands (nucleation). The thermodynamic theory of nucleation and the thermodynamically determined film growth modes are presented. The influence of deposition rate and temperature on the nucleation characteristics is discussed. Nucleation is not only determined by thermodynamics, therefore kinetic aspects of nucleation are also highlighted. After nucleation, numerous distinct islands that are dispersed on the substrate grow by incorporating adatoms and the vapor phase atoms, until they coalesce with other islands (crystal growth). The coalesced islands rearrange themselves through grain boundary migration, which gives rise to new single crystalline or polycrystalline structures (grain growth). The final structure and morphology of the thin film

is strongly dependent on the presence (or absence) of grain restructuration, which is determined by the mobility of the grain boundaries. A convenient way of describing the evolution of polycrystalline films is by means of the so-called, structure zone models. A basic structure zone model for pure metals and an extended structure zone model (where impurities are considered) are briefly outlined.

Part B explores the relation between the deposition conditions (target-to-substrate distance and O_2 partial pressure) and the chemical composition of the thin films. The set-up used to deposit the thin films is presented, along with the principles of electron probe microanalysis that is employed to experimentally determine the film composition. The latter is also predicted theoretically by using two approaches: (i) an analytical relation that utilizes the fact that the deposition rate varies inversely as the square of the target-substrate distance and (ii) a Monte–Carlo-based simulation of the sputter deposition process (SIMTRA code). The remarkable agreement between the experimental and simulated compositions indicates that the implementation of the SIMTRA code with appropriate values for sputter yields allows for the prediction of the stoichiometry in multielement thin films.

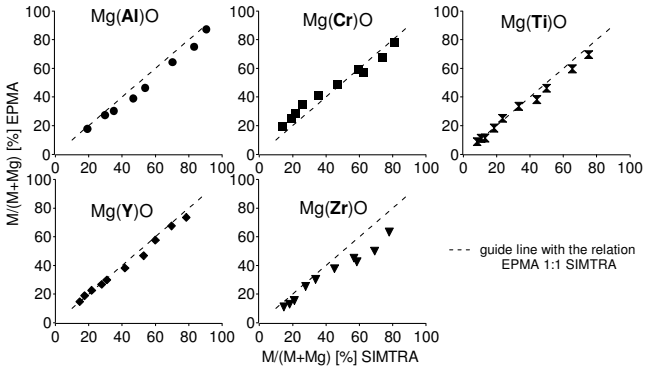

Part C elucidates the effect of deposition conditions and the chemical composition on the film structure formation and crystallographic properties. X-ray diffractometry (XRD), transmission electron microscopy (TEM) and scanning electron microscopy (SEM) are the techniques chosen to assist this task. From the angular XRD scans, it is found that under the given experimental conditions, pure MgO films grow with a (111) preferential out-of-plane orientation. Adding another metal M to MgO results in changes in the lattice parameter, which are in agreement with Vegard's law. It is therefore, concluded, that M is in solid solution with MgO. In addition, an increase of the M content yields a deterioration of the film crystallinity and formation of amorphous films, at relatively large M contents. To explain the transition from crystalline-to-amorphous, a reasoning based on the difference in the cation electron valence number is developed. The MgO structure can be seen as a stable packing of MgO octahedra. Substituting Mg^{2+} by another M^{n+} (with n>2), results in vacancies formation in order for the charge neutrality of the crystal to be maintained. When half of the MgO octahedra are replaced by either vacancies or another metal, the structure collapses, explaining the occurrence of the crystalline-to-amorphous transition at a M/(M+Mg) ratio 35-45%. An additional feature is that the M^{n+} cation has a different radius than Mg^{2+}, which also influences the structure. This is taken into account by developing a second approach that is

based on the so-called hard sphere model, which correlates disorder and structural stability using the notion of the packing density. Therefore, the substitution of Mg by M is resembled by relating a hard sphere to each filled octahedral position in the MgO structure. In this way, it is shown that the Mg-M-O structure undergoes a crystalline-to-amorphous transition at the same values of packing density and for the same reasons as those predicted by the hard sphere model. In the transition region (for packing densities between 0.495 and 0.545) the film structure consists of nanocrystals embedded in an amorphous matrix, similar to the coexistence of the two phases (crystalline and amorphous) in the hard-sphere model.

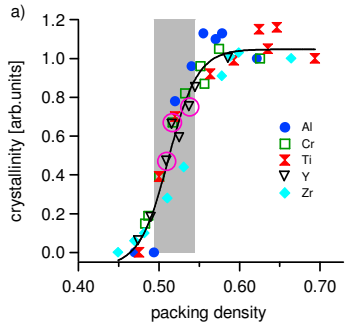

All the deposited Mg-M-O films are biaxially aligned, while they are crystalline. It is found that when the two sputtering cathodes are equipped with the same target material (Mg), the in-plane alignment is defined by the source closest to the substrate, i.e., by the largest material flux. Thus, films exhibiting either single or double in-plane alignment can be deposited. Double in-plane alignment is also observed for the Mg-Al-O and Mg-Cr-O films, while Mg-Ti-O, Mg-Zr-O and Mg-Y-O exhibit single in-plane alignment. It is argued that the double in-plane alignment in the case of Mg-Al-O and Mg-Cr-O films is promoted by the larger diffusivity of Al and Cr compared to Ti, Zr, and Y. The grains and the columns of the Mg-Al-O, Mg-Cr-O and Mg-Ti-O films are found to be tilted towards the Al, Cr and Ti flux, respectively, while for the Mg-Zr-O and Mg-Y-O the tilt occurs towards the Mg material flux. The tilt of the grains can be understood from the compositional gradient over the film and from the difference of the two cation radii in the Mg-M-O cell, which triggers a distortion in the lattice. The stacking of the distorted cells in the grain results in a tilt of the columns. Both, grains and columns, tilt towards the direction of the material flux with the smallest cation radius.

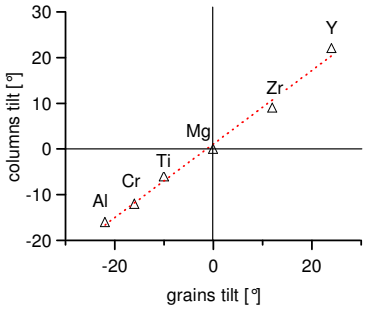

Deposition of Mg-Al-O films at elevated temperatures (300, 500 and 700 °C) does not lead to the formation of the spinel structure (predicted by the phase diagram for the systems with the composition MgM_2O_4). On the contrary, solid solutions are obtained. Films deposited at

700°C become amorphous at larger Al contents, as compared to the films deposited at room temperature. However, the high temperature films exhibit, at relatively high Al contents, phase separation in MgO- and Al_2O_3-rich regions, i.e. the maximum amount of Al that can be incorporated in the MgO lattice is smaller than that of films deposited at room temperature. Mg-Cr-O films deposited at 700 °C do not exhibit the spinel structure either. Pure Cr_2O_3 deposited at high temperature is found to be crystalline. The Mg-Al-O films deposited without intentional substrate heating and at 700 °C are subjected to post deposition annealing. It is found that the films deposited at room temperature start to form the spinel structure at a lower annealing temperatures, as compared to the films deposited at 700 °C. Since the latter films exhibit phase separation, the behavior described above is attributed to the proximity between the Mg-Al-O solid solution (abundant in films deposited at room temperature) and the spinel structure.

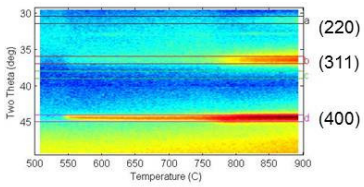

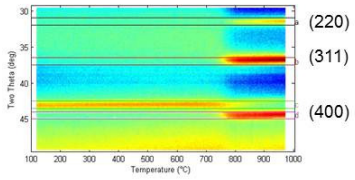

In part D a number of functional properties, i.e. mechanical, optical, and electrical properties, surface topography and energy, are studied in order to highlight how composition and crystallinity can affect these properties. An overview of the characterization techniques - nanoindentation, transmission spectroscopy, impedance spectroscopy, contact angle and atomic force microscopy - employed for the film characterization is presented. It is found that the properties do not have a monotonous behavior as a function of the chemical composition, meaning that they do not follow a simple rule of mixtures. The properties are affected by the chemical composition of the film and by its crystallinity. The significance of the influence of the composition and the crystallinity is material and property dependent. By using the packing density it is possible to decouple the influence of the crystallinity from the influence of the composition, distinguishing regions where the composition (or crystallinity) has a dominant influence on the properties of the films.

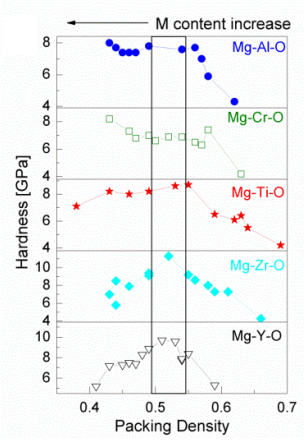

Samenvatting

De thesis is een bijdrage tot het fundamenteel onderzoek naar de groeimechanismen bij de sputterdepositie van dunne lagen van ternaire oxides met als algemene formule Mg-M-O, waarbij M een metaal verschillend van Mg is. De doelstellingen van deze studie zijn:

1) De efficiënte controle van de laagsamenstelling door het opstellen van relaties tussen de depositieomstandigheden en de chemische samenstelling van afgezette Mg-M-O dunne lagen.
2) Het begrijpen van het effect van de depositieomstandigheden en de chemische samenstelling op de microstructuur en textuur van de Mg-M-O dunne lagen.
3) Het blootleggen van het verband tussen de microstructuur, textuur en chemische samenstelling met een aantal functionele eigenschappen van de Mg-M-O dunne lagen.

De lagen werden afgezet door middel van reactief magnetron sputterdepositie. Hiertoe werden twee magnetrons naar hetzelfde substraat gebruikt. Deze multibron benadering laat toe om de chemische samenstelling van de laag gemakkelijk te wijzigen. Daarenboven resulteert deze confocale opstelling van de bronnen tot schuine inval van de opbouwende atomen waardoor de laag unieke kristallografische eigenschappen verkrijgt. De elementen M (=Al, Cr, Ti, Y en Zr) in Mg-M-O lagen werden gekozen omwille van hun sterk variërende kationgrootte en valentie. Het effect van de substitutie van Mg door één van deze elementen in de MgO structuur op de laaggroei vormt het kernthema van deze thesis.

In deel A van deze thesis worden de basisaspecten van magnetron sputterdepositie behandeld. Een goede beschrijving van dit proces is noodzakelijk om de doelstellingen en onderzoeksresultaten van deze thesis te begrijpen. Deel A start met een overzicht van de ion-vastestofinteracties, en de factoren die de sputteropbrengst, de energie en de angulaire distributie van de gesputterde deeltjes beïnvloeden. Daarnaast wordt de invloed van het toevoegen van een reactief gas aan het magnetron plasma behandeld. De basisaspecten van dunne filmgroei komen daarna aan bod. De groei van een dunne film start met de condensatie van de dampfase op het substraat (adsorptie). De geadsorbeerde atomen (of adatomen) kunnen voldoende energie hebben om zich over het oppervlak te bewegen (oppervlakdiffusie). Tijdens de diffusie op het oppervlak vormen zij met andere atomen stabiele eilanden (nucleatie). De nucleatietheorie, steunend op een aantal thermodynamische principes, wordt kort behandeld. Tal van kinetische processen beïnvloeden echter ook het nucleatieproces. Sommige ervan worden ook in dit inleidend deel belicht. Na de nucleatie groeien de gevormde eilanden verder door adatomen en atomen uit de dampfase in te vangen. Dit proces gaat verder tot de eilanden elkaar raken. Het samenvloeien van deze kristalletjes, en het herschikken van de gevormde korrelgrenzen kan de verdere laaggroei beïnvloeden. De finale textuur en microstructuur van de dunne laag is sterk afhankelijk van het al dan niet optreden van korrelgrensmigratie en vergelijkbare processen. Een interessante manier om de microstructurele evolutie tijdens de laaggroei te beschrijven zijn zogenaamde ‘structuur-zonemodellen’. Twee dergelijke modellen worden kort toegelicht in dit onderdeel van de

thesis: het structuurzonemodel voor de groei van zuivere materialen, en een uitgebreid structuurzonemodel waarbij de rol van onzuiverheden wordt behandeld.

Deel B beschrijft de onderzoeksresultaten waarbij de relatie tussen de depositieomstandigheden (target-substraatafstand en zuurstof partieeldruk) en de chemische samenstelling van de afgezette lagen werd onderzocht. De gebruikte depositieopstelling wordt in detail beschreven, samen met de basisprincipes van EPMA (Electron Probe MicroAnalysis). Deze laatste techniek werd gebruikt om de samenstelling van de lagen te bepalen. De chemische samenstelling werd ook op twee verschillende manieren voorspeld. Een eerste manier is een zuiver analytische manier gebruikmakend van het verband tussen de depositiesnelheid en de target-substraatafstand. De tweede manier steunt op Monte Carlo simulaties met de code SIMTRA. De goede overeenkomst tussen de gesimuleerde en experimentele samenstelling toont aan dat deze code, gebruikmakende van geschikte waarde voor de sputteropbrengst, toelaat om de stoichiometrie van multi-element dunne lagen te voorspellen.

Deel C onderzoekt het effect van de depositieomstandigheden en de chemische samenstelling op de microstructuur en de textuur van de lagen. X-straaldiffractie (XRD), tranmissie elektronenmicroscopie (TEM) en rasterelektronen microscopie (SEM) zijn de aangewende technieken om deze relatie te begrijpen. XRD metingen in Bragg-Brentano configuratie tonen aan dat de samenstellende kristalletjes van zuivere MgO dunne lagen met een preferentiële (111) uit-het-vlak orientatie groeien. De toevoeging van een andere metaal M resulteert in een verandering van de roosterparameter in overeenstemming met de empirische wet van Vegard. Op basis hiervan kan besloten worden dat de Mg-M-O lagen kunnen beschreven worden als vastestofoplossingen (solid solutions) van MgO en het M metaaloxide. Het verhogen van de M concentratie heeft nog een tweede belangrijk effect, namelijk een vermindering van de kristalliniteit van de laag. Bij hoge concentraties wordt uiteindelijk een amorfe laag gevormd. Om deze overgang van een kristallijne naar amorfe laag te beschrijven werd een eenvoudig model opgesteld gebaseerd op de vorming van metaalvacatures. De MgO structuur kan worden aanzien als een stabiele stapeling van MgO octaëders. Door Mg^{2+} te vervangen door M^{n+} (met n>2) worden metaalvacatures gevormd om zo de ladingsneutraliteit van de structuur te bewaren. Wanneer de helft van deze octaëders wordt vervangen door ofwel een vacature ofwel door een octaëder gerelateerd aan het M metaalion, blijkt de MgO structuur niet meer stabiel. Op deze wijze kan het optreden van de kristallijn-naar-amorf transitie bij een M/(M+Mg) verhouding van 35-45% verklaard worden. Dit eenvoudige model werd verder uitgebouwd tot een meer volwaardig model gebaseerd op het zogenoemde harde-sfeermodel. In dit laatste model treedt eveneens een transitie op steunend op de wanorde veroorzaakt door de pakkingdichtheid van de harde sferen te verminderen. Door aan elke gevulde octaëder in de Mg-M-O structuur een harde sfeer toe te kennen, kan dit model gebruikt worden om de kristallijne-naar-amorfe transitie te beschrijven. Gebruikmakend van dit model wordt aangetoond dat alle Mg-M-O lagen zich op dezelfde wijze gedragen wanneer de M concentratie wordt verhoogd. In het transitiegebied tussen kristallijn en amorf worden in overeenstemming met het harde-sfeermodel, bij een pakkingdichtheid tussen 0.495 en 0.545 beide fasen samen vastgesteld, d.i. nanokristallijn materiaal in een amorfe matrix.

De kristallijne Mg-M-O lagen zijn biaxiaal gealigneerd. Het groeimechanisme werd onderzocht door eerst MgO dunne lagen af te zetten met twee bronnen voorzien van een Mg target. Uit deze studie blijkt dat de oriëntatie van kristallen in het substraatvlak bepaald wordt door de bron dichtst bij het substraat. Bij vergelijkbare afstanden worden twee tegenovergestelde in-het-vlakoriëntaties vastgesteld. Deze textuur wordt ook waargenomen bij de depositie van Mg-Al-O en Mg-Cr-O dunne lagen. Voor Mg-Ti-O, Mg-Zr-O en Mg-Y-O wordt, ondanks gebruik van twee bronnen, slechts één in-het-vlakoriëntatie vastgesteld. Het onderscheid tussen deze twee groepen is vermoedelijk gebaseerd om het verschil in de oppervlakmobiliteit van Al en Cr in vergelijking met Ti, Zr en Y. De kristallen en de opbouwende kolommen van de laag zijn bij de Mg-M-O lagen gekanteld. De kantelhoek is materiaalafhankelijk. Bij Al, Cr en Ti kantelen ze weg van de Mg bron, terwijl het omgekeerde wordt vastgesteld bij Y en Zr. De oorsprong van het kantelen ligt in de compositiegradiënt en het verschil in de straal tussen het Mg en het M kation. Hierdoor ontstaat een distorsie van het rooster. Het stapelen van de vervormde eenheidscellen leidt tot het kantelen van de kolommen.

De depositie van Mg-Al-O dunne lagen op hoge substraattemperatuur (300, 500 en 700°C) leidt niet tot de vorming van de spinelstructuur met een samenstelling $MgAl_2O_4$ zoals verwacht op basis van het fasediagram. Ook bij hoge substraattemperatuur wordt een (gedeeltelijke) vastestofoplossing bekomen. Bij depositie bij 700°C als substraattemperatuur schuift de transitie van kristallijn-naar-amorf op naar hogere Al concentraties maar dit is te wijten aan de faseseparatie in MgO en Al_2O_3, of met andere woorden er wordt minder Al in de MgO structuur opgenomen. Ook bij de depositie van Mg-Cr-O dunne lagen op hoge substraattemperatuur wordt geen spinelvorming vastgesteld. In tegenstelling tot Al wordt bij Cr, zonder toevoeging van Mg, kristallijn Cr_2O_3 gevormd. Het gedrag bij opwarmen van de laag na depositie (post-annealing) van Mg-Al-O dunne lagen afgezet zonder substraatverwarming en met substraatverwarming (bij 700°C) werd vergeleken. De vormingstemperatuur van de spinelfase treedt vroeger op bij de samples afgezet zonder substraatverwarming.

In deel D van deze thesis worden een aantal functionele eigenschappen en hun relatie met de samenstelling en de kristalliniteit onderzocht. Eerst worden de karakteriseringstechnieken kort beschreven. Voor de mechanische eigenschappen is dit nano-indentatie. De optische eigenschappen werden bestudeerd met optische transmissie spectroscopie. Elektrische eigenschappen werden met impedantiespectroscopie bestudeerd. Voor de oppervlakenergie en de oppervlakruwheid werd gekozen voor respectievelijk contacthoekmetingen en AFM (Atomic Force Microscopy). Voor tal van eigenschappen werd geen monotoon gedrag in functie van de laagsamenstelling vastgesteld. Dit betekent dat deze eigenschappen niet het resultaat zijn van de optelsom van de eigenschappen van de individuele oxides. Door het voorgestelde model voor de kristallijne-naar-amorfe transitie te gebruiken kan de invloed van de chemische samenstelling en de kristalliniteit op deze functionele eigenschappen van elkaar onderscheiden worden.

Appendices

A. Mg-M-O Stoichiometry

A1

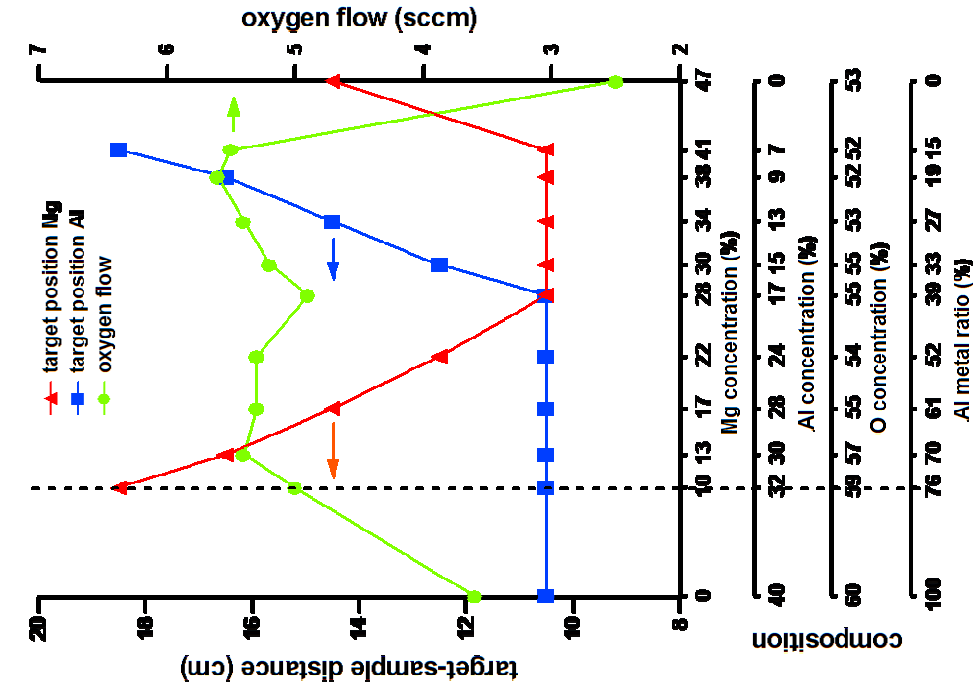

A2

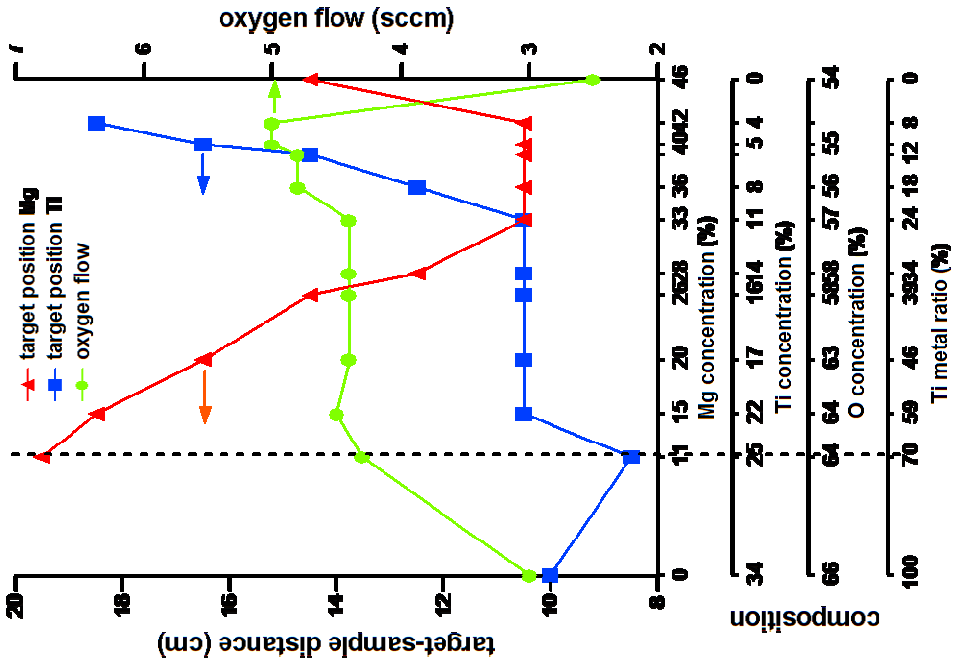

A3

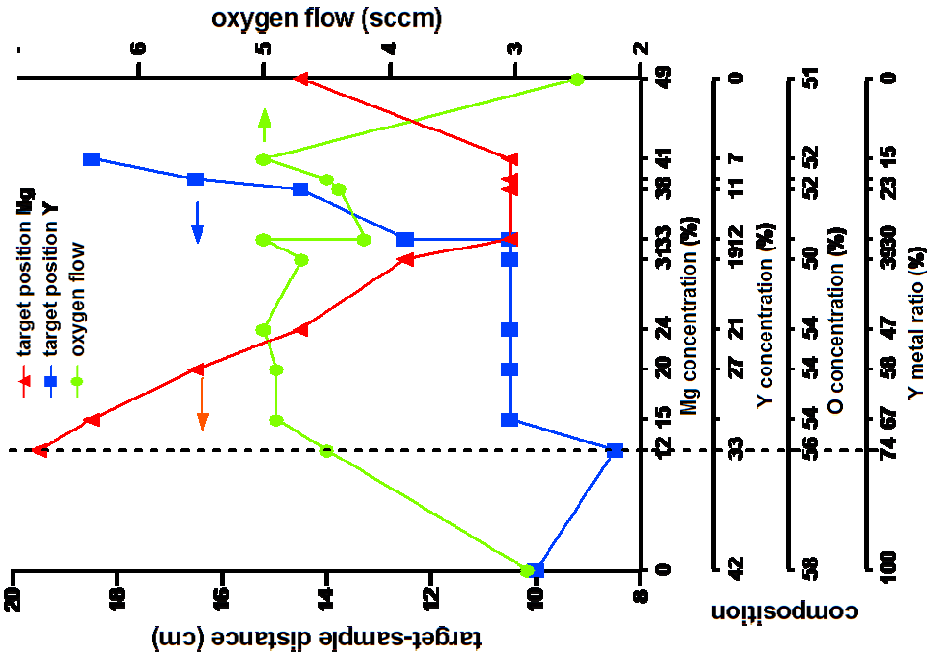

A4

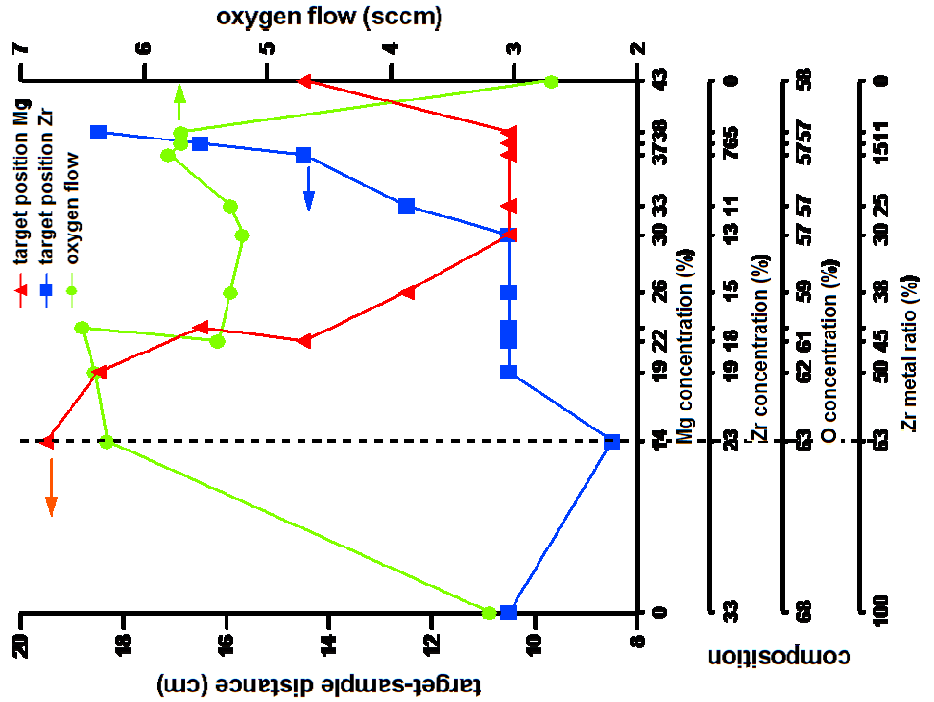

Figure A.1-A.4: Series of Mg-Al-O, Mg-Ti-O, Mg-Y-O and Mg-Zr-O thin films, respectively. The dotted lines are guidelines which relates the sample composition (the 4 horizontal axes which represent respectively the Mg, Al (or Ti, Zr or Y), O concentration and the Al (Ti, Y or Zr) metal ratio) to the experimental conditions, i.e. the target-to-substrate distance (left hand axis) and the oxygen flow (right hand axis).

B. ICDD Data Information

Pattern: 00-045-0946 ***Radiation =*** 1.540598 ***Quality :*** High

MgO

Magnesium Oxide
Periclase, syn
Lattice : Face-centered cubic
S.G. : Fm-3m (225)
a = 4.21120
Z = 4
Sample preparation: MgO (Heraeus, 99.99 %) annealed in open Au crucible
at 800 C for 1 week.
Additional pattern: To replace 4-829.
General comments: Validated by calculated pattern 43-1022.
Data collection flag: Ambient.
Kern, A., Doetzer, R., Eysel, W., Mineralogisch-Petrographisches Inst., Univ. Heidelberg, Germany., ICDD Grant-in-Aid (1993)
Radiation : CuKa1
Lambda : 1.54060
SS/FOM : F10=101(0.0099,10)
Filter : Monochromator crystal
d-sp : Diffractometer
Internal standard : Si

2th	*i*	*h*	*k*	*l*
36.937	4	1	1	1
42.917	100	2	0	0
62.304	39	2	2	0
74.691	5	3	1	1
78.630	10	2	2	2
94.051	8	4	0	0
105.734	2	3	3	1
109.765	19	4	2	0
127.285	14	4	2	2
143.754	4	5	1	1

Pattern: 00-021-1152 ***Radiation =*** 1.540598 ***Quality :*** High

$MgAl_2O_4$

Magnesium Aluminum Oxide
Spinel, syn
Lattice : Face-centered cubic
S.G. : Fd-3m (227)
a = 8.08310
Z = 8
Sample source or locality: The sample was furnished by H.R. Shell, Bureau
of Mines, College Park, Maryland, USA.
Sample preparation: Shell used a carbon electrode furnace and removed an
excess of MgO with hot HCl after crushing.
Temperature of data collection: Pattern taken at 25 C.
Optical data: B=1.718
Data collection flag: Ambient.
Natl. Bur. Stand. (U.S.) Monogr. 25, volume 9, page 25 (1971)
CAS Number: 1302-67-6
Radiation : CuKa1
Lambda : 1.54050
SS/FOM : F29= 58(0.0151,33)
Filter : Monochromator crystal
d-sp : Not given
Internal standard : Ag

2th	*i*	*h*	*k*	*l*
19.029	35	1	1	1
31.272	40	2	2	0
36.853	100	3	1	1
38.525	4	2	2	2
44.833	65	4	0	0
55.660	10	4	2	2
59.371	45	5	1	1
65.243	55	4	4	0
68.642	4	5	3	1
74.132	4	6	2	0
77.326	8	5	3	3
78.405	2	6	2	2
82.645	6	4	4	4
85.762	2	5	5	1
90.977	6	6	4	2
94.099	12	7	3	1
99.347	8	8	0	0
107.908	2	6	6	0
111.230	8	7	5	1
112.321	2	6	6	2
116.923	6	8	4	0
120.509	2	9	1	1
121.702	2	8	4	2
126.769	2	6	6	4
130.739	8	9	3	1
138.073	18	8	4	4
142.989	2	7	7	1
152.693	2	10	2	0
160.661	12	9	5	1

Pattern : 00-010-0351 ***Radiation =*** 1.540598 ***Quality :*** High
$MgCr_2O_4$
Magnesium Chromium Oxide
Magnesiochromite, syn
Lattice : Face-centered cubic
S.G. : Fd-3m (227)
a = 8.33300
Z = 8
Sample preparation: Sample prepared at NBS, Gaithersburg, Maryland, USA, by fusion of MgO and Cr2 O3 in carbon arc.
Analysis: Spectroscopic analysis showed <1.0% Na, Si; <0.1% Al, Ca, Fe; <0.01% Cu, Ni, Sr, Ti.
Temperature of data collection: Pattern taken at 26 C.
General comments: Measured density from *Dana's System of Mineralogy, 7th Ed.*, **I** 709.
Additional pattern: To replace 20-674.
Color: Dark brownish green
Data collection flag: Ambient.
Natl. Bur. Stand. (U.S.), Circ. 539, volume 9, page 34 (1960)
Radiation : CuKa1
Lambda : 1.54050
SS/FOM : F28= 81(0.0101,34)
Filter : Beta
d-sp : Not given

2th	*i*	*h*	*k*	*l*
18.419	65	1	1	1
30.325	14	2	2	0
35.715	100	3	1	1
37.345	14	2	2	2
43.407	55	4	0	0
47.516	6	3	3	1
53.853	4	4	2	2
57.441	40	5	1	1
63.055	55	4	4	0
66.287	14	5	3	1
71.553	2	6	2	0
74.603	14	5	3	3
75.635	10	6	2	2
79.647	10	4	4	4
82.645	10	5	5	1
87.533	4	6	4	2
90.462	12	7	3	1
95.371	6	8	0	0
103.319	1	8	2	2
106.351	8	7	5	1
107.382	2	6	6	2
111.536	8	8	4	0
114.752	6	9	1	1
123.709	6	9	3	1
129.836	10	8	4	4
133.782	4	7	7	1
145.951	10	9	5	1
147.723	4	10	2	2

Pattern : 00-041-1105 ***Radiation =*** 1.540598 ***Quality :*** High
Y_2O_3
Yttrium Oxide
Also called: yttria
Lattice : Body-centered cubic
S.G. : Ia-3 (206)
a = 10.60410
Z = 16
Sample preparation: Annealed for 48 hours at 1200 C.
General comments: Average relative standard deviation in intensity of the ten strongest reflections for three specimen mounts = 2%.
General comments: Validated by a calculated pattern.
Additional pattern: To replace 25-1200.
Data collection flag: Ambient.
Martin, K., McCarthy, G., North Dakota State University, Fargo, North Dakota, USA., ICDD Grant-in-Aid (1989)
Radiation : CuKa1
Lambda : 1.54060
SS/FOM : F30=160(0.0060,31)
Filter : Monochromator crystal
d-sp : Diffractometer
Internal standard : Si

2th	*i*	*h*	*k*	*l*
16.692	1	2	0	0
20.495	13	2	1	1
29.150	100	2	2	2
31.532	1	3	2	1
33.784	24	4	0	0
35.907	5	4	1	1
37.909	1	4	2	0
39.847	6	3	3	2
41.695	1	4	2	2
43.499	8	4	3	1
46.899	2	5	2	1
48.541	39	4	4	0
50.129	2	4	3	3
51.668	1	6	0	0
53.211	5	6	1	1
54.699	1	6	2	0
56.174	4	5	4	1
57.622	25	6	2	2
59.042	5	6	3	1
60.441	4	4	4	4
61.822	2	5	4	3
63.180	1	6	4	0
64.528	3	7	2	1
65.860	1	6	4	2
69.778	2	6	5	1
71.061	4	8	0	0
72.339	3	8	1	1
73.602	2	8	2	0
74.858	2	6	5	3
76.113	1	6	6	0
77.348	3	8	3	1
78.590	6	6	6	2
79.814	1	7	5	2
81.040	4	8	4	0
82.258	1	8	3	3
83.483	1	8	4	2
84.696	2	9	2	1
85.903	1	6	6	4
87.121	2	8	5	1
89.537	2	9	3	2
90.751	4	8	4	4
91.960	2	9	4	1
93.175	1	10	0	0
94.381	1	10	1	1
95.590	3	10	2	0
96.811	1	9	4	3
98.033	3	10	2	2
99.254	2	10	3	1
101.714	2	8	7	1
102.967	2	10	4	0
104.199	1	10	3	3
105.455	2	10	4	2
106.703	1	9	5	4
109.235	2	11	2	1
110.519	1	8	8	0
113.121	1	10	4	4
114.479	1	11	3	2
115.803	1	10	6	0
117.151	1	11	4	1
118.503	2	10	6	2
119.948	1	9	6	5

C. Publication List

Contributions to Scientific Journals:

- M. Saraiva, H. Chen, W. P. Leroy, S. Mahieu, N. Jehanathan, O. Lebedev, V. Georgieva, R. Persoons, and D. Depla, *Influence of Al Content on the Properties of MgO Grown by Reactive Magnetron Sputtering*, Plasma Processes and Polymers **6**, S751 (2009).
- V. Georgieva, M. Saraiva, N. Jehanathan, O. I. Lebelev, D. Depla, and A. Bogaerts, *Sputter-deposited Mg-Al-O thin films: linking molecular dynamics simulations to experiments*, Journal of Physics D-Applied Physics **42** (6) (2009).
- M. Saraiva, V. Georgieva, S. Mahieu, K. Van Aeken, A. Bogaerts, and D. Depla, *Compositional effects on the growth of Mg(M)O films*, Journal of Applied Physics **107** (3), 034902 (2010).
- N. Jehanathan, V. Georgieva, M. Saraiva, D. Depla, A. Bogaerts, and G. Van Tendeloo, *The influence of Cr and Y on the micro structural evolution of Mg-Cr-O and Mg-Y-O thin films*, Thin Solid Films **519** (16), 5388 (2011).
- M. Saraiva and D. Depla, *Texture and microstructure in co-sputtered Mg-M-O (M=Mg, Al, Cr, Ti, Zr, and Y) films*, (submitted for publication).
- M. Saraiva, R. Persoons and D. Depla, *Composition-Crystallinity-Property Relations in Mg-M-O films*, (submitted for publication).

Publications in journals without a reader committee:

- D. Depla, M. Saraiva and J. Lamas, *Dual magnetron sputtering of mixed oxide layers*, Belvac, October, (2011).

Contributions to Scientific Meetings:

- M. Saraiva, H. Chen, W. P. Leroy, S. Mahieu, N. Jehanathan, O. Lebedev, V. Georgieva, R. Persoons, and D. Depla, *Influence of Al Content on the Properties of MgO Grown by Reactive Magnetron Sputtering*, PSE2008,Garmisch-Partenkirchen, 14-19th September, (2008), poster presentation.
- M. Saraiva, H. Chen, W. P. Leroy, S. Mahieu, N. Jehanathan, O. Lebedev, V. Georgieva, R. Persoons, D. Depla, *Characterization of $Mg_xAl_yO_z$ thin films grown by reactive magnetron sputtering*, ICTF14-RSD2008, Gent, 17-20th November, (2008), oral presentation.
- V. Georgieva, M. Saraiva, N. Jehanathan, O. I. Lebedev, G. Van Tendeloo, D. Depla and A. Bogaerts, *Simulation and experimental study of Mg-Cr-O and Mg-Y-O thin films deposited by reactive magnetron sputtering*, DPSXXXII, Antwerp, September, (2009), poster presentation.
- M. Saraiva, V. Georgieva, S. Mahieu, K. Van Aeken, A. Bogaerts, D. Depla, *Compositional effects on the growth of Mg(M)O films*, RSD2009, Manchester, 10-11th December, (2009), oral presentation.

- M. Saraiva, V. Georgieva, S. Mahieu, R. Persoons, A. Bogaerts, D. Depla, *Understanding the growth of doped MgO*, E-MRS2010, Strasbourg, 7-11th June, (2010), poster presentation.
- V. Georgieva, M. Saraiva, N. Jehanathan, G. Van Tendeloo, D. Depla and A. Bogaerts, *Structure and properties of $Mg_xAl_yO_z$ thin films deposited by dual magnetron sputtering*, SPSSM, Stuttgart, 27thJune-2ndJuly, (2010), poster presentation.
- M. Saraiva, V. Georgieva, S. Mahieu, N. Jehanathan, A. Bogaerts, R. Persoons, D. Depla, *Understanding the growth of doped MgO,* PSE2010, 13-17th September, Garmisch-Partenkirchen, (2010), oral presentation.
- V. Georgieva, M. Saraiva, N. Jehanathan, G. Van Tendeloo, D. Depla, and A. Bogaerts. *Molecular dynamics simulations and experimental study of complex oxide thin film growth*, PSE2010, 13-17th September, Garmisch-Partenkirchen, (2010), oral presentation.
- M. Saraiva, V. Georgieva, N. Jehanathan, S. Mahieu, A. Bogaerts, R. Persoons, D. Depla, *Understanding the growth of doped MgO*, BCS2010, October, Brussels, (2010), oral presentation.
- V. Georgieva, M. Saraiva, N. Jehanathan, G. Van Tendeloo, D. Depla and A. Bogaerts, *Computational study of the activation energy barriers for surface diffusion during the oxide thin film growth process,* RSD2010, Ghent, 9-10th December, (2010), oral presentation.
- M. Saraiva, V. Georgieva, N. Jehanathan, S. Mahieu, A. Bogaerts, R. Persoons, D. Depla, *Fundamental aspects of mixed oxide thin film growth*, ICMCTF2011, 2-6th May, San Diego, (2011), oral presentation.
- V. Georgieva, M. Saraiva, N. Jehanathan, G. Van Tendeloo, D. Depla and A. Bogaerts, *Computational study of complex oxide thin film growth with emphasis on surface diffusion during the growth process,* ICMCTF2011, 2-6th May, San Diego, (2011), oral presentation.
- M. Saraiva, D. Depla, L.C. Costa, M.A. Valente and M.P.F. Graça, *Dielectric properties of NbOx thin films grown by DC magnetron sputtering*, E-MRS2011, 9-13th May, Nice, (2011), poster presentation.
- N. Jehanathan, M. Saraiva, D. Depla and G. Van Tendeloo, *Microstructure evolution of Mg-Al-O, Mg-Cr-O and Mg-Y-O thin films synthesized by reactive magnetron sputtering*, MCM2011, September, Urbino, (2011), oral presentation.
- D. Depla, M. Saraiva and J. Lamas, *Dual magnetron sputtering of mixed oxide thin films*, ISPP20122, Kyoto, (2011), 6-8th July, oral presentation (invited).
- D. Depla and M. Saraiva, *Biaxial aligned thin films*, RSD2011, Linköping, 8-9th December, (2011), oral presentation.
- D. Depla, M. Saraiva and J. Lamas, *Magnetron sputter deposition of biaxial aligned thin films*, EMA2012, Orlando, 18-20th January, (2012), oral presentation (invited).

Acknowledgments

This journey started when I left Portugal, 5 years ago. Since then, many people have crossed my path, contributing at some moment in time in one way or another to this work. It is impossible to acknowledge all these persons, as this list is quasi infinite. Nevertheless, I do feel like some people have been really crucial, and this is the place where I would like to express my gratitude to all of them.

First of all, I would like to thank my advisor Prof. Diederik Depla for the fact that he gave me the opportunity to join his group, created a stimulating working environment, provided me without hesitation with the means and the facilities to realize this work and was always available for discussions and helpful with ideas.

I would like to express my gratitude to Prof. Albano Cavaleiro, for opening the door for the beginning of this journey (coming to Belgium) and for the support given through all the way.

I would also like to thank the members of the reading and examination committee for their time and effort examining my work.

I would like to thank Dr. Rosita Persoons, Dr. Violeta Georgieva, Dr. Neeru Jehanathan, Dr. Oleg Lebedev, Prof. Annemie Bogaerts and Prof. Gustaaf Van Tendeloo for the collaboration work in the framework of the SBO project. Prof. Isabel Van Driessche I thank for the opportunity to perform the *ex-situ* heat treatments. I am also grateful to Prof. Pedro Graça and Prof. Manuel Valente, who received me so well at Aveiro University and guided me through the dielectrical properties world.

Within the Solid State Sciences Department, I start to thank all *Draftjes* for the good working environment, the help provided when requested and (very important) for the fun. A special thank word to Stijn for being more stubborn than me and to Wouter who "had to cope" with me in the office – it was a pleasure! I also acknowledge the restless assistance of Olivier, who always found the time and the way to help me. Gilbert en Lode, die me altijd een helpende hand geboden hebben wanneer ik het nodig had, dank u wel. To Werner, who has introduced me to the *in-situ* XRD world; and Philippe, for all the help with the optical measurements and trying to turn $MgAl_2O_4$ into a luminescent material – thank you. I am also grateful to the rest of the S1 colleagues, for providing a good working environment. Charlotte and Adela, I would like to thank for the countless lunches and coffee breaks.

Because life is more than work and I cannot live without an outside S1-life, I would like to take the opportunity to thank several special people who I am lucky enough to have in my life. To my friends, the ones I already had and the ones I met during this journey: you know you are an important part of my life. A very special word goes to Ba and Sylvie, from whom I never felt I was distant; to Marjan, Elena and Ana whom made me feel like I also have a family in Ghent; to Nuno, who made integration an easy task, for friendship and support through these years; and to Clara, who makes me smile and wanting to be a better person.

To Kostas, I am deeply thankful for not having given up on me during the last months (not even when my bad mood persisted for long periods) and for all the support: without you the last sprint would have been painful!

Last but not least, quero agradecer à minha família que sempre respeitou as minhas escolhas: muito obrigada pelo apoio e paciência! Continuam a fazer-me falta...

Obrigada,

Marta Saraiva